

See discussions, stats, and author profiles for this publication at: <https://www.researchgate.net/publication/231701196>

# Synthesis and Analysis of Zwitterionic Spherical Polyelectrolyte Brushes in Aqueous Solution

ARTICLE in MACROMOLECULES · FEBRUARY 2011

Impact Factor: 5.8 · DOI: 10.1021/ma102927c

---

CITATIONS

32

READS

43

---

## 5 AUTHORS, INCLUDING:



Frank Polzer

Humboldt-Universität zu Berlin

39 PUBLICATIONS 1,020 CITATIONS

[SEE PROFILE](#)



Matthias Ballauff

Helmholtz-Zentrum Berlin

433 PUBLICATIONS 13,371 CITATIONS

[SEE PROFILE](#)

**SCHRIFTENREIHE DES HZB · EXAMENSARBEITEN**

**Composites of Spherical  
Polyelectrolyte Brushes and  
Nanoparticles – Synthesis,  
Characterization and Their  
Use in Catalysis**

Frank Polzer

Dissertation

Institut für Weiche Materie und funktionale Materialien

Februar 2011

HZB-B 24

## **Berichte des Helmholtz-Zentrums Berlin (HZB-Berichte)**

Das Helmholtz-Zentrum Berlin für Materialien und Energie gibt eine Serie von Berichten über Forschungs- und Entwicklungsergebnisse oder andere Aktivitäten des Zentrums heraus. Diese Berichte sind auf den Seiten des Zentrums elektronisch erhältlich. Alle Rechte an den Berichten liegen beim Zentrum außer das einfache Nutzungsrecht, das ein Bezieher mit dem Herunterladen erhält.

## **Reports of the Helmholtz Centre Berlin (HZB-Berichte)**

The Helmholtz Centre Berlin for Materials and Energy publishes a series of reports on its research and development or other activities. The reports may be retrieved from the web pages of HZB and used solely for scientific, non-commercial purposes of the downloader. All other rights stay with HZB.

ISSN 1868-5781

doi: <http://dx.doi.org/10.5442/d0018>

# **Composites of Spherical Polyelectrolyte Brushes and Nanoparticles**

---

## **Synthesis, Characterization and Their Use in Catalysis**

### **DISSERTATION**

Zur Erlangung des akademischen Grades eines  
Doktors der Naturwissenschaften (Dr. rer. nat.)  
im Fach Chemie der Fakultät für Biologie, Chemie und  
Geowissenschaften der

Universität Bayreuth

Vorgelegt von

Frank Polzer

Geboren in Erlangen, Deutschland

Bayreuth 2011



---

# Table of Contents

<b>1. Introduction.....</b>	<b>1</b>
1.1. Manganese Oxide Nanoparticles .....	2
1.2. Nanoparticles in Catalysis.....	4
1.3. Stabilization of Nanoparticles in Solution .....	7
1.4. Spherical Polyelectrolyte Brushes for the Stabilization of Nanoparticles in Solution .....	8
1.5. X-Ray Absorption Fine Structure Spectroscopy on Nanosized Materials.....	10
1.6. Cryogenic Transmission Electron Microscopy on Nanosized Materials.....	13
1.7. Objective of this Thesis .....	14
1.8. References.....	15
<b>2. Overview .....</b>	<b>23</b>
2.1. Formation of Ultrathin Birnessite-Type Nanoparticles Immobilized on Spherical Polyelectrolyte Brushes.....	25
2.2. Structural Analysis of Colloidal MnO <sub>x</sub> Composites.....	27
2.3. Catalytic Oxidation of an Organic Dye by MnO <sub>x</sub> Nanoparticles Immobilized on Spherical Polyelectrolyte Brushes .....	29
2.4. Kinetic Analysis of the Catalytic Reduction of 4-Nitrophenol by Metallic Nanoparticles Immobilized in Spherical Polyelectrolyte Brushes.....	31
2.5. Synthesis and Analysis of Zwitterionic Spherical Polyelectrolyte Brushes in Aqueous Solution .....	33
2.6. Individual Contributions to Joint Publications .....	35
<b>3. Formation of Ultrathin Birnessite-Type Nanoparticles Immobilized on Spherical Polyelectrolyte Brushes .....</b>	<b>39</b>
3.1. Abstract .....	40
3.2. Introduction.....	41
3.3. Experimental Section .....	42
3.4. Results and Discussion .....	43
3.5. Conclusions.....	50
3.6. Acknowledgements.....	50

---

3.7.	Supporting Information.....	51
3.8.	References.....	52
<b>4.</b>	<b>Structural Analysis of Colloidal MnO<sub>x</sub> Composites.....</b>	<b>57</b>
4.1.	Abstract.....	58
4.2.	Introduction.....	59
4.3.	Experimental Section .....	60
4.4.	Results and Discussion .....	62
4.5.	Conclusion .....	75
4.6.	Acknowledgements.....	76
4.7.	Supporting Information.....	76
4.8.	References.....	77
<b>5.</b>	<b>Oxidation of an Organic Dye Catalyzed by MnO<sub>x</sub> Nanoparticles .....</b>	<b>83</b>
5.1.	Abstract.....	84
5.2.	Introduction.....	85
5.3.	Experimental Section .....	87
5.4.	Results and Discussion .....	88
5.5.	Conclusions.....	98
5.6.	Acknowledgements.....	98
5.7.	Supporting information.....	99
5.8.	References.....	100
<b>6.</b>	<b>Kinetic Analysis of Catalytic Reduction of 4-Nitrophenol by Metallic Nanoparticles Immobilized in Spherical Polyelectrolyte Brushes ....</b>	<b>103</b>
6.1.	Abstract.....	104
6.2.	Introduction.....	105
6.3.	Experimental Section .....	107
6.4.	Results and Discussion .....	108
6.5.	Conclusion .....	117
6.6.	Acknowledgment .....	117
6.7.	References.....	117
<b>7.</b>	<b>Synthesis and Analysis of Zwitterionic Spherical Polyelectrolyte Brushes in Aqueous Solution .....</b>	<b>121</b>

---

7.1.	Abstract .....	122
7.2.	Introduction.....	123
7.3.	Experimental Section .....	124
7.4.	Results and Discussion .....	126
7.5.	Conclusion .....	134
7.6.	Acknowledgements.....	135
7.7.	Supporting Information.....	135
7.8.	References.....	137
<b>8.</b>	<b>Summary/Zusammenfassung .....</b>	<b>141</b>
	Summary.....	141
	Zusammenfassung .....	142
<b>A</b>	<b>List of Publications .....</b>	<b>145</b>
A1.	Publications of this Thesis .....	145
A2.	Publications as a co-Author .....	145
A3.	Patents submitted during the Course of the Thesis.....	146
<b>B</b>	<b>Presentations at International Conferences and Meetings.....</b>	<b>147</b>
<b>C</b>	<b>Abbreviations .....</b>	<b>149</b>
<b>D</b>	<b>Danksagung .....</b>	<b>151</b>
<b>E</b>	<b>Schlusserklärung.....</b>	<b>153</b>

---

---

Die vorliegende Arbeit wurde in der Zeit von August 2007 bis Februar 2011 in Bayreuth am Lehrstuhl Physikalische Chemie I und am Helmholtz Zentrum Berlin für Materialien und Energie unter Betreuung von Herrn Prof. Dr. Matthias Ballauff angefertigt.

Vollständiger Abdruck der von der Fakultät Biologie, Chemie und Geowissenschaften der Universität Bayreuth genehmigten Dissertation zur Erlangung des akademischen Grades eines Doktors der Naturwissenschaften (Dr. rer. nat.)

Dissertation eingereicht am: 16. Februar 2011

Tag der Zulassung durch die Prüfungskommission: 25. Juni 2011

Tag des wissenschaftlichen Kolloquiums: 05. Juli 2011

Amtierender Dekan:

Prof. Dr. Stephan Clemens

Prüfungsausschuss:

Prof. Dr. Matthias Ballauff (Erstgutachter)

Prof. Dr. Josef Breu (Zweitgutachter)

Prof. Dr. Axel H. E. Müller (Vorsitz)

Prof. Dr. George Papastavrou



---

Well there's those that do  
And those that just do talking  
We're all going through hell  
It's burn or keep on walking

Randy Blythe



---

**Meinem Großvater**

---





# 1. Introduction

Over the last decades nanotechnology has grown to one of the most promising technologies of this century. Since the 1980s scientific literature on nanoparticles has increased exponentially and reached an impressive plateau of about 16.000 publications per year in 2008.<sup>1</sup> In addition, funding of nanotechnology research is globally estimated to about \$12.4 billion per year.<sup>2</sup> The term “nano” is related to the Greek word for “dwarf” and therefore already implies the tiny dimensions of the particles. But despite their importance, nanoparticles are roughly defined as microscopic particles whose sizes are not bigger than 100 nm in diameter.<sup>3</sup> Since the definition is just arbitrarily related to the size and no other restrictions are made, such particles can consist of inorganic, organic or hybrid materials.<sup>4,5,6,7,8,9</sup> Nowadays, nanoparticles of most of the known elements and their compounds have been successfully generated.<sup>10,11,12,13</sup> Despite the progress in nanotechnology, there are still problems to overcome and questions left unanswered. One issue that should be mentioned is the lack of knowledge about the harm of nanoparticles interacting with living tissue.<sup>14</sup>

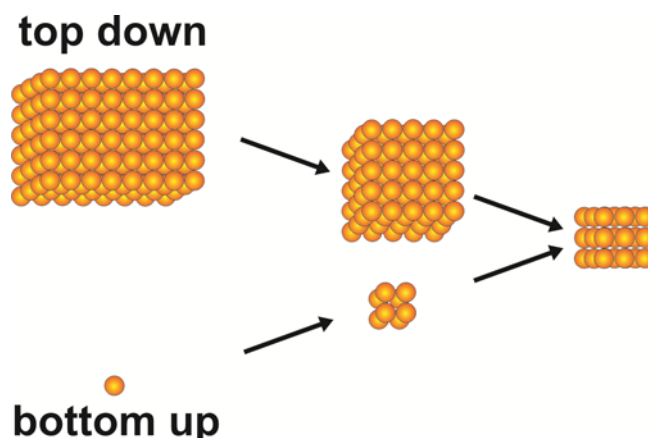


**Figure 1.0.1.** Schematic representation of the two principles of the preparation of nanosized materials. The top down approach decreases the particle size starting from bulk materials using physical methods. In contrast, the bottom up approach starts with molecular precursors and generates nanoparticles by chemical and/or physical methods.

In general, two methods for the preparation of particles in the nanometer scale exist: the top down approach is related to the generation of small particles by a decrease in the size of granular matter by physical methods (see Figure 1.0.1).<sup>15,16</sup> In contrast, the bottom up approach starts from small building blocks, e.g. molecular precursors, and generates particles in the nanometer size by self-assembly and self-organization processes.<sup>17,18</sup> Since the top down approach has poor control of particle size and shape most studies focus on the bottom up principle. The control of the dimensions and topologies of nanoparticles is of particular interest due to findings that the properties of nanoparticles depend strongly on their size and

shape.<sup>19,20,21</sup> This fact has directly led to a huge number of studies investigating the control of the dimensions as well as of the morphology of nanoparticles.<sup>22,23,24</sup> In principle, nanoparticles and their assemblies can be subdivided according to their dimensionality into 1D, 2D and 3D particles.<sup>25</sup>

Due to the huge variety of different nanoparticulate materials available, the characteristics of these particles differ strongly. In general, the properties can be divided into three groups. Surface-dependent properties are properties the bulk material also possess but that become dominant at high surface-to-volume ratios, e.g. for catalytic applications of nanoparticles (see Figure 1.0.2a). Second, size-dependent properties that are directly related to the small size, e.g. in Bragg stacks or in photonic crystals.<sup>26,27</sup> Lastly, there exist size-dependent quantum effects. This means a direct influence of the size of nanoparticles on their electronic structure, e.g. the size-dependent surface plasmon shift in metal nanoparticles (Figure 1.0.2b).<sup>28,29,30</sup>

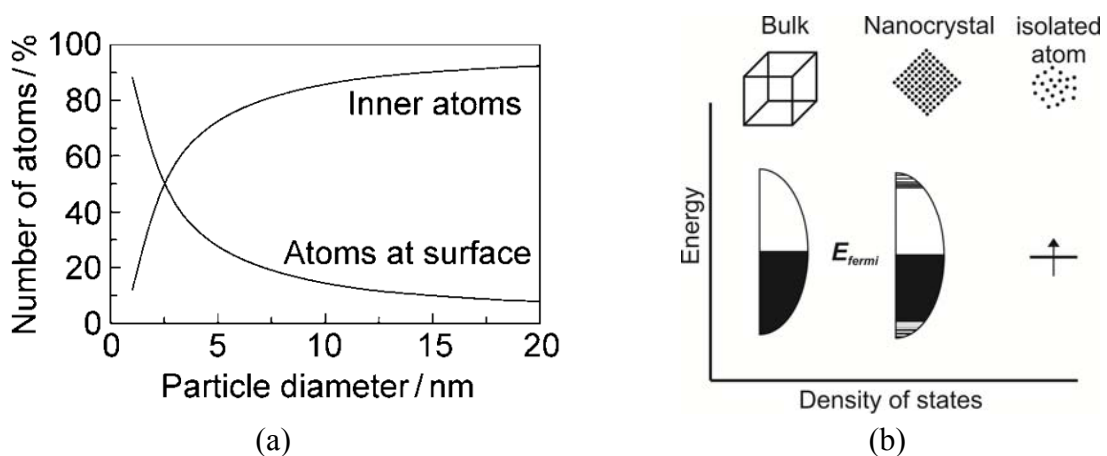


**Figure 1.0.2.** (a) Dependence of the size of gold nanoparticles onto the ratio of inner atoms to atoms at the surface.<sup>31</sup> (b) Illustration of the influence of the size of metallic nanoparticles onto the density of states. Particles with sizes between the size of small molecules and that of bulk metal display electronic structures, reflecting the electronic band structure of the nanoparticles, owing to quantum-mechanical rules.<sup>32</sup>

Applications of nanoparticles are wide-ranging and include medical applications like drug delivery<sup>33</sup> and sensing<sup>34</sup>, coatings<sup>35</sup>, waste water treatment<sup>36</sup>, energy conversion<sup>37</sup> and storage<sup>38</sup> and many others more.<sup>39</sup> Besides all of these interesting applications, the use of nanoparticles in catalysis seems to be one of the most promising.<sup>40,41,42</sup> This will be discussed further in section 1.2.

## 1.1. Manganese Oxide Nanoparticles

Manganese oxide nanoparticles include all common oxidation states of manganese, such as  $\text{MnO}$ ,  $\text{Mn}_2\text{O}_3$ ,  $\text{Mn}_3\text{O}_4$ ,  $\text{MnO}_2$  and also mixed valent compounds ( $\text{MnO}_x\text{NP}$ ).<sup>43,44,45,46,47,48</sup> There exist numerous reports about the synthesis of all different kinds of  $\text{MnO}_x\text{NP}$  including 1D, 2D

---

and 3D structures.<sup>49</sup> Applications of manganese oxide nanostructured materials mostly focus on the use as electrode materials for energy storage, for magnetic data storage, as ion exchange materials, and for catalysis.<sup>50,51,52,53</sup>

With its wide range of polymorphs, MnO<sub>2</sub> has received the most attention among the different manganese oxides. All different polymorphs are built from the same basic unit, that is the MnO<sub>6</sub> octahedra (see Figure 1.1.1a). Due to the different linkage of the MnO<sub>6</sub> octahedra, α-, β-, γ- and δ-MnO<sub>2</sub> also possess distinct properties.<sup>54</sup> δ-MnO<sub>2</sub> consists predominantly of edge-sharing MnO<sub>6</sub> units that form a layered topology similar to that of clay minerals like silicates or aluminosilicates.<sup>55</sup>

One of the most intensely studied compounds in the family of layered manganese oxides is birnessite.<sup>56,57,58,59,60</sup> This phyllosilicate is composed of hexagonal sheets of predominantly edge-shared MnO<sub>6</sub> octahedra.<sup>61,62</sup> Typically, the interlayers between single sheets bear hydrolyzable cations.<sup>63</sup> The cations balance the negative charges of the sheets.<sup>64</sup> These negative surface charges are due to the presence of vacancies within the ab-plane of the sheets.<sup>65,66</sup> Furthermore, a net charge can arise by the incorporation of a certain amount of corner-shared Mn<sup>3+</sup> octahedra.<sup>67,68</sup> The intercalation can be used for the sorption of other positively charged compounds which directly leads to applications in waste water treatment.<sup>69,70</sup> In addition, the cation exchange of alkali metal ions by more bulky cations, e.g. organic cations, surfactants, polyelectrolytes, etc., leads to a swelling of the interlayer distance in aqueous solution.<sup>71,72,73</sup> This effect can be used for adjacent delamination of the hexagonal sheets.<sup>74,75</sup> Exfoliation refers to the generation of single layers of sheets which is mostly achieved by multi-step processes.<sup>76,77,78,79</sup> There exist only a few reports on the synthesis of single lamellae of layered manganese oxides, e.g. birnessite.<sup>80,81</sup> The generation of single layered nanosheets is desirable because of their large specific surface area.<sup>80</sup> The surface can directly serve as a highly active catalyst or it can be further functionalized by organic ligands. Furthermore, octahedral layered (OL) manganese oxides can be used as building blocks for layer-by-layer self-assemblies and pillared MnO<sub>x</sub> structures.<sup>82,83</sup> OL manganese oxides can also be converted into 1D tunnel structures that are termed octahedral molecular sieves (OMS).<sup>84,85,86</sup> Some common crystallographic structures of these materials are shown in Figure 1.1.1.

OMS and OL materials offer a broad range of different properties depending on their architecture, the average oxidation state and the interlayer cations.<sup>87</sup> These parameters are very sensitive to the synthetic route and proved to have major impact on the catalytic properties.<sup>88,89,90</sup>

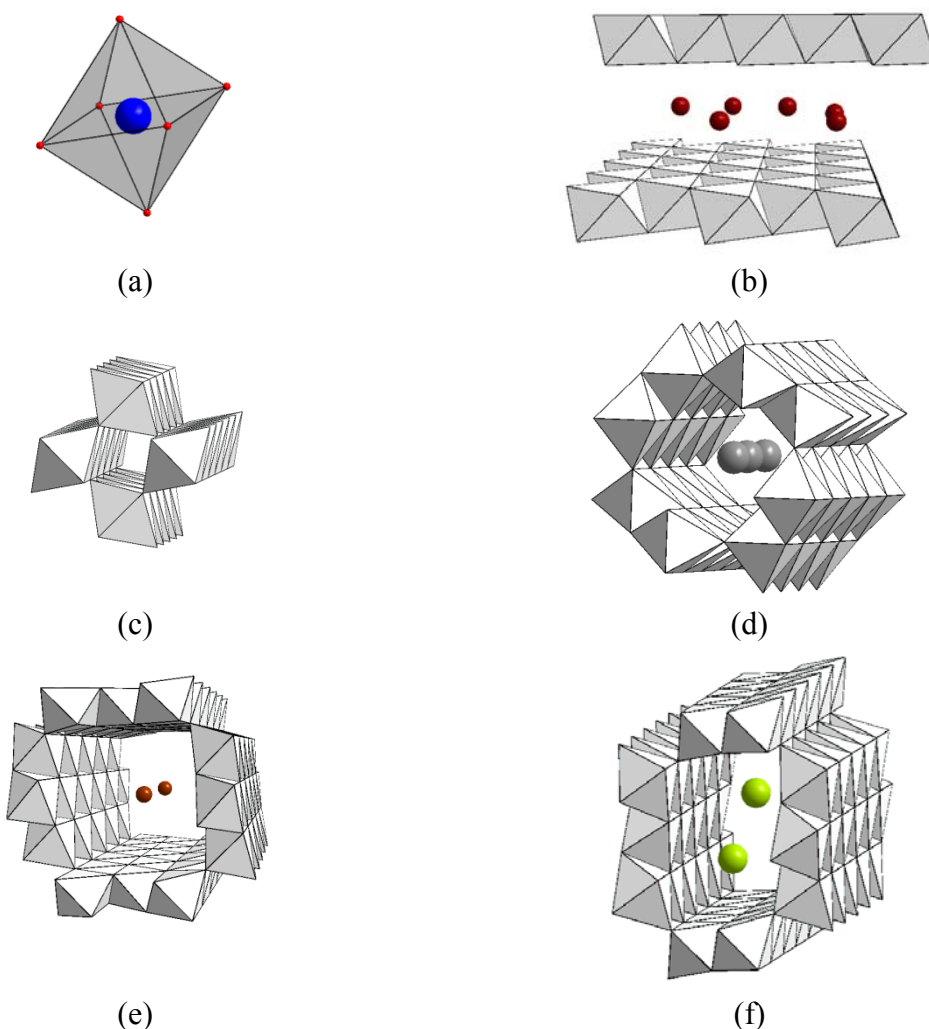


**Figure 1.1.1.** Crystallographic structures of different OL and OMS structures. (a) Structure of  $\text{MnO}_6$  octahedra (Mn blue sphere, O red sphere) which is the building block of all OL and OMS materials. (b) Na-Birnessite (Na red sphere); (c) Pyrolusite; (d) K-Cryptomelane (K grey sphere); (e) Mg-Todorokite (Mg brown sphere) and (f) Ba-Romanechite (Ba green sphere).

## 1.2. Nanoparticles in Catalysis

Nanoparticles made their breakthrough as catalyst materials after Haruta *et al.*<sup>91,92</sup> reported on the high performance of gold nanoparticles on the CO oxidation in the late 1980s. At the same time Hutchings *et al.* discovered the activity of gold nanoparticles for the hydrochlorination of acetylene.<sup>93</sup> Since then, a vast amount of studies have been conducted on the catalytic activity of nanoparticles.<sup>9,94</sup> Those include most kinds of nanoparticles and different catalytic reactions, e.g. oxidation reactions, hydrogenation reactions, reductions, coupling reactions, photocatalytic reactions, etc.<sup>11,33,42</sup>

Besides the numerous works on applied catalysis with nanoparticles many studies have been conducted to elucidate the activity of nanosized matter. Hence, different kinds of model reactions for detailed investigations have been established. These include reduction or oxidation reactions of a variety of different dye molecules which enables *in situ* investigations by UV/visible spectroscopy (UV/vis).<sup>95,96,97</sup> One aspect of these studies was to elucidate the size-dependence of the catalytic activity of nanoparticles, e.g. gold nanoparticles.<sup>98,99,100</sup> Another focus has been laid on the influence of the shape of nanoparticles on their catalytic activity.<sup>101,102</sup> Though there exists a high number of different investigations, there is still a lack of comprehension of the mechanism of reactions catalyzed by nanoparticles.

In principle, surface catalyzed reactions can be divided into two distinct mechanisms: the Eley-Rideal mechanism (ER) and the Langmuir-Hinshelwood mechanism (LH).<sup>103</sup> The basic catalyst cycle for a LH mechanism is depicted in Figure 1.2.1.

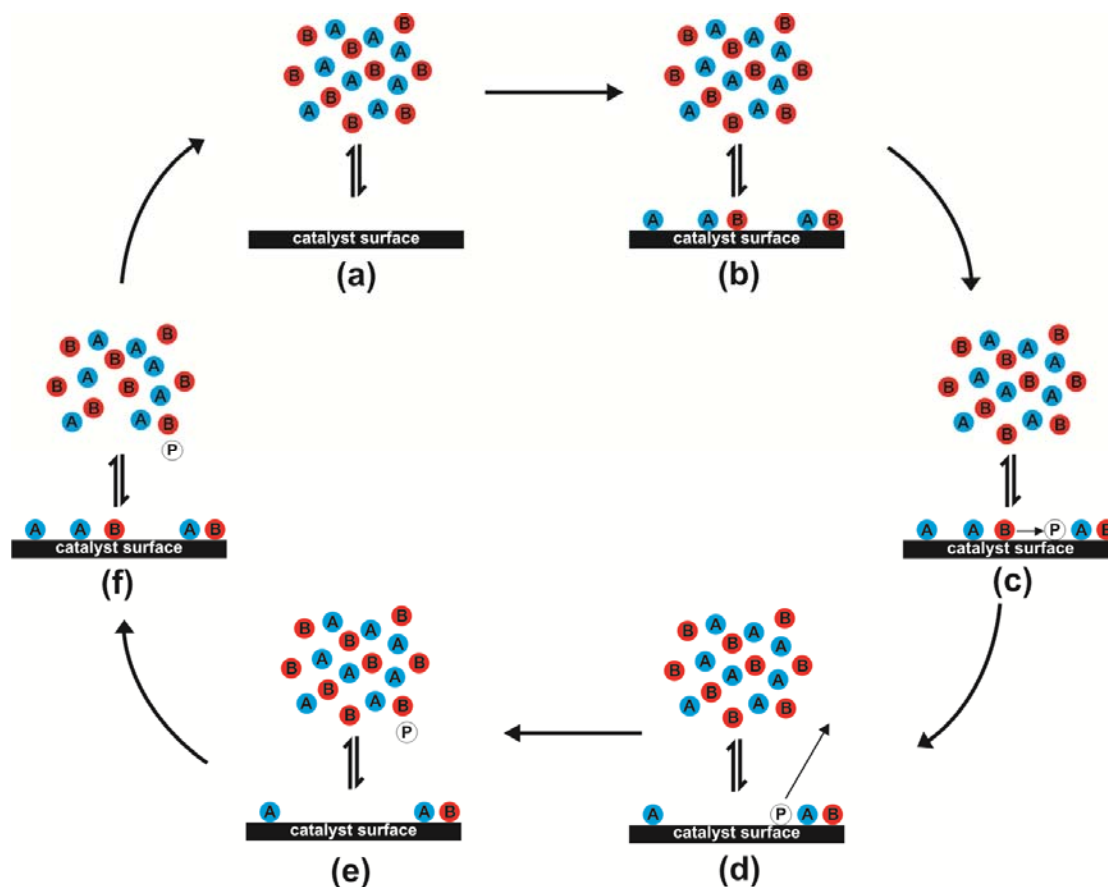


**Figure 1.2.1.** Illustration of a catalytic cycle of a bimolecular surface reaction via a Langmuir-Hinshelwood mechanism. Reactant A and B concomitantly adsorb onto the catalyst surface in a reversible step (a & b) which is followed by an irreversible bimolecular surface reaction of A and B (c). The reaction product P desorbs from the catalyst surface (d) and leaves free active sites on the catalyst (e). In the end, the catalytic cycle can start again by the adsorption of further reactants (f & a).

The main characteristic of LH reactions is that both reactants have to be adsorbed onto the catalyst surface.<sup>104</sup> The adsorption process is described by a Langmuir isotherm

$$\theta_i = \frac{K_i c_i}{1 + K_i c_i} \quad (1.2.1)$$

where  $\theta_i$  is the surface coverage of the reactant  $i$ ,  $K_i$  represents the adsorption constant of  $i$  and  $c_i$  its concentration respectively.<sup>105</sup>

The adsorbed reactants undergo a surface reaction, which is the rate determining step of the cycle. Subsequently the reaction product desorbs from the catalyst surface, leaving free sites on the catalyst for the start of a new cycle. This is schematically depicted in Figure 1.2.1. In contrast, in an ER mechanism, only one of the reactants is adsorbed onto the catalyst surface. This species reacts via a collision with a molecule from the bulk phase.

There exist marked differences between the two mechanisms concerning the dependency of concentration of the reactants on the rate of reaction ( $r$ ). For a LH mechanism, the scheme in Figure 1.2.2 shows the course of  $r$  with increasing concentration of reactant A. At a low surface coverage  $\theta$  of A, the surface is predominantly occupied by B and the reaction between A and B is hindered. The curve goes through a maximum, since the adsorption of A becomes more likely with an increasing concentration. At higher concentrations of A,  $r$  is decreasing again since the surface is blocked by this species and surface reaction between A and B is hindered again (see Figure 1.2.2).<sup>103</sup>

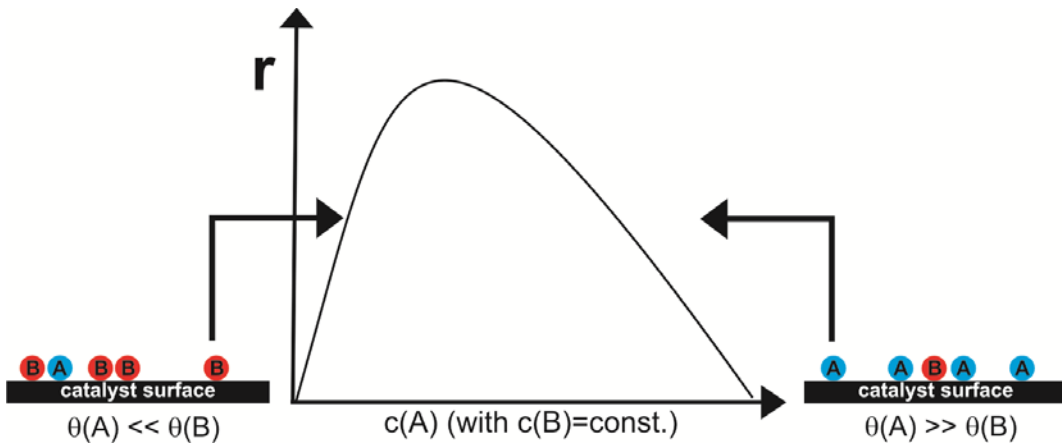


**Figure 1.2.2.** Illustration of the dependence of the concentration of reactant A on the rate of the reaction  $r$  according to a LH mechanism assuming one type of active site. If the surface is predominantly occupied by one of the species, the surface reaction is hindered and therefore  $r$  decreases. Since the surface coverage  $\theta$  is determined by Langmuir isotherms it depends on the concentration of the reactants and their adsorption constants, respectively.

An irreversible, bimolecular surface reaction where both reactants are adsorbed onto the surface (see Figure 1.2.2) can be described by the following equation:<sup>103</sup>

$$r = \frac{kS(K_A c_A)(K_B c_B)}{(1 + K_A c_A + K_B c_B)^2} \quad (1.2.2)$$

Here,  $S$  represents the total surface area of the catalyst,  $K_A$  and  $K_B$  are the adsorption constants for A and B. The concentrations of A and B are expressed by  $c_A$  and  $c_B$ , respectively. The kinetic constant of the surface reaction of A and B is expressed by  $k$ .

For an ER mechanism there is no such dependence described by Eq. 1.2.2. In fact, the course follows that of a Langmuir isotherm since at some point an increase of B does not lead a further increase of  $r$ . This is because B has to react with adsorbed A and if the concentration of B exceeds the concentration of adsorbed A, neither an increase nor a decrease of  $r$  follows.<sup>103</sup>

The number of studies investigating the mechanism of catalyzed benchmark reactions with nanoparticles is scarce so far.<sup>106,107</sup> The main reasons for that are the limited stability and the detailed characterization of small nanoparticles.<sup>41</sup> Therefore, new ways for the stabilization of very small nanoparticles in solution are required. It would be an asset if the stabilizing agent did not block the active surface of the nanoparticles since this would significantly affect the catalytic studies.<sup>108</sup> If these requirements are fulfilled, more detailed insights of the catalytic mechanisms will be possible in combination with state of the art characterization techniques.

### 1.3. Stabilization of Nanoparticles in Solution

Since most of the methods for the generation of nanoparticles are conducted in aqueous medium or in an organic solvent, the stabilization of these particles against coagulation is of great importance.<sup>19,109</sup> If no stabilization is provided, uncontrolled growth with subsequent Ostwald ripening will occur. This leads to agglomeration and precipitation. The agglomeration is caused by van der Waals forces that lead to an attraction of particles at short particle distances. If no repulsive forces are present nanoparticles tend to aggregate.<sup>110</sup> The stabilization mechanism of surface charged colloidal particles is described by the theory of Derjaguin, Landau, Verwey and Overbeek (DLVO theory).<sup>111,112,113</sup>

For most applications, agglomeration leads to a loss of the functionality of nanoparticles due to the strong relation between the properties of the nanoparticles to their size and shape, e.g. in catalysis.<sup>19</sup> In general, nanoparticles can be stabilized in two different ways. Either the nanoparticles are modified at their surface or they are immobilized onto support particles that provide sufficient stabilization against coagulation.<sup>40</sup> For both principles two different kinds of stabilization mechanisms and a combination of both can be distinguished. A schematic representation of electrostatic, steric and electrosteric stabilization is given in Figure 1.3.1.<sup>40,114</sup>

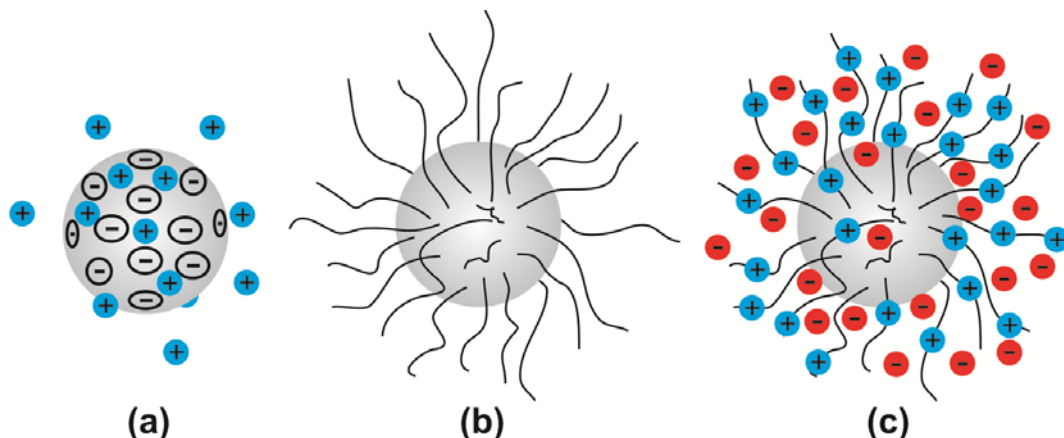


**Figure 1.3.1.** Illustration of the different principles of stabilizing colloidal particles. (a) Electrostatic stabilization by charges that are either chemically bound on the surface (surface functionalization) or affixed by selective adsorption. (b) Steric stabilization can either be achieved by adsorption or by grafting of polymer chains onto the colloidal particles. (c) Electrosteric stabilization of colloidal particles by charged polymer chains represents a combination of both stabilization mechanisms.

As already mentioned, nanosized materials can also be stabilized by the immobilization onto support particles. This can be achieved either by adsorption of the nanoparticles or by *in situ* generation of the nanoparticles on/inside of the support. The principles of the stabilization mechanisms of the support particles remain identical to those discussed in the section above. If nanoparticles are immobilized onto support particles, so-called synergistic effects (also support effects) have to be taken into account.<sup>115</sup> This term is related to an enhancement of any distinct property of the nanoparticles due to the interactions with the support material.<sup>116,117</sup>

#### 1.4. Spherical Polyelectrolyte Brushes for the Stabilization of Nanoparticles in Solution

A spherical polyelectrolyte brush (SPB) is a spherical, solid particle onto which long polyelectrolyte chains are densely grafted (see Figure 1.4.1).<sup>118</sup> Hereby, the distance between two neighboring grafted chains has to be lower than the chains radius of gyration  $R_g$  in a good solvent.<sup>119,120</sup> Figure 1.4.1 shows a schematic illustration of a SPB with its main characteristic parameters.

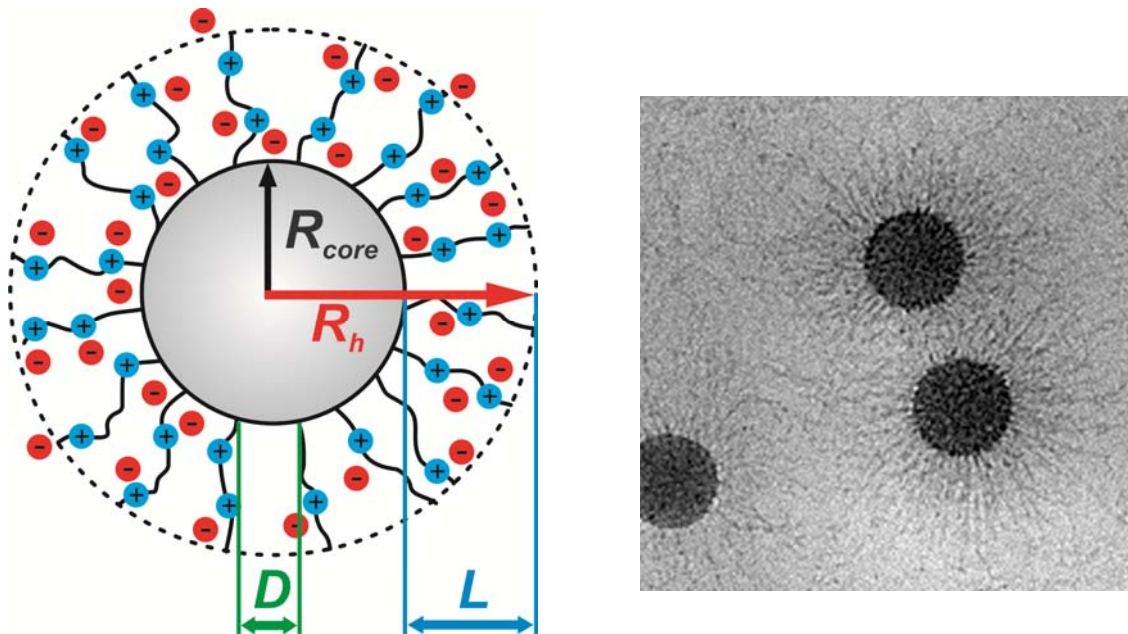


**Figure 1.4.1.** Illustration of a spherical polyelectrolyte brush. The core consists of a hydrophobic polymer, e.g. poly(styrene), onto which polyelectrolyte chains are densely grafted.  $R_{core}$  represents the radius of the core particle,  $R_h$  is the hydrodynamic radius of the SPB,  $L$  is the hydrodynamic thickness of the shell layer ( $= R_h - R_{core}$ ) and  $D$  is the distance between the grafted chain ends. The polyelectrolyte chains are strongly stretched in aqueous solution due to the osmotic pressure inside of the shell layer. This can be seen in the cryoTEM micrograph of anionic SPBs with a pSS shell.<sup>121</sup>

In principle, SPBs can be classified by the type of polyelectrolyte present in the shell. An annealed SPB is a brush particle with a weak polyelectrolyte forming the shell, e.g. poly(acrylic acid). In contrast, the shell of a quenched SPB consists of a strong polyelectrolyte, e.g. poly(sodium styrene sulfonate). The difference of the two classes of SPB is that the charge density of an annealed SPB can be influenced by changing the pH, whereas for a quenched SPB no pH dependence is present.<sup>118</sup>

The high electrostatic interaction of the densely grafted polyelectrolyte chains leads to a number of new properties in comparison to uncharged grafted macromolecules. An essential characteristic is given by the confinement of the counter ions of the polyelectrolyte chains within the shell layer.<sup>118,122,123</sup> This leads to a swelling of the polyelectrolyte shell due to the high osmotic pressure of the confined counter ions in salt free solution. The effect of the confinement of the counter ions has successfully been used for the generation of nanoparticles within the shell of the SPB.<sup>124</sup> Charged molecular precursors can be introduced into the shell by a controlled exchange of the counter ions. In a second step, the precursors can be reduced to nanoparticles.<sup>125,126</sup> The ion exchange can either be enhanced by the introduction of multivalent counter ions or by ions that possess specific interactions with the charged groups of the shell. After reduction of the charged precursors, nanoparticles are directly generated and immobilized within the shell of the SPB. Using this approach, a number of different noble metal nanoparticles and their alloys have been successfully synthesized.<sup>127,128,129,130</sup>

This method proved to have a number of advantages. In general, the nanoparticles generated in SPBs are strongly bound to the carrier particle and are of small size. The small size evidently leads to a high surface to volume ratio whereas the immobilization helps to prevent the uncontrolled release of nanoparticles into the surrounding media.<sup>124</sup> Therefore, the immobilization of nanoparticles onto colloidal stable particles simplifies the handling of nanoparticles, which is one of the main purposes of so-called mesostructured materials. In particular, this becomes important because nanosized materials are suspected to cause harm to living tissue. Furthermore, the immobilization of nanoparticles on colloidal particles is advantageous for applications in catalysis because it helps to separate the catalyst from the reaction solution, e.g. by filtration.<sup>40,124</sup> This improves the recyclability of the catalytic active composite particles and also it prevents the leaching of nanoparticles in the reaction products.<sup>40</sup> The catalytic activity of composite materials of nanoparticles at SPBs has been shown in various studies.<sup>124,126</sup> These include hydrogenation reactions, oxidation and epoxidation reactions as well as coupling reactions like the Heck-Suzuki reaction.<sup>131,132,133,134</sup>

## 1.5. X-Ray Absorption Fine Structure Spectroscopy on Nanosized Materials

The characterization of nanoparticles is sometimes challenging, especially if they are immobilized onto support particles. This is due to the fact that nanoparticles synthesized at mild conditions are often highly disordered materials exhibiting poor diffraction patterns obtained by PXRD.<sup>135</sup> In addition, the small particle size leads to a broadening of the reflections of the lattice planes. Furthermore, the presence of support particles is often accompanied by a high amorphous background of the composite material which complicates investigations by methods like PXRD or high resolution TEM (HRTEM).

Due to these difficulties, additional methods should be considered for the analysis of nanostructured composite materials. Since X-ray fine structure (XAFS) measurements can be made on elements of minority and even trace abundance it provides a unique and direct measurement of the chemical and physical state of dilute species in a variety of systems. XAFS spectra can be measured for essentially every element on the periodic table. Importantly, no long range order within the compounds is required for XAFS measurements. This makes XAFS one of the few structural probes available for non-crystalline and highly disordered materials, even including solutions.

XAFS refers to the details of how X-rays are absorbed by an atom at energies near and above the core-level binding energies of that atom. These spectra are especially sensitive to the coordination chemistry, formal oxidation state, and the distances, coordination number and species of the atoms immediately surrounding the selected element. Because of this dependence, XAFS provides a practical way to determine the chemical state and local atomic structure for a selected atomic species.<sup>136</sup>

The X-ray absorption spectrum is typically divided into two regimes: The X-ray absorption near-edge spectroscopy (XANES) with its typical range of up to 100 eV from the absorption

edge. Secondly, the extended X-ray absorption fine structure spectroscopy (EXAFS) spanning a range from the XANES region up to 1000 eV above the absorption edge. The two regions have the same physical origin, but a distinction is convenient for the interpretation. Whereas XANES is strongly sensitive to the formal oxidation state and the coordination chemistry of the absorbing atom, the EXAFS is used to investigate the distances, coordination number, and species of the neighbors of the absorbing atom.<sup>137,138</sup>

In simple terms, for XAFS the dependence of the energy on the absorption coefficient  $\mu$  at and above the binding energy of a known core level of a known atomic species is measured. According to Lambert-Beers' law,  $\mu$  is related to the X-ray intensity as follows:

$$I = I_0 e^{-\mu t} \quad (1.5.1)$$

Here,  $I_0$  represents the incident X-ray intensity,  $I$  is the transmitted X-ray intensity and  $t$  is the thickness of the sample.

The absorption coefficient is related to the energy of the X-ray beam  $E$  by

$$\mu \approx \frac{\rho Z^4}{AE^3} \quad (1.5.2)$$

where  $\rho$  and  $Z$  are the sample density and the atomic number of the absorbing element.  $A$  represents the atomic mass of the absorber. Due to the  $Z^4$  dependence,  $\mu$  is very sensitive to the chemical nature of the absorber.<sup>136</sup>

For EXAFS, the oscillation above the absorption edge is of major interest and the EXAFS function can be written as:

$$\chi(E) = \frac{\mu(E) - \mu_0(E)}{\Delta\mu_0(E)} \quad (1.5.3)$$

$\mu(E)$  is the measured absorption coefficient,  $\mu_0(E)$  is a smooth background function representing the absorption of an isolated atom, and  $\Delta\mu_0$  is the measured jump in the absorption  $\mu(E)$  at the threshold energy  $E_0$ .

$\chi(E)$  is converted into  $\chi(k)$  because the absorption process of EXAFS is treated best by the wave behavior of the photoelectron. For this conversion the following relation is used:

$$k = \sqrt{\frac{2m(E - E_0)}{\hbar^2}} \quad (1.5.4)$$

The wavelength of the photoelectron is expressed by  $k$ , whereas  $m$  represents the electron mass,  $\hbar$  is Planck's constant and  $E_0$  is the energy at the absorption edge.

The EXAFS equation that is used for fitting measured XAFS spectra can finally be written as:

$$\chi_i(k) = \frac{(N_i S_0^2) F_{eff,i}(k)}{k R_i^2} \sin[2kR_i + \varphi_i(k)] e^{-2\sigma_i^2 k^2} e^{\frac{-2R_i}{\lambda(k)}} \quad (1.5.5)$$

where  $F_{eff,i}(k)$ ,  $\varphi(k)$  and  $\lambda(k)$  are the effective scattering amplitude of the photoelectron, the phase shift of the photoelectron and the mean free path of the photoelectron, respectively.  $R_i$  is the half path length of the photoelectron.  $N_i$  represents the number of coordinating atoms and  $S_0^2$  is the passive electron reduction factor, whereas  $\sigma^2$  represents the mean square displacement of the bond length between absorbing and scattering atom and can be understood as a thermal disorder.<sup>136</sup>

An illustration of the X-ray absorption process is presented and described in Figure 1.5.1.

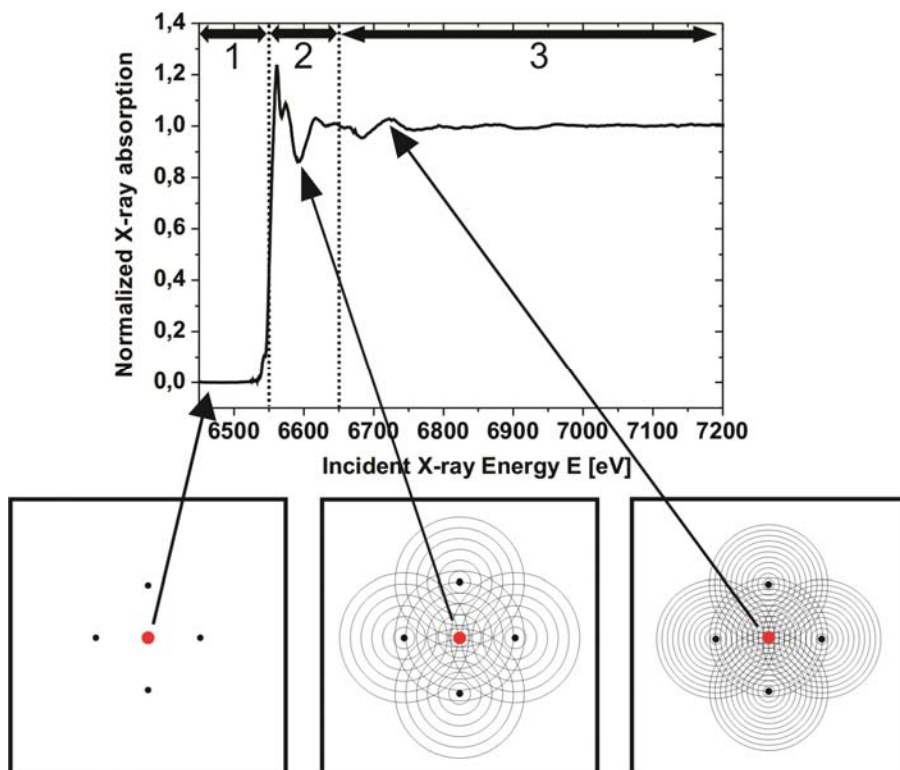


**Figure 1.5.1.** Illustration of the X-ray absorption process. The X-ray absorption spectrum was measured at the Manganese K-edge. The schemes below the XAFS represent the Mn absorber atom (red dot) with four of the six neighboring oxygen atoms (black dots) at different incident X-ray energies. The concentric circles represent the crest of the photoelectron waves that are produced by X-ray absorption of the absorbing atom and by the scattering from the oxygen neighbors. If the X-ray energy is below the absorption edge of the absorber no photoelectron is produced (region 1). At energies close above the edge energy, the wavelength of the photoelectron is longer than at higher energies (region 2). The backscattered waves produce a minimum in the absorption coefficient  $\mu$  because outgoing and scattered parts of the photoelectron are out of phase and meet at a minimum at the absorbing atom. At higher X-ray energies the wavelength is shorter resulting in a maximum of  $\mu$  because the outgoing and scattered parts of the photoelectron are in phase and meet at a maximum at the absorbing atom (region 3).<sup>136</sup>

The EXAFS equation can be used to determine important parameters like  $N$ ,  $R$  or other  $\sigma^2$ . Due to the sine term of the EXAFS equation, Fourier transformation of  $\chi(k)$  results in peaks at distances related to  $R_i$ , that is, the interatomic distance between the absorber and the coordinating atoms. Furthermore, it provides information about the species of the neighboring atoms since the scattering factors are dependent on the atomic number of the neighbors surrounding the absorbing atom.

There are many examples where XAFS proved to be a powerful tool for structural investigations of poorly crystalline or disordered materials.<sup>139</sup> These studies also include investigations on composite materials.<sup>66</sup> Combined with scattering methods like PXRD and imaging methods like HRTEM and cryoTEM, XAFS is a helpful technique to elucidate the structure of nanoparticles and its composite materials.

## 1.6. Cryogenic Transmission Electron Microscopy on Nanosized Materials

CryoTEM has become a powerful tool for investigations of soft matter samples and for investigations of self-assembled structures since its establishment in the late 1980s.<sup>140,141,142,143,144</sup> At present, the technique provides high resolution and direct imaging of dispersed samples *in situ* including 3D imaging.<sup>145,146</sup> Comparison of cryoTEM micrographs to TEM images and results from scattering methods like small angle X-ray scattering and small angle neutron scattering can provide detailed information about nanostructured materials, soft matter and self-assembled samples. Recent work of Crassous *et al.* showed that cryoTEM images can be quantitatively used for simulations of small angle scattering patterns.<sup>147</sup> This proved that direct imaging by cryoTEM of dispersed samples is complementary to scattering methods.

The main requirement for direct imaging is the preservation of the structure of the sample. This is achieved by rapid freezing of the sample to obtain so-called vitrified samples. Therefore, a few  $\mu\text{L}$  of solution is put on a carbon or polymer coated TEM metal grid (see Figure 1.6.1).

Blotting of the droplet ensures the generation of thin films with a typical diameter of approximately 100-300 nm.<sup>148</sup> A rapid plunging of the grid into a reservoir of the cryogen, e.g. typically liquid ethane, converts the solvent into a solid-like, glassy state.<sup>149,150</sup> The sample is transferred to a cooled sample holder to avoid recrystallization and to limit sublimation of the vitrified solvent during the investigations.<sup>151</sup> Since the solvent molecules are vitrified during the fast cooling, self-assembled structures or composite materials are not likely to rearrange to new structures.<sup>152</sup> Hence, this method provides direct imaging of dispersed samples.

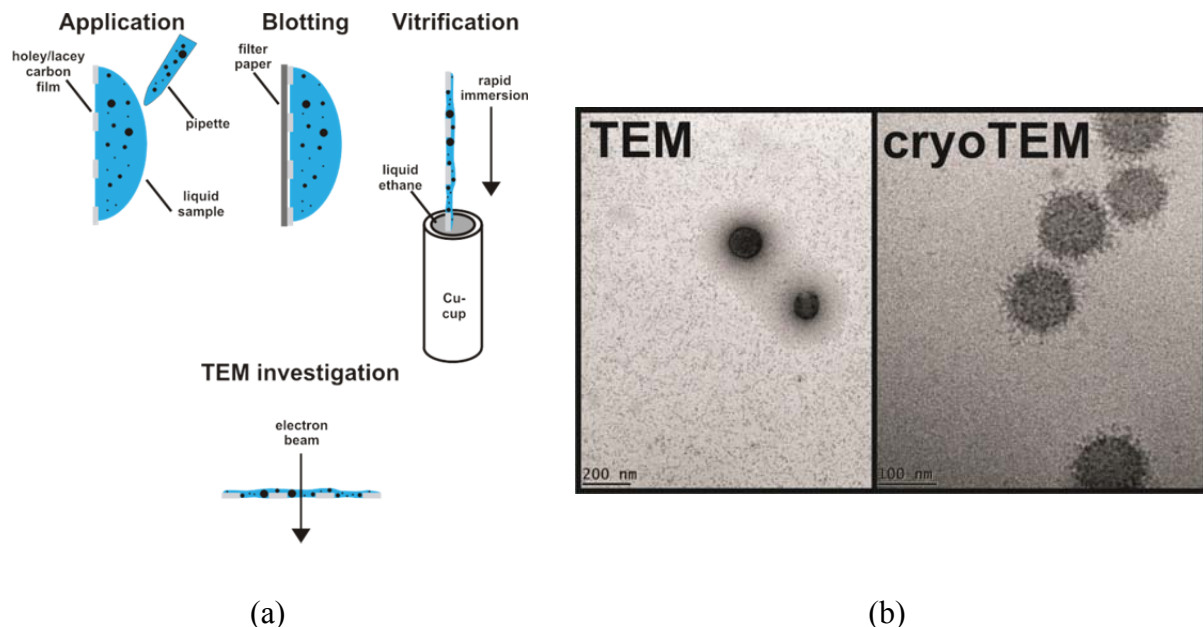


**Figure 1.6.1.** (a) Scheme of the preparation of cryoTEM samples on a carbon supported TEM grid according to Cui *et al.*<sup>153</sup> A few  $\mu\text{L}$  of sample are put on a grid coated with a holey carbon support film. The liquid film is treated with filter paper to generate film thicknesses of typically 100-500 nm. The film is vitrified by plunging into liquid ethane. (b) Comparison of TEM and cryoTEM images of SPB with a zwitterionic corona in 0.1 M CsI solution.

CryoTEM has been used for structural investigations on SPBs and their solution behavior as well as on related core-shell particles with a poly(n-isopropyl acrylamide) microgel shell.<sup>121,147,154</sup> It also proved to be a powerful method for investigations on surfactant-SPB complexes.<sup>155</sup> Due to its nanometer resolution, cryoTEM is also a suitable method for studies on composite materials of nanoparticles immobilized on SPBs.<sup>129,156,157</sup>

Though cryoTEM avoids most of the artifacts present in TEM in the dried state under high-vacuum conditions, other artifacts exist. Cui *et al.* gave a comprehensive summary of the most important artifacts of cryoTEM regarding sample preparation and imaging in the review on cryoTEM of amphiphiles in solution.<sup>153</sup> Being aware of the artifacts existing in cryoTEM, the method provides helpful additional information of dispersed nanostructured systems.

## 1.7. Objective of this Thesis

The objective of this thesis is the synthesis of cationic SPBs by photoemulsion polymerization and their characterization. The SPB particles will be used for the preparation and immobilization of manganese oxide nanoparticles. The mechanism of the synthesis and the structure of the composite material are investigated by DLS, TEM, cryoTEM, powder X-ray diffraction (PXRD) and energy dispersive X-ray analysis (EDX). Special emphasis is put on XAFS analysis of the manganese dioxide nanoparticles immobilized on the SPBs.

The composite material is then tested for its catalytic activity with regard to oxidation reactions. Therefore, the catalytic oxidation of morin by hydrogen peroxide is established as a model reaction. Special focus is put on the mechanism of the heterogeneous catalytic reaction.

In addition, noble metal nanoparticles immobilized on cationic SPBs are used for investigations of the mechanism of the catalytic reduction of 4-nitrophenol (Nip) by sodium borohydride ( $\text{NaBH}_4$ ).

Finally, a new kind of SPB with a zwitterionic polymer shell is synthesized via aqueous atom transfer radical polymerization. The core-shell particles are characterized by DLS, TEM, cryoTEM and zeta potential measurements. Based on the results, a model for the solution behavior of the zwitterionic SPB is presented. Furthermore, salt and temperature dependent measurements are conducted to investigate the upper critical solution temperature behavior and the anti-polyelectrolyte effect of the zwitterionic shell.

## 1.8. References

- <sup>1</sup> Goesmann, H.; Feldmann, C. *Angew. Chem. Int. Ed.* **2010**, *49*, 1362-1395.
- <sup>2</sup> Sargent, J. F. *Nanotechnology: A Policy Primer*; CRS Report for Congress, 2008.
- <sup>3</sup> The Royal Society and The Royal Academy of Engineering. *Nanoscience and Nanotechnology: Opportunities and Uncertainties*; The Royal Society, 2004; available at <<http://www.nanotec.org.uk>>.
- <sup>4</sup> Jun, Y. W.; Choi, J. S.; Cheon, J. *Angew. Chem. Int. Ed.* **2006**, *45*, 3414-3439.
- <sup>5</sup> Park, J.; Joo, S. G.; Kwon, S. G.; Jang, Y.; Hyeon, T. *Angew. Chem. Int. Ed.* **2007**, *46*, 4630-4660.
- <sup>6</sup> Chen, A.; Holt-Hindle, P. *Chem. Rev.* **2010**, *110*, 3767-3804.
- <sup>7</sup> Cost, R.; Saunders, A. E.; Banin, U. *Angew. Chem. Int. Ed.* **2010**, *49*, 4878-4897.
- <sup>8</sup> Nayak, S.; Lyon, L. A. *Angew. Chem. Int. Ed.* **2005**, *44*, 7686-7708.
- <sup>9</sup> Carbone, L.; Cozzoli, P. D. *Nano Today* **2010**, *5*, 449-493.
- <sup>10</sup> Pinna, N.; Niederberger, M. *Angew. Chem.* **2008**, *120*, 2-16.
- <sup>11</sup> Ferrando, R.; Jellinek, J.; Johnston, R. L. *Chem. Rev.* **2008**, *108*, 845-910.
- <sup>12</sup> Fernández-García, M.; Martínez-Arias, A.; Hanson, J. C.; Rodriguez, J. A. *Chem. Rev.* **2004**, *104*, 4063-4104.
- <sup>13</sup> Fan, J.; Chu, P. K. *Small* **2010**, *6*, 2080-2098.
- <sup>14</sup> Hansen, S. F.; Maynard, A.; Braun, A.; Tickner, J. A. *Nature Nanotech.* **2008**, *3*, 444-447.
- <sup>15</sup> Craighead, H. G. *Science* **2000**, *290*, 1532-1535.
- <sup>16</sup> Wang, Y.; Xia, Y. *Nano Lett.* **2004**, *4*, 2047-2050.
- <sup>17</sup> Feldheim, D. L.; Grabar, K. C.; Natan, M. J.; Mallouk, T. E. *J. Am. Chem. Soc.* **1996**, *118*, 7640-7641.
- <sup>18</sup> Balzani, V. *Pure Appl. Chem.* **2008**, *80*, 1631-1650.

- <sup>19</sup> Burda, C.; Chen, X.; Narayanan, R.; El-Sayed, M. A. *Chem. Rev.* **2005**, *105*, 1025-1102.
- <sup>20</sup> Narayanan, R.; El-Sayed, M. A. *J. Phys. Chem. B* **2005**, *109*, 12663-12676.
- <sup>21</sup> Sau, T. K.; Rogach, A. L.; Jäckel, F.; Klar, T. A.; Feldmann, J. *Adv. Mater.* **2010**, *22*, 1805-1825.
- <sup>22</sup> Grzelczak, M.; Vermant, J.; Furst, E. M.; Liz-Marzán, L. M. *ACS Nano* **2010**, *4*, 3591-3605.
- <sup>23</sup> Polshettiwar, V.; Baruwati, B.; Varma, R. S. *ACS Nano* **2009**, *3*, 728-736.
- <sup>24</sup> Glotzer, S. C.; Solomon, M. J. *Nature Mater.* **2007**, *6*, 557-562.
- <sup>25</sup> Srivastava, S.; Kotov, N. A. *Soft Matter* **2007**, *3*, 945-955.
- <sup>26</sup> Wu, Z.; Lee, D.; Rubner, M. F.; Cohen, R. E. *Small* **2007**, *3*, 1445-1451.
- <sup>27</sup> Sanders, J. V. *Acta Crystallogr. Sect. A* **1968**, *24*, 427-434.
- <sup>28</sup> Parak, W. J.; Manna, L.; Simmel, F. C.; Gerion, S.; Alivisatos, P. *Quantumdots in Nanoparticles* (Ed.: Schmidt, G.); Wiley-VCH: Weinheim, 2004.
- <sup>29</sup> Daniel, M.-C.; Astruc, D. *Chem. Rev.* **2004**, *104*, 293-346.
- <sup>30</sup> Henglein, A. *Chem. Rev.* **1989**, *89*, 1861-1873.
- <sup>31</sup> Alsfasser, R.; Janiak, C.; Klapötke, T. M.; Meyer, H. J. *Moderne Anorganische Chemie* (Ed.: Riedel, E.); de Gruyter: Berlin, 2007.
- <sup>32</sup> Alivisatos, A. P. *Science* **1996**, *271*, 933-937.
- <sup>33</sup> Ferrari, M. *Nature Rev.* **2005**, *5*, 161-171.
- <sup>34</sup> Medintz, I. L.; Uyeda, H. T.; Goldman, E. R. *Nature Mat.* **2005**, *4*, 435-446.
- <sup>35</sup> Caruso, R. A.; Susha, A.; Caruso, F. *Chem. Mater.* **2001**, *13*, 400-409.
- <sup>36</sup> Arabatzis, I. M.; Stergiopoulos, T.; Andreeva, D.; Kitova, S.; Neophytides, S. G.; Falaras, P. *J. Catal.* **2003**, *220*, 127-135.
- <sup>37</sup> Tian, B.; Zheng, X.; Kempa, T. J.; Dang, Y.; Yu, N.; Huang, J. Lieber, C. M. *Nature* **2007**, *449*, 885-171.
- <sup>38</sup> Che, G.; Lakshmi, B. B.; Fisher, E. R.; Martin, C. R. *Nature* **1998**, *393*, 346-349.
- <sup>39</sup> Lu, A.-H.; Salabas, E. L.; Schüth, F. *Angew. Chem. Int. Ed.* **2007**, *46*, 1222-1244.
- <sup>40</sup> Roucoux, A.; Schulz, J.; Patin, H. *Chem. Rev.* **2002**, *102*, 3757-3778.
- <sup>41</sup> Shiju, N. R.; Gulians, V. V. *Appl. Catal. A: General* **2009**, *356*, 1-17.
- <sup>42</sup> Astruc, D. *Nanoparticles in Catalysis*; Wiley-VCH: Weinheim, 2008.
- <sup>43</sup> Débart, A.; Paterson, A. J.; Bao, J.; Bruce, P. G. *Angew. Chem.* **2008**, *120*, 1-5.
- <sup>44</sup> Fischer, A. E.; Pettigrew, K. A.; Rolison, D. R.; Stroud, R. M.; Long, J. W. *Nano Lett.* **2007**, *7*, 281-286.
- <sup>45</sup> Wang, X.; Li, Y. *J. Am. Chem. Soc.* **2002**, *124*, 2880-2881.
- <sup>46</sup> Li, P.; Nan, C.; Wei, Z.; Lu, J.; Peng, Q.; Li, Y. *Chem. Mater.* **2010**, *22*, 4232-4236.
- <sup>47</sup> Djerdj, I.; Arcon, D.; Jaglicic, Z.; Niederberger, M. *Phys. Chem. C* **2007**, *111*, 3614-3623.
- <sup>48</sup> Schladt, T. D.; Graf, T.; Tremel, W. *Chem. Mater.* **2009**, *21*, 3183-3190.

- <sup>49</sup> Wang, N.; Cao, X.; He, L.; Zhang, W.; Gou, L.; Chen, C.; Wang, R.; Yang, S. *J. Phys. Chem. C* **2008**, *112*, 365-369.
- <sup>50</sup> Ammundsen, B.; Paulsen, J. *Adv. Mater.* **2001**, *13*, 943-956.
- <sup>51</sup> Espinal, L.; Suib, S. L.; Rusling, J. F. *J. Am. Chem. Soc.* **2004**, *126*, 7676-7682.
- <sup>52</sup> Ge, J. P.; Hu, Y. X.; Biasini, M.; Beyermann, W. P.; Yin, Y. D. *Angew. Chem. Int. Ed.* **2007**, *46*, 4342-4345.
- <sup>53</sup> Sun, S. H.; Zeng, H. J.; *J. Am. Chem. Soc.* **2002**, *124*, 8204-8205.
- <sup>54</sup> Liang, S.; Teng, F.; Bulgan, G.; Zong, R.; Zhu, Y. *J. Phys. Chem. C* **2008**, *112*, 5307-5315.
- <sup>55</sup> Feng, Q.; Kanoh, H.; Ooi, K. *J. Mater. Chem.* **1999**, *9*, 319-333.
- <sup>56</sup> Ma, Y.; Luo, J.; Suib, S. L. *Chem. Mater.* **1999**, *11*, 1972-1979.
- <sup>57</sup> Yang, D. S.; Wang, M. K. *Chem. Mater.* **2001**, *13*, 2589-2594.
- <sup>58</sup> Ching, S.; Petrovay, D. J.; Jorgensen, M. L.; Suib, S. L. *Inorg. Chem.* **1997**, *36*, 883-890.
- <sup>59</sup> Ching, S.; Landrigan, A. L.; Jorgensen, M. L.; Suib, S. L. *Chem. Mater.* **1995**, *7*, 1604-1606.
- <sup>60</sup> Petkov, V.; Ren, Y.; Saratovsky, I.; Pastén, P.; Gurr, S. J.; Hayward, M. A.; Poeppelmeier, K. R.; Gaillard, J.-F. *ACS Nano* **2009**, *2*, 445-445.
- <sup>61</sup> Giovanelli, R.; Stähli, E.; Feitknecht, W. *Helv. Chim. Acta* **1970**, *53*, 453-464.
- <sup>62</sup> Post, J. E.; Veblen, D. R. *Am. Miner.* **1990**, *75*, 477-489.
- <sup>63</sup> Gaillot, A.-C.; Drits, V. A.; Plancon, A.; Lanson, B. *Chem. Mater.* **2004**, *16*, 1890-1905.
- <sup>64</sup> Silvester, E. Manceau, A.; Drits, V. A. *Am. Mineral.* **1997**, *82*, 962-978.
- <sup>65</sup> Gaillot, A.-C.; Flot, D.; Drits, V. A.; Manceau, A.; Burghammer, M.; Lanson, B. *Chem. Mater.* **2003**, *15*, 4666-4678.
- <sup>66</sup> Saratovsky, I.; Wightman, P. G.; Pastén, P. A.; Gaillard, J.-F.; Poeppelmeier, K. R. *J. Am. Chem. Soc.* **2006**, *128*, 11188-11198.
- <sup>67</sup> Gaillot, A.-C.; Drits, V. A.; Manceau, A.; Lanson, B. *Micropor. Mesopor. Mater.* **2007**, *98*, 267-282.
- <sup>68</sup> Grangeon, S.; Lanson, B.; Miyata, N.; Tani, Y.; Manceau, A. *Am. Mineral.* **2010**, *95*, 1608-1616.
- <sup>69</sup> Taillefert, M.; MacGregor, B. J.; Gaillard, J. F.; Lienemann, C. P.; Perret, D.; Stahl, D. A. *Environ. Sci. Technol.* **2001**, *13*, 778-786.
- <sup>70</sup> Dyer, A.; Pillinger, M.; Newton, J.; Hajula, R.; Moeller, T.; Amin, S. *Chem. Mater.* **2000**, *12*, 3798-3804.
- <sup>71</sup> Gao, Q.; Giraldo, O.; Tong, W.; Suib, S. L. *Chem. Mater.* **2001**, *13*, 778-786.
- <sup>72</sup> Ressler, T.; Brock, S. L.; Wong, J.; Suib, S. L. *J. Phys. Chem. B* **1999**, *103*, 6407-6420.
- <sup>73</sup> Wang, Z. M.; Liu, Z.; Yamashita, N.; Kanoh, H.; Ooi, K. *Langmuir* **2002**, *18*, 1957-1962.
- <sup>74</sup> Omomo, Y.; Sasaki, T.; Wang L.; Watanabe M. *J. Am. Chem. Soc.* **2003**, *125*, 3568-3575.
- <sup>75</sup> Liu, Z.; Ma, R.; Ebina, Y.; Takada, K.; Sasaki, T. *Chem. Mater.* **2007**, *19*, 6504-6512.
- <sup>76</sup> Osada, M.; Sasaki, T. *J. Mater. Chem.* **2009**, *19*, 2503-2511.

- <sup>77</sup> Sasaki, T.; Watanabe, M.; Hashizume, H.; Yamada, H.; Nakazawa, H. *J. Am. Chem. Soc.* **1996**, *118*, 8329-8335.
- <sup>78</sup> Fukuda, K.; Nakai, I.; Ebina, Y.; Tananka, M.; Mori, T.; Sasaki, T. *J. Phys. Chem. B* **2006**, *110*, 17070-17075.
- <sup>79</sup> Liu, Z. H.; Ooi, K.; Kanoh, H.; Tang, W.-P.; Tomida, T. *Langmuir* **2000**, *16*, 4154-4164.
- <sup>80</sup> Kai, K.; Yoshida, Y.; Kageyama, H.; Saito, G.; Ishigaki, T.; Furukawa, Y.; Kawamata, J. *J. Am. Chem. Soc.* **2008**, *130*, 15938-15943.
- <sup>81</sup> Oaki, Y.; Imai, H. *Angew. Chem. Int. Ed.* **2007**, *46*, 4951-4955.
- <sup>82</sup> Schaak, R. E.; Mallouk, T. E. *Chem. Mater.* **2000**, *12*, 2513-2516.
- <sup>83</sup> Liu, Z.-H.; Ooi, K.; Kanoh, H.; Tang, W.; Yang, X.; Tomida, T. *Chem. Mater.* **2001**, *13*, 473-478.
- <sup>84</sup> Shen, Y. F.; Zerger, R. P.; DeGuzman, R. N.; Suib, S. L.; McCurdy, L.; Potter, D. I.; O'Young, C. L. *Science* **1993**, *260*, 511-515.
- <sup>85</sup> Shen, X.-F.; Ding, Y.-S.; Liu, J.; Cai, J.; Laubernds, K.; Zerger, R. P.; Vasiliev, A.; Aindow, M.; Suib, S. L. *Adv. Mater.* **2005**, *17*, 805-809.
- <sup>86</sup> Yuan, J.; Li, W.-N.; Gomez, S.; Suib, S. L. *J. Am. Chem. Soc.* **2005**, *127*, 15184-14185.
- <sup>87</sup> Brock, S. L.; Duan, N.; Rong Tian, Z.; Giraldo, O.; Zhou, H.; Suib, S. L. *Chem. Mater.* **1998**, *10*, 2619-2628.
- <sup>88</sup> Suib, S. L. *J. Mater. Chem.* **2008**, *18*, 1623-1631.
- <sup>89</sup> Son, Y. C.; Makwana, V. D.; Howell, A. R.; Suib, S. L. *Angew. Chem. Int. Ed.* **2001**, *40*, 4280-4283.
- <sup>90</sup> Liu, J.; Son, Y.-S.; Cai, J.; Shen, X.; Suib, S. L.; Aindow, M. *Chem. Mater.* **2004**, *16*, 276-285.
- <sup>91</sup> Haruta, M.; Kobayashi, T.; Sano, H.; Yamada, N. *Chem. Lett.* **1987**, *16*, 405-408.
- <sup>92</sup> Haruta, M.; Yamada, N.; Kobayashi, T.; Iijima, S. *J. Catal.* **1989**, *115*, 301-309.
- <sup>93</sup> Nkosi, B.; Coville N. J.; Hutchings, G. J. *J. Chem. Soc. Chem. Commun.* **1988**, *1*, 71-72.
- <sup>94</sup> Lipshutz, B. H.; Yamamoto, Y.; *Chem. Rev.* **2008**, *108*, 2793-2795.
- <sup>95</sup> Pradhan, N.; Pal, A.; Pal, T. *Colloid Surf. A* **2002**, *196*, 247-257.
- <sup>96</sup> Sau, T. K.; Pal, A.; Pal, T. *J. Phys. Chem. B* **2001**, *105*, 9266-9272.
- <sup>97</sup> Burda, C.; Lou, Y.; Chen, X.; Samia, A. C. S., Stout, J.; Gole, J. L. *Nano Lett.* **2003**, *3*, 1049-1051.
- <sup>98</sup> Panigrahi, S.; Basu, S.; Praharaj, S.; Pande, S.; Jana, S.; Pal, A.; Gosh, S. K.; Pal, T. *J. Phys. Chem. C* **2007**, *111*, 4596-4605.
- <sup>99</sup> Zhou, X.; Xu, W.; Liu, G.; Panda, D.; Peng, C. *J. Am. Chem. Soc.* **2010**, *132*, 138-146.
- <sup>100</sup> Tsunoyama, H.; Sakurai, H.; Negishi, Y.; Tsukuda, T. *J. Am. Chem. Soc.* **2005**, *127*, 9374-9375.
- <sup>101</sup> Zeng, J.; Zhang, Q.; Chen, J.; Xia, Y. *Nano Lett.* **2010**, *10*, 30-35.
- <sup>102</sup> Tian, N.; Zhou, Z.-Y.; Sun, S.-G.; Ding, Y.; Wang, Z. L. *Science* **2007**, *316*, 732-735.

- <sup>103</sup> Vannice, M. A. *Kinetics of Catalytic Reactions*; Springer Science + Business Media: Philadelphia, PA, 2005.
- <sup>104</sup> Boudart, M.; Djéga-Mariadassou, G. *Kinetics Heterogeneous Catalytic Reactions*; Princeton Press: Princeton, NJ, 1984.
- <sup>105</sup> Langmuir, I. *J. Am. Chem. Soc.* **1918**, *40*, 1361-1403.
- <sup>106</sup> Narayanan, R.; El-Sayed, M. A.; *J. Phys. Chem. B* **2005**, *109*, 12663-12676.
- <sup>107</sup> Narayanan, R.; El-Sayed, M. A.; *J. Am. Chem. Soc.* **2003**, *125*, 8340-8347.
- <sup>108</sup> Astruc, D.; Lu, F.; Aranzaes, J. R. *Angew. Chem. Int. Ed.* **2005**, *44*, 7852-7872.
- <sup>109</sup> Vollath, D. *Nanomaterials*; Wiley-VCH: Weinheim, 2008.
- <sup>110</sup> Bishop, K. J. M.; Wilmer, C. E.; Soh, S.; Grzybowski, B. A. *Small* **2009**, *5*, 1600-1630.
- <sup>111</sup> Derjaguin, B. V.; Landau, L. D. *Acta Physicochim. USSR* **1941**, *14*, 633-662.
- <sup>112</sup> Verwey, E. J. W.; Overbeek, J. Th. G. *Theory of the stability of lyophobic colloids*, Elsevier: Amsterdam, 1948.
- <sup>113</sup> Evans, D. F.; Wennerström, H. *The Colloidal Domain*, Wiley-VCH: New York, 1999.
- <sup>114</sup> Cushing, B. L.; Kolesnichenko, V. L.; O'Connor, C. J. *Chem. Rev.* **2004**, *104*, 3893-3946.
- <sup>115</sup> Claus, P.; Brückner, A.; Mohr, C.; Hofmeister, H. *J. Am. Chem. Soc.* **2000**, *122*, 11430-11439.
- <sup>116</sup> Haruta, M. *Catal. Today* **1997**, *36*, 153-166.
- <sup>117</sup> White, R. J.; Luque, R.; Budarin, V. L.; Clark, J. H.; Macquerrie, D. J. *Chem. Soc. Rev.* **2009**, *38*, 481-494.
- <sup>118</sup> Ballauff, M. *Prog. Polym. Sci.* **2007**, *32*, 1135-1151.
- <sup>119</sup> Rühe, J. *Adv. Polym. Sci.* **2004**, *165*, 79-150.
- <sup>120</sup> Advincula, R. C., Brittain, W. J.; Caster, K. C.; Rühe, J. *Polymer Brushes*; Wiley-VCH: Weinheim, 2004
- <sup>121</sup> Wittemann, A.; Drechsler, M.; Talmon, Y.; Ballauff, M. *J. Am. Chem. Soc.* **2005**, *127*, 9688-9689.
- <sup>122</sup> Pincus, P. *Macromolecules* **1991**, *24*, 2912-2919.
- <sup>123</sup> Borisov, O. V.; Birshtein, T. M.; Zhulina, E. B. *J. Phys. II (France)*, **1991**, *1*, 521-526.
- <sup>124</sup> Lu, Y.; Wittemann, A.; Ballauff, M. *Macromol. Rapid Commun.* **2009**, *30*, 806-815.
- <sup>125</sup> Sharma, G.; Ballauff, M. *Macromol. Rapid Commun.* **2004**, *25*, 547-557.
- <sup>126</sup> Mei, Y.; Sharma, G.; Lu, Y.; Drechsler, M.; Irrgang, T.; Kempe, R.; Ballauff, M. *Langmuir* **2005**, *21*, 12229-12234.
- <sup>127</sup> Lu, Y.; Mei, Y.; Schrinner, M.; Drechsler, M.; Möller, M. W.; Breu, J.; Ballauff, M. *J. Phys. Chem. B* **2007**, *111*, 7676-7681.
- <sup>128</sup> Schrinner, M.; Polzer, F.; Mei, Y.; Lu, Y.; Haupt, B.; Göldel, A.; Drechsler, M.; Preussner, J.; Glatzel, U.; Ballauff, M. *Macromol. Chem. Phys.* **2007**, *208*, 1542-1547.
- <sup>129</sup> Mei, Y.; Lu, Y.; Polzer, F.; Drechsler, M.; Ballauff, M. *Chem. Mater.* **2007**, *19*, 1062-1069.

- <sup>130</sup> Schrinner, M.; Möller, M.; Thun, J.; Kauffmann, Y.; Breu, J.; Talmon, Y.; Ballauff, M. *Science* **2009**, *323*, 617-620.
- <sup>131</sup> Sharma, G.; Mei, Y.; Lu, Y.; Ballauff, M.; Irrgang, T.; Kempe, R. *J. Catal.* **2007**, *246*, 10-14.
- <sup>132</sup> Proch, S.; Mei, Y.; Rivera Villanueva, J. M.; Lu, Y.; Karpov, A.; Ballauff, M.; Kempe, R. *Adv. Synth. Catal.* **2008**, *350*, 493-500.
- <sup>133</sup> Schrinner, M.; Proch, S.; Mei, Y.; Kempe, R.; Miyajima, N.; Ballauff, M. *Adv. Mater.* **2008**, *20*, 1928-1933.
- <sup>134</sup> Malysheva, Y. B.; Gushchin, A.V.; Mei, Y.; Lu, Y.; Ballauff, M.; Proch, S.; Kempe, R.; *Eur. J. Inorg. Chem.* **2008**, *3*, 379-383.
- <sup>135</sup> Hara, D.; Shirakawa, J.; Ikuta, H.; Uchimoto, Y.; Wakihara, M.; Miyanaga, T.; Watanabe, I. *J. Mater. Chem.* **2003**, *13*, 897-903.
- <sup>136</sup> Kelly, S. D.; Hesterberg, D.; Ravel, B. *Analysis of soils and minerals using X-ray absorption spectroscopy. Methods of soil analysis, Part 5 - Mineralogical methods.*, (Eds.: Ulery, A. L. and Drees, L. R.); Soil Science Society of America: Madison, WI, 2008.
- <sup>137</sup> Stöhr, J. *NEXAFS Spectroscopy*; Springer Verlag: Berlin, 1992.
- <sup>138</sup> Koningsberger, D. C.; Prins, R. *X-ray Absorption: Principles, Applications, Techniques of EXAFS SEXAFS, and XANES*; Wiley: New York, 1988.
- <sup>139</sup> Kobayashi, S.; Kotegoda, R. M.; Uchimoto, Y.; Wakihara, M. *J. Mater. Chem.* **2004**, *14*, 1843-1848.
- <sup>140</sup> Bellare, J. R.; Davis, H. T.; Scriven, L. E.; Talmon, Y. *J. Electron Microsc. Tech.* **1988**, *10*, 87-111.
- <sup>141</sup> Almgren, M.; Edwards, K.; Karlsson, J. *Colloids Surf. A* **2000**, *174*, 3-21.
- <sup>142</sup> Talmon, Y. in *Modern Characterization Methods of Surfactant Systems* (Ed.: Binks, B. P.); Marcel Dekker Inc: New York, 1999.
- <sup>143</sup> Almgren, M.; Edwards, K.; Gustafsson, J. *Curr. Opin. Colloid Interface Sci.* **1996**, *1*, 270-278.
- <sup>144</sup> Frederik, P. M.; Sommerdijk, N. *Curr. Opin. Colloid Interface Sci.* **2005**, *10*, 245-249.
- <sup>145</sup> Bremer, A.; Henn, C.; Engel, A.; Baumeister, W.; Aebi, U. *Ultramicroscopy* **1992**, *46*, 85-111.
- <sup>146</sup> Nudelmann, F.; de With, G.; Sommerdijk, N. A. J. M. *Soft Matter* **2011**, *7*, 17-24.
- <sup>147</sup> Crassous, J. J.; Rochette, C. N.; Wittemann, A.; Schrinner, M.; Drechsler, M.; Ballauff, M. *Langmuir* **2010**, *25*, 7862-7871.
- <sup>148</sup> Friedrich, H.; Frederik, P. M.; de With, G.; Sommerdijk, N. A. J. M. *Angew. Chem. Int. Ed.* **2010**, *49*, 7850-7858.
- <sup>149</sup> Dubochet, J.; Mc Dowall, A. W. *J. Microsc.* **1981**, *124*, 3-4.
- <sup>150</sup> Dubochet, J.; Chang, J. J.; Freeman, R.; Lepault, J.; Mc Dowall, A. W. *Ultramicroscopy* **1982**, *10*, 55-61.

- <sup>151</sup> Falls, A. H.; Wellinghoff, S. T.; Talmon, Y.; Thomas, E. L. *J. Mater. Sci.* **1983**, *18*, 2752-2764.
- <sup>152</sup> Vinson, P. K.; Bellare, J. R.; Davis, H. T.; Miller, W. G.; Scriven, L. E. *Colloid Interface Sci.* **1991**, *142*, 74-91.
- <sup>153</sup> Cui, H.; Hodgdon, T. K.; Klaer, E. W.; Abegauz, L.; Danino, D.; Lubovsky, M.; Talmon, Y.; Pochan, D. J. *Soft Matter* **2007**, *3*, 945-955.
- <sup>154</sup> Crassous, J. J.; Wittemann, A.; Siebenbürger, M.; Schrinner, M.; Drechsler, M.; Ballauff, M. *Colloid Interface Sci.* **2008**, *286*, 805-812.
- <sup>155</sup> Samokhina, L.; Schrinner, M.; Ballauff, M. *Langmuir* **2007**, *23*, 3615-3619.
- <sup>156</sup> Lu, Y.; Spyra, P.; Mei, Y.; Pich, A.; Ballauff, M. *Macromol. Chem. Phys.* **2007**, *208*, 254-261.
- <sup>157</sup> Lu, Y.; Mei, Y.; Walker, R.; Drechsler, M.; Ballauff, M. *Polymer* **2006**, *47*, 4985-4995.

*References*

---

## 2. Overview

The main objective of this thesis was the synthesis of  $\text{MnO}_x\text{NP}$  and to immobilize these nanoparticles onto a colloidal stable carrier particle. The support particles consist of a PS core particle with a typical diameter of about 100 nm onto which long polyelectrolyte chains are chemically grafted. These systems are denoted as SPBs and possess a high colloidal stability in aqueous solution.

- In Chapter 3, a detailed description of the synthesis of the composite material is presented. In addition, the composite material was characterized extensively by TEM and cryoTEM to elucidate its structure. A comparison of PXRD patterns of different reference compounds to the diffraction pattern of the composite material gave first insights into the crystallographic structure of the  $\text{MnO}_x\text{NP}$  immobilized on SPBs which led to the development of a model for the composite system.
- Chapter 4 is dedicated to a detailed analysis of the crystallographic structure of the  $\text{MnO}_x\text{NP}$  by XAFS measurements to overcome the problems of the missing long-range order of the nanoparticles which hampered the characterization by PXRD. Special emphasis has been laid on the local structure of the  $\text{MnO}_x\text{NP}$  around the Mn absorber with regards to differences of the structure of the composite material in the dried and in the dispersed state. Additionally, a new kind of composite material composed of star-shaped pTMAEMC homopolymer and  $\text{MnO}_x\text{NP}$  was synthesized and characterized.
- The composite material of  $\text{MnO}_x\text{NP}$  immobilized on SPBs was tested for its catalytic activity on the oxidation of morin by hydrogen peroxide which is presented in Chapter 5. Therefore, the kinetic model of a Langmuir-Hinshelwood mechanism for heterogeneous catalyzed reactions has been applied to the oxidation reaction.
- In analogy to that, Chapter 6 deals with the analysis of the reduction of 4-nitrophenol by sodium borohydride in the presence of composite particles of SPB and gold and platinum nanoparticles. A Langmuir-Hinshelwood model was applied to this catalytic reaction. Furthermore, the induction period observed during the investigations was analyzed in detail and could be subscribed to a surface reconstruction of the nanoparticles.
- Chapter 7 presents the synthesis and characterization of novel SPB particles with a zwitterionic shell. The synthesis of the shell was conducted by aqueous ATRP. A combination of DLS, TEM and cryoTEM measurements lead to the conclusion that the zwitterionic shell of pMEDSAH is predominantly in a collapsed state with a minor part of the chains reaching out of the collapsed layer. This has been assigned to an internal phase separation of the zwitterionic shell. Temperature- and salt-dependent DLS

measurements proved the responsive behavior to external stimuli of the zwitterionic shell that leads to a swelling of the latter.

This doctoral thesis comprises five publications given in the Chapters 3, 4, 5, 6 and 7.

## 2.1. Formation of Ultrathin Birnessite-Type Nanoparticles Immobilized on Spherical Polyelectrolyte Brushes

We studied the *in-situ* generation of  $\text{MnO}_x\text{NP}$  on cationic SPBs with a shell of poly(2-trimethyl ammoniumethyl methacrylate chloride) (pTMAEMC). First, we investigated the synthesis of the  $\text{MnO}_x\text{NP}$  by varying the parameters like the amount of added  $\text{KMnO}_4$ , the speed of the addition and the temperature. This study showed that no reducing agent is needed to generate the  $\text{MnO}_x\text{NP}$ . In addition, the reduction by the monomer units of the polyelectrolyte shell could be ruled out. Based on these findings we developed the mechanism of a basic catalyzed reduction of the  $\text{MnO}_4^-$  ions within the brush layer.

Furthermore, DLS measurements showed that the brush thickness decreases upon the immobilization of the  $\text{MnO}_x\text{NP}$  indicating the interaction of the negatively charged nanoparticles with the positively charged polyelectrolyte chains of the shell. This was confirmed by zeta potential measurements and proves the excellent stabilization of the  $\text{MnO}_x\text{NP}$  by the pTMAEMC shell.

A comparison of the composite particles by TEM and cryoTEM revealed that there is a significant difference in the morphology of the  $\text{MnO}_x\text{NP}$  immobilized onto SPBs between the dried state and the aqueous dispersed state (see Figure 2.1.1). This was assigned to a collapse of the ultrathin platelet-like nanoparticles onto the PS core of the SPB upon drying (see Figure 2.1.1a). In contrast to that, the  $\text{MnO}_x\text{NP}$  are also present in the polyelectrolyte shell of the SPB which is confirmed by the cryoTEM micrograph in Figure 2.1.1b.

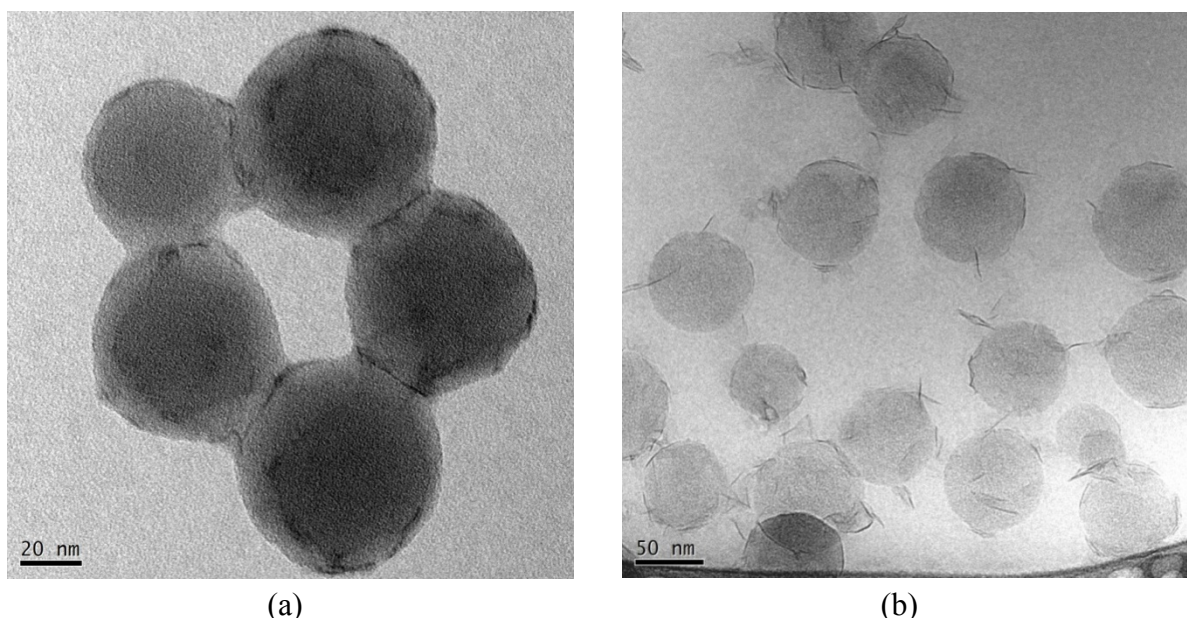


**Figure 2.1.1.** (a) TEM micrograph and (b) cryoTEM micrograph of the composite material TMAEMC- $\text{MnO}_x\text{-}5$  comprised of cationic SPB particles and  $\text{MnO}_x\text{NP}$ . Marked differences of the composite materials exist between the dried state and the aqueous dispersed state as can be seen by comparing the two micrographs.

A comparison of the PXRD patterns of the composite material to reference compounds, e.g. H<sup>+</sup>-birnessite and K<sup>+</sup>-birnessite, lead to the conclusion that the MnO<sub>x</sub>NP are composed of hexagonal lamellae of birnessite (see Figure 2.1.2). This mixed valent manganese oxide possesses a layered topology and is composed of predominantly edge-shared MnO<sub>6</sub> octahedra. The missing *00l* reflections of the composite material in combination with the electron micrographs prove that the MnO<sub>x</sub>NP are composed of single or only a few stacks of lamellae of birnessite. Additionally, the *hk* bands at 36.5° and 65° in 2θ prove a disorder along the stacking axis of the lamellae.

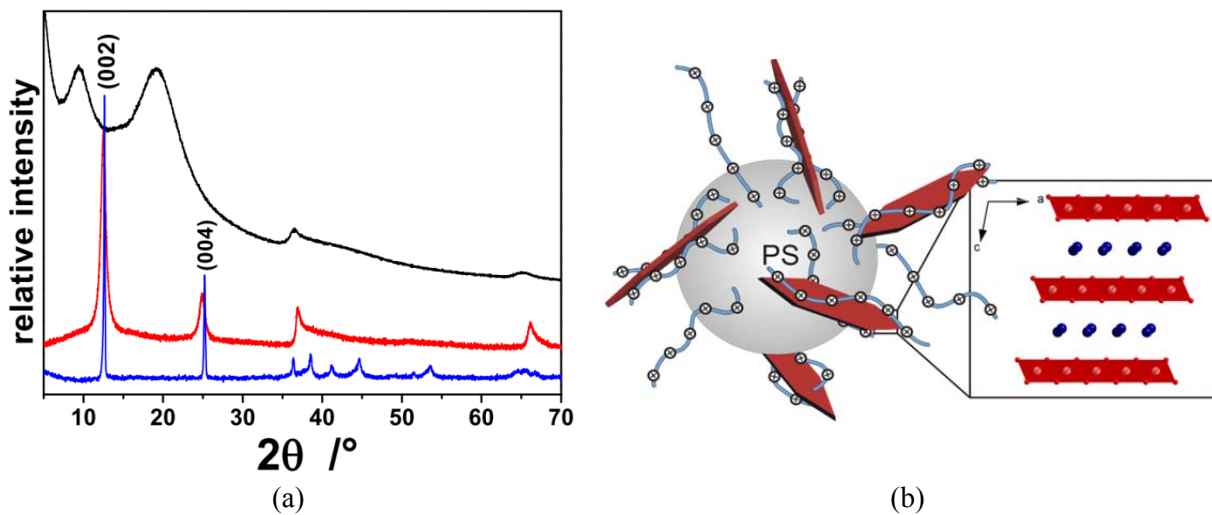


**Figure 2.1.2.** (a) PXRD patterns of the composite material TMAEMC-MnO<sub>x</sub>-5, H<sup>+</sup>-birnessite and K<sup>+</sup>-birnessite. The missing *00l* reflections and the *hk* bands at 36.5° and 65° in 2θ in combination with the electron micrographs prove the generation of ultrathin platelet-like MnO<sub>x</sub>NP exhibiting a disorder along the c-axis. (b) Schematic model of the composite material TMAEMC-MnO<sub>x</sub>-5. The negatively charged MnO<sub>x</sub>NP are stabilized by the cationic pTMAEMC chains. The MnO<sub>x</sub>NP are composed of edge-shared MnO<sub>6</sub> octahedra (Mn white spheres, O red spheres) that form into layers with intercalated K<sup>+</sup>-ions and water molecules (blue spheres) between the layers.

The full publication can be found in Chapter 3.

## 2.2. Structural Analysis of Colloidal MnO<sub>x</sub> Composites

This work reports the first synthesis of MnO<sub>x</sub>NP with a layered topology stabilized by star-shaped pTMAEMC homopolymer. The reduction of KMnO<sub>4</sub> was started by the addition of 2-butanol since no *in-situ* generation of MnO<sub>x</sub>NP was observed, as found for the synthesis of MnO<sub>x</sub>NP@SPB particles. The disk-like nanoparticles exhibit an average diameter of about 5 nm as shown in the HRTEM micrograph in Figure 2.2.1. PXRD measurements reveal a similar structure of the MnO<sub>x</sub>NP stabilized by star-shaped pTMAEMC compared to that of the composite particles described in Chapter 2.1.

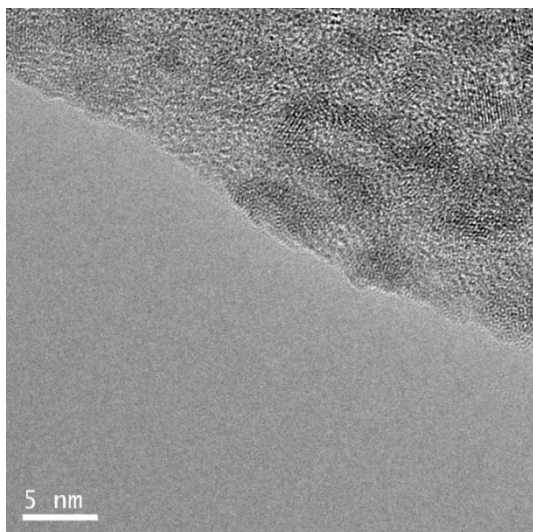


**Figure 2.2.1.** HRTEM micrograph of the composite material composed of star-shaped pTMAEMC homopolymer and MnO<sub>x</sub>NP. The image shows the MnO<sub>x</sub>NP visible as dark, disk-like particles embedded in the polymer. At some spots, lattice planes of the MnO<sub>x</sub>NP are visible.

The lack of long-range order in the MnO<sub>x</sub>NP complicated the detailed analysis of the inorganic material by conventional PXRD measurements. Therefore, XAFS measurements were conducted to probe the local structure around the Mn atom within the MnO<sub>x</sub>NP stabilized either by cationic SPBs or by star-shaped pTMAEMC homopolymer. Firstly, the XANES spectra were used to determine the average oxidation states of the Mn of the MnO<sub>x</sub>NP by comparing the position of the absorption edge to that of different manganese oxide reference compounds. This showed that the average oxidation state of Mn of the composite material is between 3.5 - 3.7 indicating the mixed valency of Mn within the crystallographic structure. A qualitative comparison of the EXAFS spectra of the different composite materials to those of H<sup>+</sup>-birnessite and K<sup>+</sup>-birnessite prove similarities in the crystallographic structure as already expected by PXRD analysis. The  $\chi(k)k^3$  spectra as well as the Fourier transformed spectra of all composite materials and of birnessite reference compounds are shown in Figure 2.2.2.

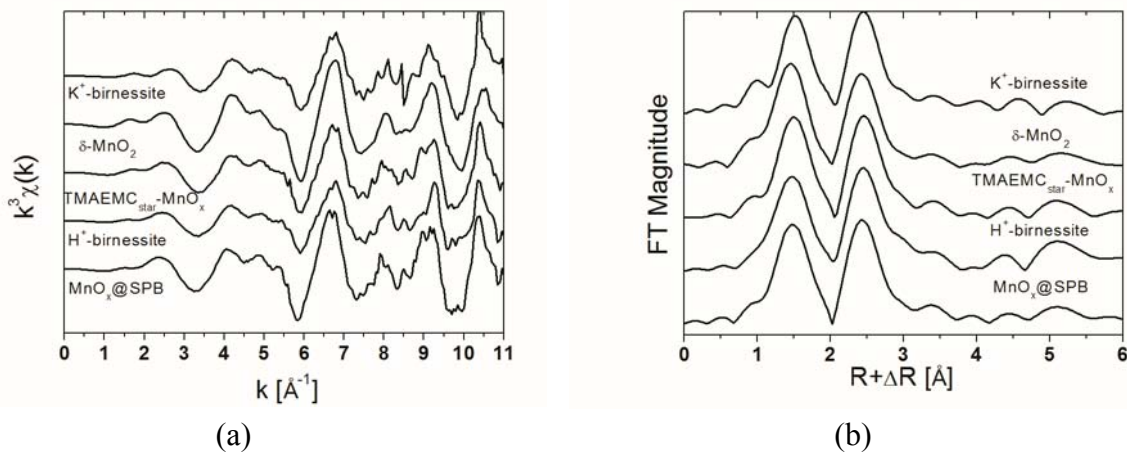


**Figure 2.2.2.** (a)  $\chi(k)k^3$  spectra of the composite materials and the reference compounds. (b) Corresponding Fourier transforms of the  $\chi(k)$  spectra for the composite materials and the reference compounds. Both graphs demonstrate the excellent agreement of the crystallographic structure of the MnO<sub>x</sub>NP composite materials with the phyllo-manganate reference compounds.

Lastly, a quantitative analysis of the EXAFS spectra of the MnO<sub>x</sub>NP immobilized on cationic SPBs was conducted to clarify if the difference observed by TEM and cryoTEM of the structure of the composite material has an influence on the local structure of the Mn of the MnO<sub>x</sub>NP. The best fit results of this analysis are shown in Figure 2.2.3.

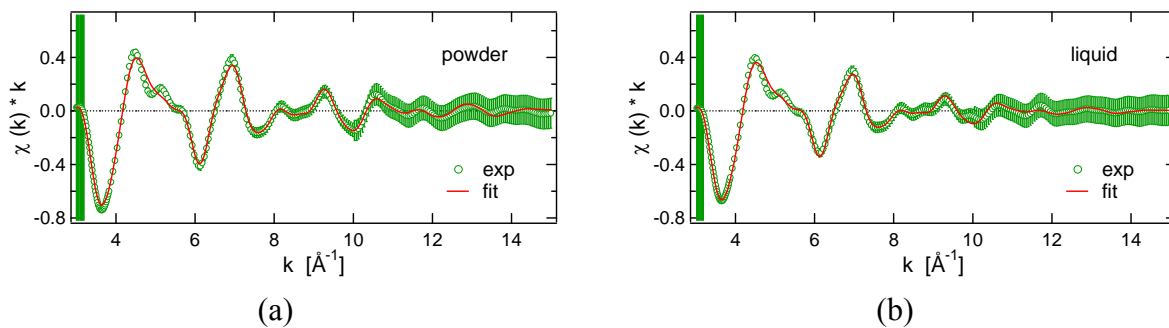


**Figure 2.2.3.** (a)  $\chi(k)k$  spectra for the composite material MnO<sub>x</sub>NP@SPB in the dried state and (b) in the aqueous dispersed state. The red curve shows the best fit for each experimental data.

The fit results show that there is no marked difference in the local structure of the Mn between the dried state and the aqueous dispersed state. Thus, the hexagonal sheets composed of MnO<sub>6</sub> octahedra show a significant contraction along the c-axis of about 4 % compared to the model for bulk birnessite. This contraction is accompanied by a slight elongation within the ab-plane, that is, the 2D expansion of the hexagonal sheets.

The full publication can be found in Chapter 4.

### 2.3. Catalytic Oxidation of an Organic Dye by $\text{MnO}_x$ Nanoparticles Immobilized on Spherical Polyelectrolyte Brushes

The composite material  $\text{MnO}_x\text{NP}@\text{SPB}$  was tested for its catalytic activity on the oxidation of morin by hydrogen peroxide ( $\text{H}_2\text{O}_2$ ). This reaction is well known as a model reaction for testing stain bleaching catalysts for laundry applications.

The reaction kinetics was treated as pseudo-first order due to an excess of  $\text{H}_2\text{O}_2$  during the course of the oxidation. The presence of isosbestic points in the UV/vis spectrum proved the absence of any side products during the catalytic decomposition of morin. Furthermore, a linear dependence of the catalyst concentration on the apparent rate constant  $k_{app}$  was shown.

The mechanism of the kinetic oxidation was modeled by a Langmuir-Hinshelwood approach for a bimolecular surface reaction. The characteristic Langmuir-Hinshelwood plots are shown in Figure 2.3.1. Both data sets were modeled with the same set of parameters.

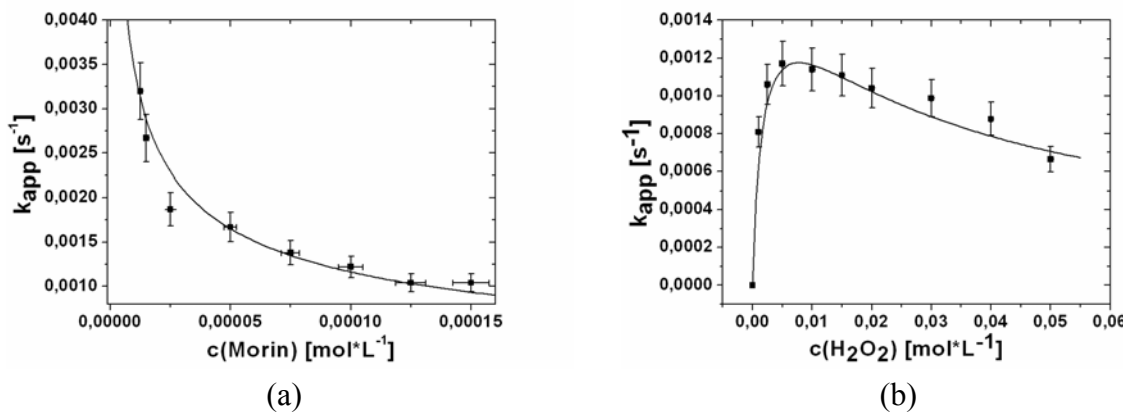


**Figure 2.3.1.** Langmuir-Hinshelwood kinetics of the catalytic oxidation of morin by  $\text{H}_2\text{O}_2$  in the presence of  $\text{MnO}_x\text{NP}$  immobilized on SPBs. (a) Dependence of the concentration of morin ( $c(\text{H}_2\text{O}_2) = \text{const.}$ ) on the apparent rate constant  $k_{app}$ . (b) Influence of the concentration of  $\text{H}_2\text{O}_2$  on  $k_{app}$  ( $c(\text{morin}) = \text{const.}$ ).

Figure 2.3.2 shows a schematic model of the Langmuir-Hinshelwood mechanism for the catalytic decomposition of morin by  $\text{H}_2\text{O}_2$  in the presence of  $\text{MnO}_x\text{NP}@\text{SPB}$ . Both reactants adsorb onto the nanoparticle surface where they undergo a surface reaction. The decomposition product M-DP desorbs from the active site of the catalyst and the catalytic cycle can begin again.

By fitting both plots using the Langmuir-Hinshelwood equation, the adsorption constants for both reactants as well as the kinetic rate constant of the surface reaction could be determined. The model was furthermore expanded by Freundlich exponents for both reactants. This parameter takes the surface heterogeneities into account that directly influence the adsorption process.

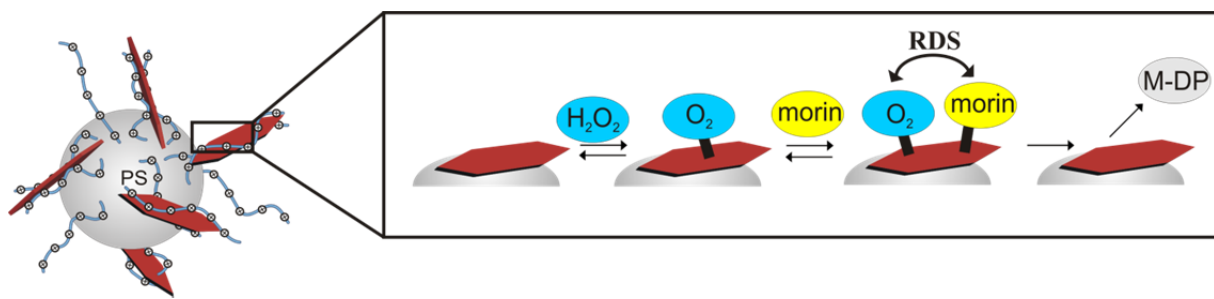


**Figure 2.3.2.** Schematic representation of the Langmuir-Hinshelwood model of the catalytic oxidation of morin by  $\text{H}_2\text{O}_2$  in the presence of  $\text{MnO}_x\text{NP}@\text{SPB}$ .  $\text{H}_2\text{O}_2$  molecules decompose on the catalyst surface and react with the adsorbed morin molecules. After the desorption of the oxidation product a new catalytic cycle can start.

At high concentrations of one of the reactants, the surface is blocked predominantly by this reactant, depending on its adsorption constant. Due to this mechanism the rate of the reaction decreases because both reactants need to be adsorbed to undergo the surface reaction.

This paper provides the first full description of the oxidation of morin by  $\text{H}_2\text{O}_2$  in the presence of  $\text{MnO}_x\text{NP}$ . Since this reaction is a benchmark for catalysts with respect to their activity for stain bleaching, this work serves as a starting point for a more systematic approach of studying different nanoparticulate bleaching catalysts.

The full publication can be found in Chapter 5.

## 2.4. Kinetic Analysis of the Catalytic Reduction of 4-Nitrophenol by Metallic Nanoparticles Immobilized in Spherical Polyelectrolyte Brushes

The kinetic reduction of 4-nitrophenol was studied in detail by applying a Langmuir-Hinshelwood model to the reaction. Therefore, UV/vis measurements of the reduction of 4-nitrophenol with gold and platinum nanoparticles immobilized on SPBs were conducted. Figure 2.4.1a shows a typical course of a time-dependent measurement at the absorption maximum of 4-nitrophenol.

One additional aspect of this study was the investigation of the induction period of the reduction that is, a time range where no reaction takes place though all reactants are present in the system (see Figure 2.4.1a). It could be shown that  $t_0$  is dependent on the concentration of 4-nitrophenol (see Figure 2.4.1b), on the catalyst concentration and on the temperature of the reaction solution. The induction period was explained by a surface reconstruction of the nanoparticles due to the adsorption of 4-nitrophenol on the highly curved nanoparticles.

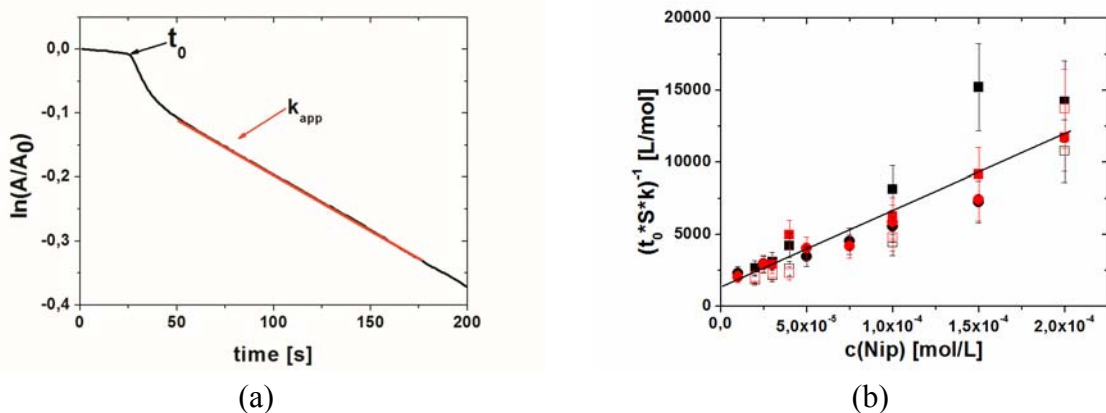


**Figure 2.4.1.** (a) Time-dependent normalized absorption measured at 400 nm during the catalytic reduction of 4-nitrophenol (Nip) by  $\text{NaBH}_4$  in the presence of noble metal nanoparticles immobilized on SPBs. First, an induction period  $t_0$  is observed where no reduction takes place. The following linear regime is defined as the start of the catalytic reaction and is used for the determination of the apparent rate constant  $k_{app}$  applying a pseudo first-order rate law. Figure 2.4.1b demonstrates that the inverse induction time normalized by the kinetic constant  $k$  scales linearly with the concentration of Nip. Here the black color represents the  $\text{BH}_4^-$  concentration of 10 mM and the red color a concentration of 5 mM. The line herein represents a least-square fit of all data indicating a small but finite intercept.

The influence of the two reactants, 4-nitrophenol and  $\text{BH}_4^-$ , on the apparent reaction constant  $k_{app}$  was investigated by UV/vis measurements (see Figure 2.4.2). It could be shown for Au as well as for Pt nanoparticles that  $k_{app}$  is increasing with decreasing 4-nitrophenol concentration. Furthermore, an increase in the concentration of  $\text{BH}_4^-$  led to an increase of  $k_{app}$  going through a shallow maximum. These findings were interpreted by means of a Langmuir-Hinshelwood model that describes the reaction in terms of a competitive adsorption on the

catalyst surface. Both adsorbed species undergo a surface reaction leading to a reduction of 4-nitrophenol to 4-aminophenol.

All curves were fitted with the same set of parameters which proved the applicability of the kinetic model for the reduction of 4-nitrophenol. The Langmuir-Hinshelwood model was expanded by the introduction of Freundlich exponents that take into account surface heterogeneities of the catalyst. By this method, the adsorption constants for both reactants as well as the rate constant of the surface reaction and the Freundlich exponents could be determined.

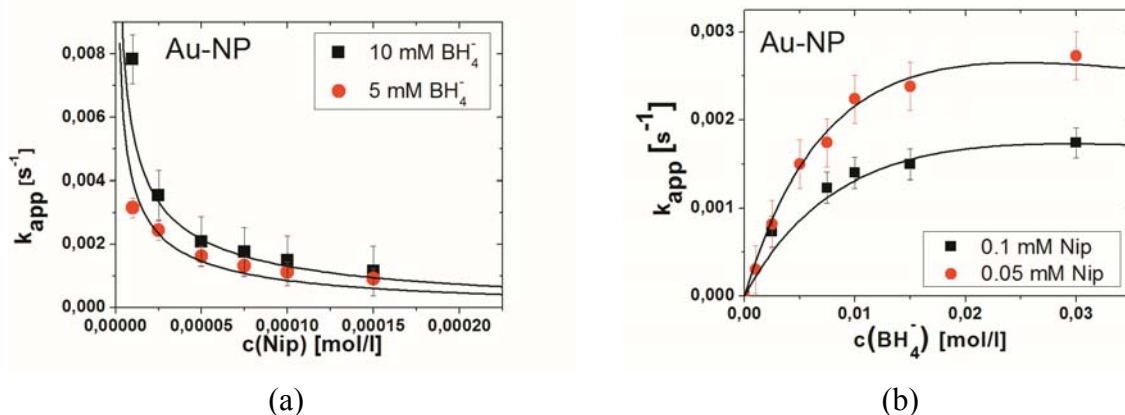


**Figure 2.4.2.** Langmuir-Hinshelwood kinetics of the catalytic reduction of 4-nitrophenol by NaBH<sub>4</sub> in the presence of gold nanoparticles immobilized on SPBs. (a) Dependence of the concentration of morin ( $c(\text{NaBH}_4) = \text{const.}$ ) on the apparent rate constant  $k_{\text{app}}$ . (b) Influence of the concentration of NaBH<sub>4</sub> on  $k_{\text{app}}$  ( $c(\text{Nip}) = \text{const.}$ ). All fits (black solid curves) were calculated using the same set of parameters for the Langmuir-Hinshelwood model.

This work provides first mechanistic insights into the mechanism of the reduction of 4-nitrophenol by noble metal nanoparticles. By applying the Langmuir-Hinshelwood model, a better understanding of the differences in the activity of the different nanoparticles towards the reduction of 4-nitrophenol could be achieved.

The full publication can be found in Chapter 6.

## 2.5. Synthesis and Analysis of Zwitterionic Spherical Polyelectrolyte Brushes in Aqueous Solution

We presented for the first time the generation of a zwitterionic SPB by grafting zwitterionic chains consisting of pMEDSAH from a PS-co-DVB core via aqueous atom transfer radical polymerization.

Significant differences of the expansion of the brush shell were observed by a combination of DLS, TEM and cryoTEM measurements. Figure 2.5.1 indicates the differences for all three described methods. This investigation led to the conclusion that the zwitterionic shell undergoes an internal phase separation. This means that most of the chains are located at a surface-near layer due to the formation of aggregates of 3 or more monomer units. A minor part of the pMEDSAH chains is reaching out further into solution and contributes to the hydrodynamic radius  $R_h$  measured by DLS.

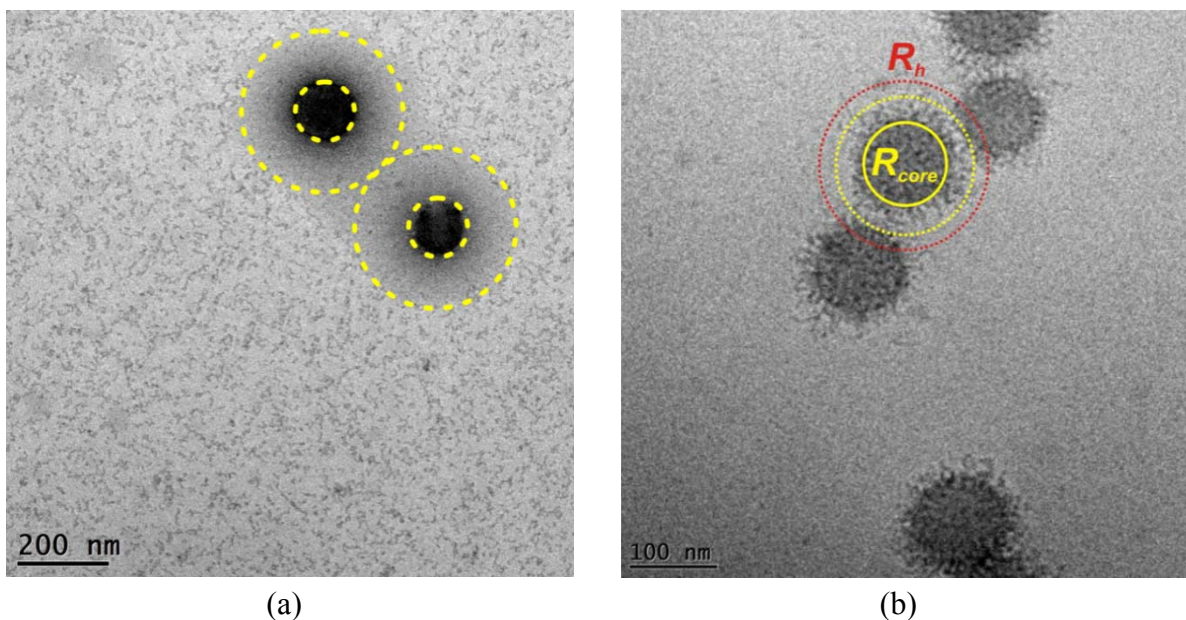


**Figure 2.5.1.** (a) TEM micrograph of the zwitterionic SPB in 0.1 M CsI solution. A spherical shell of pMEDSAH (outer yellow dotted circle) can be seen around the PS-co-DVB core particles (dark spherical objects). (b) cryoTEM micrograph of the zwitterionic SPB *in-situ* in 0.1 M CsI solution. Due to the interaction of  $\text{Cs}^+$  and  $\text{I}^-$  as counter ions of the pMEDSAH brush, the electron density, and therefore the contrast is enhanced significantly. The red dotted circle shows the hydrodynamic radius  $R_h$  as determined by DLS whereas the yellow dotted circle represents the radius of the SPB as observed by cryoTEM.

The zwitterionic SPBs were tested for their responsive behavior in aqueous solution to the temperature and to the addition of salt. The latter led to a swelling of the zwitterionic corona of about 40 % which is shown in Figure 2.5.2a. Remarkably, the onset of the swelling is at about 0.5 M NaCl whereas no increase in the brush thickness is observed at lower salt concentrations.

The presence of an upper critical solution temperature was investigated by temperature-dependent DLS measurements. The results shown in Figure 2.5.2b prove that there is a distinct swelling of the zwitterionic corona in the range between 20 °C and 75 °C which could be further enhanced by the addition of KCl. The swelling is completely reversible.

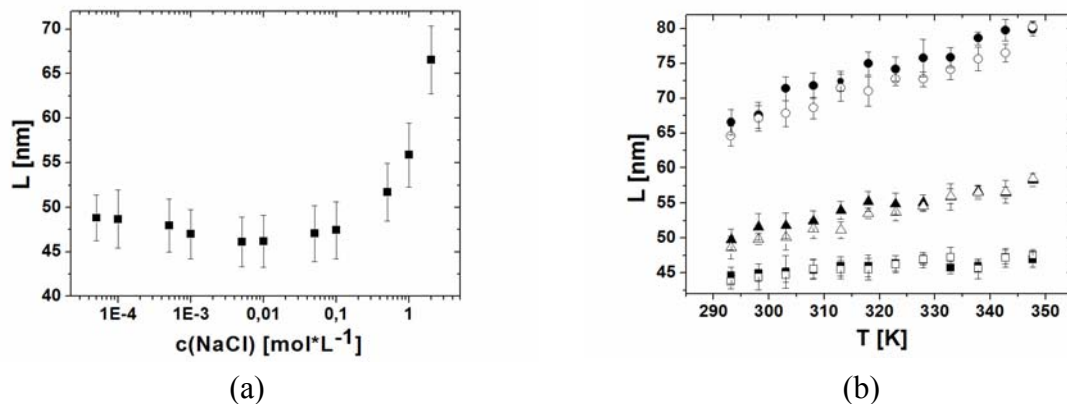


**Figure 2.5.2.** (a) Influence of the concentration of NaCl on the hydrodynamic brush thickness  $L$  of the zwitterionic SPB. The addition of salt leads to a pronounced swelling of the zwitterionic corona at salt concentration above 0.5 M. (b) Influence of the temperature on the hydrodynamic brush thickness  $L$  without the addition of KCl (■ heating, □ cooling), 1 M KCl (▲ heating, △ cooling) and 2 M KCl (● heating, ○ cooling). The zwitterionic corona is swelling upon heating of the sample whereas adjacent cooling leads to a re-shrinking. The effect can be significantly enhanced by the addition of salt.

Additional zeta potential measurements could show that the negative surface potential of the zwitterionic SPB is due to the presence of negative charges of the PS-co-DVB core particles. These charges could be traced back to the presence of remaining surfactant and of incorporated fragments of initiator molecules due to the core synthesis.

The full publication can be found in Chapter 7.

## 2.6. Individual Contributions to Joint Publications

The results presented in this thesis were obtained in close collaboration with different co-workers and published or submitted as indicated below. The individual contribution of each co-author to the publications is listed. The asterisk denotes the corresponding author.

### Chapter 3

This work has been published in *Chemistry of Materials* under the title “Formation of Ultrathin Birnessite-Type Nanoparticles Immobilized on Spherical Polyelectrolyte Brushes” by Frank Polzer, Daniel A. Kunz, Josef Breu and Matthias Ballauff\*.

- I conducted the synthesis and characterization of the cationic SPBs. Furthermore, I did all the synthetic work for the *in-situ* generation of the birnessite-type nanoparticles and all TEM and cryoTEM measurements. Furthermore, I wrote the paper.
- Daniel A. Kunz assisted during the synthesis of the manganese oxide reference compounds. He conducted the PXRD measurements and contributed to their discussion.
- Prof. Josef Breu wrote the discussion of the PXRD results. He also contributed to the scientific discussion.
- Prof. Matthias Ballauff contributed to the scientific discussion.

### Chapter 4

This work has been submitted to the *Journal of Colloids and Polymer Science* under the title “Structural Analysis of Composites of MnO<sub>x</sub> and a Polymer Colloid” by Frank Polzer, Elisabeta Holub-Krappe, Hermann Rossner, Alexei Erko, Holm Kirmse, Felix Plamper, Alexander Schmalz, Axel H. E. Müller and Matthias Ballauff\*.

- I conducted the synthesis of the composite materials and the reference compounds and their characterization including cryoTEM imaging. Furthermore, I wrote the publication.
- Felix Plamper and Alexander Schmalz synthesized and characterized the star-shaped p(TMAEMC) homopolymer.

- Hermann Rossner assisted with the EXAFS evaluation and contributed to the discussion of the XANES and EXAFS section of the publication. Furthermore, he wrote the description of the Bayes-Turchin approach for the EXAFS evaluation.
- Elisabeta Holub-Krappe contributed to the scientific discussion on XANES and EXAFS.
- Prof. Alexei Erko contributed to the discussion of the XAFS measurements and introduced me into the KMC2 beamline at BESSY II.
- Holm Kirmse introduced me into the technique of HRTEM and contributed to the discussion of this method.
- Prof. Matthias Ballauff and Prof. Axel H. E. Müller contributed to the scientific discussion.

## **Chapter 5**

This work is accepted by the *Journal of Catalysis* under the title “Catalytic Oxidation of an Organic Dye by MnO<sub>x</sub> Nanoparticles” by Frank Polzer, Stefanie Wunder and Matthias Ballauff\*.

- I conducted the synthesis of the composite particles and its characterization. The UV/vis measurements and their evaluation considering the activation energy, the LH kinetics at room temperature were done by me. Furthermore, I wrote the paper.
- Stefanie Wunder proved the reproducibility of the synthesis and the UV/vis measurements. Furthermore, she contributed the study of the influence of the buffer concentration, the temperature dependence of the LH kinetics as well as the effect of oxygen on the reaction kinetics. She also took part in the scientific discussion.
- Prof. Matthias Ballauff contributed to the scientific discussion.

## **Chapter 6**

This work has been published in the *Journal of Physical Chemistry C* under the title “Kinetic Analysis of Catalytic Reduction of 4-Nitrophenol by Metallic Nanoparticles Immobilized in Spherical Polyelectrolyte Brushes” by Stefanie Wunder, Frank Polzer, Yan Lu, Yu Mei and Matthias Ballauff\*.

- I conducted the synthesis and characterization of the gold nanoparticles immobilized onto SPBs. Furthermore, I did all TEM measurements of the composite materials. All UV/vis measurements concerning kinetic reduction of 4-nitrophenol using composite particles with gold nanoparticles were conducted and evaluated by myself. I established the Langmuir-Hinshelwood model for the description of the reaction mechanism.
- Stefanie Wunder and Yan Lu synthesized the platinum nanoparticle immobilized on SPBs. Furthermore the Langmuir-Hinshelwood model was modified by Stefanie Wunder taking into account the Freundlich exponents of the adsorbents. Stefanie Wunder conducted all the measurements of the Pt nanoparticle composite materials concerning the kinetic reduction of 4-nitrophenol. The data for Pt and Au nanoparticles were evaluated using the Langmuir-Freundlich model by Stefanie Wunder.
- Prof. Matthias Ballauff contributed to the scientific discussion.

## **Chapter 7**

This work has been published in *Macromolecules* under the title “Synthesis and Analysis of Zwitterionic Spherical Polyelectrolyte Brushes in Aqueous Solution” by Frank Polzer, Johannes Heigl, Christian Schneider, Oleg Borisov and Matthias Ballauff\*.

- I conducted the synthesis of the zwitterionic SPB and all measurements of this work including TEM, cryoTEM, DLS and zeta potential measurements.
- Johannes Heigl assisted the work during the course of his bachelor work under my supervision.
- Christian Schneider provided the fits of the zeta potential measurements and helped with their discussion.
- Prof. Matthias Ballauff and Oleg Borisov contributed to the scientific discussion.

*Overview*

---

### **3. Formation of Ultrathin Birnessite-Type Nanoparticles Immobilized on Spherical Polyelectrolyte Brushes**

*Frank Polzer,<sup>§</sup> Daniel A. Kunz,<sup>‡</sup> Josef Breu,<sup>‡</sup> Matthias Ballauff<sup>§\*</sup>*

<sup>§</sup>Helmholtz-Zentrum Berlin für Materialien und Energie GmbH, Hahn-Meitner-Platz 1,  
14109 Berlin, Germany, and Department of Physics, Humboldt University Berlin, Newtonstr.  
15, 12489 Berlin, Germany

<sup>‡</sup> Department of Inorganic Chemistry I, University of Bayreuth, 95440 Bayreuth, Germany

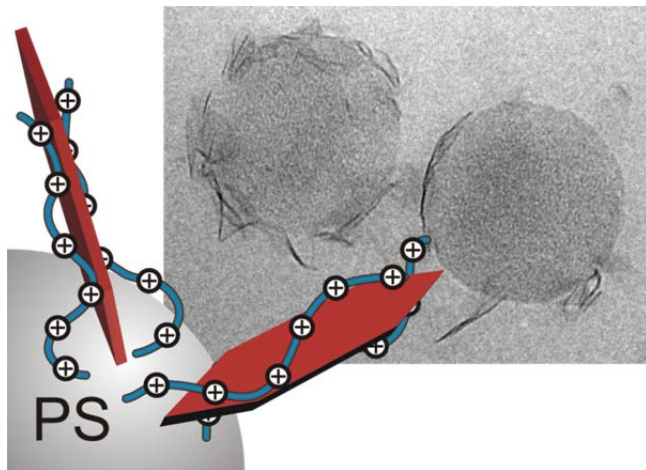
Email: [Matthias.Ballauff@helmholtz-berlin.de](mailto:Matthias.Ballauff@helmholtz-berlin.de)

#### **Published in Chemistry of Materials**

Reproduced with permission from  
*Chemistry of Materials*, **2010**, *22*, 2916.  
© 2010 American Chemical Society.

**DOI:** [10.1021/cm100226h](https://doi.org/10.1021/cm100226h)

### 3.1. Abstract



A new route of *in situ* formation and stabilization of ultrathin, needle-like manganese dioxide nanoparticles ( $\text{MnO}_2\text{NP}$ ) in aqueous solution by using spherical polyelectrolyte brush (SPB) particles is presented. The SPBs that act as carrier particles consist of a solid polystyrene core of about 50 nm radius onto which long chains of the positively charged polyelectrolyte poly(2-trimethyl ammonium ethyl methacrylate chloride) (pTMAEMC) are grafted to yield a overall radius of about 85 nm. Potassium permanganate ( $\text{KMnO}_4$ ) is directly reduced within the brush layer of these particles due to the basic environment within this layer. This mechanism seems to limit the size of the  $\text{MnO}_2\text{NP}$  to the dimensions of the brush layer. Powder X-ray diffraction, (PXRD), transmission electron microscopy (TEM) and cryogenic transmission electron microscopy (cryoTEM) prove that birnessite-type  $\text{MnO}_2\text{NP}$  with a  $c^*$ -disorder are generated on the SPB without adding any reducing agent. The birnessite nanoparticles have an average length of 20 nm and a breadth of ca. 1.6 nm. They are composed of single lamellae or of ultrathin stacks of very few lamellae. Energy-dispersive X-ray spectroscopy (EDX) demonstrates that most of the charges of the thin birnessite platelets are balance by potassium ions. The excellent stabilization by the SPB carrier particles in aqueous solution can be traced back to a strong interaction of the birnessite particles with the positively charged pTMAEMC chains of the SPB.

### **3.2. Introduction**

Manganese oxide materials and especially manganese dioxide ( $\text{MnO}_2$ ) that appears in a wide variety of polymorphs such as  $\alpha$ -,  $\beta$ -,  $\gamma$ -, and  $\delta$ - $\text{MnO}_2$  have attracted great interest recently. This is due to the possible applications as e.g. electrode materials,<sup>1,2</sup> catalysts,<sup>3,4</sup> ion exchange,<sup>5</sup> and magnetic materials.<sup>6,7</sup> All different polymorphs are based on the  $\text{MnO}_6$  octahedron and differ in the linkage of these basic units.<sup>8</sup> In principle, the synthesis can be achieved by the oxidation of  $\text{Mn}^{2+}$ , by the reduction of permanganate ( $\text{MnO}_4^-$ ) or by direct conversion of manganese oxides ( $\text{Mn}_2\text{O}_3$ ,  $\text{MnOOH}$ , etc.).<sup>9,8,10,11</sup> The physical and chemical properties of these materials change when downsized to the nanoscopic scale and great efforts have been made to design  $\text{MnO}_2$  nanometer-sized structures of different size and shape.<sup>12,13,14,15,16</sup> Hence, a number of different morphologies have been realized, as e.g. one-dimensional (1D) structures (nanorods, nanowires, nanofibers, etc.), two-dimensional (2D) structures (nanosheets, etc.) and three-dimensional (3D) structures (ball-like core-corona particles, nanodisks, etc.).<sup>8,17,18,19,20</sup>

Among these manganese oxides, birnessite has attracted particular attention because of its unique properties and its use as an intermediate for the preparation of other  $\text{MnO}_2$  based materials such as octahedral molecular sieves.<sup>21,22</sup> Birnessite is a phyllo-manganate meaning a layered structure of hydrous manganese oxide comprised of edge-sharing octahedra containing predominantly  $\text{Mn}^{4+}$  cations as central ions. Due to the presence of  $\text{Mn}^{3+}$  cations and/or vacant octahedral sites a net layer charge arises that is compensated by the incorporation of different cations into the interlamellar space. Typically, these interlayer cations are hydrated.<sup>23,24,25,26</sup> The interlayer cations can be exchanged against various other ions such as tetraalkylammonium ions or positively charged aluminium based oligo-cations such as Keggin ions.<sup>27,28,29,30</sup> The intercalation of bulky counter ions can furthermore be used to expand the interlayer space and finally delaminate the hexagonal sheets to gain single lamellae of birnessite.<sup>31</sup> This delamination process is well known from layered silicates or similarly structured materials, e.g. layered double hydroxides. Moreover, it is important for the generation of ultrathin films and for the building of layer-by-layer structures.<sup>32</sup> The generation of delaminated or exfoliated (stacks of only a few lamellae) birnessites is usually a tedious multistep process which involves the intercalation of bulky ions and subsequent delamination.<sup>28,33,34</sup> To our best knowledge there is only one report in literature of single step routes to created ultrathin birnessite materials.<sup>35</sup> Aqueous suspensions of these particles do not exhibit a high colloidal stability and are difficult to handle because of their high surface area and the large lateral dimensions of the platelets of up to  $0.5 \mu\text{m}$ . Applications in e.g. catalysis, however, require stable colloidal systems that can be easily synthesized in at kg scale.

In this paper we present the synthesis and comprehensive characterization of ultrathin birnessite nano-needles that are affixed to spherical polyelectrolyte brushes (SPBs).<sup>36</sup> The SPBs used herein consist of a solid polystyrene (PS) core onto which long polyelectrolyte chains (PE chains) are densely grafted (see Figure 3.2.1). Here we use the strong polyelectrolyte poly(2-trimethylammonium ethyl methacrylate chloride) (pTMAEMC) which carries positive charges. Recent work has shown that the immobilization of metallic or oxidic

nanoparticles on SPB is a promising way to colloidal stable composite particles with a high catalytic activity.<sup>37,38,39,41</sup> Moreover, cationic polyelectrolytes have recently been used successfully to create and stabilize thin films of birnessite.<sup>42,43</sup>

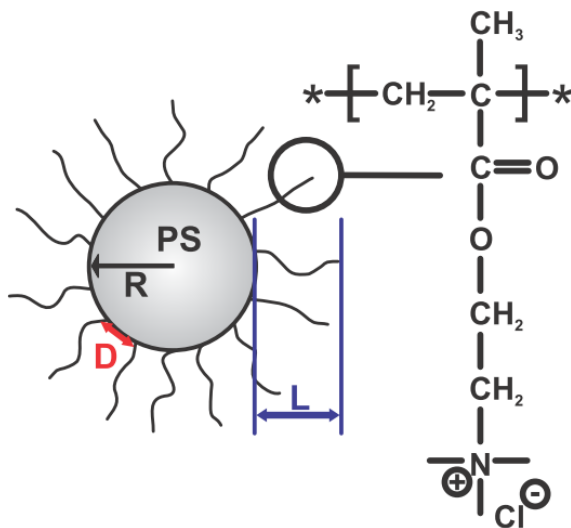


**Figure 3.2.1.** Scheme of a cationic spherical polyelectrolyte brush with brush monomer 2-trimethylammonium ethyl methacrylate chloride (TMAEMC). Here  $R$  represents the hydrodynamic radius of the polystyrene core,  $L$  stands for the contour length of the polyelectrolyte chains and  $D$  is the average distance of junctions of polyelectrolyte chains on the surface of the core particle.

Here we demonstrate that cationic spherical polyelectrolyte brushes can be used to prepare and immobilize ultrathin birnessite needles by adding  $\text{KMnO}_4$  solution to the aqueous suspension of the SPB. The resulting composite particles exhibit an excellent colloidal stability and open new venues for the use of birnessite as catalyst in aqueous systems.

### 3.3. Experimental Section

**Materials.** All chemicals were of analytical grade and used without further purification. 2-trimethylammonium ethyl methacrylate chloride (TMAEMC) was received from Polysciences.  $\text{KMnO}_4$  was purchased from Fluka and used as received. Water used in all of our work described here was 18  $\text{M}\Omega$  Millipore water.

**Synthesis of the Cationic SPB.** Cationic SPB TMAEMC-40 was synthesized and characterized as described recently.<sup>44</sup> In a typical run, 62.5 g of 2-[p-(2-hydroxy-2-methylpropiope-none)]-ethylene glycol-methacrylate (HMEM) functionalized polystyrene latex were dispersed in water to give a solid content of 3.5 wt %. After addition of 56.0 g of TMAEMC to the dispersion and the mixture was degassed and cooled down to 8 °C. The polymerization was started by irradiation of the dispersion by UV light.<sup>45</sup> The reaction was irradiated and cooled for 30 minutes. The dispersion was purified by ultrafiltration (UF) until the conductivity of the serum reached values lower than 3  $\mu\text{S}\cdot\text{cm}^{-1}$ .

**Synthesis of the MnO<sub>2</sub>NP immobilized on SPB.** The dispersion of SPB was diluted with water to a solid content of about 1.0 wt %. The mixture was bubbled with nitrogen under stirring for half an hour to remove oxygen. Afterwards, 20 mL of a 0.04 M solution of KMnO<sub>4</sub> were injected and the solution was stirred for 12 h. The composite particles were cleaned with water by UF until the conductivity of the serum reached a value of lower than 3  $\mu\text{S}\cdot\text{cm}^{-1}$ .

**Synthesis of the H<sup>+</sup>-birnessite.** This compound was synthesized according to McKenzie et al.<sup>46</sup> In a typical reaction, 1.58 g KMnO<sub>4</sub> were dissolved in 100 mL water and 1.64 mL of concentrated hydrochloric acid (HCl) were added dropwise to the solution. The precipitate was filtered and cleaned by dialysis against water.

**Synthesis of the K<sup>+</sup>-birnessite.** K<sup>+</sup>-birnessite was synthesized by the thermal decomposition of KMnO<sub>4</sub> at 800 °C for 16 h. In a typical run, 5.0 g of KMnO<sub>4</sub> were heated at 2 °C·min<sup>-1</sup> to 800 °C and kept for 16 h at this temperature, before cooling down with 1 °C·min<sup>-1</sup>. The product was washed with water until the filtrate became clear.<sup>47</sup>

**Methods.** Transmission electron microscopy (TEM) and cryogenic transmission electron microscopy (cryoTEM) measurements were conducted with a Zeiss EM922 EFTEM (Zeiss NTS GmbH, Oberkochen, Germany) as described recently.<sup>48</sup> Dynamic light scattering (DLS) was performed with an ALV 4000 (Peters) light scattering goniometer. Samples for powder X-ray diffraction (PXRD) were prepared onto a silicon zero-background plate via a back-loading technique to minimize textural effects. PXRD patterns were obtained using nickel filtered Cu-K<sub>α</sub> radiation (1.54187 Å) on a Bragg-Brentano-type diffractometer (Panalytical XPERT-PRO) equipped with an X'Celerator Scientific RTMS detector. Energy dispersive X-ray spectroscopy (EDX) was conducted with a Zeiss 1530 FESEM. The number of amino groups of the SPB, and therefore the core to shell ratio, was determined by potentiometric titration of TMAEMC-40 with 0.01 M silver nitrate (AgNO<sub>3</sub>) standard solution (Merck) using a WTW cond 197i conductometer. The amount of MnO<sub>2</sub> immobilized on the SPB was determined by thermal gravimetric analysis (TGA) using a Mettler Toledo STARe system. Zeta potential measurements were performed with a Malvern Zetasizer Nano ZS.

### 3.4. Results and Discussion

**Synthesis.** The synthesis of the cationic spherical polyelectrolyte brushes was conducted as described in previous work.<sup>44</sup> The hydrodynamic radius  $R_h$  of the polystyrene-co-HMEM core due to DLS measurements is 42.7 nm ± 0.3 nm. After the photoemulsion polymerization,  $R_h$  of the cationic SPB increased to 84.7 nm ± 0.5 nm due to the grafting-from process of polyelectrolyte chains consisting of pTMAEMC onto the core particles. The pTMAEMC shell thus grafted from the surface of the core particles has a  $R_h$  of 42.0 nm ± 0.8 nm. Potentiometric Titration with 0.01 M AgNO<sub>3</sub> standard solution gives the total number of charges on one particle. This analysis showed that the SPB used in this study had a core-to-shell mass weighted ratio of 6.6 to 1. Thus, the weight fraction of the shell is approximately

one third of the weight. The precise determination of this mass ratio is important for the mechanistic studies given below.

After adding the  $\text{KMnO}_4$  solution to the dispersion of the cationic SPBs (see Figure 3.4.1), the process of the reduction of the  $\text{MnO}_4^-$  ions could be directly seen by the fading of the color from purple to brown. The  $\text{MnO}_4^-$  ions are exchanged against the chloride counter ions of the polyelectrolyte brush and a p(TMAEM MnO<sub>4</sub>) precursor is formed with the quaternized ammonium groups of the polymer chains. We conclude that this reaction step is similar to the synthesis of layered  $\text{MnO}_2$  structures using low molecular weight tetraalkylammonium halogenides according to Brock *et al.*<sup>29</sup> Thus, the precursor is reduced *in situ* inside the brush layer and  $\text{MnO}_2$  nanoparticles are formed. This reaction seems to be promoted by the slight basic environment within the brush layer which results from possible diffusion of  $\text{OH}^-$  ions into the positively charged brush. Additionally, the generated  $\text{MnO}_2$  nanoparticles may be able to act as a catalyst for further reduction of  $\text{KMnO}_4$ .

In order to elucidate this reaction further, we studied the influence of different reaction conditions for the formation of the  $\text{MnO}_2\text{NP}$ . We varied the amount of added  $\text{KMnO}_4$  solution, the rate of addition, and the temperature. Increasing the amount of  $\text{MnO}_4^-$  ions leads to an increase of the total amount of  $\text{MnO}_2\text{NP}$ . An important finding is that the amount of inorganic nanoparticles still increases even if the molar amount of  $\text{KMnO}_4$  exceeds the amount of functional groups in the brush layer. This is a clear indication that  $\text{KMnO}_4$  does not react with the monomer units of the brush. Varying the amount of  $\text{KMnO}_4$  does not have a significant influence on the size or the structure of the formed  $\text{MnO}_2\text{NP}$ , which was proven by cryoTEM and PXRD (see below). The overall size of the nanoparticles is only limited by the dimensions of the SPB, which again demonstrates that their formation proceeds along the polyelectrolyte chains via a p(TMAEM MnO<sub>4</sub>) precursor. Moreover, the dosage time of the  $\text{KMnO}_4$  solution did not affect any properties of the nanoparticles. Furthermore there were no noteworthy effects related to the dosage rate of the  $\text{KMnO}_4$  solution. The generation of the particle seems to proceed very fast since a color shift is visible within a few seconds after  $\text{KMnO}_4$  addition. Increasing the temperature to 90 °C leads to a slight increase of the total amount of  $\text{MnO}_2\text{NP}$  formed on the SPB without changing the shape or the grade of crystallinity of the nanoparticles (see Figure S3.2). Working at elevated temperatures, however, has negative influence on the stability of the composite system since coagulation processes are promoted.

The mechanism of particle formation thus implies that the reduction takes place only in the brush layer of the SPB, and the generated nanoparticles are directly stabilized by the pTMAEMC chains. This explains why there are virtually no free  $\text{MnO}_2\text{NP}$  in solution as will become evident by the analysis of the system by TEM and cryoTEM below. Another explanation for this finding is that  $\text{MnO}_2\text{NP}$  usually possess a negative surface charge.<sup>29</sup> Therefore these particles are bound to the SPB by ionic interaction of the oppositely charged pTMAEMC shell. Measurements of the zeta potential support this conclusion since there is a notable decrease of the potential after the  $\text{MnO}_2\text{NP}$  have been generated within the polyelectrolyte shell of the SPB. Moreover, DLS measurements demonstrated that the hydrodynamic radius of the SPB decreases from 82.7 nm to 66.0 nm after the formation of the nanoparticles. This fact can be explained by the interaction of the positively charged

pTMAEMC chains with the negatively charged MnO<sub>2</sub>NP leading to a bridging of the chains of the shell and a decrease of the hydrodynamic radius as schematically depicted in Figure 3.4.3. Schrinner *et al.* discussed this effect in their studies of the mechanism of the formation of gold nanoparticles within cationic SPBs.<sup>38</sup> The strong interaction of the MnO<sub>2</sub>NP with the polyelectrolyte chains leads to an excellent colloidal stability of the composite particles that allows us to purify them by extensive ultrafiltration against pure water. This point will become important when analyzing the structure of the MnO<sub>2</sub>NP.

**Table 3.1. Characterization of the Composite Particles of Cationic SPBs and MnO<sub>2</sub>NP Used in This Study**

sample name	n(TMAEMC) : n(KMnO <sub>4</sub> ) <sup>a</sup>	rate of KMnO <sub>4</sub> addition / mL·h <sup>-1</sup>	m(MnO <sub>2</sub> ) wt% <sup>b</sup>	T / °C
SPB-MnO <sub>2</sub> -1	2 / 1	40	3.15	RT
SPB-MnO <sub>2</sub> -2	2 / 1	3600	3.08	RT
SPB-MnO <sub>2</sub> -5	1 / 1	40	4.90	RT
SPB-MnO <sub>2</sub> -8	2 / 3	40	6.46	RT
SPB-MnO <sub>2</sub> -9	1 / 1	40	5.79	90

<sup>a</sup>molar ratio of quaternized ammonium groups in the brush layer to the added molar amount of KMnO<sub>4</sub>, <sup>b</sup>relating to the solid composite particle

**TEM and CryoTEM Studies.** We now turn to the analysis of the particles by transmission electron microscopy (TEM). Figure 3.4.1a displays the TEM pictures of the particles that refer to the dry state whereas cryoTEM images in Figure 3.4.1b and 3.4.1c display the structure of the composite particles in the aqueous phase, that is, directly *in-situ*. The cryoTEM micrographs show that the MnO<sub>2</sub>NP are of needle-like shape and have a typical breadth of 1.6 nm and an average length of 20 nm. The thickness of the particles derived from the cryoTEM micrographs indicates that the nanoparticles consist mainly of single lamella or ultrathin stacks of very limited numbers of lamellae. We conclude from the habitus of the nanocrystals together with the analysis by PXRD given below that the modification of MnO<sub>2</sub> given here is birnessite. Since structures with a thickness of a few nm of birnessite show a poor electron contrast in cryoTEM, only particles vertically aligned with their ab plane to the electron beam are clearly visible. This becomes evident looking at Figure 3.4.1c. The dark, thin needle-like particles are stacks of octahedral layers of MnO<sub>2</sub> where the basal planes are within the angle of vision. In some cases individual birnessite particles are aligned parallel to each other. This indicates a layer-by-layer structure of the polyelectrolyte and the nanoparticles resulting from their opposite charge. This is in good agreement with the proposed particle generation mechanism which is shown in Figure S3.1. In contrast to that, thin lamellae oriented horizontally with the ab plane to the electron beam are hardly visible

(see Figure 3.4.1c). This is also due to the high background caused by the solid polystyrene lattices.

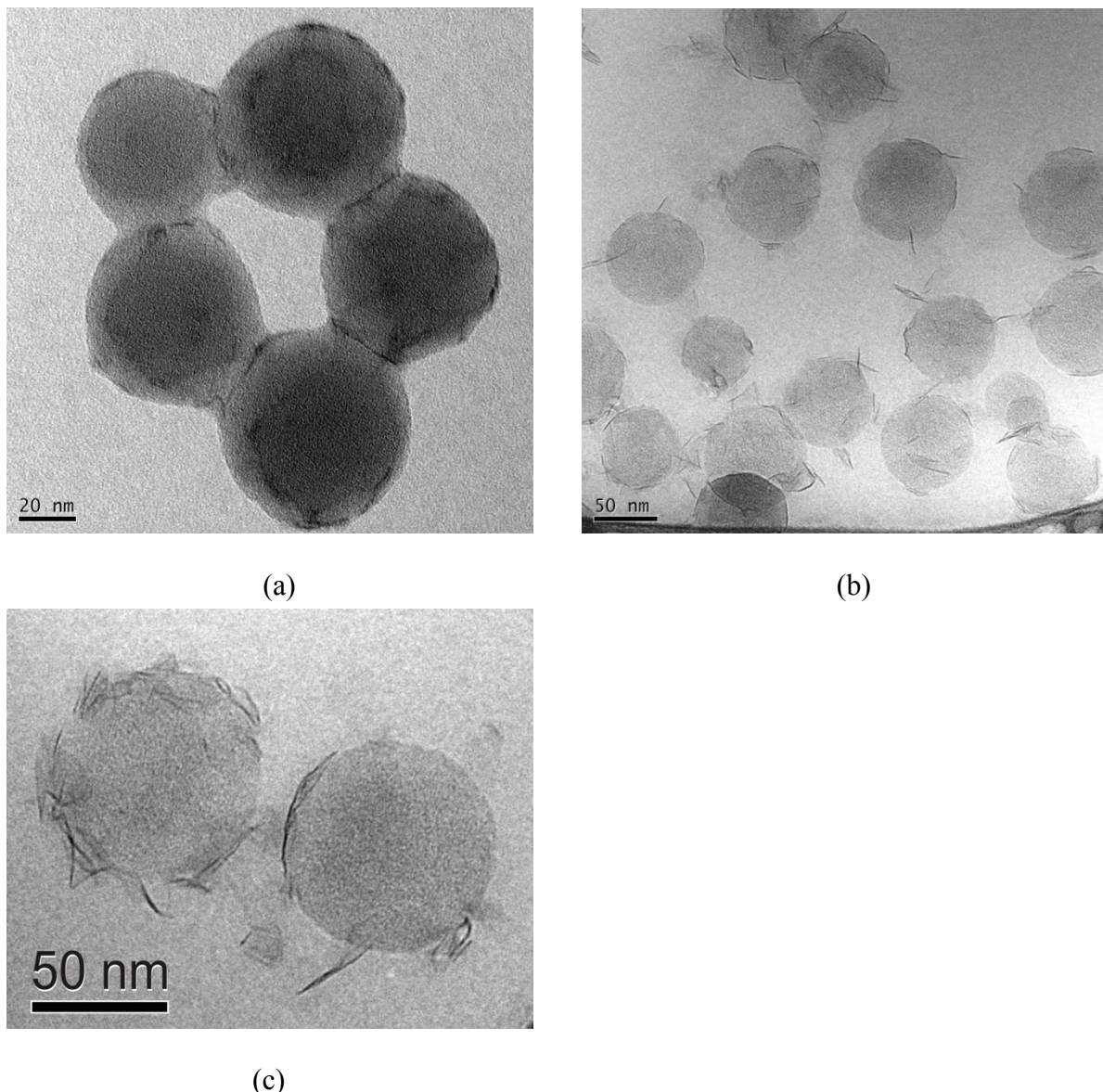


**Figure 3.4.1.** TEM of the composite system SPB-MnO<sub>2</sub>-8 (a) and cryoTEM of the same system (b and c) shows the structural difference of the MnO<sub>2</sub>NP immobilized on the SPB in the dried and the dispersed state. Whereas TEM indicates a more isotropic structure of the nanoparticles, the vitrified sample shows the formation of MnO<sub>2</sub> nano-needles immobilized on the SPBs.

As already mentioned above, the length of the MnO<sub>2</sub>NP does not exceed the dimensions of the brush layer which proves the mechanism of a polymer-assisted nanoparticle growth and stabilization. In addition, there are no free MnO<sub>2</sub>NP in the solution, which is in good agreement with previous results of other work.<sup>40,42,49</sup> This point is important for possible applications, because separation of the nanoparticles from the solution is simplified by immobilizing them on SPBs by e.g. centrifugation or filtration.

The comparison between the TEM and the cryoTEM micrographs demonstrates that the structure obtained by both methods differs strongly. Obviously, the drying necessary for the TEM pictures leads to a collapse of the fine needle-like nanoparticles. Moreover, the drying leads to a loss of the interlayer water in the birnessite structures which will quickly evaporate under the conditions of TEM.

**Structural Characterization by X-Ray Diffraction.** The assignment of the modification can be corroborated by wide-angle diffractograms to be discussed in the following. In order to elucidate the structure of the nanoparticles generated on the SPB, two well-known birnessite modifications ( $H^+$ -birnessite, see Ref.<sup>46</sup>;  $K^+$ -birnessite, see Ref.<sup>47</sup>) have been synthesized for comparison. The PXRD patterns of the composite particles, of  $H^+$ -birnessite, and  $K^+$ -birnessite are shown in Figure 3.4.2. The series of  $00l$  reflections between  $10^\circ$  and  $30^\circ$  in  $2\theta$  of the birnessite modifications contain crucial information on the  $d$ -spacing between consecutive lamellae and the thickness of the stacks and shall therefore be discussed in more detail: The PXRD analysis shows a regular 3D ordering in the case of the  $K^+$ -birnessite. For this material, both the stacking vector and the mutual position of stacked lamellae are well defined ( $c^*$ -ordered). The  $H^+$ -birnessite is, however, much less ordered as indicated by firstly a broadening of the  $00l$  reflections and secondly the absence of any reflections of mixed indices, for instance the  $104$  reflection which is missing in  $H^+$ -birnessite but is clearly visible in case of the  $K^+$ -birnessite. Instead of symmetrically shaped peaks of reflections of mixed indices, for  $H^+$ -birnessite, besides the  $00l$  series, only l-shaped  $hk$ -bands are observed in the diffractogram, for instance the  $10$ -band at  $36^\circ$  in  $2\theta$ . This lack of reflections of mixed indices indicates that in  $H^+$ -birnessite the individual lamellae are stacked turbostratically meaning that the relative position and/or orientation of adjacent lamellae in the stack are random ( $c^*$ -disordered). The  $hk$ -bands are thus the result of a 2D interference within the plane of the lamellae. Furthermore, the broadening of the  $00l$  reflections indicates that the stacks formed in  $H^+$ -birnessite or considerably thinner than in  $K^+$ -birnessite.

The PXRD pattern of the  $MnO_2$ NP formed in the composite material are yet again distinctly different as compared to both  $K^+$ -birnessite and  $H^+$ -birnessite. Please note that the two very broad peaks in the diffractogramm of the composite particles at  $9.4^\circ$  and  $19.1^\circ$  ( $2\theta$ ) can be assigned to the bare SPB. In this angular region, neither  $K^+$ -birnessite nor  $H^+$ -birnessite exhibit any peaks. Besides these peaks due to the SPB carrier, only  $hk$ -bands are observed. The positions of these are in good agreement with what is found for  $H^+$ -birnessite suggesting that the lateral dimensions of the lamellae are similar in  $H^+$ -birnessite and the  $MnO_2$ NP in the composite material. However, most surprisingly, the  $00l$  series is not visible at all in case of the composite particles. Since the much less intense  $10$ -band is clearly observable, the basal peaks should also be above the detection limit and the lack of the  $00l$ -peaks is therefore not due to the high background caused by the carrier particles. The intensities of the  $00l$ -peaks can be diminished by three different mechanisms. 1. Random interstratification, meaning that interlayer distances between the individual consecutive lamellae in the stack vary and thus partially destroy the regular alteration of the electron density along the stacking direction. 2. Although utmost precautions have been taken in the sample preparation to minimize texture, a

certain degree of preferred orientation in the samples of  $K^+$ -birnessite and  $H^+$ -birnessite will be unavoidable due to the platy particle morphology, while in the composite material a random orientation of the  $MnO_2$ NP is assured by the SPB carrier. This definitive lack of preferred orientation might in turn reduce the intensities of the  $00l$ -series. While small contributions of random interstratification and reduction of preferred orientation may not be ruled out, the cryoTEM micrographs showing very thin  $MnO_2$ NP suggest that the non-visibility of the basal reflection actually is related to 3. the thickness of the stacks. As the stacks of lamellae become thinner and thinner the full width at half maximum values will steadily increase and the basal peaks will be broadened and pushed into the background. Finally, the  $00l$ -series will fade away completely when the material is delaminated into single lamellae. At this stage all inner surfaces (interlamellar space) will have been converted into external surfaces. Thus the lack of  $00l$  peaks in the diffractogram of the composite material suggests that the  $MnO_2$ NP in the composite material will be at least highly exfoliated, possibly even partially delaminated into single lamella. Evidently, single lamellae of birnessite exhibit a strong negative charge that must be balanced by counter ions. Here, EDX measurements that will be discussed in the following provide valuable information.

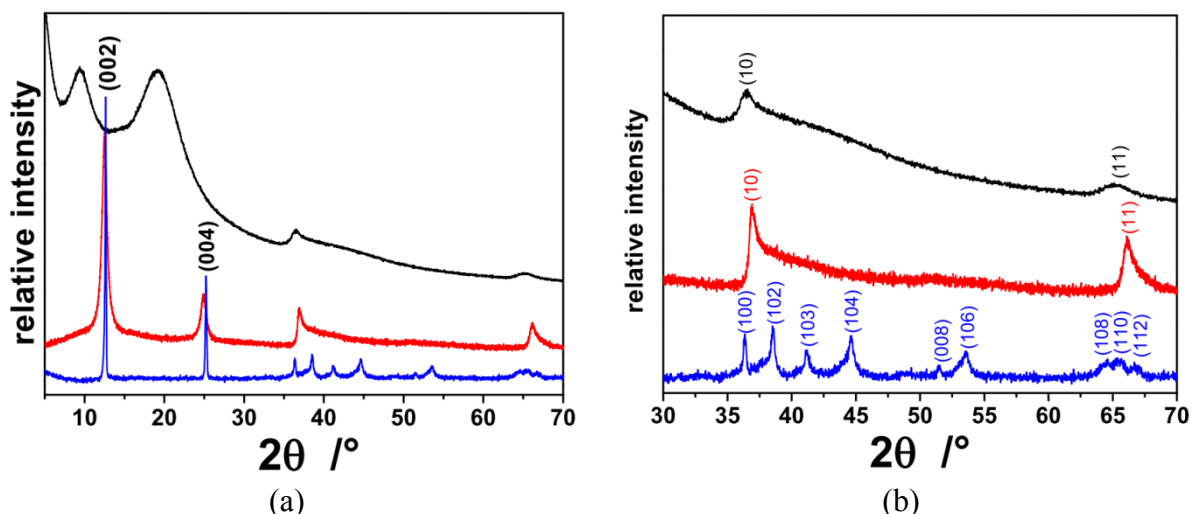


**Figure 3.4.2.** (a) PXRD patterns of the composite particle (black line), the  $c^*$ -disordered  $H^+$ -birnessite (red line) and the  $c^*$ -ordered  $K^+$ -birnessite (blue line). The two broad peaks of the composite material in the first part of the pattern can be assigned to the bare SPB, whereas the  $hk$ -bands at  $36^\circ$  und  $65^\circ$   $2\theta$  are due to the  $c^*$ -disordered birnessite nano-needles (b). Please note the lack of any  $00l$  reflections for the composite material.

**Energy Dispersive X-ray Spectroscopy.** The EDX spectrum of the composite particles shows high contents of potassium (K) and chlorine (Cl) (see supporting information in Figure S3.3). The potassium ions ( $K^+$  ions) refer to either interlayer cations in exfoliated  $MnO_2$ NP with birnessite structure or to  $K^+$  ions absorbed to external surfaces of delaminated lamellae. Since the samples have been thoroughly purified by ultrafiltration, the appreciable amount of  $K^+$  ions cannot be explained by the presence of the ions in the aqueous phase. Moreover, due to the positive charge of pTMAEMC chains, other positive ions will be mostly excluded from

the brush layer. Hence, we concluded that the  $K^+$  ions are bound to internal or external surfaces of the lamellae of birnessite. Charges at the external surface of the nanoparticles are thus balanced by the pTMAEMC chains and by condensed  $K^+$  ions. The presence of chloride ions ( $Cl^-$  ions) indicates that these ions are not completely replaced by the  $MnO_4^-$  ions as counter ions of the pTMAEMC chains even if an excess of  $KMnO_4$  is used. This indicates that the reduction and condensation reaction of  $MnO_4^-$  to form birnessite-type nano-needles is significantly faster than the exchange of  $Cl^-$  and  $MnO_4^-$  ions itself.

This is in good agreement with the fact that the dosage rate of  $KMnO_4$  solution to the SPB dispersion did not affect the reaction. Furthermore  $Cl^-$  ions can only stay inside the brush layer as counterions of pTMAEMC chains. This leads to the conclusion that only a small fraction of the negative charges of the birnessite-type nano-needles is balanced by the pTMAEMC itself and that the charges are mostly compensated by the  $K^+$  ions in the interlayer which is in good agreement with the potassium fraction seen in the EDX spectrum. As a consequence, after the reduction of the  $MnO_4^-$ , the  $Cl^-$  ions have to balance most of the charges of the pTMAEMC chains again. This finding may be used to further increase the total amount of  $MnO_2$ NP since the exchange and reduction of  $MnO_4^-$  ions should repeatedly be possible. This is in full accord with the above finding that the molar fraction of TMAEMC functional groups can be exceeded by the added  $KMnO_4$  leading to an increase in the total  $MnO_2$ NP content of the composite particles (see Table 3.1).

Combining the results of TEM, PXRD, and EDX, the schematic structure of the composite particles shown in Figure 3.4.3 may be derived.

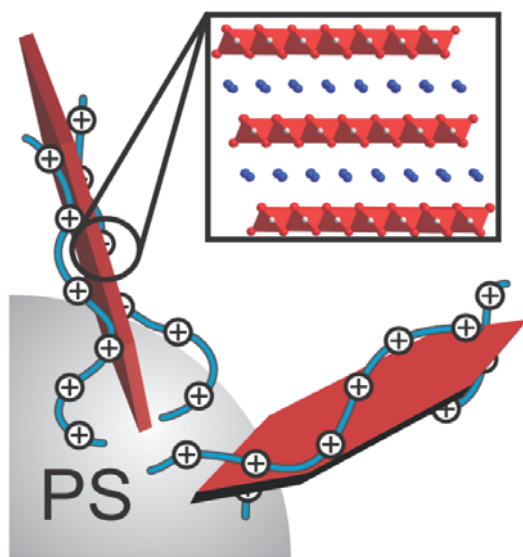


**Figure 3.4.3.** Schematic representation of the stabilization of the layered birnessite structure by the cationic pTMAEMC chains of the SPB. Ultra-thin, turbostratically disordered stacks and delaminated lamellae are sandwiched between pTMAEMC chains and thus tightly immobilized by electrostatic forces between SPB carrier and  $MnO_2$ NP. The inset shows the crystal structure of a  $K^+$ -birnessite (water molecules in the interlayer are not shown).

Birnessite-type single lamellae and ultra-thin, turbostratically disordered stacks of only very few lamellae are sandwiched between cationic pTMAEMC chains and thus are tightly immobilized by electrostatic interactions between the SPB carrier and the negative surface charge of MnO<sub>2</sub>NP. Nevertheless, the high contents of K<sup>+</sup> ions found by EDX analysis prove that most of the negative charges of the internal and external surfaces of the birnessite-type nanoparticles are not balanced by pTMAEMC chains bound to the external surface but instead by intercalated and surface-adsorbed K<sup>+</sup> ions, respectively. A penetration/intercalation of the pTMAEMC chains between birnessite lamellae seems not to occur, since steric hindrance of large ions leads to a decreasing probability for intercalation with increasing ion radius.<sup>28</sup> Instead the pTMAEMC chains interact with the external surface charge only. This is in good agreement with the finding that the length of the nanoparticles does not exceed the size of the polyelectrolyte chains.

### **3.5. Conclusions**

A facile route has been developed for the preparation of ultrathin birnessite-type nano-needles within SPBs by in situ reduction of KMnO<sub>4</sub> precursor molecules. We conclude that the KMnO<sub>4</sub> reacts with the quaternized ammonium groups of the brush polymer to form a p(TMAEM MnO<sub>4</sub>) precursor which gets directly reduced by the basic environment within the brush layer. This leads to a polyelectrolyte-directed growth and stabilization of the nanoparticles which causes a size limitation of the MnO<sub>2</sub>NP by the brush extention. TEM micrographs reveal a collapsed structure of the birnessite nanoparticles immobilized on SPB due to drying effects and the loss of interfacial bound water between the single lamellae. In contrast to that, cryoTEM images confirm the needle-like nanoparticles with an average length of 20 nm and a breadth of 1.6 nm are well distributed among the carrier particle and that no MnO<sub>2</sub>NP are in free solution. CryoTEM and the PXRD analysis point out that the needles exhibit a *c*<sup>\*</sup>-disordered birnessite type structure of the MnO<sub>2</sub>. The excess charge of these nano-needles is mostly balanced by K<sup>+</sup> ions which could be inferred from the EDX analysis. Hence, we obtained ultrathin birnessite-type nanostructures without further delamination processes. Moreover, the composites of the SPB and the nanoparticles exhibit an excellent colloidal stability. These properties make the composite particles a promising material for applications in catalysis. Work along this direction is under way.

### **3.6. Acknowledgements**

We thank the Deutsche Forschungsgemeinschaft, Sonderforschungsbereich 840 Bayreuth and the Henkel AG & Co. KGaA for the financial support. The authors are indebted to Benjamin Goßler for EDX measurements.

### 3.7. Supporting Information

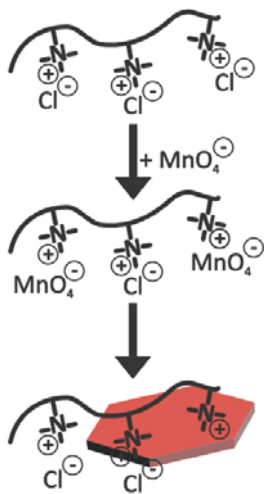


**Figure S3.1.** Proposed mechanism for the MnO<sub>2</sub>NP generation at SPB. By adding KMnO<sub>4</sub> solution to the SPB dispersion, a TAA MnO<sub>4</sub> precursor is formed which gets instantly reduced inside the brush layer. As a consequence, birnessite-type MnO<sub>2</sub>NP (red hexagon) are generated which are stabilized by the PE chains of the SPBs.

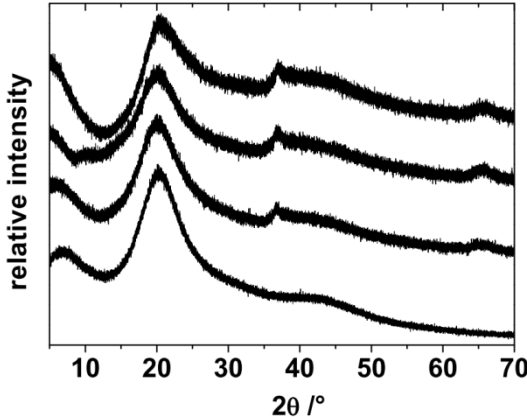


**Figure S3.2.** PXRD patterns of the bare SPB TMAEMC-40 and the composite systems SPB-MnO<sub>2</sub>-5, SPB-MnO<sub>2</sub>-8 and SPB-MnO<sub>2</sub>-9 from undermost to uppermost curve. The *hk*-reflections of the composite systems refer to the birnessite nano-needles that exhibit only a 2D order within the ab-layer plane.

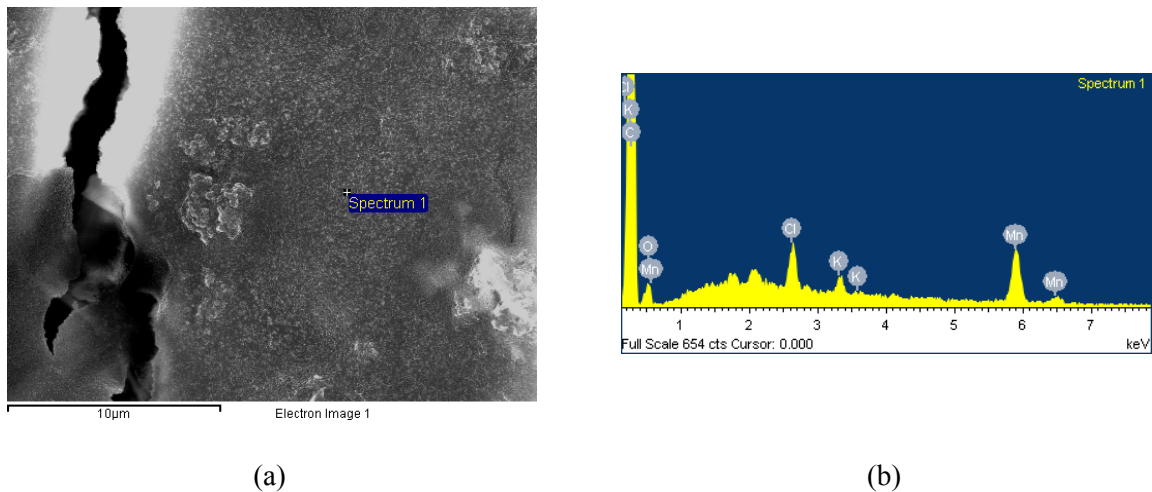


**Figure S3.3.** (a) SEM image of the sample SPB-MnO<sub>2</sub>-8 and (b) the corresponding EDX pattern that indicates the formation of the MnO<sub>2</sub>NP with K<sup>+</sup>-ions inside the interlayers of birnessite.

### 3.8. References

- <sup>1</sup> Débart, A.; Paterson, A. J.; Bao, J.; Bruce, P. G. *Angew. Chem.* **2008**, *120*, 1-5.
- <sup>2</sup> Fischer, A. E.; Pettigrew, K. A.; Rolison, D. R.; Stroud, R. M.; Long, J. W. *Nano Letters* **2007**, *7*, 281-286.
- <sup>3</sup> Son, Y. C.; Makwana, V. D.; Howell, A. R.; Suib, S. L. *Angew. Chem.* **2001**, *40*, 4280-4283.
- <sup>4</sup> Espinal, L.; Suib, S. L.; Rusling, J. F. *J. Am. Chem. Soc.* **2004**, *126*, 7676-7682.
- <sup>5</sup> Shen, Y. F.; Zerger, R. P.; DeGuzman, R. N.; Suib, S. L.; McCurdy, L.; Potter, D. I.; O'Young, C. L. *Science* **1993**, *260*, 511-515.
- <sup>6</sup> Zhu, H. T.; Luo, J.; Yang, H. X.; Laing, J. K.; Rao, G. H.; Li, J. B.; Du, Z. M. *J. Phys. Chem. C* **2008**, *112*, 17089-17094.
- <sup>7</sup> Ge, J.; Zhou, L.; Yang, F.; Tang, B.; Wu, L.; Tung, C. *J. Phys. Chem. B* **2006**, *110*, 17854-17859.
- <sup>8</sup> Wang, N.; Cao, X.; He, L.; Zhang, W.; Gou, L.; Chen, C.; Wang, R.; Yang, S. *J. Phys. Chem. C* **2008**, *112*, 365-369.
- <sup>9</sup> Liu, Z.-H.; Ooi, K.; Kanoh, H.; Tang, W.; Yang, X.; Tomida, T. *Chem. Mater.* **2001**, *13*, 473-478.
- <sup>10</sup> Chen, R.; Zavalji, P.; Whittingham, M. S. *Chem. Mater.* **1996**, *8*, 1275-1280.
- <sup>11</sup> Ma, R.; Bando, Y.; Zhang, L.; Sasaki, T. *Adv. Mater.* **2004**, *16*, 918-922.
- <sup>12</sup> Burda, C.; Chen, X.; Narayanan, R.; El-Sayed, M. A. *Chem. Rev.* **2005**, *105*, 1025-1102.
- <sup>13</sup> Alivisatos, A. P. *Science* **1996**, *271*, 933-937.
- <sup>14</sup> Liang, S.; Teng, F.; Bulgan, G.; Zong, R.; Zhu, Y. *J. Phys. Chem. C* **2008**, *112*, 5307-5315.

- <sup>15</sup> Luo, J.; Zhu, H. T.; Fan, H. M.; Liang, J. K.; Shi, H. L.; Rao, G. H.; Li, J. B.; Du, Z. M.; Shen, Z. X. *J. Phys. Chem. C* **2008**, *112*, 12594-12598.
- <sup>16</sup> Portevault, D.; Cassaignon, S.; Nassif, N.; Baudrin, E.; Jolivet, J.-P. *Angew. Chem. Int. Ed.* **2008**, *47*, 6441-6444.
- <sup>17</sup> Wang, X.; Li, Y. *J. Am. Chem. Soc.* **2002**, *124*, 2880-2881.
- <sup>18</sup> Oaki, Y.; Imai, H. *Angew. Chem. Int. Ed.* **2007**, *46*, 4951-4955.
- <sup>19</sup> Fukuda, K.; Nakai, I.; Ebina, Y.; Tananka, M.; Mori, T.; Sasaki, T. *J. Phys. Chem. B* **2006**, *110*, 17070-17075.
- <sup>20</sup> Portevault, D.; Cassaignon, S.; Baudrin, E.; Jolivet, J.-P. *Chem. Mater.* **2008**, *20*, 6140-6147.
- <sup>21</sup> Cai, J.; Liu, J.; Suib, S. L. *Chem. Mater.* **2002**, *14*, 2071-2077.
- <sup>22</sup> Yang., D. S.; Wang, M. K. *Chem. Mater.* **2001**, *13*, 2589-2594.
- <sup>23</sup> Post, J. E.; Veblen, D. R. *Am. Miner.* **1990**, *75*, 477-489.
- <sup>24</sup> Ching, S.; Petrovay, D. J.; Jorgensen, M. L.; Suib, S. L. *Inorg. Chem.* **1997**, *36*, 883-890.
- <sup>25</sup> Gaillot, A.-C.; Drits, V. A.; Plancon, A.; Lanson, B. *Chem. Mater.* **2004**, *16*, 1890-1905.
- <sup>26</sup> Gaillot, A.-C.; Flot, D.; Drits, V. A.; Manceau, A.; Burghammer, M.; Lanson, B. *Chem. Mater.* **2003**, *15*, 4666-4678.
- <sup>27</sup> Tang, W. P.; Kanoh, H.; Yang, X. J.; Ooi, K. *Chem. Mater.* **2000**, *12*, 3271-3279.
- <sup>28</sup> Liu, Z. H.; Ooi, K.; Kanoh, H.; Tang, W.-P.; Tomida, T. *Langmuir* **2000**, *16*, 4154-4164.
- <sup>29</sup> Brock, S. L.; Sanabria, M.; Urban, V.; Thiagarajan, P.; Potter, D. I.; Suib, S. L. *J. Phys. Chem. B* **1999**, *103*, 7416-7428.
- <sup>30</sup> Wong, S. T.; Cheng, S. *Inorg. Chem.* **1992**, *31*, 1164-1172.
- <sup>31</sup> Liu, Z.; Ma, R.; Ebina, Y.; Takada, K.; Sasaki, T. *Chem. Mater.* **2007**, *19*, 6504-6512.
- <sup>32</sup> Möller, M. W.; Handge, U. A.; Kunz, D. A.; Lunkenbein, T.; Altstädt, V.; Breu, J. *ASC Nano* **2010**, *4*, 717-724.
- <sup>33</sup> Gao Q.; Giraldo, O.; Tong, W.; Suib, S. L. *Chem. Mater.* **2001**, *13*, 778-786.
- <sup>34</sup> Omomo, Y.; Sasaki, T.; Wang, L. Z.; Watanabe, M. *J. Am. Chem. Soc.* **2003**, *125*, 3568-3575.
- <sup>35</sup> Kai, K.; Yoshida, Y.; Kageyama, H.; Saito, G.; Ishigaki, T.; Furukawa, Y.; Kawamata, J. *J. Am. Chem. Soc.* **2008**, *130*, 15938-15943.
- <sup>36</sup> Ballauff, M. *Prog. Polym. Sci.*, **2007**, *32*, 1135-1151.
- <sup>37</sup> Lu, Y.; Wittemann, A.; Ballauff, M. *Macromol. Rapid Commun.* **2009**, *30*, 806-815.
- <sup>38</sup> Schrinner, M.; Polzer, F.; Mei, Y.; Lu, Y.; Haupt, B.; Göldel, A.; Drechsler, M.; Preussner, J.; Glatzel, U.; Ballauff, M. *Macromol. Chem. Phys.* **2007**, *208*, 1542-1547.
- <sup>39</sup> Schrinner, M.; Proch, S.; Mei, Y.; Kempe, R.; Miyajima, N.; Ballauff, M. *Adv. Mater.*, **2008**, *20*, 1928-1933.
- <sup>40</sup> Mei, Y.; Sharma, G.; Lu, Y.; Drechsler, M.; Irrgang, T.; Kempe, R.; Ballauff, M. *Langmuir* **2005**, *21*, 12229-12234.

## References

---

- <sup>41</sup> Schrinner, M.; Möller, M.; Thun, J.; Kauffmann, Y.; Breu, J.; Talmon, Y.; Ballauff, M. *Science* **2009**, *323*, 617-620.
- <sup>42</sup> Nakayama, M.; Tagashira, H. *Langmuir* **2006**, *22*, 3864-3869.
- <sup>43</sup> Lvov, Y.; Munge, B.; Giraldo, O.; Ichinose, I.; Suib, S. L.; Rusling, J. F. *Langmuir* **2000**, *16*, 8850-8857.
- <sup>44</sup> Sharma, G.; Ballauff, M. *Macromol. Rapid Commun.* **2004**, *25*, 547-557.
- <sup>45</sup> Schrinner, M.; Haupt, B.; Wittemann, A. *Chem. Eng. J.* **2008**, *144*, 138-145.
- <sup>46</sup> McKenzie, R. M. *Mineral. Mag.* **1978**, *38*, 493-502.
- <sup>47</sup> Kim, S. H.; Kim, S. J.; Oh, S. M. *Chem. Mater.* **1999**, *11*, 557-563.
- <sup>48</sup> Wittemann, A.; Drechsler, M.; Talmon, Y.; Ballauff, M. *J. Am. Chem. Soc.*, **2005**, *127*, 9688-9689.
- <sup>49</sup> Lu, Y; Spyra, P.; Mei, Y; Pich, A.; Ballauff, M. *Macromol. Chem. Phys.* **2007**, *208*, 254-261.



*References*

---

## **4. Structural Analysis of Colloidal MnO<sub>x</sub> Composites**

*Frank Polzer,<sup>1</sup> Elizabeta Holub-Krappe,<sup>1</sup> Hermann Rossner,<sup>1</sup> Alexei Erko,<sup>1</sup> Holm Kirmse,<sup>2</sup>*

*Felix Plamper,<sup>3</sup> Alexander Schmalz,<sup>4</sup> Axel H. E. Müller,<sup>4</sup> Matthias Ballauff<sup>1\*</sup>*

<sup>1</sup>Helmholtz-Zentrum Berlin für Materialien und Energie GmbH, Hahn-Meitner-Platz 1,  
14109 Berlin, Germany and Department of Physics, Humboldt University Berlin, Newtonstr.  
15, 12489 Berlin, Germany

<sup>2</sup>Department of Physics, Humboldt University Berlin, Newtonstr. 15, 12489 Berlin

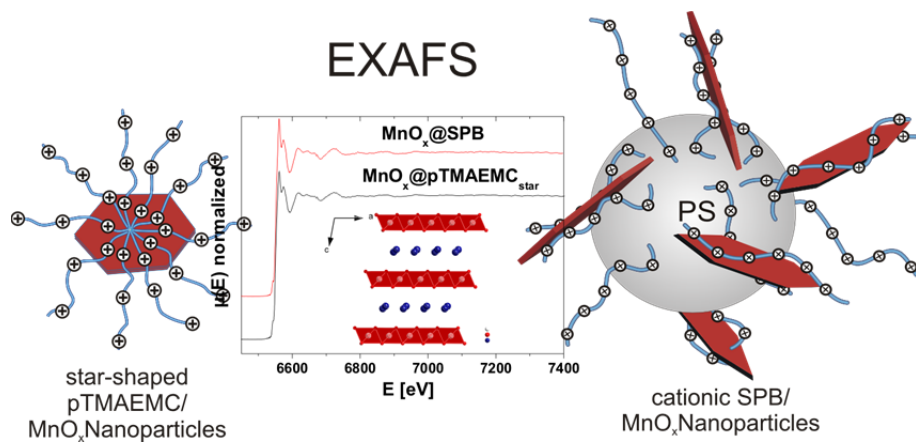
<sup>3</sup>Physical Chemistry II, RWTH Aachen, Landoltweg 2, 52056 Aachen

<sup>4</sup>Macromolecular Chemistry II, University of Bayreuth, Universitätsstr. 30, 95447 Bayreuth

Email: [Matthias.Ballauff@helmholtz-berlin.de](mailto:Matthias.Ballauff@helmholtz-berlin.de)

**Submitted to the Journal of Colloid and Polymer Science**

#### 4.1. Abstract



We report on the detailed structure of  $\text{MnO}_x$  nanoparticles ( $\text{MnO}_x\text{NP}$ ) which are either stabilized by cationic spherical polyelectrolyte brushes or by star-shaped cationic polyelectrolyte chains. In both cases, the polycation is composed of 2-(trimethylammonium)ethyl methacrylate chloride (TMAEMC). The analysis by transmission electron microscopy (TEM), cryogenic transmission electron microscopy (cryoTEM) and powder X-ray diffraction (PXRD) leads to the conclusion that the  $\text{MnO}_x$  nanoparticles in aqueous dispersed state are composed of only a few or even single lamellae of c-disordered potassium birnessite ( $\text{K}^+$ -birnessite). Using star-shaped pTMAEMC homopolymer for the synthesis of composite particles we obtain  $\text{MnO}_x\text{NP}$  with an average diameter of about 5 nm.  $\text{MnO}_x\text{NP}$  immobilized on cationic spherical polyelectrolyte brush (SPB) have a length of about 20 nm and a width of 1.6 nm. Comparison of the extended X-ray absorption fine structure (EXAFS) spectra of the  $\text{MnO}_x$  composites with reference spectra leads to the conclusion that all materials include c-disordered birnessite-type nanoparticles. A comparison of the energy shift of Mn K-edge absorption peak of the X-ray absorption near edge structure (XANES) spectra of different manganese oxide reference materials with the different  $\text{MnO}_x\text{NP}$  revealed an average oxidation state of about 3.5 - 3.7 for synthesized compounds. No distinct structural difference is found when comparing the dried samples to samples dispersed in water. A comparison of the EXAFS data of the birnessite nanoparticles with the crystal structure of macroscopic systems showed a compression in the c-direction accompanied by a slight elongation within the ab-plane of the layered material.

## 4.2. Introduction

Mixed valent manganese oxides (MnO<sub>x</sub>) with layered topologies have been studied in literature extensively in recent years.<sup>1,2</sup> These structures can be synthesized in a wide-spread variety by changing the key parameters such as the porosity, the nature of interlayered cations, the degree of interlayer hydration, the average oxidation state of manganese and the number of cation vacancies within the layer.<sup>3,4,5</sup> The control over these parameters has led to a number of applications of layered MnO<sub>x</sub>, most notably as catalysts and as new types of electrode materials for lithium ion secondary batteries.<sup>6,7,8,9,10</sup> One extensively studied material is birnessite, a phyllosilicate composed of predominantly edge-sharing MnO<sub>6</sub> octahedra.<sup>11,12</sup> The mixed valence of such materials due to cation vacancies and/or the presence of Mn<sup>3+</sup> cations within the MnO<sub>x</sub> layers leads to a negative charge in the layers.<sup>13,14,15,16</sup> This excess charge is balanced by the incorporation of different cations within the interlayers which makes these oxides suitable for heavy metal sorption from waste water or similar systems.<sup>17</sup>

There are several reports in literature about the synthesis of nanometer-sized layered MnO<sub>x</sub> materials.<sup>18</sup> Most of the methods that create highly delaminated or even exfoliated layers of MnO<sub>x</sub> are low temperature solution-based methods because of the strong tendency of these structures for coagulation and precipitation.<sup>19,20,21,22</sup> These mild reaction conditions lead mostly to highly disordered materials. Disorder may be a favourable side effect in some cases, e.g. for applications as cathode materials.<sup>23</sup> However, the lack of a long-range ordered crystalline phase and the nano-scale size complicates the analysis of such oxides by conventional methods such as PXRD.<sup>24,25</sup> Therefore investigations have been conducted using X-ray absorption fine structure (XAFS) measurements in order to identify and analyze highly disordered nanometer sized MnO<sub>x</sub> materials.<sup>26,27,28,29</sup> Thus, Fukuda and co-workers studied the local structure of Mn by XANES and EXAFS of exfoliated unilamellar crystallites of manganese oxide nanosheets.<sup>30</sup> MnO<sub>x</sub>NP in different bacteria have been characterized by XAFS successfully by Saratovsky *et al.* and Grangeon *et al.*<sup>31,32</sup> Ressler and co-workers presented a detailed analysis of MnO<sub>x</sub> colloids with intercalated tetraalkylammonium ions.<sup>33</sup> Therein it was shown that EXAFS can be used to investigate structural changes of MnO<sub>x</sub> colloids due to sol-gel transition processes. All studies proved that EXAFS is well suited for the analysis of dispersed MnO<sub>x</sub> colloids.

We have recently shown that by adding potassium permanganate (KMnO<sub>4</sub>) to a dispersion of cationic SPB, ultrathin platelet-like MnO<sub>x</sub>NP are generated *in-situ*.<sup>34</sup>

**Figure 4.2.1** displays the synthesis of these composite particles in a schematic fashion: The SPB consists of a solid polystyrene (PS) core onto which long cationic chains of TMAEMC are chemically grafted. The addition of KMnO<sub>4</sub> leads to an ion exchange of MnO<sub>4</sub><sup>-</sup> against the chloride counter ions of the brush layer. The reduction of the MnO<sub>4</sub><sup>-</sup> precursor in the basic environment of the brush layer leads to the generation of MnO<sub>x</sub>NP of layered topology which was proven by TEM and cryoTEM studies recently.<sup>34</sup> The ultra-thin platelets are stabilized

against coagulation by the immobilization onto the cationic SPB.<sup>34</sup> This room temperature method creates and immobilizes highly delaminated MnO<sub>x</sub>NP. Excellent colloidal stability of these MnO<sub>x</sub>NP could be achieved by the stabilization provided by the support particles.

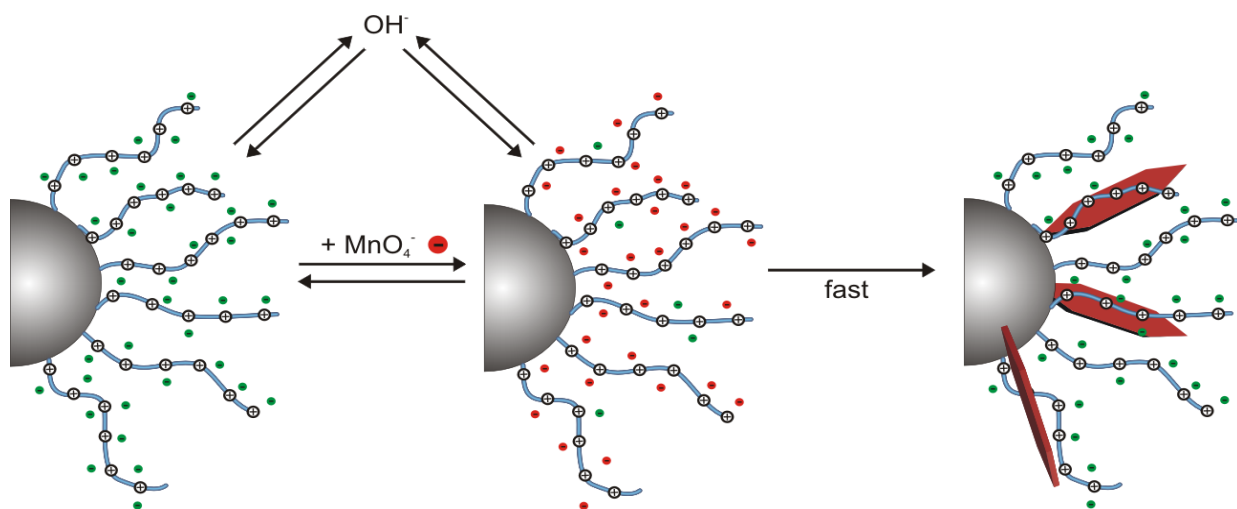


**Figure 4.2.1.** Mechanism of the generation of MnO<sub>x</sub>NP@SPB. Permanganate ions partially exchange against the chloride counter ions of the brush layer. Due to the high charge density of the brush layer, OH<sup>-</sup> ions are able to diffuse into the brush. The permanganate ions undergo an OH<sup>-</sup> catalyzed reduction so that MnO<sub>x</sub>NP are formed *in situ* inside of the brush layer. No reducing agent needs to be added.

In this study, the concept of stabilization by cationic polyelectrolytes has been extended to MnO<sub>x</sub>NP coupled to star-shaped polyelectrolytes composed of the same type of chains as for the SPB. In this way the influence of the carrier system that serves as nano-reactor for the synthesis of the MnO<sub>x</sub>NP can be investigated in further detail.

As shown in our previous work, detailed characterization of the inorganic component of the composite material is difficult due to the low degree of order of the MnO<sub>x</sub>NP and the high polymer content.<sup>34</sup> Therefore, we herein present the analysis of the MnO<sub>x</sub>NP by PXRD, HRTEM and XAFS to elucidate the crystalline structure of the highly delaminated layered inorganic nanoparticles. A further point addressed here is a comparison from EXAFS data obtained on dried and on composite particles dispersed in aqueous solution.

### 4.3. Experimental Section

**Materials.** All chemicals were of analytical grade and used without further purification. TMAEMC was received from Polysciences. KMnO<sub>4</sub> was purchased from Fluka and used as received. MnO, Mn<sub>2</sub>O<sub>3</sub>, Mn<sub>3</sub>O<sub>4</sub> and MnO<sub>2</sub> were received from Aldrich and had a purity  $\geq$  99.99 %. The reference materials were checked for phase purity by PXRD measurements. Water used in all of our work described here was 18 MΩ Millipore water.

**Synthesis of cationic SPB.** Cationic SPB TMAEMC-40 was synthesized and characterized as described elsewhere.<sup>35</sup>

**Synthesis of star-shaped pTMAEMC homopolymer.** The synthesis via atom transfer radical polymerization (ATRP) followed the same route as reported earlier in another work.<sup>36,37</sup> For quaternization of star shaped poly(2-dimethylammonium)ethyl methacrylate) (pDMAEMA), the polymer was dissolved in acetone and a threefold excess of methyl iodide was added. The solution became turbid due to the insolubility of the resulting star-shaped quaternized polyelectrolyte. The polymer was dialyzed against a thirtyfold excess of 0.1 M KCl solution to obtain star-shaped pTMAEMC (pTMAEMC<sub>star</sub>) and purification was done by adjacent dialysis against water. The star-shaped pDMAEMA with a cyclodextrine core has an average number of arms of 9.5 each with an average degree of polymerization  $DP_{\text{arm}}$  of 170.<sup>36</sup> The quaternization of the tertiary amino functions of the star-shaped polymer with methyl iodide was quantitative according to NMR measurements.

**Synthesis of MnO<sub>x</sub>NP@SPB.** A detailed description of the synthesis has been published recently.<sup>34</sup> In a typical run, 50 mL of dispersion of SPB with a solid content of about 1.0 wt% was bubbled with nitrogen under stirring for half an hour to remove oxygen. Then, 20 mL of a 0.04 M solution of KMnO<sub>4</sub> were injected and the solution was stirred for 12 hours. The composite particles were cleaned with water by ultrafiltration until the conductivity of the serum reached a value of lower than 3  $\mu\text{Scm}^{-1}$ .

**Synthesis of MnO<sub>x</sub>NP@pTMAEMC<sub>star</sub>.** The composite materials were synthesized according to the report of Sala *et al.*<sup>38</sup> for the preparation of tetraalkyl ammonium permanganate. A given amount of pTMAEMC<sub>star</sub> was dissolved in 20 mL of water. KMnO<sub>4</sub> was subsequently introduced into the solution with vigorous stirring. The molar ratio of TMAEMC to KMnO<sub>4</sub> was chosen as. The resulting aqueous solution was freeze dried. Then, 0.5824 g of pTMAEMC<sub>star</sub>/KMnO<sub>4</sub> powder were re-dissolved in 80 mL of water and the reduction was started by the addition of 80 mL of 2-butanol with vigorous stirring. This procedure is similar to the method described by Brock *et al.*<sup>39</sup>. The MnO<sub>x</sub> colloids dispersed in the aqueous phase were separated from the 2-butanol phase using a separation funnel. The resulting MnO<sub>x</sub>NP stabilized by pTMAEMC<sub>star</sub> were purified by dialysis against water with a molecular cut off of about 5 kDa.

**Synthesis of reference compounds.** H<sup>+</sup>-birnessite was synthesized according to McKenzie *et al.*<sup>40</sup> birnessite was synthesized by the thermal decomposition of KMnO<sub>4</sub> at 800 °C for 16 h.<sup>41</sup> The synthesis of δ-MnO<sub>2</sub> was conducted based on the work of Villalobos *et al.*<sup>42</sup>

**Methods.** High resolution transmission electron microscopy (HRTEM) micrographs were done using a JEOL JEM 2200FS field emission TEM with an acceleration voltage of 200 kV. Samples were prepared by putting 2  $\mu\text{L}$  of a 0.1 wt% dispersion of composite material onto a carbon coated copper grid with a mesh size of 200  $\mu\text{m}$ . The grids were dried for at least one day in a desiccator before being transferred into the TEM column. CryoTEM measurements were performed with a Zeiss EM922 EFTEM (Zeiss NTS GmbH, Oberkochen, Germany) as described recently.<sup>43</sup> Dynamic light scattering (DLS) was performed with an ALV 4000 (ALV GmbH, Langen, Germany) light scattering goniometer. Samples for PXRD were prepared onto a silicon zero-background plate via a back-loading technique to minimize textural

effects. PXRD patterns were obtained using nickel filtered Cu-K $\alpha$  radiation (1.54187 Å) on a Bragg-Brentano-type diffractometer (Bruker D8). The amount of Mn immobilized on the SPB was determined by inductive-coupled plasma optical emission spectroscopy (ICP-OES) using a Vista-Pro radial (Varian) system.

**X-ray absorption spectroscopy.** The measurements were carried out at the KMC-2 beamline at BESSY II (Helmholtz-Zentrum Berlin für Materialien und Energie GmbH, Berlin, Germany).<sup>44,45</sup> All powder samples were finely ground and fixed by two layers of Kapton tape in the sample holder. A Mn reference foil was measured before the runs to assure energy alignment. A total number of 4 to 7 spectra were recorded to improve the measurement statistics. The metal foil energy edge was determined according to the first inflection point of the absorption edge by the first derivative and was set to 6539 eV. All spectra were recorded in fluorescence and transmission geometry where the incident intensity of the X-ray beam was determined with an ionization chamber. A step size of 2 eV was used in the pre-edge region which was decreased to 0.5 eV for the pre-edge feature and the XANES. The average oxidation state of the samples was determined by a calibration of the edge energies of reference compound with known oxidation state. Therefore, XANES spectra of MnO, MnO<sub>2</sub>, Mn<sub>2</sub>O<sub>3</sub>, and Mn<sub>3</sub>O<sub>4</sub> were recorded.

A smooth atomic background was subtracted from each spectrum using the AutoBK algorithm.<sup>46</sup> The data were normalized to a step height of one. This helps to choose the Fermi Energy  $E_0$  consistently as the first inflection point of the adsorption edge step. The AutoBK algorithm uses  $E_0$  for the determination of the photoelectron wave number  $k$ :  $k = (2m(E - E_0)/\hbar^2)^{1/2}$ , where  $m$  is the electron mass,  $\hbar$  is Planck's constant and  $E$  is the incident beam energy.<sup>47,48</sup> According to this equation, the measured EXAFS  $\chi(E)$  is converted into  $\chi(k)$ . The background polynomial spline parameters used by the AutoBK algorithm<sup>46</sup> were chosen similar ( $R_{bkg} = 1.1$ ) for all MnO<sub>x</sub>NP samples to obtain the same background functions. The  $R_{bkg}$  value is the maximum frequency component in  $R$ -space, below which the contributing Fourier components are considered to be a part of the background.<sup>49</sup> The background was subtracted from each single  $\chi(E)$  measurement and then the resulting  $\chi(k)$  data sets for one sample were merged. The data reduction was performed using the software Athena<sup>50</sup>. All data were fit in  $R$ -space using theoretical amplitudes and phases for single- and multiple-scattering paths calculated from the crystal structure using the *ab initio* code FEFF.<sup>51</sup> The Fourier transformations were conducted using similar photoelectron wavenumber ranges of about  $3 \text{ \AA}^{-1} \leq k \leq 12.5 \text{ \AA}^{-1}$ . A Hanning window function was used to dampen the oscillations at the endpoints.

#### 4.4. Results and Discussion

**Synthesis of MnO<sub>x</sub>NP Composite Materials.** The SPBs used for the synthesis of the composite materials consists of a polystyrene core onto which long chains of the cationic polyelectrolyte TMAEMC are chemically grafted.<sup>34</sup> The PS core has a hydrodynamic radius  $R_h$  of 47.2 nm whereas the hydrodynamic brush thickness  $L$  was determined to 38.2 nm

according to dynamic light scattering measurements. The synthesis proceeds by photoemulsion polymerization which was described in detail recently.<sup>52</sup>

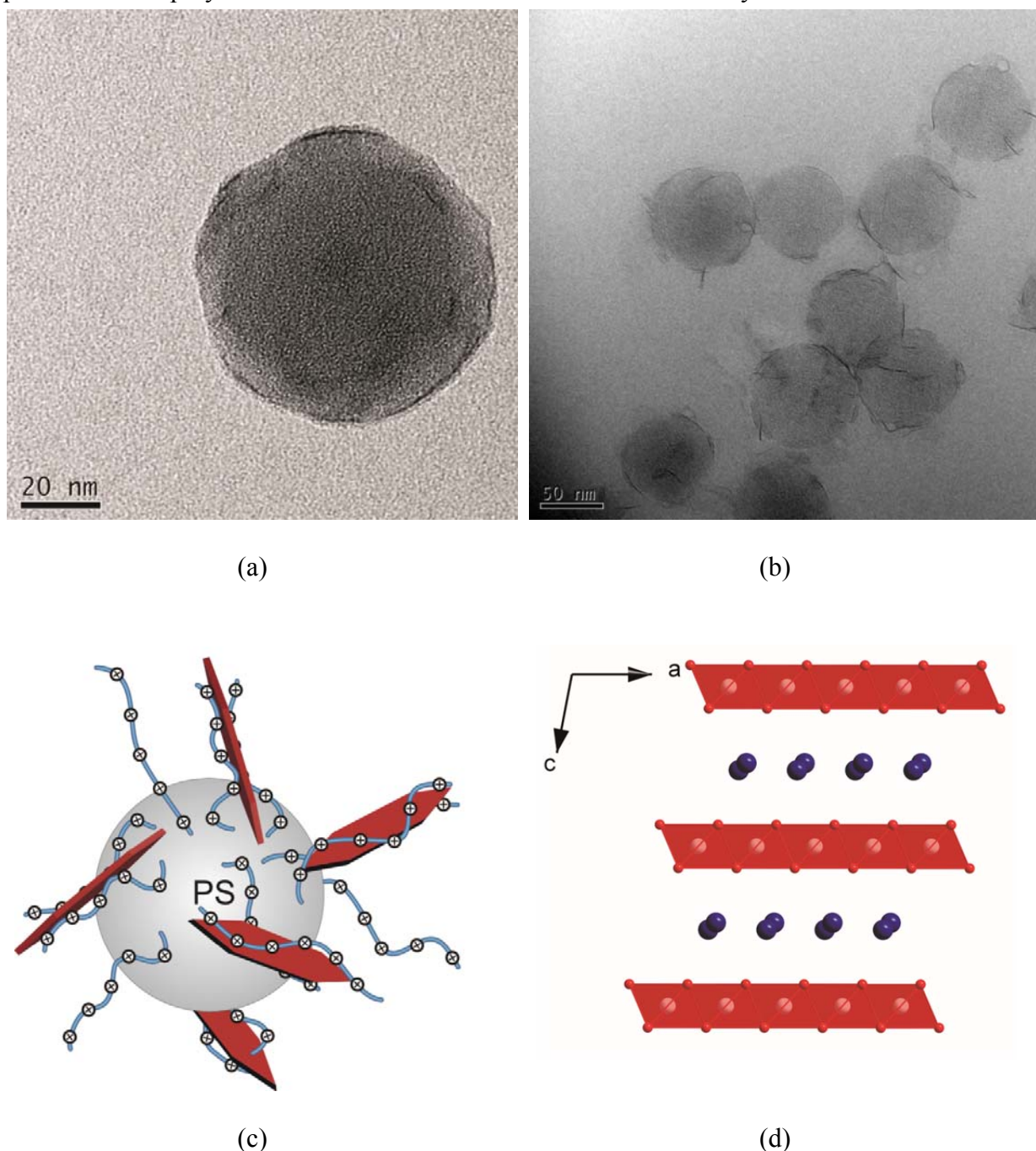


**Figure 4.4.1.** (a) TEM micrograph of MnO<sub>x</sub>NP@SPB. The PS core particles of the cationic SPB are visible as gray spheres whereas the MnO<sub>x</sub>NP appear as black objects decorating the carrier particles. (b) CryoTEM micrograph of the MnO<sub>x</sub>NP@SPB. The polystyrene core particles of the cationic SPB are visible as gray spheres whereas the MnO<sub>x</sub>NP appear as black needle-like objects decorating the carrier particles. The corresponding schematic model of the composite system is given in Figure 4.4.1c. The platelet-like MnO<sub>x</sub>NP are generated directly within the brush layer of the SPB and concomitantly stabilized by the support due to Coulomb interaction of the positively charged pTMAEMC chains and the negatively charged nanoparticles. The crystallographic structure of birnessite is displayed in Figure 4.4.1d. The

$\text{MnO}_6$  octahedra (Mn white dots, O red dots) form into layers via edge-sharing. The layers are separate from each other by hydrated interlayer cations, e.g. potassium cations (blue dots).

The TEM micrograph in Figure 4.4.1a of the composite particles shows that the PS core particle of the cationic SPB is decorated with  $\text{MnO}_x\text{NP}$ . Particles are best visible when located at the edge of the PS core particles. The dark elongated  $\text{MnO}_x\text{NP}$  at the edge of the PS core particles in Figure 4.4.1a show better contrast because they are arranged with the c-axis perpendicular to the electron beam. In contrast to that, platelets in the middle of a PS sphere are hardly visible. Here, the PS background is significantly higher. Moreover, it is unlikely for the platelet-like  $\text{MnO}_x\text{NP}$  to lie down onto the PS particles along their stacking axis. Rather, the  $\text{MnO}_x\text{NP}$  lie flat down on the spherical PS particles with their ab-plane. Since the  $\text{MnO}_x\text{NP}$  are only composed of a few lamellae or even just single lamellae, they show a poor electron contrast and are hardly visible.

Imaging by cryoTEM, that is *in-situ*, provides a better way of visualizing the  $\text{MnO}_x\text{NP}$  (see Figure 4.4.1b). The nanoparticles are of platelet-like shape and have a length of about 20 nm with a width of 1.8 nm in average. In aqueous dispersion the  $\text{MnO}_x\text{NP}$  are located within the pTMAEMC brush layer. This led to the conclusion that the nanoparticles are stabilized by the cationic polymer chains. This is due to the Coulomb interactions of the oppositely charged pTMAEMC chains with the negatively charged  $\text{MnO}_x\text{NP}$ .

A comparison of Figure 4.4.1b to the results from the TEM picture in Figure 4.4.1a where the dried state of the composite system is displayed reveals a marked change in the structure of the immobilized  $\text{MnO}_x\text{NP}$ . The ultrathin sheets of  $\text{MnO}_x\text{NP}$  are collapsing upon drying onto the PS core particles. Since the nanoparticles are of platelet-like form and only a few nm thick, a collapse onto strongly curved surface upon drying might have influence on crystallographic structure of the  $\text{MnO}_x\text{NP}$ . In the following this point will be further pursued by an analysis using EXAFS.

In addition to the investigation by TEM and cryoTEM, HRTEM studies of the dried composite materials have been done to elucidate the crystallographic structure of the nanoparticles. Figure 4.4.2a shows a HRTEM micrograph of the  $\text{MnO}_x\text{NP}@\text{SPB}$  prepared on a lacey carbon grid. The SPB particles decorated with the  $\text{MnO}_x\text{NP}$  are sticking to the lacey film. This enables one to obtain a better contrast of the nanoparticles immobilized on the amorphous carrier particles since no background of a support film is present. In Figure 4.4.2a, crystallites of  $\text{MnO}_x\text{NP}$  are lying on the surface of the amorphous polymer particles with their lattice planes being visible. The presence of atom columns points out to the fact that at least some of the  $\text{MnO}_x\text{NP}$  are not completely delaminated. Due to the high number of lattice planes of birnessite showing similar d-spacing there are several possibilities for the orientation of the crystallites shown in Figure 4.4.2b. The most probable orientation of the crystallite displayed in Figure 4.4.2a is [111] which can be rationalized as follows: First, the d-spacings obtained from Figure 4.4.2b are in good agreement within the limits of error with the corresponding d-spacings of the [111] orientation of birnessite (see Table S4.1). Second, the tilt between the three lattice planes in the crystallite in Figure 4.4.2b resembles the calculated diffraction pattern displayed in Figure 4.4.2d. Please note that the calculated

diffraction pattern has been rotated to match the orientation of the crystallite shown in Figure 4.4.2b.

Furthermore, the [111] orientation gives a good explanation for the tilting of the crystallite towards a [101] orientation as it can be seen in the lower left part of the crystallite in Figure 4.4.2b. Due to this tilt, only the (11̄2) lattice plane can be resolved by the HRTEM image. We assign this tilt to a crystal defect related to the particle formation. This indicates a highly distorted crystallographic structure of the MnO<sub>x</sub>nanoparticles which matches well with our previous results. This indicates a distorted crystallographic structure of the nanoparticles which matches well with our previous results.<sup>34</sup>

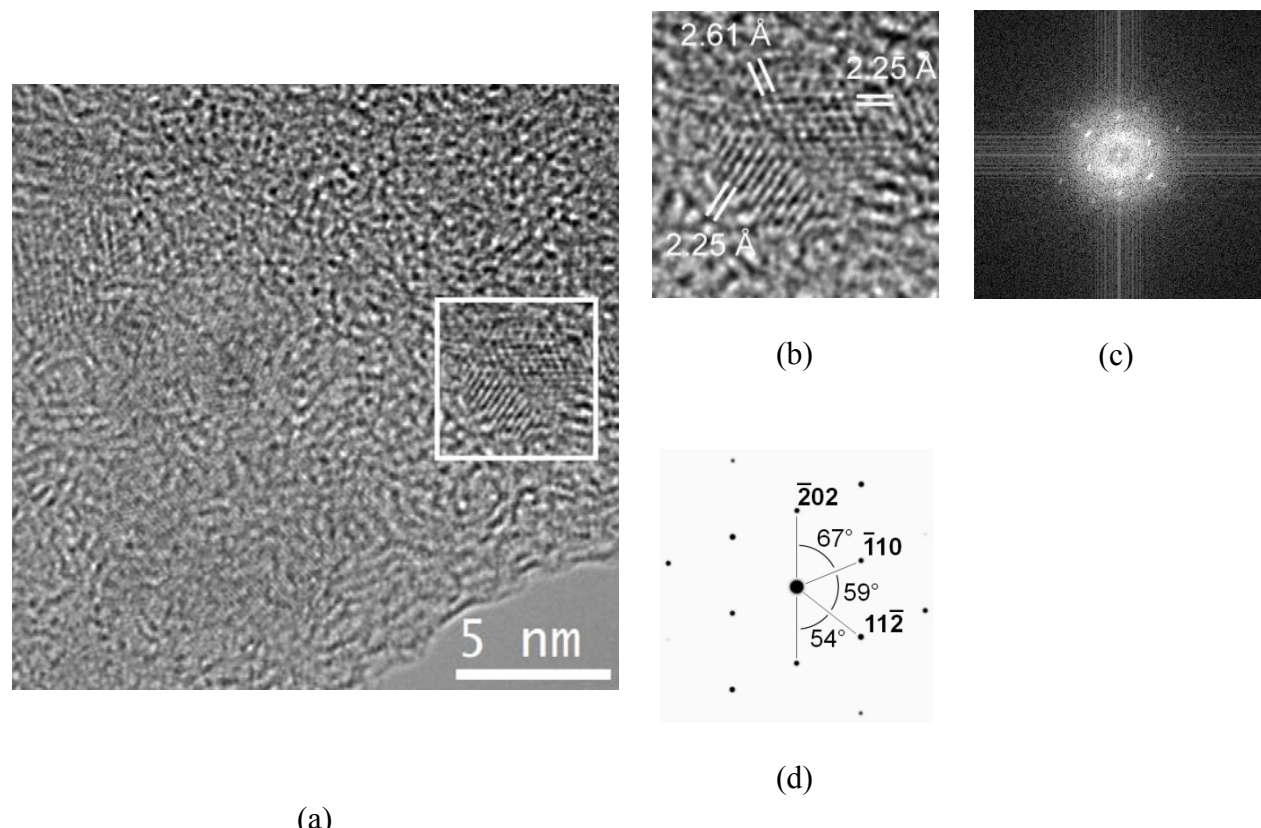


**Figure 4.4.2.** (a) HRTEM of dried MnO<sub>x</sub>NP@SPB prepared on a lacey carbon copper grid. Lattice planes of MnO<sub>x</sub> crystallites are visible in the composite material as indicated in the framed area. (b) Magnification of the lattice planes of the framed area of Figure 4.4.2a. Analysis of the lattice plane distances of this area gave a [111] orientation of birnessite. (c) The corresponding diffractogram of Figure 4.4.2b obtained by Fourier transformation proves the presence of three different lattice planes of the [111] orientation of the MnO<sub>x</sub>NP. (d) Calculated diffraction pattern for the [111] orientation of a monoclinic birnessite.

We now turn to the discussion of the synthesis of the MnO<sub>x</sub>NP@pTMAEMC<sub>star</sub>. In contrast to the synthesis of MnO<sub>x</sub>NP@SPB, the addition of KMnO<sub>4</sub> to an aqueous solution of the pTMAEMC<sub>star</sub> did not lead to the generation of MnO<sub>x</sub>NP at neutral pH. The fact that a reducing agent is needed indicates that there is no reaction of the pTMAEMC chains with

KMnO<sub>4</sub>. This is in good agreement with recent findings that the generation of MnO<sub>x</sub>NP inside a pTMAEMC brush layer is catalyzed by OH<sup>-</sup> ions inside the cationic brush layer of SPBs.<sup>34</sup> Due to the higher charge density, and therefore the higher exchange capacity of a SPB in comparison to a star-shaped homopolymer, the OH<sup>-</sup> concentration is significantly higher within the brush layer of a SPB. Hence, in case of the pTMAEMC<sub>star</sub> the pH is not sufficiently high enough to reduce the MnO<sub>4</sub><sup>-</sup>-ions. Thus, the generation of the nanoparticles stabilized by pTMAEMC<sub>star</sub> has been induced by the addition of 2-butanol. The redox process can be followed by a fading of the purplish color of KMnO<sub>4</sub> to brown, indicating the generation of MnO<sub>x</sub>NP.

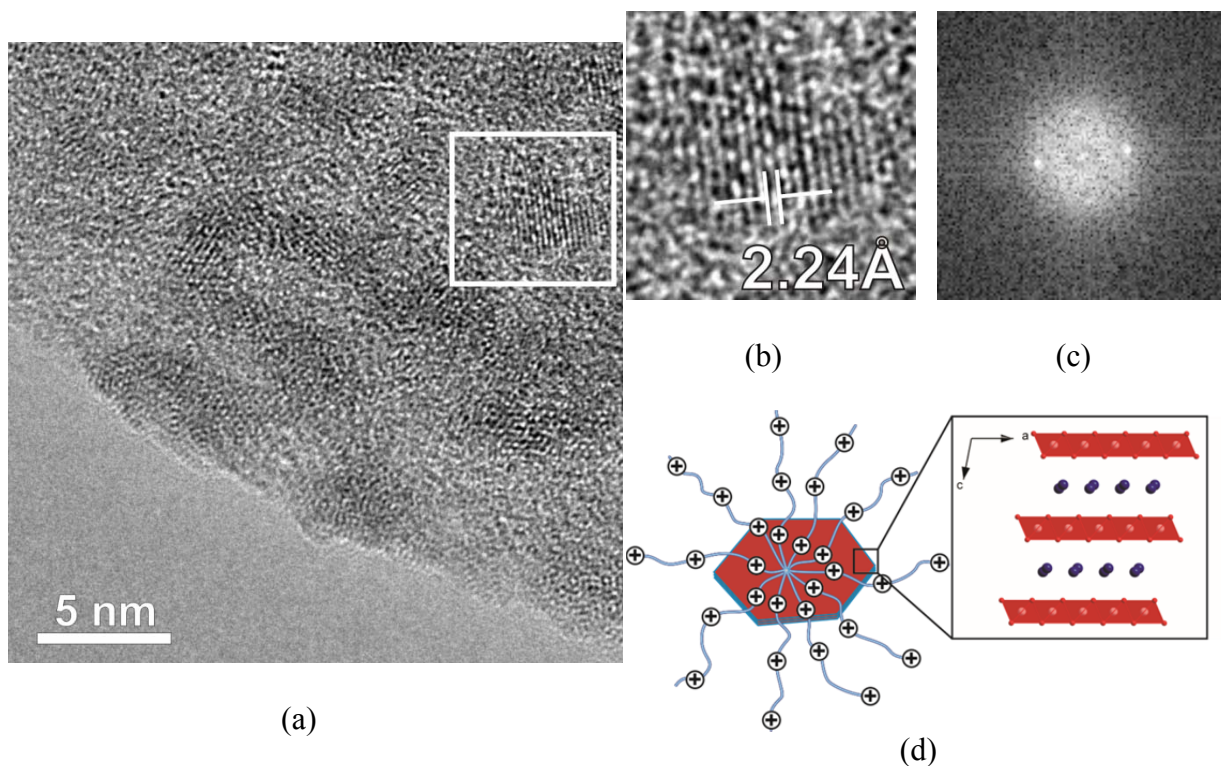


**Figure 4.4.3.** (a) HRTEM micrograph of MnO<sub>x</sub>NP@pTMAEMC<sub>star</sub> on a lacey carbon grid in the dried state. The MnO<sub>x</sub>NP are visible as dark objects embedded in the TMAEMC<sub>star</sub> matrix. The lattice planes of the MnO<sub>x</sub>NP are clearly visible. The white square in Figure 4.4.3a shows the selected area for the micrograph in Figure 4.4.3b and its corresponding diffractogram in Figure 4.4.3c. Schematic representation of the composite material composed of pTMAEMC<sub>star</sub> and MnO<sub>x</sub>NP. The negatively charged, platelet-like MnO<sub>x</sub>NP with a typical diameter of 2-5 nm are stabilized by the cationic pTMAEMC<sub>star</sub> polymer due to electrosteric stabilization. The crystallographic structure of a birnessite composed of Mn central atoms (white spheres) surrounded by 6 oxygen atoms (red spheres) is displayed next to the composite material. The predominantly edge-shared MnO<sub>6</sub> octahedra of the birnessite form into layers with intercalated K<sup>+</sup>-ions and water molecules (blue spheres) between these layers.

HRTEM micrographs in Figure 4.4.3 show the MnO<sub>x</sub>NP together with the pTMAEMC<sub>star</sub> in the dried state. The nanoparticles are displayed as dark objects with a disk-like shape.

Lattice planes are clearly visible. As already discussed, there are a large number of similar d-spacings within the crystallographic structure of the birnessite. The lattice planes in Figure 4.4.3b show a d-spacing of 2.24 Å, most probably referring to (11̄2) or (20̄2) lattice planes of a [111] orientation according to the discussion of the HRTEM micrographs for MnO<sub>x</sub>@SPB. A second lattice plane is indicated by the diffractogram in Figure 4.4.3c but could not be resolved by the HRTEM imaging. The weak contrast of the MnO<sub>x</sub>NP in the TEM micrographs points to the fact that the particles are composed of a low number of stacks of lamellae only.

Based on the investigations by TEM and the high colloidal stability of the composite material in water, the negatively charged, disk-like MnO<sub>x</sub>NP (typical diameter ca. 2-5 nm) are stabilized by the cationic pTMAEMC<sub>star</sub> that adsorbs onto the MnO<sub>x</sub>NP due to Coulomb interactions (Figure 4.4.3d). The adsorbed pTMAEMC<sub>star</sub> stabilizes the small nanoparticles against coagulation in aqueous solution due to steric and electrostatic interactions. Due to the stabilization by pTMAEMC<sub>star</sub> the MnO<sub>x</sub>NP exhibit a high colloidal stability over several months. The size is in the same magnitude observed for MnO<sub>x</sub>NP synthesized in the presence tetraalkyl ammonium ions as reported previously by Brock *et al.*<sup>27</sup> The MnO<sub>x</sub>NP generated in the presence of pTMAEMC<sub>star</sub> are significantly smaller than those synthesized within the cationic SPB. This could be evidence for a polymer directed growth of the MnO<sub>x</sub>NP since the pTMAEMC chains of the star shaped polymer are shorter compared to the pTMAEMC chains of the SPB.

Since the HRTEM studies only represent a small local area of the sample and due to the fact that a large number of different lattice planes with similar d-spacing are present in birnessite structures, further investigations by PXRD and by XAFS are necessary to get complete information about the crystallographic structure of the MnO<sub>x</sub>NP.

The results are shown in Figure 4.4.4. In principal, the diffraction pattern for the MnO<sub>x</sub>NP@pTMAEMC<sub>star</sub> material proves that the nanoparticles can be characterized as c-disordered birnessite with a small crystal size. Here, we would like to add that extremely small birnessite crystallites composed of only a few, randomly stacked lamellae are sometimes termed as δ-MnO<sub>2</sub> in literature.<sup>42,53,54,55</sup> Due to the absence of *00l* reflections, which correspond to the interlayer distance of stacked lamellae in the c-axis, the MnO<sub>x</sub>NP are composed only of a few or even of single lamellae (see Figure S4.1). This agrees with the low electron contrast of the MnO<sub>x</sub>NP in the TEM micrographs in Figure 4.4.1.

As already discussed in a previous work, the maximum of the *hk* bands at about 36° and 65° in 2θ of MnO<sub>x</sub>NP@SPB matches with the corresponding reflections of a birnessite whereas the maximum of the *hk* bands of the c-disordered H<sup>+</sup>-birnessite is slightly shifted to 36.3° and 65.4° in 2θ. This slight shift can either be traced back to small differences of d-values of the corresponding lattice planes or might be an effect of the small crystallite size. It is well known for turbostratically disordered smectites, which also possess a 2D layered topology that the maxima of the strongly asymmetric bands do not superimpose with the d-value of a specific reflection anymore.<sup>56</sup> The reason for this fact is that the structure factor influences the shape of the *hk* bands when the crystallites come to nanoscopic dimensions so that the maxima of the *hk* bands do not match the reflections of the corresponding lattice planes. Nevertheless,

the maxima of the  $hk$  bands fit well with the reflections of the corresponding c-ordered birnessite as shown in Figure 4.4.4. The pattern of the  $\text{MnO}_x\text{NP}@\text{pTMAEMC}_{\text{star}}$  composite matches with that of the  $\text{MnO}_x\text{NP}@\text{SPB}$  and therefore can also be assigned to a c-disordered birnessite structure. Since both composites show structural similarities according to the PXRD patterns we conclude that the pTMAEMC chains play an important role in the particle generation mechanism.

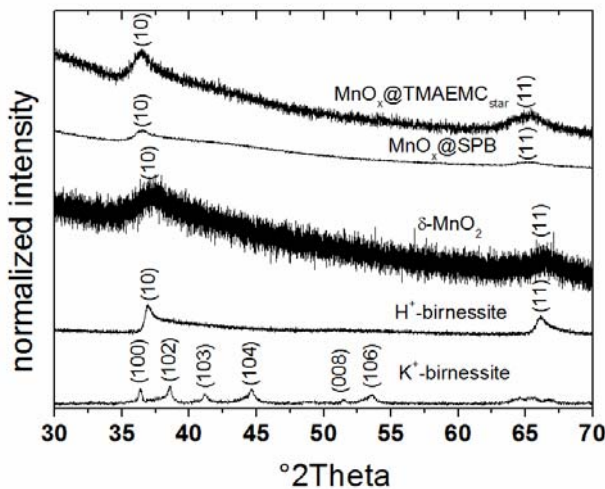


**Figure 4.4.4.** PXRD pattern of  $\text{MnO}_x\text{NP}@\text{pTMAEMC}_{\text{star}}$ ,  $\text{MnO}_x\text{NP}@\text{SPB}$ ,  $\delta\text{-MnO}_2$ ,  $\text{H}^+$ -birnessite and birnessite. The reflection at around  $36.5^{\circ}$  and  $65^{\circ}$  in  $2\theta$  refer to the  $hk$  bands due to a disorder in c-direction of the composite materials and the  $\text{H}^+$ -birnessite of the hexagonal sheets composed of  $\text{MnO}_6$  octahedra. Figure S4.1 shows the PXRD patterns of the compounds from  $15^{\circ}$  to  $70^{\circ}$  in  $2\theta$ .

However, no detailed structural analysis as e.g. interatomic distances is possible by analyzing the very weak and broad  $hk$  bands in PXRD. For this purpose, XAFS measurements were conducted to elucidate the local structure around the manganese atoms.

### X-ray Absorption Near Edge Structure (XANES)

The background corrected and normalized XANES spectra measured at the Mn K-edge for the  $\text{MnO}_x\text{NP}@\text{SPB}$  and for  $\text{K}^+$ - and  $\text{H}^+$ -birnessite are presented in Figure 4.4.5. The spectra contain several characteristics like a pre-edge peak, the white line, the high energy shoulder and a second peak at 6580 eV. The pre-edge peak arises from dipole forbidden quadrupole allowed  $\text{Mn } 1\text{s} \rightarrow 3\text{d}$  inner atomic transition in an octahedral environment.<sup>57,58</sup> The intensity of the pre-edge peak is enhanced if  $\text{Mn(III)}\text{O}_6$  octahedra with reduced inversion symmetry due to Jahn-Teller distortion are present.<sup>33</sup>

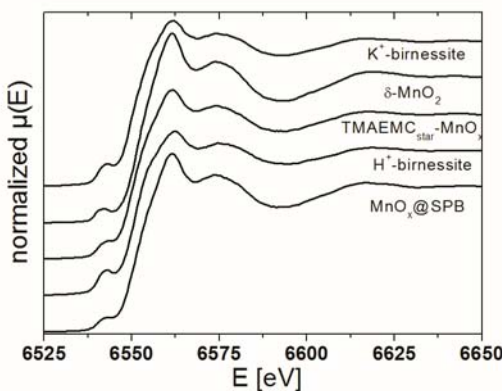


**Figure 4.4.5.** XANES spectra of composite samples and reference compounds H<sup>+</sup>-birnessite, birnessite and δ-MnO<sub>2</sub>. MnO<sub>x</sub>NP@SPB and MnO<sub>x</sub>NP@pTMAEMC<sub>star</sub>. All samples show the characteristic pre-edge feature below the Mn K-edge due to the octahedral crystal field splitting between e<sub>g</sub> and t<sub>2g</sub> orbitals.<sup>39</sup>

The XANES region can be also used for a first differentiation of the samples from the huge amount of different layered MnO<sub>x</sub> structures known so far. Therefore the XANES spectra of MnO<sub>x</sub>NP@SPB and MnO<sub>x</sub>NP@pTMAEMC<sub>star</sub> were compared to the most probable candidates for crystallographic similarity based on the PXRD study. Figure 4.4.5 shows a comparison of the XANES and for K<sup>+</sup>- and H<sup>+</sup>-birnessite and δ-MnO<sub>2</sub>, and proves the excellent agreement of the MnO<sub>x</sub>NP of the composite materials with the reference compounds. This implies that these structures are closely related and that MnO<sub>x</sub>NP@SPB and MnO<sub>x</sub>NP@pTMAEMC<sub>star</sub> are mainly composed of edge-sharing MnO<sub>6</sub> octahedra that form a layered topology. As it can be seen from Figure 4.4.5, the shape and the position of the main peak and the high energy shoulder of the XANES of MnO<sub>x</sub>@SPB shows better agreement with the one of δ-MnO<sub>2</sub>. MnO<sub>x</sub>NP@pTMAEMC<sub>star</sub> composite matches better to the spectrum of a triclinic K<sup>+</sup>-birnessite. This is in compliance with the results of Ressler *et al.* which showed that MnO<sub>x</sub> nanoparticles, generated by the reduction of KMnO<sub>4</sub> with alcohols in the presence of tetraalkylammonium ions, possess similar structure than triclinic K<sup>+</sup>-birnessite.<sup>33</sup>

The XANES spectrum is very sensitive to the oxidation state of the sample and its coordination chemistry.<sup>49</sup> Due to the diversity of different layered minerals composed of MnO<sub>6</sub> octahedra and their differences in the average oxidation state, the analysis of the XANES region can give important a priori information on the sample. Therefore a comparison of the K-edge positions of the samples and of the reference compounds with well-defined average oxidation state has been done. The energy of the X-ray absorption edge is increasing with increasing oxidation state. This is due to the fact that the successive removal of electrons from the absorbing atom is raising the electron binding energy.<sup>59</sup> The linear relationship of the edge position determined by the maximum of the first derivative and the Mn oxidation state is shown in Figure S4.2.<sup>33</sup> This plot proves the excellent linear dependency of the average oxidation state of Mn on the Mn K-edge positions for various manganese oxides as expected. The average oxidation states of the MnO<sub>x</sub>NP samples were determined

based on this calibration and the results are summarized in Table 4.1. Though the pre-edge feature is also sensitive to the average oxidation state, an analysis of the edge position is more straightforward and less ambiguous.<sup>33</sup>

The average oxidation state of  $\text{MnO}_x@\text{SPB}$  and of  $\text{MnO}_x\text{NP}@p\text{TMAEMC}_{\text{star}}$  is about 3.7 and 3.5, respectively. This indicates that the samples are predominantly of  $\text{Mn}^{4+}$  cations including a fraction of manganese cations in a lower oxidation state.<sup>39,60</sup> This finding points towards a birnessite structure that includes also  $\text{Mn}^{3+}$  sites and not only  $\text{Mn}^{4+}$  sites as found for systems with hexagonal sheet symmetry, e.g.  $\delta\text{-MnO}_2$ .<sup>42</sup> The accuracy of the average oxidation state determination via the X-ray absorption edge has an error of about 10%.<sup>31,61</sup> The error is higher than for methods like titration reduction/oxidation techniques.<sup>62,63,64,65</sup> However, the analysis of composite materials by titration techniques may be problematic since it is not assured that only the inorganic part, namely  $\text{MnO}_x$ , is exclusively oxidized or reduced by the titrant.<sup>31</sup>

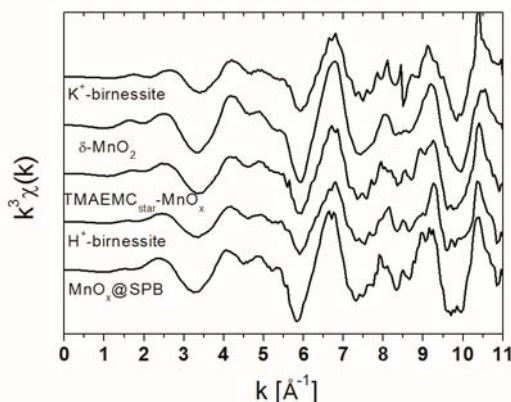
**Table 4.1. Edge Positions and Average Mn Oxidation States of Manganese Oxide Compounds**

sample	absorption edge position [eV]	average oxidation state of Mn
$\text{H}^+$ -birnessite	6550.5	$3.7 \pm 0.3$
birnessite	6549.1	$3.3 \pm 0.3$
$\text{MnO}_x\text{NP}@\text{SPB}$ (powder)	6550.7	$3.7 \pm 0.3$
$\text{MnO}_x\text{NP}@p\text{TMAEMC}_{\text{star}}$	6549.9	$3.5 \pm 0.3$

### Extended X-ray Absorption Fine Structure (EXAFS)

Since layered structured  $\text{MnO}_x$  materials exist in a great variety, a qualitative comparison with reference compounds is necessary for choosing a proper crystallographic model for the polymer supported  $\text{MnO}_x\text{NP}$  samples. In our previous work we could already show that the  $\text{MnO}_x\text{NP}$  have similar PXRD patterns than that of phyllosilicates like  $\text{H}^+$ - and  $\text{K}^+$ -birnessite.<sup>34</sup> The experimental  $\chi(k)$  spectra of those reference compounds and of the composite materials are displayed in Figure 4.4.6 in a range of  $0 \text{ \AA}^{-1} \leq k \leq 11 \text{ \AA}^{-1}$ . It should be noted at this point that in our case EXAFS only probes the local environment around the Mn central atom within a distance of about 6 Å. Therefore, neighboring atoms in adjacent layers along the crystallographic c-axis are not considered in this analysis. In general, the all spectra show a good agreement in this range indicating similarity in the crystallographic structure, making a differentiation rather difficult. It proves that the birnessite materials are closely related to each other. For  $\text{MnO}_x\text{NP}@p\text{TMAEMC}_{\text{star}}$ ,  $\text{K}^+$ -birnessite shows slightly

more spectral similarities according to Figure 4.4.6. The MnO<sub>x</sub>NP@SPB matches best to δ-MnO<sub>2</sub> in between 2 Å<sup>-1</sup> and 5 Å<sup>-1</sup> compared to the other two reference compounds.



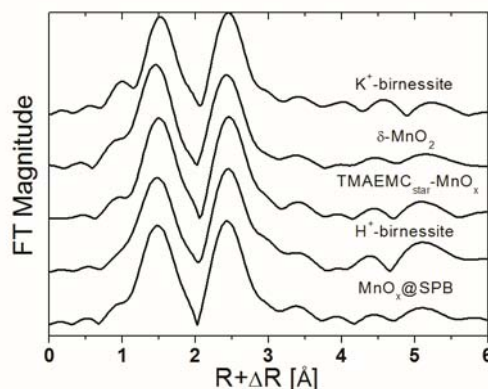
**Figure 4.4.6.** Experimental Mn K-edge EXAFS signal,  $\chi(k)k^3$ , of composite particles MnO<sub>x</sub>NP@SPB and MnO<sub>x</sub>NP@pTMAEMC<sub>star</sub> and of reference compounds K<sup>+</sup>- and H<sup>+</sup>-birnessite and δ-MnO<sub>2</sub>. The composite materials show a good agreement with the reference samples in the range of  $2 \text{ \AA}^{-1} \leq k \leq 11 \text{ \AA}^{-1}$ .

Figure 4.4.7 shows the Fourier transformed (FT)  $k^2$ -weighted  $\chi(k)$  functions of H<sup>+</sup>-birnessite, K<sup>+</sup>-birnessite, δ-MnO<sub>2</sub>, MnO<sub>x</sub>NP@SPB and MnO<sub>x</sub>NP@pTMAEMC<sub>star</sub>. The spectra are not phase corrected for the phase shift associated with the scattering process of the photoelectron so that the peak distances in this plot shifted to lower  $R$  values of about 0.4 Å. Therefore the first peak corresponding to the six oxygen atoms of the first shell located at a distance of ~1.9 Å appears at ~1.5 Å in Figure 4.4.7. The peak at around 2.5 Å represents the distance between two edge-shared MnO<sub>6</sub> octahedra. The spectra in R-space are dominated by the first two shells around the scattering center which is common for phyllosilicates. Another important feature of layered manganese oxide with a mixed valency is an additional peak at about 3.1 Å which is due to the presence of Mn-Mn corner sharing. There is no significant signal around this peak distance for the composite materials displayed in Figure 4.4.7 leading to the conclusion that the amount of corner-shared MnO<sub>6</sub> units is negligible in these samples. The average oxidation states for the two composite materials of about 3.5 - 3.7 for the composite materials (see Table 4.1) then might be traced back to the presence of Mn<sup>3+</sup> ions acting as interlayer, charge compensating cations. This is common for poorly crystalline hexagonal birnessite structures which mostly are generated at mild reaction conditions like it is the case for both composite materials and the H<sup>+</sup>-birnessite. The peak at around 5.2 Å is due to the focusing effect and refers to a Mn-Mn distance of three edge-shared MnO<sub>6</sub> units located along a center line.<sup>66,67</sup> The forward scattering through the center atom increases the backscattering power and therefore the amplitude contribution of  $\chi(k)$  of the third atom in the row.<sup>68</sup> The amplitude of the backscattering signal of the third atom is strongly dependent on the dihedral angle between the three atoms in the row. The peak is decreasing with increasing deviation from the dihedral angle from 180° and hence the intensity of the focusing peak can be used as

a measure for the dihedral angle.<sup>69,70</sup> This was shown by Ressler *et al.* based on theoretical calculations of Fourier transformed XAFS of four edge-shared MnO<sub>6</sub> octahedra.<sup>33</sup> There is no pronounced focusing peak for the composite materials presented in Figure 4.4.7 which indicates a deviation of a collinear arrangement of neighboring MnO<sub>6</sub> octahedra. This finding matches well with the disordered structure found by PXRD and HRTEM measurements which do not suggest a long-range ordered material.

After a qualitative discussion of the XAFS data we now turn to the quantitative analysis of the EXAFS of MnO<sub>x</sub>NP@SPB. The comparison of TEM and cryoTEM micrographs revealed significant differences in the morphology of the MnO<sub>x</sub>NP in the dried and the dispersed state as already shown. Therefore the local structure of the MnO<sub>x</sub>NP was investigated in both states by EXAFS measurements to analyze if differences exist.

The comparison of XANES and qualitative EXAFS spectra revealed a good agreement of the composite material MnO<sub>x</sub>NP@SPB with the birnessite reference compounds. We chose the crystallographic structure of a monoclinic birnessite according to Post *et al.* for the theoretical EXAFS calculations.<sup>13</sup> Please note that we also tried fitting the data with a hexagonal *P*6<sub>3</sub>/mmc but within the limits of error a differentiation between both structures could not be achieved. A list of the parameters of the first two nearest neighboring shells of the crystallographic structure is given in Table 4.2.



**Figure 4.4.7.** Fourier transformed experimental Mn K-edge  $\chi(k)k^2$  functions of MnO<sub>x</sub>NP composites and of H<sup>+</sup>- and K<sup>+</sup>-birnessite and δ-MnO<sub>2</sub> (non-phase corrected). The first peak corresponds to the Mn-O distance whereas the second peak at about 2.5 Å corresponds to the Mn-Mn distance between two edge-shared MnO<sub>6</sub> octahedra.

For the quantitative EXAFS analysis the Bayes-Turchin method was used,<sup>71</sup> based on the standard EXAFS equation.<sup>72</sup> This approach compares the measured absorption coefficient  $\mu_{exp}$  with the corresponding model data computed by the FEFF code.<sup>51</sup> The Bayes-Turchin method uses correction parameters for the atomic-like background absorption besides the usual structure parameters and yields fit parameters with uncertainties consistently calculated from the experimental and model uncertainties. These were assigned as follows:  $\Delta\mu_{exp}/\mu_{exp} = 0.5\%$  for  $k < 10 \text{ \AA}^{-1}$  and  $0.75\%$  for  $k \geq 10 \text{ \AA}^{-1}$ ,  $\Delta f_j/f_j = 7\%$  and  $\Delta\phi_j = 0.07 \text{ rad}$  for scattering

amplitudes and phases for each path  $j$ , respectively, and the uncertainty of the mean free electron path was set to  $\Delta\lambda/\lambda = 10\%$ . A total number of 86 scattering paths were used and the experimental and model EXAFS oscillations were Fourier filtered with  $R$ -window between 0 Å and 6 Å. The truncation error, which describes the uncertainty of the fit with respect to the truncation of the multiple-scattering series, was calculated for relative scattering amplitude of 4 %.

In an EXAFS analysis usually the Debye-Waller factor  $\sigma_j^2$  is fitted for each scattering path or estimated from Debye models. Here we use the approach that  $\sigma_j^2$  has a thermal disorder component  $\sigma_{j,therm}^2$  and a structural disorder component  $\sigma_{j,struc}^2$ . For a perfect crystal structure the latter component should be small and independent of temperature and usually is neglected at elevated temperatures. In our case we have to consider significant disorder and therefore both components were treated as fitting parameters, where  $\sigma_{j,struc}^2$  just depends on the number of atoms  $N_j$  in path  $j$ ,  $\sigma_{j,struc}^2 = \sigma_{struc}^2 N_j / 2$ . At the beginning  $\sigma_{struc}^2$  was set to 0.001 [Å<sup>2</sup>] and  $\sigma_{j,therm}^2$  was calculated according to the Debye model with Debye temperature of  $\Theta_{Debye} = 400$  K. During the fitting procedure  $\sigma_{j,therm}^2$  of the two oxygen bonds at  $R_1 \approx R_2 \approx 1.9$  Å and the two manganese bonds at  $R_3 \approx R_4 \approx 2.8$  Å were adjusted with restrictions  $\sigma_{1,therm}^2 = \sigma_{2,therm}^2$  and  $\sigma_{3,therm}^2 = \sigma_{4,therm}^2$ .

**Table 4.2. Crystallographic Structure of Monoclinic Birnessite to Derive Theoretical EXAFS Phases and Amplitudes (C2/m,  $a = 5.0$  Å,  $b = 2.850$  Å,  $c = 7.336$  Å,  $\beta = 103.18^\circ$ )<sup>13</sup>**

shells <sup>a</sup>	pairs <sup>b</sup>	CN <sup>c</sup>	$R^d$ [Å]
first shell	Mn-O	4	1.908
	Mn-O	2	1.910
second shell	Mn-Mn	2	2.850
	Mn-Mn	4	2.878

<sup>a</sup> nearest neighbor shells around the Mn absorber; <sup>b</sup> corresponding atom pair of the shell; <sup>c</sup> coordination number of the atom pairs; <sup>d</sup> radial distance of the absorber and the scattering atoms

The data reduction of the  $\mu(E)$  spectra of both samples was conducted in the same way to minimize an influence on the extracted  $\chi(k)$ . The number of fitting parameters was minimized by the introduction of two independent cell expansion factors:  $\alpha_{ab}$  represents the expansion of the atom coordinates within the ab-plane whereas  $\alpha_c$  is the expansion factor along the c-axis of the atom coordinates that is, the stacking axis of MnO<sub>x</sub> sheets. The coordination numbers were fixed to the values from the crystallographic information file.<sup>13</sup> The amplitude reduction factor  $S_0^2$  was set to a value of 0.9. The EXAFS analysis was conducted in  $k$ -space and restricted to a distance in  $R$ -space of 6 Å. As a consequence, adjacent layers of hydrous MnO<sub>x</sub>NP are not included in the EXAFS fits since they are typically more than 7 Å apart.

Hence, the investigations by EXAFS presented herein are limited to the ab-plane within individual hexagonal sheets. This restriction plays no role here inasmuch the long-range order of the  $\text{MnO}_x\text{NP}$  has already been deduced from PXRD measurements.

The results of the least square fits for the  $\text{MnO}_x\text{NP}@\text{SPB}$  in the dried and in the dispersed state are summarized in Table 4.3, and the fits of the experimental data are presented in Figure 4.4.8. The expansion factors indicate that the  $\text{MnO}_x$  nanosheets are compressed along the c-axis of about 4 % whereas they are slightly elongated within the ab-plane, that is, the two dimensional expansion of the hexagonal sheets composed of the  $\text{MnO}_6$  octahedra. The error correlations between the parameters shown in Table 4.3 stayed below 0.5 even for  $\sigma_{\text{struc}}^2$  and  $\sigma_{j,\text{therm}}^2 R$ -factors are below 0.006 and summarized in Table 4.3.

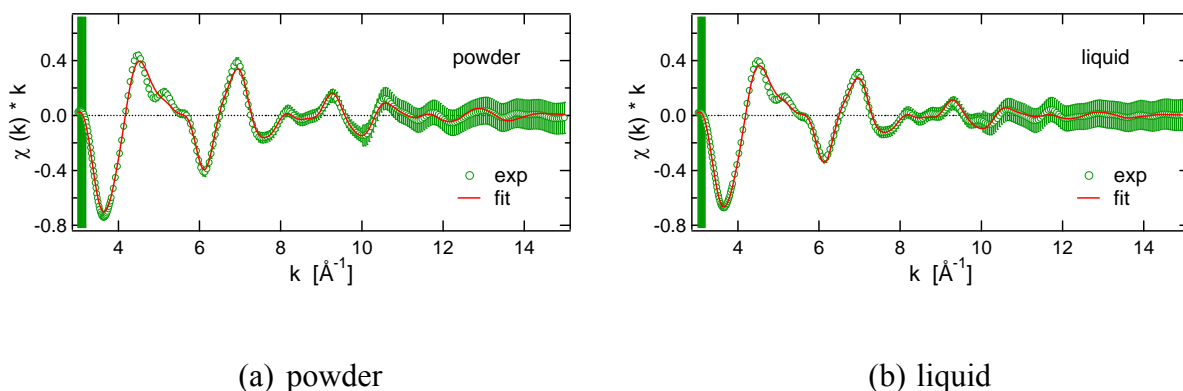


**Figure 4.4.8.** Experimental EXAFS functions  $\chi(k)$  weighted by wave number  $k$  are shown by open green circles together with the uncertainties. The solid curves are the most probable curves resulting from the fits.

To verify the new geometrical parameters the fitting procedure was repeated using the new crystal parameters  $a = 5.023 \text{ \AA}$ ,  $b = 2.86289 \text{ \AA}$ ,  $c = 7.044 \text{ \AA}$  for the solid sample of  $\text{MnO}_x\text{NP}@\text{SPB}$ , and  $a = 5.015 \text{ \AA}$ ,  $b = 2.858 \text{ \AA}$ ,  $c = 7.052 \text{ \AA}$  for the liquid sample of  $\text{MnO}_x\text{NP}@\text{SPB}$ . All other starting values were not changed. The results shown in Table 4.3 were reproduced within standard deviations.

Fukuda et al. observed an elongation within the ab-plane of layered  $\text{MnO}_x$  nanosheets after delamination.<sup>30</sup> They claimed that this is due to a decrease in the average oxidation state of the  $\text{MnO}_x\text{NP}$  during the delamination process. The authors also find an expansion in the thickness of the platelets in c-direction, that is, an overall expansion of the crystallographic volume. As already mentioned, we have herein observed a slight elongation along the ab-plane which is accompanied by a compression with regards to the c-direction of a single platelet, that is, along the stacking direction of the layered  $\text{MnO}_x\text{NP}$ . This is a new finding for  $\text{MnO}_x\text{NP}$  with layered topology which might be an effect of the small crystallite size together with the high degree of delamination of the platelets.

**Table 4.3. EXAFS Best Fit Results of MnO<sub>x</sub>NP@SPB in Dried and in Aqueous Dispersed State for the First Two Shells.**

parameter	MnO <sub>x</sub> @SPB (powder)	MnO <sub>x</sub> @SPB (liquid)
$E_0$ [eV]	$6543.0 \pm 0.3$	$6543.1 \pm 0.3$
$\alpha_{ab}^a$	$1.004 \pm 0.005$	$1.009 \pm 0.005$
$\alpha_c^b$	$0.960 \pm 0.005$	$0.961 \pm 0.006$
$\sigma^2(\text{Mn-O})^c [\text{\AA}^2]$	$0.00124 \pm 0.00075$	$0.00263 \pm 0.00088$
$\sigma^2(\text{Mn-Mn})^d [\text{\AA}^2]$	$0.00414 \pm 0.00078$	$0.00572 \pm 0.00090$
$\sigma^2_{\text{struc}}^e [\text{\AA}^2]$	$0.00083 \pm 0.00036$	$0.00153 \pm 0.00040$
R-factor <sup>f</sup>	0.0059	0.0034

<sup>a</sup> cell expansion factor for the ab-plane, <sup>b</sup> cell expansion factor for the c-axis, <sup>c</sup> Debye-Waller factor for the first shell, <sup>d</sup> Debye-Waller factor for the second shell, <sup>e</sup> structural disorder component. <sup>f</sup> standard goodness-of-fit parameter

Despite the significant differences observed by a comparison of the morphology of the composite particles in TEM and cryoTEM, the EXAFS analysis could prove that no significant difference in the local environment of the Mn of the MnO<sub>x</sub>NP in the dried and in the aqueous dispersed state is present. The Debye-Waller factors  $\sigma^2$  are higher for the liquid sample indicating a higher disorder in comparison to the powder sample. The  $\sigma^2$  includes the structural disorder  $\sigma_{\text{struc}}^2$  as well as the thermal disorder. Since no temperature dependent measurements of  $\sigma^2$  are available and correlations of the thermal and structural disorder are present, no detailed interpretation of the  $\sigma^2$  can be made at this point.

## 4.5. Conclusion

We presented the analysis of birnessite nanoparticles supported by cationic star-shaped pTMAEMC homopolymer. The MnO<sub>x</sub>NP stabilized by pTMAEMC<sub>star</sub> are of disk-like shape with a diameter between 2 - 5 nm. A combination of HRTEM, PXRD and XAFS analysis revealed that the MnO<sub>x</sub>NP@pTMAEMC<sub>star</sub> shows a structure closely related to the MnO<sub>x</sub>NP@SPB which has been identified as randomly stacked birnessite-type nanoparticles of small crystallite size. In addition, a XANES analysis proved the findings of the PXRD measurements and revealed oxidation states between 3.5 - 3.7 for the composite materials. The analysis of the EXAFS data of MnO<sub>x</sub>NP@SPB in the dried and in the dispersed state showed that no significant effect on the crystallographic parameters is observed, despite the significant structural difference between the TEM and cryoTEM micrographs of the

## Acknowledgements

---

composite material. Furthermore, the analysis could show that the crystallographic structure of the  $\text{MnO}_x\text{NP}$  in both samples is compressed about 4 % in c-direction compared to a triclinic birnessite whereas a slight elongation within the Mn layer that is the ab-plane, has been observed.

## 4.6. Acknowledgements

We thank the Deutsche Forschungsgemeinschaft and the Henkel AG & Co. KGaA for the financial support.

## 4.7. Supporting Information

**Table S4.1. Lattice Planes Available in the 111 Orientation of  $\text{K}^+$ -Birnessite with the Corresponding Calculated and Experimental  $d$ -Spacings.**

$hkl^a$	$d_{\text{calc}}^b [\text{\AA}]$	$d_{\text{exp}}^c [\text{\AA}]$
$\bar{1}10$	2.478	$2.61 \pm 0.13$
$11\bar{2}$	2.121	$2.25 \pm 0.11$
$20\bar{2}$	2.265	$2.25 \pm 0.11$

<sup>a</sup> Miller indices of the lattice planes; <sup>b</sup> calculated  $d$ -spacing of the lattice planes; <sup>c</sup> experimental  $d$ -spacing obtained from HRTEM micrographs in Figure 4.4.2b.

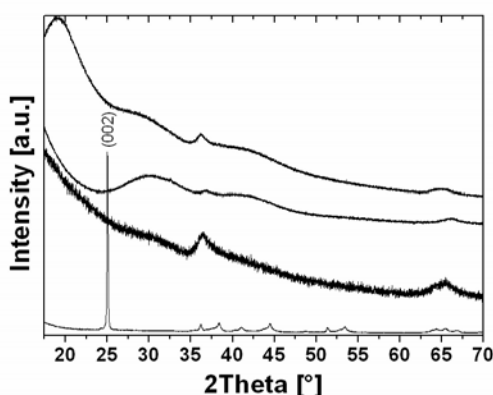


**Figure S4.1.** PXRD pattern of  $\text{MnO}_x\text{NP}@p\text{TMAEMC}_{\text{star}}$ ,  $\text{MnO}_x\text{NP}@SPB$ ,  $\text{H}^+$ -birnessite and  $\text{K}^+$ -birnessite in top down order.

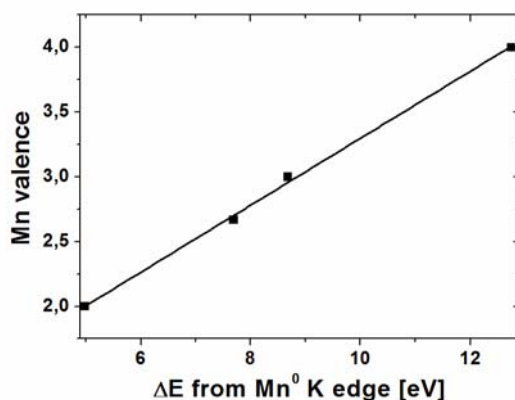


**Figure S4.2.** Manganese average oxidation state calibration. The absorption edges of different manganese oxide references were used to determine the average oxidation state of the different birnessite nanoparticles. The point of inflection was determined by the maximum of the 1<sup>st</sup> derivative of the Mn K-edge X-ray absorption spectra.

#### 4.8. References

- <sup>1</sup> Suib, S. L. *J. Mater. Chem.* **2007**, *18*, 1623-1631.
- <sup>2</sup> Wang, X.; Li, Y. *Pure Appl. Chem.* **2006**, *78*, 1-64.
- <sup>3</sup> Brock, S. L.; Duan, N.; Tian, Z. R.; Giraldo, O.; Zhou, H.; Suib, S. L. *Chem. Mater.* **1998**, *10*, 2619–2628.
- <sup>4</sup> Suib, S. L. *Acc. Chem. Res.* **2007**, *41*, 479–487.
- <sup>5</sup> Cai, J.; Liu, J.; Suib, S. L. *Chem. Mater.* **1998**, *10*, 2619–2628.
- <sup>6</sup> Aronson, B. J.; Kinser, A. K.; Passerini, S.; Smyrl, W. H.; Stein, A. *Chem. Mater.* **1999**, *11*, 949–957.
- <sup>7</sup> Shen, X.-F.; Ding, Y.-S.; Liu, J.; Cai, J.; Laubernds, K.; Zerger, R. P.; Vasiliev, A.; Aindow, M.; Suib, S. L. *Adv. Mater.* **2005**, *17*, 805-809.
- <sup>8</sup> Sakai, N.; Ebina, Y.; Takada, K.; Sasaki, T. *J. Phys. Chem. B* **2005**, *109*, 9651-9655.
- <sup>9</sup> Yang, D. S.; Wang, M. K. *Chem. Mater.* **2001**, *13*, 2589–2594.
- <sup>10</sup> Zhu, S.; Zhou, H.; Hibino, M.; Honma, I.; Ichihara, M. *Adv. Funct. Mater.* **2005**, *15*, 381–386.
- <sup>11</sup> Gaillot, A.-C.; Flot, D.; Drifts, V. A.; Manceau, A.; Burghammer, M.; Lanson, B. *Chem. Mater.* **2003**, *15*, 4666–4678.
- <sup>12</sup> Feng, Qu.; Kanoh, H.; Ooi, K. *J. Mater. Chem.* **1999**, *9*, 319-333.
- <sup>13</sup> Post, J. E.; Veblen, D. R.; *Am. Mineral.* **1990**, *75*, 477-489.
- <sup>14</sup> Drifts, V. A.; Silvester, E. J.; Gorshkov, A. I.; Manceau, A. *Am. Mineral.* **2002**, *87*, 1631-1645.
- <sup>15</sup> Ching, S.; Petrovay, D. J.; Jorgensen, M. L.; Suib, S. L. *Inorg. Chem.* **1997**, *36*, 883-890.

## References

---

- <sup>16</sup> Feng, Q.; Kanoh, H.; Miyai, Y.; Ooi, K. *Chem. Mater.* **1995**, *7*, 1226-1232.
- <sup>17</sup> Lanson, B.; Drits, V. A.; Gaillot, A. C.; Silvester, E.; Plancon, A.; Manceau, *Am. Mineral.* **2002**, *87*, 1631-1645.
- <sup>18</sup> Liu, Z.H.; Ooi, K.; Kanoh, H.; Tang, W.-P.; Tomida, T. *Langmuir* **2000**, *16*, 4154-4164.
- <sup>19</sup> Kai, K.; Yoshida, Y.; Kageyama, H.; Saito, G.; Ishigaki, T.; Furukawa, Y.; Kawamata, J. *Am. Chem. Soc.* **2008**, *130*, 15938-15943.
- <sup>20</sup> Gao, Q.; Giraldo, O.; Tong, W.; Suib, S. L. *Chem. Mater.* **2001**, *13*, 778-786.
- <sup>21</sup> Omomo, Y.; Sasaki, T.; Wang L.; Watanabe M. *J. Am. Chem. Soc.* **2003**, *125*, 3568-3575.
- <sup>22</sup> Oaki, Y.; Imai, H. *Angew. Chem. Int. Ed.* **2007**, *46*, 4951-4955.
- <sup>23</sup> Croguennec, L.; Deniard, P.; Brec, R.; Lecerf, A. *J. Mater. Chem.* **1997**, *7*, 511-516.
- <sup>24</sup> Hara, D.; Shirakawa, J.; Ikuta, H.; Uchimoto, Y.; Wakihara, M.; Miyanaga, T.; Watanabe, I. *J. Mater. Chem.* **2003**, *13*, 897-903.
- <sup>25</sup> Petkov, V.; Ren, Y.; Saratovsky, I.; Pastén; P.; Gurr, S. J.; Hayward, M. A.; Poeppelmeier, K. R.; Gaillard, J.-F. *ACS Nano* **2009**, *3*, 441-445.
- <sup>26</sup> Kobayashi, S.; Kotegoda, I. R. M.; Uchimoto, Y. Wakihara, M. *J. Mater. Chem.* **2004**, *14*, 1843-1848.
- <sup>27</sup> Brock, S. L.; Sanabria, M.; Urban, V.; Thiagarajan, P. Potter, D. I.; Suib, S. L. *J. Phys. Chem. B* **2001**, *105*, 5404-5410.
- <sup>28</sup> Silvester, E. Manceau, A.; Drits, V. A. *Am. Mineral.* **1997**, *82*, 962-978.
- <sup>29</sup> Gaillot, A.-C.; Drits, V. A.; Manceau, A.; Lanson, B. *Micropos. Mesopor. Mater.* **2007**, *98*, 267-282.
- <sup>30</sup> Fukuda, K.; Nakai, I.; Ebina, Y.; Tananka, M.; Mori, T. Sasaki, T. *J. Phys. Chem. B* **2006**, *110*, 17070-17075.
- <sup>31</sup> Saratovsky, I.; Wightman, P. G.; Pastén, P. A.; Gaillard, J.-F.; Poeppelmeier, K. R. *J. Am. Chem. Soc.* **2006**, *128*, 11188-11198.
- <sup>32</sup> Grangeon, S.; Lanson, B.; Miyata, N.; Tani, Y.; Manceau, A. *Am. Mineral.* **2010**, *95*, 1608-1616.
- <sup>33</sup> Ressler, T.; Brock, S. L.; Wong, J.; Suib, S. L. *J. Phys. Chem. B* **1999**, *103*, 6407-6420.
- <sup>34</sup> Polzer, F.; Kunz, D. A.; Breu, J.; Ballauff, M. *Chem. Mater.* **2010**, *22*, 2916-2922.
- <sup>35</sup> Sharma, G.; Ballauff, M. *Macromol. Rapid Commun.* **2004**, *25*, 547-557.
- <sup>36</sup> Plamper, F. A.; Schmalz, A.; Penott-Chang, E.; Drechsler, M.; Jusufi, A.; Ballauff, M.; Müller, A. H. E. *Macromolecules* **2007**, *40*, 5689-5697.
- <sup>37</sup> Qiu, J.; Charleux, B.; Matyjaszewski, K. *Prog. Polym. Sci.* **2001**, *26*, 2083-2134.
- <sup>38</sup> Sala, T.; Sargent, M. V. J. *J. Chem. Soc., Chem. Commun.* **1978**, 253-254.
- <sup>39</sup> Brock, S. L.; Sanabria, M.; Urban, V.; Thiagarajan, P. Potter, D. I.; Suib, S. L. *J. Phys. Chem. B* **1999**, *103*, 7416-7428.
- <sup>40</sup> McKenzie, R. M. *Mineral. Mag.* **1978**, *38*, 493-502.

- <sup>41</sup> Kim, S. H.; Kim, S. J.; Oh, S. M. *Chem. Mater.* **1999**, *11*, 557-563.
- <sup>42</sup> Villalobos, M.; Toner, B.; Bargar, J.; Sposito, G. *Geochim. Cosmochim. Acta* **2003**, *67*, 2649-2662.
- <sup>43</sup> Crassous, J. J.; Rochette, C. N.; Wittemann, A.; Schrinner, M.; Drechsler, M.; Ballauff, M. *Langmuir* **2009**, *25*, 7862-7871.
- <sup>44</sup> Erko, A.; Packe, I.; Hellwig, C.; Fieber-Erdmann, M.; Pawlitzki, O.; Veldkamp, M.; Gudat, W. *AIP Conference Proc.* **2000**, *521*, 415-418.
- <sup>45</sup> Erko, A.; Packe, I.; Gudat, W.; Abrosimov, N.; Firsov, A. *SPIE Rev.* **2000**, *4145*, 122-128.
- <sup>46</sup> Newville, M.; Livins, P.; Yacoby, Y.; Stern, E. A.; Rehr, J. J. *Phys. Rev. B* **1993**, *47*, 14126-14131.
- <sup>47</sup> Newville, M.; Livins, P.; Yacoby, Y.; Rehr, J. J.; Stern, E. A. *Jpn. J. Appl. Phys., Part 1* **1993**, *32*, 125-127.
- <sup>48</sup> Ravel, B.; Newville, M.; Cross, J. O.; Bouldin, C. E.; *Physica B* **1995**, *209*, 145-147.
- <sup>49</sup> Kelly, S. D., Hesterberg, D. and Ravel, B. *Analysis of soils and minerals using X-ray absorption spectroscopy. Methods of soil analysis, Part 5 -Mineralogical methods*. Ulery, A. L. and Drees, L. R., Eds., Soil Science Society of America: Madison, WI, 2008; pp 367-463.
- <sup>50</sup> Ravel, B.; Newville, M. *J. Synchrotron Radiat.* **2005**, *12*, 537-541.
- <sup>51</sup> Zabinsky, S. I.; Rehr, J. J.; Ankudinov, A.; Albers, R.; Eller, M. *J. Phys. Rev. B* **1995**, *52*, 2995-3009.
- <sup>52</sup> Schrinner, M.; Haupt, B.; Wittemann, A. *Chem. Eng. J.* **2008**, *144*, 138-144.
- <sup>53</sup> Grangeon, S.; Lanson, B.; Lanson, M.; Manceau, A. *Mineral. Mag.* **2008**, *72*, 1279-1291.
- <sup>54</sup> δ-MnO<sub>2</sub> is a synthetic analogous to the mineral vernadite.<sup>55</sup> According to Villalobos *et al.* δ-MnO<sub>2</sub> has the same local structure as randomly stacked “acid” birnessite. The only difference is the smaller crystallite size and the fewer number of stacked layers along the c-axis as compared to birnessite.<sup>42</sup>
- <sup>55</sup> Giovanelli, R. *Mineral. Deposita (Berl.)* **1980**, *15*, 251-253.
- <sup>56</sup> Breu, J.; Seidl, W.; Stoll, A. *Z. Anorg. Allg. Chem.* **2003**, *629*, 503-515.
- <sup>57</sup> Brunelli, M.; Lanzara, A.; Saini, N. L.; Bianconi, A.; Valletta, A.; Radaelli, P. G. *J. Supercond. Chem. B* **1997**, *10*, 315-317.
- <sup>58</sup> Belli, M.; Scafati, A.; Bianconi, A.; Mobilio, S.; Paladino, L. Reale, A.; Buratini, E. *Solid State Commun.* **1980**, *35*, 355-361.
- <sup>59</sup> Koningsberger, D. C.; Prins, R. *X-ray Absorption: Principles, Applications, Techniques of EXAFS, SEXAFS, and XANES*; Wiley: New York, 1988; pp XII, 673.
- <sup>60</sup> Manceau, A.; Combes, J. M. *Phys. Chem. Miner.* **1988**, *15*, 283-295.
- <sup>61</sup> Manceau, A.; Gorshkov, A. I.; Drits, V. A. *Am. Mineral.* **1992**, *77*, 1133-1143.
- <sup>62</sup> Villalobos, M.; Toner, B.; Bargar, J.; Sposito, G. *Geochim. Cosmochim. Acta* **2003**, *67*, 2649-2662.

## References

---

- <sup>63</sup> Yang, D. S.; Wang, M. K. *Chem. Mater.* **2001**, *13*, 2589-2594.
- <sup>64</sup> Ma, Y.; Luo, J.; Suib, S. L. *Chem. Mater.* **1999**, *11*, 1972-1979.
- <sup>65</sup> Glover, D.; Schumm, B., Jr.; Kozowa, A. Handbook of Manganese Dioxide, Battery Grade; International Battery Materials, 1989; pp 25-32.
- <sup>66</sup> Manceau, A.; Gorshkov, A. I.; Drits, V. A. *Am. Mineral.* **1992**, *77*, 1144-1157.
- <sup>67</sup> Manceau, A.; Gorshkov, A. I.; Drits, V. A. *Phys. Chem. Miner.* **1988**, *15*, 283-295.
- <sup>68</sup> Lee, P. A.; Pendry, J. B.; *Phys. Rev. B* **1975**, *11*, 2795-2811.
- <sup>69</sup> Teo, B.-K. *J. Am. Chem. Soc.* **1981**, *103*, 3990-4001.
- <sup>70</sup> Rechav, B.; Sicron, N.; Yacoby, Y.; Ravel, B.; Newville, M.; Stern, E. A. *Physica C* **1993**, *209*, 55-58.
- <sup>71</sup> Krappe, H. J.; Rossner, H. H. *Phys. Scr.* **2009**, *79*, 048302.
- <sup>72</sup> E. A. Stern, *Theory of EXAFS in X-Ray Absorption*. Koningsberger, D. C. and Prins, R. Eds., Wiley, New York, 1988, p. 3-52



*References*

---

## **5. Oxidation of an Organic Dye Catalyzed by MnO<sub>x</sub> Nanoparticles**

*Frank Polzer,<sup>†</sup> Stefanie Wunder,<sup>†</sup> Yan Lu,<sup>†</sup> Matthias Ballauff<sup>†\*</sup>*

<sup>†</sup>Helmholtz-Zentrum Berlin für Materialien und Energie GmbH, Hahn-Meitner-Platz 1,  
14109 Berlin, Germany, and Department of Physics, Humboldt University Berlin, Newtonstr.  
15, 12489 Berlin, Germany

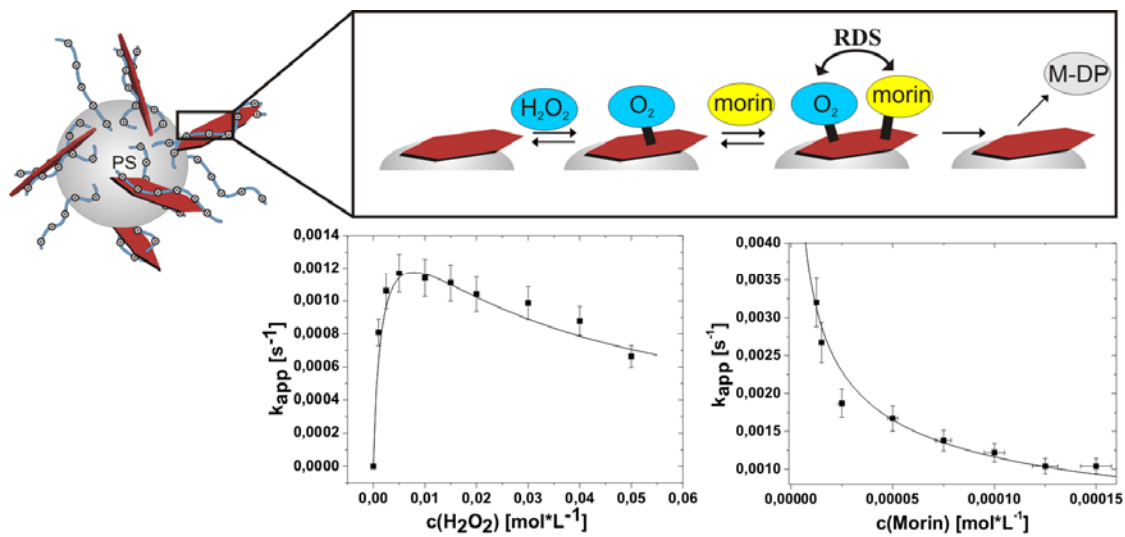
Email: [Matthias.Ballauff@helmholtz-berlin.de](mailto:Matthias.Ballauff@helmholtz-berlin.de)

**Accepted by the Journal of Catalysis**

Reproduced with permission from  
*Journal of Catalysis, 2012*  
© 2012 Elsevier.

**DOI:** <http://dx.doi.org/10.1016/j.jcat.2012.01.016>

## 5.1. Abstract



We present a study on the catalytic oxidation of the organic dye morin by hydrogen peroxide in the presence of manganese oxide nanoparticles in aqueous solution. The ultrathin manganese oxide nanoparticles consist of c\*-disordered potassium birnessite and are immobilized on spherical polyelectrolyte brushes. The catalytic activity of these composite particles was investigated using the oxidation of morin by hydrogen peroxide as a model reaction. The oxidative degradation of morin was followed by UV/vis spectroscopy leading to an apparent rate constant  $k_{app}$ . We propose a modeling of the results in terms of a Langmuir-Hinshelwood model.  $k_{app}$  can be related to the kinetic constant  $k$  and to the apparent adsorption constants of H<sub>2</sub>O<sub>2</sub> and morin. Based on this model, the dependence of  $k_{app}$  on temperature can be traced back to the activation energy of the rate constant  $k$  and the adsorption enthalpies of both educts on the surface of the nanoparticles.

## 5.2. Introduction

In the last decade, manganese oxide nanostructures have become systems of particular interest as catalysts for oxidation reactions.<sup>1,2,3,4,5</sup> There is a wide variety of polymorphs of Mn(IV) oxides such as  $\alpha$ -,  $\beta$ -,  $\gamma$ - and  $\delta$ -type MnO<sub>2</sub> that differ in their respective linkage of the basic structure, the [MnO<sub>6</sub>] octahedron.<sup>6</sup> In general, manganese oxide nanoparticles (MnO<sub>x</sub>NP) are good catalysts for the catalytic decomposition of hydrogen peroxide (H<sub>2</sub>O<sub>2</sub>).<sup>7,8,9</sup> For layered manganese oxides, the total surface can be increased by exfoliation which leads to an enhanced catalytic activity.<sup>10,11</sup> However, only a few synthetic routes are known by now which create delaminated or highly exfoliated birnessite nanoparticles, most of them being multi-step approaches.<sup>12,13,14</sup> Since nanoparticles are mostly generated by solution-based methods, aggregation may occur under the conditions of catalytic reactions. This process may lead to a marked decrease of the catalytic activity with time.

Recently, we presented a new and facile room temperature method to generate and stabilize nanometer scale layered MnO<sub>x</sub>NP onto cationic spherical polyelectrolyte brushes (SPB).<sup>15</sup> Figure 1 displays the schematic representation of the composite particles MnO<sub>x</sub>NP@SPB with a corresponding cryogenic transmission electron microscopy (cryoTEM) micrograph. The SPB consist of a solid polystyrene (PS) core onto which cationic polyelectrolyte chains are densely grafted.<sup>16</sup> By adding potassium permanganate to an cationic SPB at room temperature MnO<sub>x</sub>NP are formed directly on the carrier particles. The reduction of KMnO<sub>4</sub> leads to platelets of birnessite that are affixed to the core particles by interaction with the cationic chains. This fixation prevents the coagulation or coarsening of the nanoparticles in an effective way.<sup>16</sup> The composite particles that consist of the SPB together with the immobilized MnO<sub>x</sub>NP exhibit an excellent colloidal stability.<sup>15</sup>

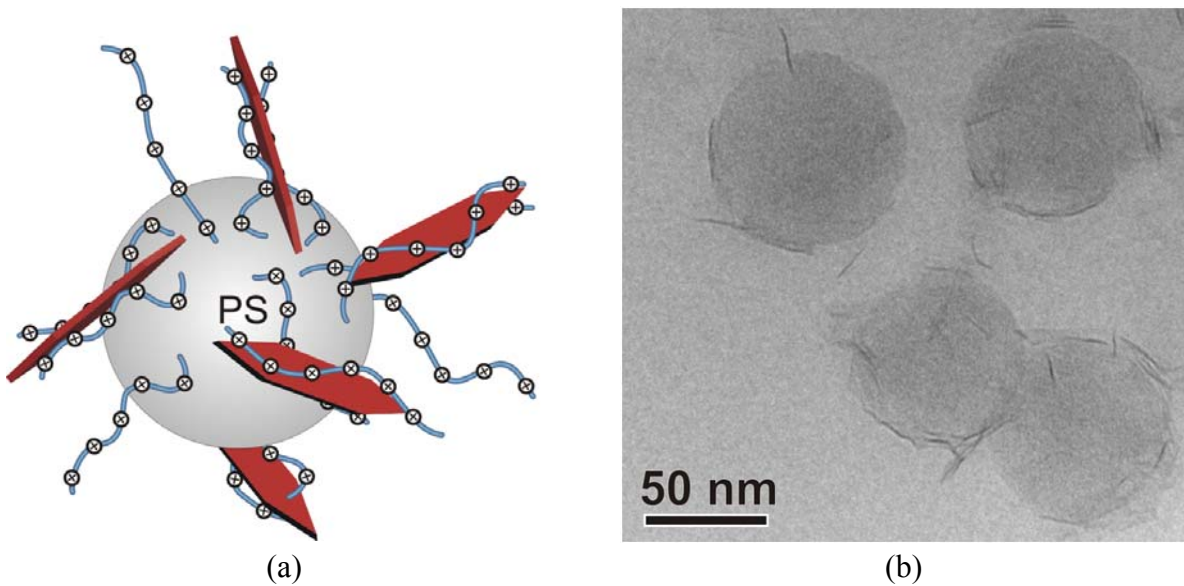


**Figure 5.2.1.** (a) Scheme of the composite material consisting of cationic spherical polyelectrolyte brushes with brush monomer 2-trimethylammonium ethyl methacrylate chloride and birnessite nanoparticles ( $\text{MnO}_x\text{NP}@\text{SPB}$ ) used in the catalytic studies. The negatively charged birnessite nanoparticles are bound to SPB carrier particles by the cationic polyelectrolyte chains. (b) CryoTEM image of the composite material  $\text{MnO}_x\text{NP}@\text{SPB}$ . Thin plate like birnessite particles are bound to the core particles. The polyelectrolyte chains are not visible because of their low contrast (see Ref. 15).

Here we present a study of the catalytic activity of  $\text{MnO}_x\text{NP}@\text{SPB}$ .<sup>15</sup> The oxidation of morin with  $\text{H}_2\text{O}_2$  was chosen as a model reaction to analyze the mechanism of the catalysis in presence of  $\text{MnO}_x\text{NP}@\text{SPB}$ . Morin belongs to a group of flavonoid plant dyes (see Figure 5.2.2).<sup>17</sup>

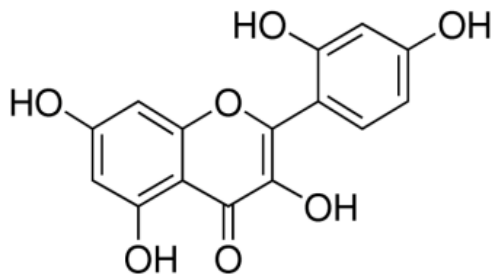


**Figure 5.2.2.** Structure of 2',3,4',5,7-pentahydroxyflavone (morin) which belongs to the group of flavonoid plant dyes. The oxidation of this polyphenolic dye is a benchmark reaction for the catalytic activity of bleach catalysts.

These polyphenolic dyes are present in tea, fruits and vegetables and can be used as model compounds for studying bleaching processes in laundry detergents.<sup>18</sup> Previous work has demonstrated that the oxidation of dyes by hydrogen peroxide is catalyzed by manganese oxide. Moreover, clear evidence was found that this oxidation is related to the surface of the

particles. For example, Segal *et al.* demonstrated that cyanine dyes can be decomposed using well-defined manganese oxide catalysts and concluded that the reaction takes place on the surface of the particles.<sup>19</sup> Gemeay *et al.* studied the oxidative decolorization of organic dyes on polyaniline/MnO<sub>2</sub> composites.<sup>20</sup> During this study, evidence for the competing adsorption of both the dye and H<sub>2</sub>O<sub>2</sub> on the surface of the catalyst was given. This was argued from the fact the rate constant goes through a distinct maximum as the function of the concentration of H<sub>2</sub>O<sub>2</sub> while it decreases with increasing concentration of the dye. Zhang *et al.* analyzed the oxidation of methylene blue with H<sub>2</sub>O<sub>2</sub> on β-MnO<sub>2</sub> nanorods<sup>21</sup> and concluded that methylene blue and H<sub>2</sub>O<sub>2</sub> adsorb onto the manganese oxide surface, where the reaction takes place. It is also interesting to note that the heterogeneous epoxidation of various alkenes with H<sub>2</sub>O<sub>2</sub> in presence of manganese oxides studied by Qi *et al.* is surface-controlled as well.<sup>22</sup> Here a reaction mechanism which involves a surface bound Mn<sup>2+</sup> was proposed. Up to now, however, a full kinetic study of the oxidation of a dye on manganese oxide is still missing.

The present investigation gives a full kinetic study of the decomposition of a dye in presence of MnO<sub>x</sub>-nanoparticles. Since the composite particle MnO<sub>x</sub>NP@SPB exhibit an excellent colloidal stability, a precise analysis of their catalytic activity in solution can be done. No problems as e.g. coagulation or coarsening which would lead to a much smaller active surface are hampering the analysis. Hence, the influence of the surface on the kinetics can be studied quantitatively. Moreover, all results will be compared to recent studies on the catalytic activity of manganese ions in aqueous solution. Fehler! Textmarke nicht definiert.<sup>23,24,25</sup> The kinetic study presented here will also provide a firm basis for future technical application of these systems in detergent formulations.

### 5.3. Experimental Section

**Materials:** All chemicals were of analytical grade and used without further purification. 2-trimethylammonium ethyl methacrylate chloride (TMAEMC) was received from Polysciences. KMnO<sub>4</sub>, Na<sub>2</sub>CO<sub>3</sub> and NaHCO<sub>3</sub> were purchased by Fluka and H<sub>2</sub>O<sub>2</sub> and morin hydrate were received from Sigma-Aldrich. The boric acid buffer solution was purchased from Carl Roth. The water used here was 18 MΩ Millipore water.

**Synthesis of MnO<sub>x</sub>NP immobilized on SPB.** The cationic SPB TMAEMC-40 was synthesized and characterized as described recently.<sup>26</sup> The synthesis of the composite particles was conducted as described in previous work.<sup>15</sup> The dispersion of SPB was diluted with water to give a solid content of about 1 wt %. Afterwards, 20 mL of a 0.04 molar solution of KMnO<sub>4</sub> were injected and the solution was stirred for 12 hours. The composite particles were cleaned with water by ultrafiltration against pure water until the conductivity of the serum reached a value of lower than 3 μS·cm<sup>-1</sup>. The overall amount of quaternized ammonium groups in the polyelectrolyte shell and the core-to-shell mass ratio were determined as 6.6 to 1 by conductivity titration. The composite particles were analyzed by inductively-coupled plasma optical emission spectroscopy (ICP-OES; Varian Vista-Pro Radial) for their

manganese content. Additionally, transmission electron microscopy (TEM) and cryogenic TEM ( Zeiss LEO 922, Zeiss NTS GmbH, Oberkochen, Germany) and powder X-ray diffraction (PXRD; Panalytical XPERT-PRO) were used for characterization. CryoTEM samples were prepared as described recently.<sup>27</sup>

**Catalysis.** All catalytic runs were performed in 3 mL optical quartz cells (Hellma). The reactions were carried out in a carbonate buffer system of sodium bicarbonate ( $\text{NaHCO}_3$ ) and sodium carbonate ( $\text{Na}_2\text{CO}_3$ ) which was adjusted by the addition of hydrochloric acid to pH 10. In order to investigate a possible influence of this buffer onto the reaction, a set of experiments was done using a borate buffer. A freshly prepared 0.4 mM morin solution was diluted with buffer to result in morin solutions with concentrations between 0.01 to 0.15 mM for all experiments. Then the desired amount of catalyst solution with a solid content of 0.1 wt % was added. In the following, the catalyst concentration is always related to the Mn content since the manganese oxide is the active species. The solution in the reference cell contained the same concentration of catalyst to subtract its weak but noticeable UV/vis-absorption. At last the required amount of  $\text{H}_2\text{O}_2$  solution was added to start the catalytic oxidation of morin. The mixture was instantaneously filled into the optical cell and the measurement was started. All solutions were kept at a given temperature before mixing. The measurements were carried out with a Lambda 650 (PerkinElmer) UV/vis spectrometer at a fixed wavelength of 410 nm, which is the absorption maximum of morin at pH 10.

## 5.4. Results and Discussion

### Synthesis of $\text{MnO}_x\text{NP}@\text{SPB}$

The synthesis and characterization of the colloidal carrier particles has been described in detail in earlier work.<sup>15</sup> TEM and dynamic light scattering analysis gave a PS core radius of  $42.7 \pm 0.3$  nm and an average thickness of the polyelectrolyte shell of  $42.0 \pm 0.8$  nm. After the addition of  $\text{KMnO}_4$  solution to the aqueous dispersion of the cationic SPB, the onset of nanoparticle formation could directly be followed by a change in the color from purple to brown due to  $\text{OH}^-$  catalyzed reduction of the  $\text{MnO}_4^-$  ions confined in the brush layer. No further reducing agent needs to be added for this reaction. The total amount of manganese in the composite particles determined by ICP-OES gave a value of 3.85 wt % for the sample used here. CryoTEM micrographs revealed an average length of 20 nm and a width of about 1.6 nm of the  $\text{MnO}_x\text{NP}$  platelets immobilized on SPB. PXRD measurements show a c\*-disordered  $\text{K}^+$ -birnessite modification of the nanoparticles.<sup>15</sup>

### Catalysis.

Previous work has demonstrated that the SPBs present an ideal carrier system inasmuch as they present no diffusion barrier for reactants that need to diffuse to the nanoparticles located inside the brush layer.<sup>28</sup> Moreover, the suspensions of these hybrid particles can be purified from soluble species in the aqueous phase by prolonged ultrafiltration.<sup>28</sup> As in previous

studies, only initial reaction rates were used for the kinetic analysis.<sup>28</sup> Given these prerequisites, the apparent rate constant  $k_{app}$  is:

$$\frac{d[\text{Morin}]}{dt} = -k_1 \cdot [\text{Morin}] \cdot [\text{H}_2\text{O}_2] = -k_{app} \cdot [\text{Morin}] \quad (5.4.1)$$

The pH was kept constant at pH 10 during the reactions using a carbonate buffer because the absorbance of morin depends on the pH. The pKa values of morin are 3.5 and 8.1.<sup>29</sup> The oxidation of morin is increasing with the pH due to the higher deprotonation of morin.<sup>17, 30</sup> Moreover, the pH will influence the decomposition rate of H<sub>2</sub>O<sub>2</sub>.<sup>31</sup> The use of a basic buffer system was necessary because MnO<sub>x</sub>NP may dissolve under acidic conditions. The leaching of MnO<sub>2</sub> at pH values higher than 9 were found to be around 1 ppb only which means that any interference of the catalytic study with manganese ions in solution can be neglected<sup>9</sup> and any interference of the catalytic study with manganese ions in solution can be neglected.

The oxidation of morin can be monitored by measuring the time resolved absorbance at 410 nm by UV/vis spectroscopy. Without any catalyst, the oxidative degradation of morin with H<sub>2</sub>O<sub>2</sub> in the carbonate buffer does not proceed in the time frame of the experiments. The corresponding spectra can be found in Figure S5.1 in the supporting information. Figure 5.4.1 shows the characteristic decrease of the absorption maximum of morin at 410 nm. In the course of the oxidation reaction a new peak at 321 nm appears which is increasing with time. The isosbestic points in Figure 5.4.1 at 361 nm and 286 nm clearly show that only a single reaction product is formed and that for a rather short time ( $t < 12\text{min}$ ) morin is oxidized without any side products. After a longer time, the isosbestic points vanish and the peak at 321 nm is decreasing again. This finding points to a secondary reaction, most probably a further oxidation of the products. However, since we use only the initial rates for the kinetic analysis, this later stage of the reaction is of no concern and we only look into the early stage where morin is oxidized to a single species. The peak at 321 nm has been assigned to an intermediate product, a substituted benzofuranone which decomposes further to 2,4 dihydroxy benzoic acid and 2,4,6 trihydroxy benzoic acid.<sup>32,33</sup> This reaction pathway is quite similar to the one of quercetin which differs with regard to only the position of one OH group. Oxidation of quercetin leads to the formation of 2,3 dihydroxy benzoic acid and 2,4,6 trihydroxy benzoic acid.<sup>34</sup> Similar findings were reported recently by Rothbart *et al.* who studied the catalytic activity of manganese complexes in solution.<sup>25</sup> Here it was shown that the oxidation of morin with H<sub>2</sub>O<sub>2</sub> in carbonate buffer solution leads to an increase of the peak at 321 nm in the beginning. After a few minutes the peak decreases again. In this case isosbestic points were visible for the first 5 spectra of the oxidation. Without any catalyst, the oxidative degradation of morin with H<sub>2</sub>O<sub>2</sub> in the carbonate buffer does not proceed in the time frame of the experiments. The corresponding spectra can be found in Figure S5.1 in the supporting information.

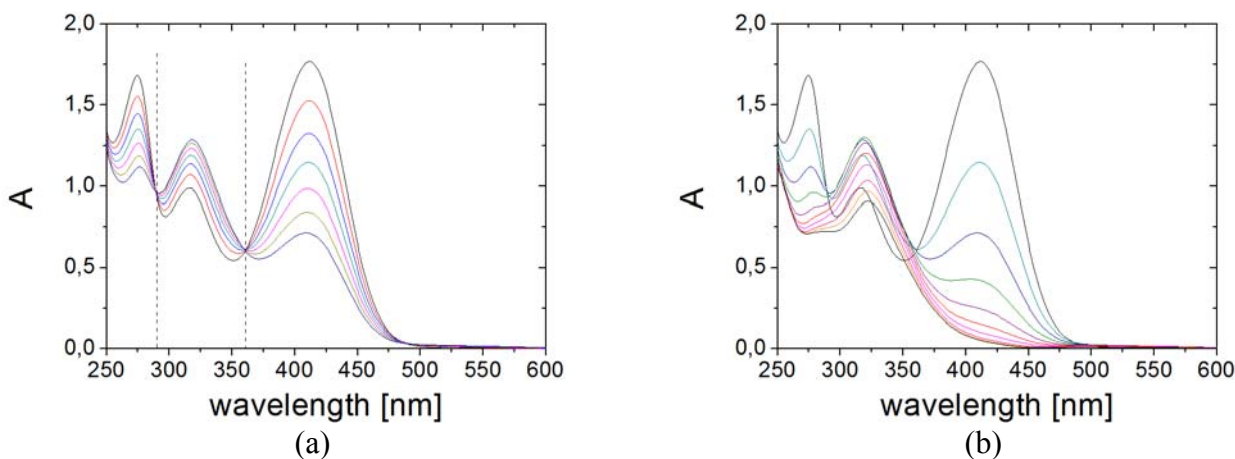


**Figure 5.4.1.** UV/vis spectra of a 0.1 mM morin solution in 50 mM carbonate buffer solution at pH 10 with a concentration of 10 mM  $\text{H}_2\text{O}_2$ . The spectrum shows a decrease of the characteristic absorption maximum at 410 nm of morin with time due to the decomposition of the polyphenolic dye by catalytic oxidation. The spectrum on the left hand side shows the reaction in the initial stage (spectra every two minutes). The isosbestic points are marked with dashed lines. On the right hand side the reaction is shown over a period of one hour with spectra taken every 6 minutes.

Topalovic and co-workers have also measured the increasing peak at 321 nm in their mechanistic study on morin oxidation with manganese 1,4,7-trimethyl-1,4,7-triazacyclononane complexes by air oxygen from air.<sup>23</sup> We also found that morin undergoes slow decomposition in aqueous solutions at pH 10 in presence of  $\text{MnO}_x@\text{SPB}$  if oxygen is present (see Figure S5.2). Under this condition, the peak at 321 nm is steadily increasing. To exclude the role of air oxygen experiments were conducted after all solutions were purged with nitrogen to exclude oxygen. No difference in the reaction rate was found by using the purged solutions. This suggested that the oxidation by air is not relevant in presence of  $\text{H}_2\text{O}_2$ .

The relative decrease of the adsorption  $A$  of morin at 410 nm could be used best to determine the kinetics of the reaction since it gives a direct measure for the decrease of the morin concentration. Typical kinetic runs showing the relative adsorption  $A/A_0$  as the function of reaction time are given in Figure 5.4.2a. The reaction immediately starts after addition of the  $\text{MnO}_x\text{NP}$  and the normalized absorption follows a linear decrease which can be well described with a first order rate law as shown in Eq. (5.4.1). The initial rate was taken from the slopes of these curves at  $t=0$ .

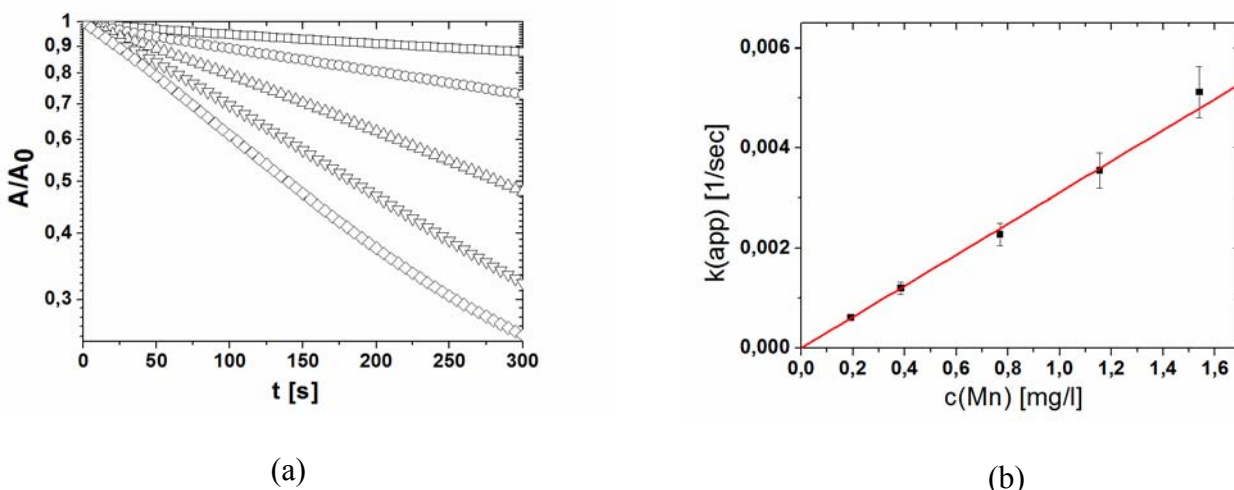


**Figure 5.4.2.** Kinetics of the oxidation of morin. (a). Relative absorption  $A/A_0$  recorded at 410 nm as the function of the reaction time. The parameters of the runs are: 0.1 mM morin solution in 10 mM carbonate buffer solution at pH 10; concentration of  $\text{H}_2\text{O}_2$ : 10 mM. The concentrations of the catalyst are:  $\square$  0.019 mg·L<sup>-1</sup>,  $\circ$  0.039 mg·L<sup>-1</sup>,  $\triangle$  0.077 mg·L<sup>-1</sup>,  $\nabla$  0.116 mg·L<sup>-1</sup> and  $\diamond$  0.154 mg·L<sup>-1</sup>. (b) Influence of the concentration of catalyst on the apparent rate constant  $k_{app}$  of the oxidation of morin with  $\text{H}_2\text{O}_2$  taken from 5.4.2a in 12.5 mM carbonate buffer.

The apparent rate constant is proportional to the amount of MnO<sub>x</sub>NP in the system as shown in Figure 5.4.2b. Here the apparent reaction rate  $k_{app}$  obtained from Figure 5.4.2a is plotted against the amount of catalyst present in the system. A strictly linear relation is found. Since leaching of Mn-species can be ruled out with the present experimental protocol, this finding is a clear indication for the involvement of the surface of the MnO<sub>x</sub>-nanoparticles in the rate-determining step.

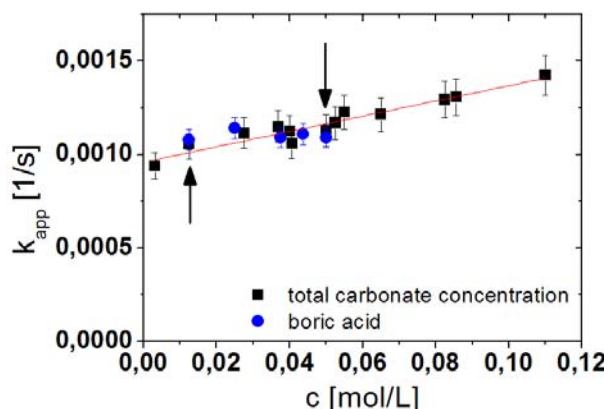


**Figure 5.4.3.** Dependence of the buffer concentration on the rate constant at 20°C for two carbonate buffer concentrations (black squares) and boric acid buffer (blue dots). The concentration of morin is 0.1 mM at pH 10 with a concentration of  $\text{H}_2\text{O}_2$  = 10 mM and a concentration of Mn in the MnO<sub>x</sub>NP = 0.39 mg·L<sup>-1</sup>. The arrows mark the carbonate concentrations used in the mechanistic study.

Before considering this point in more detail, it is necessary to discuss first the influence of the carbonate ions used as a buffer in the solution. Rothbart *et al.* found that there is a second order dependence of the rate on the concentration of hydrogen carbonate if a soluble manganese complex is used as catalyst.<sup>25</sup> This second order dependence on the bicarbonate concentration was explained by a) a complexation of the manganese salt and b) by formation of peroxocarbonate. This peroxocarbonate ion is more active than H<sub>2</sub>O<sub>2</sub> and therefore the reaction rate is accelerated.<sup>24,25</sup> The hydrogen carbonate can form a peroxocarbonate with H<sub>2</sub>O<sub>2</sub> in an equilibrium reaction and the optimal pH for this formation was approximately 8.5. Figure 5.4.3 demonstrates that there is a small increase of  $k_{app}$  with the total carbonate concentration but much less pronounced than found by Rothbart *et al.* for the manganese complexes. Moreover, a use of a boric acid buffer system led to apparent rate constants in the same range. We iterate that no reaction takes place if the catalyst is not present, that is, the presence of the carbonate ions does not suffice (Figure S5.1). Given these results we conclude that any influence of the concentration of carbonate ions onto the rate-determining step may be ruled out. The residual dependence seen in Figure 5.4.3 may well be traced back to a finite influence of the ionic strength on the catalytic activity of the MnO<sub>x</sub>NP.

Thus, we conclude that the rate-determining step of the oxidation takes place on the surface of the MnO<sub>x</sub>NP. In order to elucidate this point in further detail, two different sets of measurements have been conducted. First,  $k_{app}$  was measured for a constant concentration of H<sub>2</sub>O<sub>2</sub> while varying the concentration of morin. In a second set of measurements the concentration of morin was varied while the concentration of H<sub>2</sub>O<sub>2</sub> was kept constant. Furthermore, all measurements have been repeated at four different temperatures in order to study the activation energy of the rate-determining step. The results of the two sets of measurements are shown in Figure 5.4.4. There are two significant findings: First, the apparent reaction constant  $k_{app}$  decreases slightly for increasing concentration of morin. Secondly,  $k_{app}$  goes through a pronounced maximum for an increase of the concentration of H<sub>2</sub>O<sub>2</sub> at a constant concentration of morin. It is interesting to note that similar findings have already been reported by Gemeay *et al.* without quantitative analysis.<sup>20</sup> Evidently, the reaction cannot be controlled by the diffusion of the two reactants to the nanoparticle surface. This would lead to a monotonous increase of  $k_{app}$  with the concentration of the respective reactant.

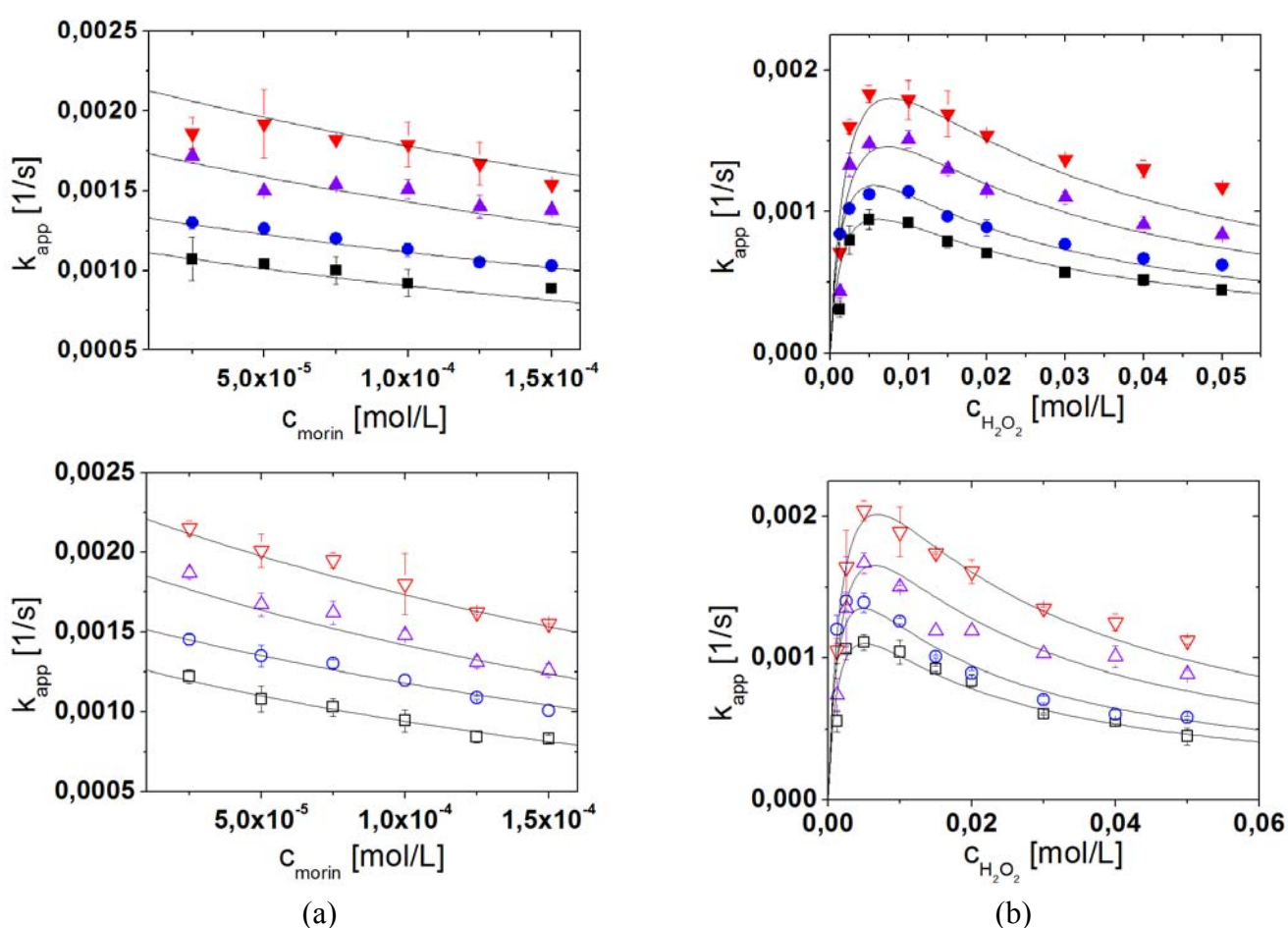


**Figure 5.4.4.** Analysis of the kinetic data of the catalytic oxidation of morin in terms of the Langmuir-Hinshelwood model. (a) Influence of the concentration of morin on the apparent rate constant  $k_{\text{app}}$  with  $c(\text{H}_2\text{O}_2) = 10 \text{ mM}$  (closed symbols) and  $5 \text{ mM}$  (open symbols), and  $c(\text{Mn}) = 0.39 \text{ mg} \cdot \text{L}^{-1}$  at four different temperatures at pH 10. (b) Influence of the concentration of  $\text{H}_2\text{O}_2$  on the apparent rate constant  $k_{\text{app}}$  of the catalytic oxidation of morin with  $c(\text{morin}) = 0.1 \text{ mM}$  (closed symbols) and  $0.05 \text{ mM}$  (open symbols), and  $c(\text{Mn}) = 0.39 \text{ mg} \cdot \text{L}^{-1}$  at four different temperatures at pH 10. The concentration of the carbonate buffer was  $50 \text{ mM}$ . The lines mark the fits by the Langmuir-Hinshelwood model. The temperatures were as following: black squares  $15^\circ\text{C}$ ; blue circles  $20^\circ\text{C}$ ; purple up triangles  $25^\circ\text{C}$  and red down triangles  $30^\circ\text{C}$ .

Based on these observations, we propose a description of the decomposition of morin by  $\text{H}_2\text{O}_2$  in terms of a Langmuir-Hinshelwood (LH) approach, that is, both reactants must be adsorbed on the surface in order to react.<sup>35,36</sup> A schematic representation of this mechanism is shown in Figure 5.4.5: First,  $\text{H}_2\text{O}_2$  molecules adsorb on the surface of the  $\text{MnO}_x\text{NP}$ . Subsequently, a surface-bound peroxy-species is generated and a water molecule is released in the reaction medium.<sup>37</sup> As discussed recently by Do *et al.*, the interaction of  $\text{H}_2\text{O}_2$  with the surface of the  $\text{MnO}_2$ -particles is a complicated many-step process.<sup>9</sup> Modeling these processes by a single adsorption step may present an approximation that is validated mainly by the

subsequent analysis. Concomitantly, morin molecules adsorb on free sites. This process can certainly be modeled by a simple Langmuir isotherm. The rate-determining step is the reaction of the adsorbed morin molecules with the active oxygen species on the surface.

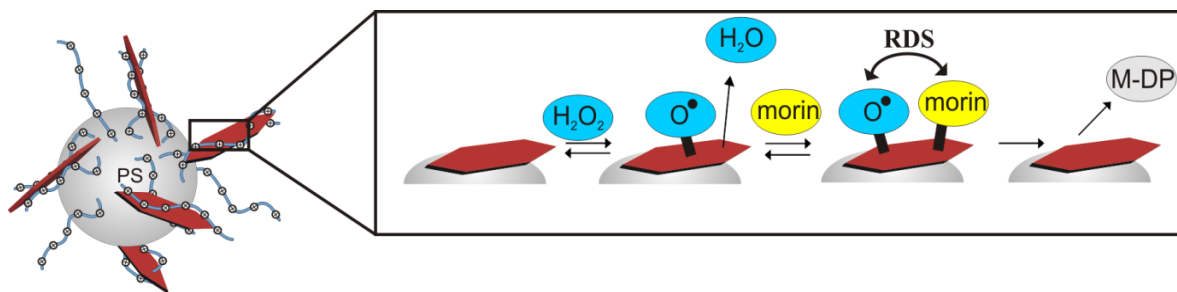


**Figure 5.4.5.** Mechanistic model of the oxidation of morin by  $\text{H}_2\text{O}_2$  in the presence of  $\text{MnOxNP}$  (red hexagons) according to a Langmuir-Hinshelwood model for a bimolecular surface reaction. The nanoparticles are immobilized into the brush layer of cationic SPB. The  $\text{H}_2\text{O}_2$  reacts on the surface leading to adsorbed active species and to a water molecule that is released. Concomitantly, morin molecules adsorb onto the nanoparticle surface and undergo a surface reaction with the active oxygen species. This is the rate determining step of the overall catalytic cycle. Finally, the decomposition product of morin (M-DP) desorbs from the catalyst surface, leaving a free active site for a new catalytic reaction.

In order to keep the analysis as general as possible, a Langmuir-Freundlich isotherm is used for modeling the adsorption of both reactants:<sup>38</sup>

$$\theta_i = \frac{(K_i c_i)^{n_i}}{1 + \sum_{j=1}^N (K_j c_j)^{n_j}} \quad (5.4.2)$$

$\theta_i$  represents the surface coverage of the compound  $i$ ,  $K_i$  is the corresponding adsorption constant and  $c_i$  the concentration of the respective compound in solution. The Langmuir-Freundlich isotherm takes surface heterogeneity into account.<sup>38,39</sup> Hence, the reaction rate is given by

$$-\frac{dc_{\text{morin}}}{dt} = \frac{kS(K_{\text{morin}}c_{\text{morin}})^n(K_{\text{H}_2\text{O}_2}c_{\text{H}_2\text{O}_2})^m}{(1 + (K_{\text{morin}}c_{\text{morin}})^n + (K_{\text{H}_2\text{O}_2}c_{\text{H}_2\text{O}_2})^m)^2} = k_{\text{app}}c_{\text{morin}} \quad (5.4.3)$$

Thus,

$$k_{\text{app}} = \frac{kS \cdot K_{\text{morin}}^n c_{\text{morin}}^{n-1} (K_{\text{H}_2\text{O}_2} c_{\text{H}_2\text{O}_2})^m}{(1 + (K_{\text{morin}} c_{\text{morin}})^n + (K_{\text{H}_2\text{O}_2} c_{\text{H}_2\text{O}_2})^m)^2} \quad (5.4.4)$$

where  $k$  is the molar rate constant per unit square of the catalyst and  $K_{\text{morin}}$  and  $K_{\text{H}_2\text{O}_2}$  are the adsorption constants of the two reactants. The parameters  $n$  and  $m$  are the Freundlich exponents for morin and  $\text{H}_2\text{O}_2$ , respectively. Eq. (5.4.4) contains the product  $S$  and  $k$ . Because of the non-regular shape of the  $\text{MnO}_x$  nanoparticles immobilized on SPB the total surface of nanoparticles cannot be determined precisely by microscopic methods like TEM. Thus, the product  $k^*S$  is used in further analysis. However, the precise proportionality between  $S$  and

$k_{app}$  has already been established with the data displayed in Figure 5.4.2b. The solid lines in Figure 5.4.4 show the best fit to the data obtained by UV/vis measurements using eq. (5.4.4). Both sets of data can be fitted with the same set of parameters. All parameters obtained from this fit are summarized in Table 5.1.

**Table 5.1: Summary of the Rate Constants and Adsorption Constants obtained by Best Fit Model according to Eq. (5.4.4) for the 50 mM carbonate buffer solution**

Temperature [°C]	$k \cdot S^a$ [mol·m <sup>2</sup> ·L <sup>-2</sup> ·s <sup>-1</sup> ]	$K_{\text{morin}}^b$ [L·mol <sup>-1</sup> ]	$K_{\text{H}_2\text{O}_2}^c$ [L·mol <sup>-1</sup> ]	$n^d$	$m^d$
15	$(1.36 \pm 0.26) \cdot 10^{-6}$	$3866 \pm$ 1157	$242 \pm$ 20	$1 \pm 0.04$	$0.87 \pm$ 0.03
20	$(1.86 \pm 0.41) \cdot 10^{-6}$	$3434 \pm$ 1174	$255 \pm$ 24	$1 \pm 0.04$	$0.86 \pm$ 0.02
25	$(2.48 \pm 0.82) \cdot 10^{-6}$	$3145 \pm 1623$	$175 \pm$ 18	$1 \pm 0.07$	$0.90 \pm$ 0.04
30	$(3.48 \pm 1.34) \cdot 10^{-6}$	$2631 \pm$ 1529	$165 \pm$ 17	$1 \pm 0.07$	$0.86 \pm$ 0.04

<sup>a</sup>  $k$ : rate constant.  $S$ : surface area <sup>b</sup>  $K_{\text{morin}}$ : adsorption constant of morin. <sup>c</sup>  $K_{\text{H}_2\text{O}_2}$ : adsorption constant of H<sub>2</sub>O<sub>2</sub>. <sup>d</sup>  $n, m$ : Freundlich exponents (see eq. (5.4.4))

The dependence of  $k_{app}$  on the concentration of both reactants morin and H<sub>2</sub>O<sub>2</sub> can be explained as follows: Since morin has a significantly higher adsorption constant than H<sub>2</sub>O<sub>2</sub> even small concentrations of morin in solution, lead to a predominant surface coverage of the nanoparticles by morin molecules. Active sites for H<sub>2</sub>O<sub>2</sub> molecules are blocked by morin so that the surface reaction, which is the rate determining step, is hindered. If the concentration of morin is decreased, the probability for the adsorption of H<sub>2</sub>O<sub>2</sub> molecules increases and the surface reaction can take place more frequently. The dependence of  $k_{app}$  on the concentration of H<sub>2</sub>O<sub>2</sub> at a constant concentration of morin can be explained in the same way. The reaction rate reaches its maximum with increasing H<sub>2</sub>O<sub>2</sub> concentration until most of the free sites of the surface are blocked.

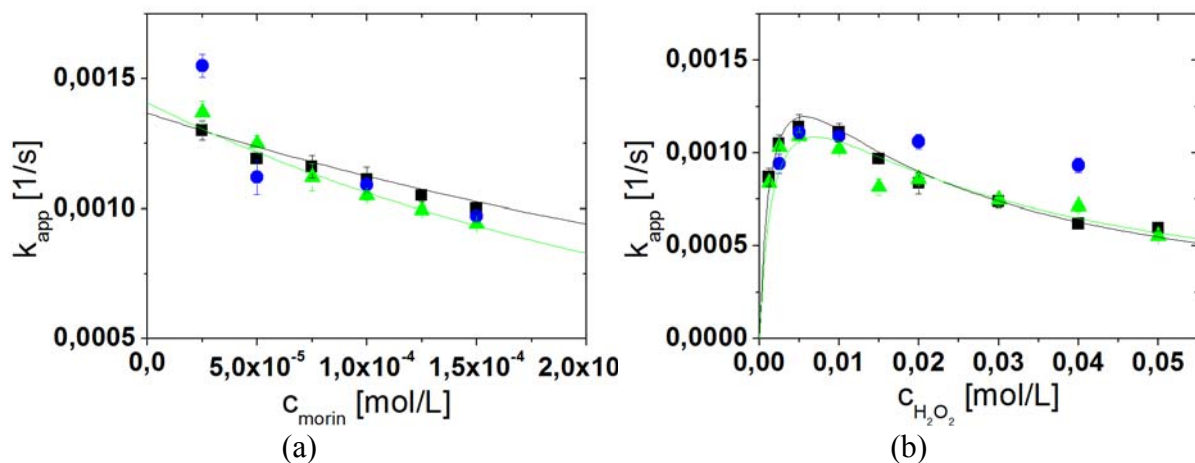


**Figure 5.4.6.** Analysis of the apparent rate constant  $k_{app}$  measured at different buffer solutions at 20 °C. Dependence of the rate constant on (a) the morin concentration at 10 mM  $\text{H}_2\text{O}_2$  and (b) the  $\text{H}_2\text{O}_2$  concentration at 0.1 mM morin. Black squares: 50 mM carbonate buffer, green triangles: 12.5 mM carbonate, blue dots: 50 mM boric acid buffer solution. The lines are the fits of the data by the Langmuir-Hinshelwood model eq. (5.4.4).

The data presented in this work could be fitted best with two independent Freundlich exponents  $n = 1$  for morin as expected and  $m = 0.87$  for  $\text{H}_2\text{O}_2$ . The latter value may be explained by surface heterogeneities.<sup>39</sup> Similar findings have been reported for other nanometric systems as e.g. for single gold nanoparticles by Zhou and co-workers<sup>40</sup> and for the case of metal nanoparticles.<sup>36</sup> The birnessite nanoparticles used here is a layered  $\text{MnO}_x$  material with a number of defects. It is composed of  $[\text{MnO}_6]$ -octahedrons which are predominantly linked via edge sharing but also contains interlayer vacancies and corner shared  $[\text{MnO}_6]$  units.<sup>41,42</sup> Hence, heterogeneities of the adsorption sites must be expected. We reiterate, however, that treating the interaction of  $\text{H}_2\text{O}_2$  with the surface of the  $\text{MnO}_x$  particles presents an approximation and caution must be exercised when interpreting the exponent  $m$ .

In order to exclude the influence of the buffer concentration on the LH approach, measurements at 20°C were performed as shown in Figure 5.4.6. Within the given limits of error, the data obtained for different buffers and different carbonate concentrations agree. There is only a small discrepancy for the highest concentrations of the borate buffer. However, the kinetic runs shown in Figure 5.4.4 have been done using a carbonate buffer at lower concentration. Hence, the influence of the buffer on the reaction may be dismissed safely (see also the discussion of Figure 5.4.3).

Within the frame of the Langmuir-Hinshelwood model, the temperature dependence of the rate constant  $k_{app}$  is given by the activation energy  $E_A$  of the rate constant  $k$  and also by the adsorption enthalpies governing the temperature dependence of the two thermodynamic constants  $K_{\text{H}_2\text{O}_2}$  and  $K_{\text{morin}}$ . Figure 5.4.7 displays the respective Arrhenius plots of  $k_{app}$  (a) and  $k^*S$  (b). The apparent activation energy  $E_{A,app}$  taken from the analysis of  $k_{app}$  is  $46 \pm 0.2$   $\text{kJ} \cdot \text{mol}^{-1}$  for 12.5 mM carbonate buffer solution. For the 50 mM carbonate buffer solution the activation energy was calculated with  $32.7 \pm 0.8$   $\text{kJ} \cdot \text{mol}^{-1}$ . As it can be seen the activation

energy of the intrinsic rate constant  $k^*S$  taken from Figure 5.4.7b is considerably higher than the activation energy of the apparent rate constant  $k_{app}$  (see Table 5.2). This difference can be understood immediately from the fact that the dependence of  $k_{app}$  on  $T$  is not only given by the activation energy of  $k$ , but also by the adsorption enthalpies of both reactants as shown in the following.

The enthalpy and entropy of adsorption were calculated using van't Hoff's equation as shown in Figure 5.4.7c. The results are listed in Table 5.2. The adsorption enthalpies for both reactants are found to be negative. The exothermic adsorption process is contained in the apparent activation energy taken from  $k_{app}$  and will hence be lower than the true activation energy found from the analysis of  $k$ . In case of the H<sub>2</sub>O<sub>2</sub> the entropy is negative. As mentioned before the adsorption of H<sub>2</sub>O<sub>2</sub> is a very complex process and the thermodynamic parameters taken therefrom defy further analysis at this stage.

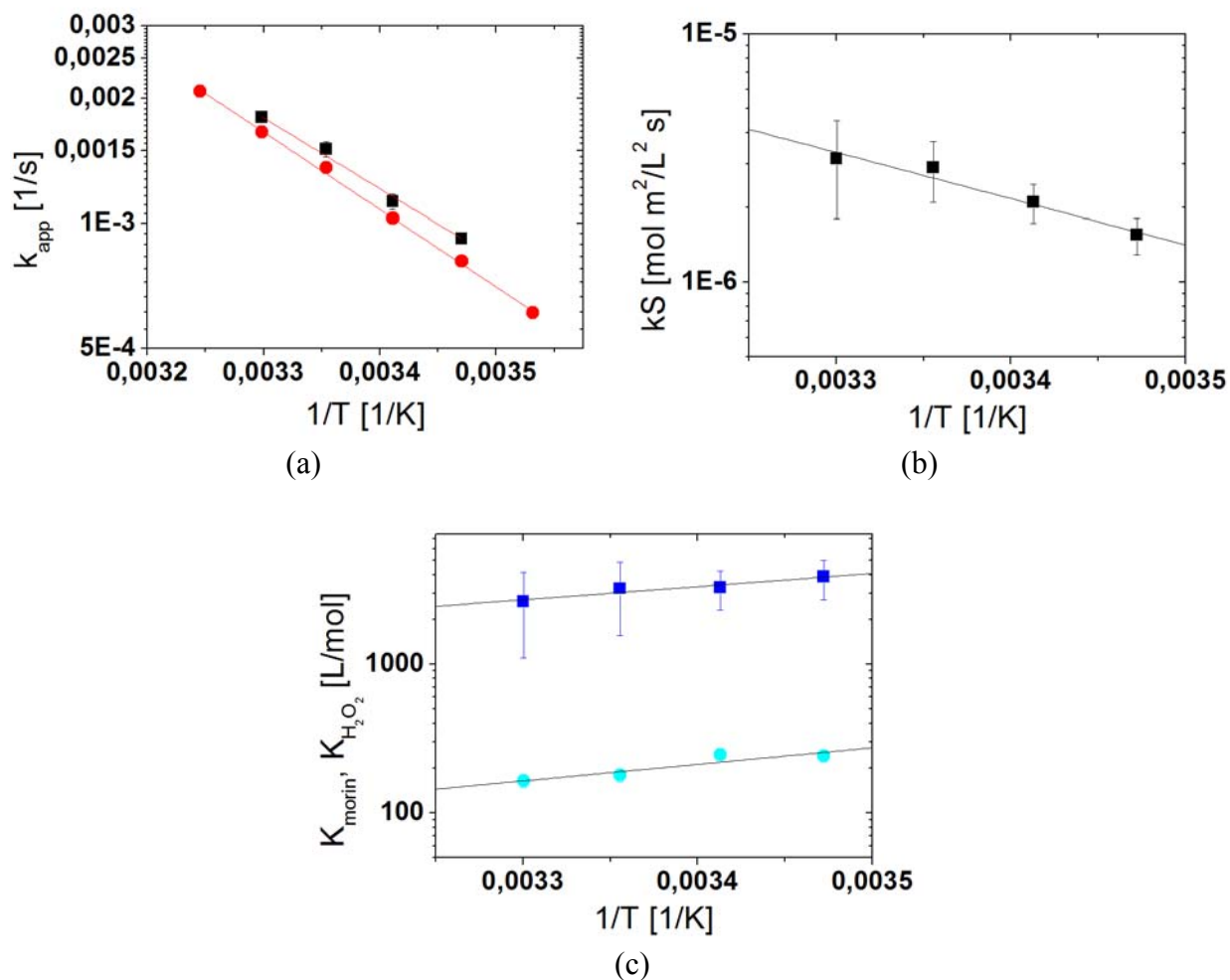


**Figure 5.4.7.** Dependence of the kinetic and thermodynamic constants on temperature as taken from the LH-approach: (a) apparent rate constant  $k_{app}$  for a 50 mM carbonate buffer (black squares) and 12.5 mM carbonate buffer (red dots); (b) rate constant  $k^*S$  and (c) adsorption constants of morin (blue squares) and H<sub>2</sub>O<sub>2</sub> (cyan dots). The graphs (b) and (c) were derived from the LH study with a 50 mM carbonate buffer at pH 10.

**Table 5.2: Summary of the Temperature Dependence of the Rate Constants and Adsorption Constants.**

	$E_A^a$ [kJ·mol <sup>-1</sup> ]	$\Delta H^b$ [kJ·mol <sup>-1</sup> ]	$\Delta S^c$ [J·mol <sup>-1</sup> ·K <sup>-1</sup> ]
$k^*S$ [mol·m <sup>2</sup> ·L <sup>-2</sup> ·s <sup>-1</sup> ]	45.8 ± 7.0	-	-
$K_{\text{Morin}}^d$ [L·mol <sup>-1</sup> ]	-	-19.8 ± 8.7	0.2 ± 29.6
$K_{\text{H}_2\text{O}_2}^e$ [L·mol <sup>-1</sup> ]	-	-20.8 ± 7.1	-26.1 ± 10.7

<sup>a</sup>  $E_a$ : activation energy. <sup>b</sup>  $\Delta H$ : enthalpy. <sup>c</sup>  $\Delta S$ : entropy. <sup>d</sup>  $K_{\text{morin}}$ : adsorption constant of morin. <sup>e</sup>  $K_{\text{H}_2\text{O}_2}$ : adsorption constant of  $\text{H}_2\text{O}_2$ .

## 5.5. Conclusions

We presented a kinetic study of the catalytic oxidation of morin by  $\text{H}_2\text{O}_2$  in aqueous solution using c\*-disordered birnessite nanoparticles immobilized on cationic SPB as catalyst. The analysis of the kinetic data suggested that the rate determining step takes place on the surface of the nanoparticles. Both reactants need to be adsorbed onto the surface of the catalyst in order to react. The adsorption process and the surface reaction are described by the thermodynamic adsorption constants  $K$  of both reactants and the kinetic constant  $k$ , respectively. The mechanism found for colloidal  $\text{MnO}_x$ -particles is hence determined by the surface of the particles. Applications therefore must ensure a sufficient colloidal stabilization in order to keep the catalyst in an active form.

## 5.6. Acknowledgements

We thank the Deutsche Forschungsgemeinschaft, and the Henkel AG & Co. KGaA for the financial support. The authors are indebted to W. von Rybinski and A. Hätzelt for helpful discussion.

## 5.7. Supporting information

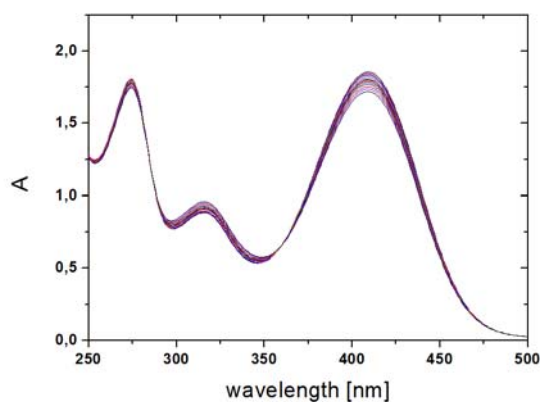


**Figure S5.1.** Oxidation of morin with H<sub>2</sub>O<sub>2</sub> without MnO<sub>x</sub>-NP in 50 mM carbonate buffer. The spectra were recorded every 2 minutes.

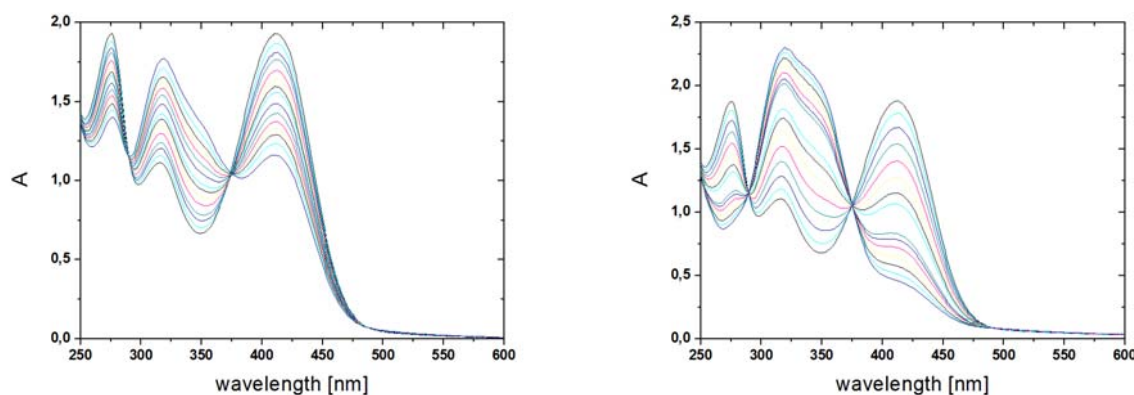


**Figure S5.2.** Oxidation of morin in presence of MnO<sub>x</sub>@SPB without H<sub>2</sub>O<sub>2</sub> in 50 mM carbonate buffer. Left hand side: solutions were purged with nitrogen before the mixing of the reactants. Right hand side: solutions were not purged with nitrogen before the mixing of the reactants. The spectra were recorded every 2 minutes.

## 5.8. References

- <sup>1</sup> Débart, A.; Paterson, A. J.; Bao, J.; Bruce, P. G. *Angew. Chem. Int. Ed.* **2008**, *47*, 4521-4524.
- <sup>2</sup> Tang, W. P.; Kanoh, H.; Yang, X. J.; Ooi, K. *Chem. Mater.* **2000**, *12*, 3271-3279.
- <sup>3</sup> Shen, Y. F.; Zerger, R. P.; DeGuzman, R. N.; Suib, S. L.; McCurdy, L.; Potter, D.I.; O'Young, C.L. *Science* **1993**, *260*, 511-515.
- <sup>4</sup> Lee, G. H.; Huh, S. H.; Jeong, J. W.; Choi, B. J.; Kim, S. H; Ri, H.-C. *J. Am. Chem. Soc.* **2002**, *124*, 12094-12095.
- <sup>5</sup> Cao, H.; Suib, S. L. *J. Am. Chem. Soc.* **1994**, *116*, 5334-5342.
- <sup>6</sup> Cheng, F. Y.; Chen, J.; Gou, X. L.; Shen, P. W. *Adv. Mater.* **2005**, *17*, 2753-2756.
- <sup>7</sup> Zhang, W.; Wang, H.; Yang, Z.; Wang, F. *Colloid Surf. A* **2007**, *304*, 60-66.
- <sup>8</sup> Broughton, D. B.; Wentworth, R. L. *J. Am. Chem. Soc.* **1947**, *69*, 741-744.
- <sup>9</sup> Do, S.-H.; Batchelor, B.; Lee, H.-K.; Kong, S.-H. *Chemosphere* **2009**, *75*, 8-12.
- <sup>10</sup> Osada, M.; Sasaki, T. *J. Mater. Chem.* **2009**, *19*, 2503-2511.
- <sup>11</sup> Kang, J.-H.; Paek, S.-M.; Hwang, S.-J.; Choy, J.-H. *J. Mater. Chem.* **2010**, *20*, 2033-2083.
- <sup>12</sup> Liu, Z.-H.; Ooi, K.; Kanoh, H.; Tang, W.-P.; Tomida, T. *Langmuir* **2000**, *16*, 4154-4164.
- <sup>13</sup> Oaki, Y.; Imai, H. *Angew. Chem. Int. Ed.* **2007**, *46*, 4951-4955.
- <sup>14</sup> Kai, K.; Yoshida, Y.; Kageyama, H.; Saito, G.; Ishigaki, T.; Furukawa, Y.; Kawamata, J.; *J. Am. Chem. Soc.* **2008**, *130*, 15938-15943.
- <sup>15</sup> Polzer, F.; Kunz, D. A.; Breu, J.; Ballauff, M. *Chem. Mater.* **2010**, *9*, 2916-2922.
- <sup>16</sup> Ballauff, M. *Prog. Polym. Sci.* **2007**, *32*, 1135-1151.
- <sup>17</sup> Wieprecht, T.; Heinz, U.; Xia, J.; Schlingloff, G.; Dannacher, J. *J. Surfact. Deterg.* **2004**, *7*, 59-66.
- <sup>18</sup> Dannacher, J. *J. Mol. Catal. A: Chem.* **2006**, *251*, 159-176.
- <sup>19</sup> Segal, S. R.; Suib, S. L. *Chem. Mater.* **1997**, *9*, 2526-2532.
- <sup>20</sup> Gemeay, A. H.; El-Sharkawy, R. G.; Mansour, I. A.; Zaki, A. B. *Appl. Catal. B: Environ.* **2008**, *80*, 106-115.
- <sup>21</sup> Zhang, W.; Yang, Z.; Wang, X.; Zhang, Y.; Wen, X.; Yang, S. *Catal. Commun.* **2006**, *7*, 408-412.
- <sup>22</sup> Qi, B.; Lou, L.-L.; Yu, K.; Bian, W.; Liu, S. *Catal. Commun.* **2011**, *15*, 52-55.
- <sup>23</sup> Topalovic, T.; Nierstrasz, V. A.; Warmkoeskerken, M. M. C. G. *Fibers Polym.* **2010**, *11*, 72-78.
- <sup>24</sup> Ember, E.; Gazzaz, H. A.; Rothbart, S.; Puchta, R.; van Eldik, R. *Appl. Cat. B-Environ.* **2010**, *95*, 179-191.
- <sup>25</sup> Rothbart, S.; Ember, E.; van Eldik, R. *Dalton Trans.* **2010**, *39*, 3264-3272.
- <sup>26</sup> Sharma, G.; Ballauff, M. *Macromol. Rapid Commun.* **2004**, *25*, 547-557.
- <sup>27</sup> Crassous, J. J.; Rochette, C. N.; Wittemann, A.; Schrinner, M.; Drechsler, M.; Ballauff, M. *Langmuir* **2009**, *25*, 7862-7871.

- <sup>28</sup> Lu, Y.; Wittemann, A.; Ballauff, M. *Macromol. Chem. Rapid Comm.* **2009**, *30*, 806-815.
- <sup>29</sup> Jovanovic, S.V.; Steenken, S.; Tosic, M.; Marjanovic, B.; Simic, M.G. *J. Am. Chem. Soc.* **1994**, *116* 4846.
- <sup>30</sup> Weprech, T.; Hazenkamp, M.; Rohwer, H.; Schlingloff, G.; Xia, J. T.; *C. R. Chim.* **2007**, *10*, 326.
- <sup>31</sup> Kitajima, N.; Fukuzumi, S.-I.; Ono, Y. *J. Phys. Chem.* **1978**, *82*, 1505-1509.
- <sup>32</sup> Topalovic, T.; Catalytic Bleaching of Cotton: Molecular and Macroscopic Aspects, University of Twente, Netherlands, 2007.
- <sup>33</sup> Colombini, M.P.; Andreotti, A.; Baraldi, C.; Degano, I.; Łucejko, J.J. *Microchem. J.* **2007**, *85*, 174.
- <sup>34</sup> Zhou, A. L.; Sadik, O. A. *J. Agric. Food. Chem.* **2008**, *56*, 12081.
- <sup>35</sup> Vannice, M. A. *Reactions*; Springer Science + Business Media: Philadelphia, PA, 2005.
- <sup>36</sup> Wunder, S.; Polzer, F.; Lu, Y.; Mei, Y.; Ballauff, M. *J. Phys. Chem. C* **2010**, *114*, 8814-8820.
- <sup>37</sup> Zhou, H.; Shen, Y. F.; Wang, J. Y.; O'Young, C.-L.; Suib, S. L. *J. Catalysis* **1998**, *176*, 321-328.
- <sup>38</sup> Rill, C.; Kolar, Z. I.; Kickelbick, G.; Wolterbeek, H. T; Peters, J.A. *Langmuir* **2009**, *25*, 2294-2301.
- <sup>39</sup> László, K.; Podkościelny, P.; Daborwski, A. *Langmuir* **2003**, *19*, 5287-5294.
- <sup>40</sup> Zhou, X. W.; Xu, G.; Liu, D.; Panda, P. Chen, J. *Am. Chem. Soc.* **2010**, *132*, 138-146.
- <sup>41</sup> Ressler, T.; Brock, S.L.; Wong, J.; Suib, S. L. *J. Phys. Chem. B* **1999**, *103*, 6407-6420.
- <sup>42</sup> Saratovsky, I.; Wightman, P.G.; Pastén, P.A.; Gaillard, J.-F.; Poepelmeier, K. R. *J. Am. Chem. Soc.* **2006**, *128*, 11188-11198.

*References*

---

## **6. Kinetic Analysis of Catalytic Reduction of 4-Nitrophenol by Metallic Nanoparticles Immobilized in Spherical Polyelectrolyte Brushes**

*Stefanie Wunder, Frank Polzer, Yan Lu, Yu Mei, Matthias Ballauff<sup>1</sup>*

<sup>1</sup>Helmholtz-Zentrum Berlin für Materialien und Energie GmbH, Hahn-Meitner-Platz 1,  
14109 Berlin, Germany, and Department of Physics, Humboldt University Berlin, Newtonstr.  
15, 12489 Berlin, Germany

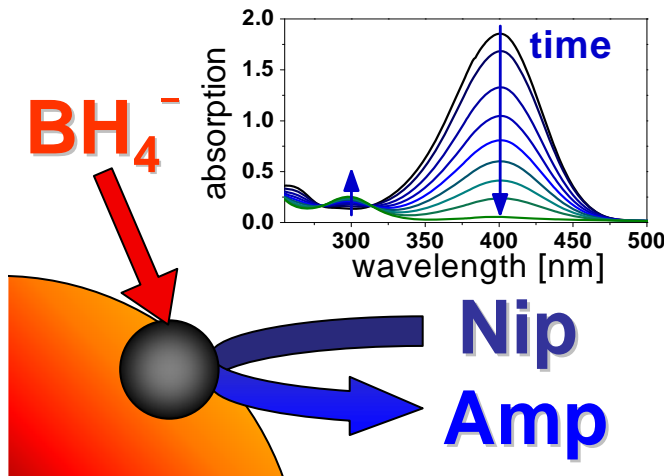
E-mail address: [Matthias.Ballauff@helmholtz-berlin.de](mailto:Matthias.Ballauff@helmholtz-berlin.de)

**Published in the Journal of Physical Chemistry C**

Reproduced with permission from  
*Journal of Physical Chemistry C*, **2010**, *114*, 8814.  
© 2010 American Chemical Society.

**DOI:** [10.1021/jp101125j](https://doi.org/10.1021/jp101125j)

## 6.1. Abstract



We present a study on the catalytic reduction of 4-nitrophenol by sodium borohydride in the presence of metal nanoparticles. The nanoparticles are embedded in spherical polyelectrolyte brushes (SPBs), which consist of a polystyrene (PS) core onto which a dense layer of cationic polyelectrolyte brushes are grafted. The average size of the nanoparticles is approximately 2 nm. The kinetic data obtained by monitoring the reduction of 4-nitrophenol by UV-vis-spectroscopy could be explained in terms of the Langmuir-Hinshelwood model: The borohydride ions transfer a surface-hydrogen species in a reversible manner to the surface. Concomitantly 4-nitrophenol is adsorbed and the rate-determining step consists of the reduction of nitrophenol by the surface-hydrogen species. The apparent reaction rate can therefore be related to the total surface  $S$  of the nanoparticles, to the kinetic constant  $k$  related to the rate-determining step and to the adsorption constants  $K_{\text{Nip}}$  and  $K_{\text{BH}4}$  of nitrophenol and of borohydride, respectively. In all cases, an induction time  $t_0$  was observed of the order of minutes. The reciprocal induction time can be treated as a reaction rate that is directly related to the kinetics of the surface reaction because there is a linear relation between  $1/(k t_0)$  and the concentration of nitrophenol in the solution. All data obtained for  $t_0$  so far and a comparison with data from literature indicates that the induction time is related to a slow surface reconstruction of the nanoparticles, the rate of which is directly related to the surface reaction.

## 6.2. Introduction

Metallic nanoparticles (NP) have been the subject of intense research during the recent years because of their potential use in catalysis.<sup>1,2,3,4</sup> In particular, redox reactions catalyzed by nanoparticles have been extensively studied.<sup>5,6,7,8,9</sup> A central problem in this field is the quantification of the catalytic activity of the nanoparticles affixed to various carrier systems. A model reaction suitable for this purpose should be well-defined, that is, no by-products should be formed. Moreover, the degree of conversion should be easily monitored by a simple and fast technique. Pal and coworkers were the first to identify the reduction of 4-nitrophenol (Nip) to 4-aminophenol (Amp) by sodium borohydride ( $\text{BH}_4^-$ ) as such a model reaction.<sup>10</sup> This reaction is catalyzed by free or immobilized nanoparticles and proceeds in aqueous solution at ambient temperature. Moreover, it can be easily monitored via UV/Vis-spectroscopy by the decrease of the strong adsorption of 4-nitrophenolate anion at 400nm, leading directly to the rate constant.<sup>11</sup> Several isosbestic points in the spectra of the reacting mixtures demonstrate that no side reaction occurs.<sup>12</sup>

This reaction has been used frequently to check the catalytic activity of the nanoparticles.<sup>13,14,15,16,17,18,19,20,21,22,23,24,25,26,27,28,29,30,31,32,33,34</sup> The number of studies directly related to the mechanism of this reaction, however, is much smaller. Esumi *et al.* investigated the catalytic activity of dendrimer-stabilized nanoparticles.<sup>25</sup> These authors concluded that the reaction is diffusion-controlled. A systematic study of the kinetics of the reaction has been presented recently by Saha *et al.* by varying the initial concentrations of borohydride, of Nip, and of the metal nanoparticles.<sup>32</sup> From their data these authors could demonstrate that the reduction of Nip must take place on the surface of the nanoparticles. Zeng *et al.* investigated the catalytic properties of Au-based nanocages, nanoboxes and particles using this model reaction in order to elucidate the role of particle morphology for the activity of the catalyst.<sup>31</sup> Special attention was paid to the induction time  $t_0$  after which the reaction starts. This induction time has been observed by a number of authors with different carrier systems<sup>10,11,16,31,36</sup> and was interpreted in terms of the time needed for the reactants to diffuse to the surface of the particles.<sup>16</sup>

A mechanistic explanation of the surface reaction was provided by Zhang *et al.* by investigating the catalytic activity of Ag nanoclusters supported on  $\text{TiO}_2$ .<sup>30</sup> These authors assume that a surface hydrogen species is first transferred to the Ag-nanoparticles by borohydride. This species reacts then with the Nip to yield the product Amp. This model would imply that the kinetics of the reaction must be modeled in terms of a Langmuir-Hinshelwood mechanism, that is, both reactants need to be adsorbed on the surface prior to reaction. However, Khalavka *et al.* recently came to the conclusion that only hydrogen needs to be adsorbed onto the surface (Eley-Rideal-mechanism).<sup>35</sup> A number of authors have also studied the activation energy  $E_A$  of this reaction by carrying out kinetic runs at different temperatures.<sup>12,17,22,24,28,31,32,33,35,36,39,43</sup> Zheng *et al.* related  $E_A$  to diffusion barriers in the system.<sup>31</sup> Thus, although the reduction of Nip by borohydride has become one of the most used benchmarks for the catalytic activity of metal nanoparticles, a comprehensive kinetic analysis of this reaction is still lacking.

Recently, we showed that SPBs are excellent systems for the generation and immobilization of metal nanoparticles.<sup>12,36,37,38</sup> Figure 6.2.1 demonstrates the SPBs as carriers for nanoparticles in a schematic fashion:

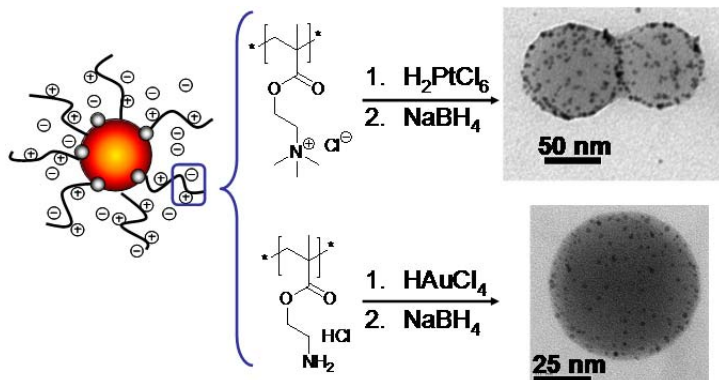


**Figure 6.2.1.** Scheme of the spherical polyelectrolyte brushes used in this study. Two different polyelectrolytes have been used for the synthesis of the metal nanoparticles: For the synthesis of platinum NP we used poly[2-(methylacryloyloxy)ethyl-trimethylammonium chloride] affixed to the polystyrene cores whereas Au-NP were synthesized using poly[(2-aminoethyl)-methacrylate hydrochloride].<sup>36,39</sup> The right-hand side displays the TEM micrographs of the composite particles.

The SPBs consist of a solid PS core onto which long chains of polyelectrolyte chains have been chemically grafted. This brush layer can be used to immobilize ions of noble metals as e.g. gold or platinum. Subsequent reduction then leads to metal nanoparticles of 1 - 3 nm in diameter that are firmly embedded in a dense mesh of the polyelectrolyte chains.<sup>39</sup> The composites of the nanoparticles and the SPBs exhibit a high colloidal stability and can be used repeatedly even under harsh conditions as e.g. in the phase-transfer hydrogenation or the Heck- and Suzuki-reaction.<sup>40,41</sup>

The reduction of Nip in the presence of these composites has been used previously in order to compare the catalytic activity of different metal nanoparticles immobilized in the same system.<sup>42</sup> In addition, this reaction has been used to test the catalytic activity of metal nanoparticles immobilized in other carrier systems like core-shell microgels or tree-like brushes.<sup>12,43</sup> Previous work demonstrated that Nip is reduced to Amp only in the presence of the composite particles; no reaction takes place in absence of the nanoparticles.<sup>36</sup> If an excess of borohydride is used, the reaction is first order in the concentration of 4-nitrophenol  $c_{\text{Nip}}$ . Moreover, the apparent kinetic rate constant  $k_{app}$  is strictly proportional to the total surface  $S$  of all metal nanoparticles.<sup>12,29,36</sup> Hence, the kinetic constants  $k_{app}$  and  $k_1$  can be defined through:

$$\frac{dc_{\text{Nip}}}{dt} = -k_{app} \cdot c_{\text{Nip}} = -k_1 \cdot S \cdot c_{\text{Nip}} \quad (6.2.1)$$

Here we aim at a full analysis of the heterogeneous reduction of Nip in the presence of metallic nanoparticles. We shall demonstrate that the reaction is surface-controlled and can be analyzed in terms of the Langmuir-Hinshelwood mechanism.<sup>44,45,46</sup> In this mechanism it is assumed that both reactants need to be adsorbed on the surface of the catalyst. The rate-determining step is given by the reaction of the adsorbed species. The adsorption/desorption equilibrium is assumed to be much faster and is modelled in terms of a Langmuir isotherm. The influence of SPB carrier particles on the reduction of 4-nitrophenol will be excluded for the study due to the open structure of the brush system.<sup>12</sup> In addition to the analysis of the reaction rate, the dependence of the induction time  $t_0$  on the various parameters will be analyzed quantitatively and related to parameters derived from the Langmuir-Hinshelwood analysis.

### **6.3. Experimental Section**

The spherical polyelectrolyte brushes and the metal nanoparticles were synthesized as described previously.<sup>37,36,39</sup> To 0.1 g of latex particles, 10 mL of an aqueous solution of 2.55 mM metal salt was added dropwise. Afterwards the mixture was stirred for 30 minutes under  $\text{N}_2$  to remove the oxygen from the liquid and then the metal ions were reduced by a threefold excess of  $\text{BH}_4^-$ . Thereafter the latex was purified via ultra filtration. Transmission electron microscopy was done using a Zeiss EM922 Omega transmission electron microscope. The TEM-micrographs of both systems are shown in Figure 6.2.1. The radius of the PS-core is 45 nm and the polyelectrolyte layer has a thickness of 86 nm in case of the Pt-NP. The carrier particles of the Au-NP have a PS-core with a radius of 43 nm. The thickness of the polyelectrolyte layer is 76 nm.

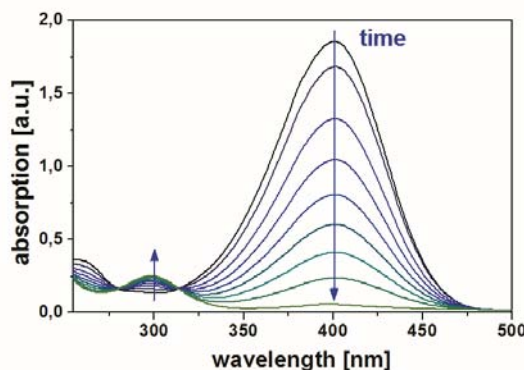
The amount of metal immobilized on the SPBs was determined by TGA using a Mettler Toledo STARe system. The samples were first dried under vacuum at 50 °C. Then ca. 8 mg of the solid composite particles was heated to 800 °C under a 60  $\text{mL}\cdot\text{min}^{-1}$  nitrogen flow with a heating rate of 10  $^{\circ}\text{C}\cdot\text{min}^{-1}$  and holding temperature at 800 °C for about 30 minutes. The size of the metal nanoparticles was calculated from the TEM-micrographs. Approximately 400 nanoparticles were measured in order to obtain the average size. The specific surface area of the nanoparticles was calculated from the average radius thus obtained and to their total mass per particle. The density of the platinum nanoparticle was taken from literature (Pt: 21.45  $\text{g}\cdot\text{cm}^{-3}$ ; Ref.<sup>36</sup>; Au: 19.32  $\text{g}\cdot\text{cm}^{-3}$  Ref.<sup>47</sup>).

The catalytic runs were performed in 3 mL optical cells made from quartz. The solutions had been purged prior to the run with  $\text{N}_2$  in order to remove  $\text{O}_2$ . After mixing fresh solutions of  $\text{BH}_4^-$  and Nip, a given amount of solutions of the composite particles was added. The solution was carefully mixed by shaking shortly before the measurement. The extinction of Nip was subsequently detected via UV-vis spectroscopy using a Lambda 650 spectrometer (Perkin Elmer) at a constant pH value of 10.

## 6.4. Results and Discussion

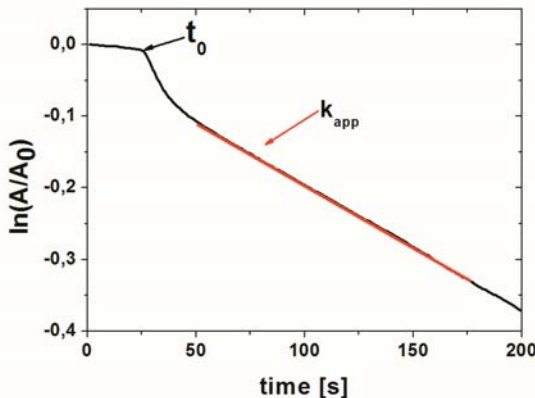
In order to compare the catalytic activity of two different metals, Au- as well as Pt-nanoparticles were generated and immobilized on suitable spherical polyelectrolyte brushes. We used platinum and gold nanoparticles in this study generated and characterized as described elsewhere.<sup>36,39,40</sup> For Au-nanoparticles we used the SPB with chains of poly[(2-aminoethyl)-methacrylate hydrochloride] attached to the surface of the SPB whereas Pt-nanoparticles were immobilized using a polyelectrolyte layer composed of poly[2-(methylacryloyloxy)ethyl-trimethylammonium chloride].<sup>39,36</sup> These SPBs were chosen to ensure optimal immobilization of the respective metal nanoparticles. The size of the nanoparticles was determined by the analysis of TEM-micrographs and the amount of metal was obtained by thermo gravimetric measurements. The average size of the nanoparticles was approximately in the same range (Au:  $1.5 \pm 0.5$  nm; Pt:  $2.3 \pm 0.4$  nm). From these data the total surface area  $S$  of the spherical metal nanoparticles could be calculated precisely, and used in the subsequent kinetic analysis. Previous work has shown that the SPB present no diffusion barrier for the reactants.<sup>12</sup> Moreover, the composite particles that consist of the SPB carriers and the metal nanoparticles exhibit an excellent colloidal stability. Hence, the kinetic analysis is neither impeded by a slow coagulation of the particles nor by an Ostwald-ripening of the nanoparticles on the carriers.

Figure 6.4.1 displays the typical evolution of the UV-vis-spectra with time in presence of Pt-nanoparticles. Similar results have been obtained for catalytic runs using the Au-nanoparticles. The isosbestic points immediately demonstrate with high precision that Nip is fully converted to aminophenol and no side reaction takes place.<sup>10,12,36</sup> It should be noted that gas bubbles of H<sub>2</sub> may evolve during the runs. These bubbles would severely impede the optical measurements because their presence would lead to a shift of the UV-vis-spectra and a loss of the isosbestic points.



**Figure 6.4.1.** Absorption spectrum of the reduction of Nip by sodium borohydride. The time between two different curves is 2 minutes. The full conversion takes place in 20 minutes. The main peak at 400 nm (nitrophenolate ions) is decreasing with reaction time (blue arrow), whereas a second peak at 300 nm (Amp) is slowly increasing. The two isosbestic points are visible at 280 nm and 314 nm.

A typical time-dependence of the UV/vis-peak of 4-nitrophenolate ions at 400 nm is shown in Figure 6.4.2. The generation of 4-nitrophenolate ions takes place immediately after addition of  $\text{BH}_4^-$  to the system. There is an induction time  $t_0$  in which no reduction takes place. Then the reaction becomes stationary and the reaction follows a first-order rate law. In the following we shall discuss first the apparent rate constant  $k_{app}$  defined through eq. (6.2.1) which was obtained from the linear slope. In a second step the induction time  $t_0$  will be analyzed.



**Figure 6.4.2.** Typical time dependence of the absorption of 4-nitrophenolate ions at 400 nm. The red portion of the line displays the linear section, from which  $k_{app}$  is taken. The induction period  $t_0$  is marked with the black arrow.

In order to obtain a full set of kinetic data,  $k_{app}$  was measured for a constant concentration of Nip at a constant temperature while varying the concentration of sodium borohydride. In a second set of experiments, the concentration of sodium borohydride was kept constant and the concentration of Nip was varied. For the Pt-nanoparticles we also varied the amount of composite particles in order to change the total surface area  $S$  of the nanoparticles in solution.

Figure 6.4.3 gives a survey of the entire set of apparent rate constants  $k_{app}$  obtained in this way. Here, Figure 6.4.3a-d refers to Pt-nanoparticles bound on SPB while Figure 6.4.3e and 6.4.3f refer to Au-nanoparticles.

## Results and Discussion

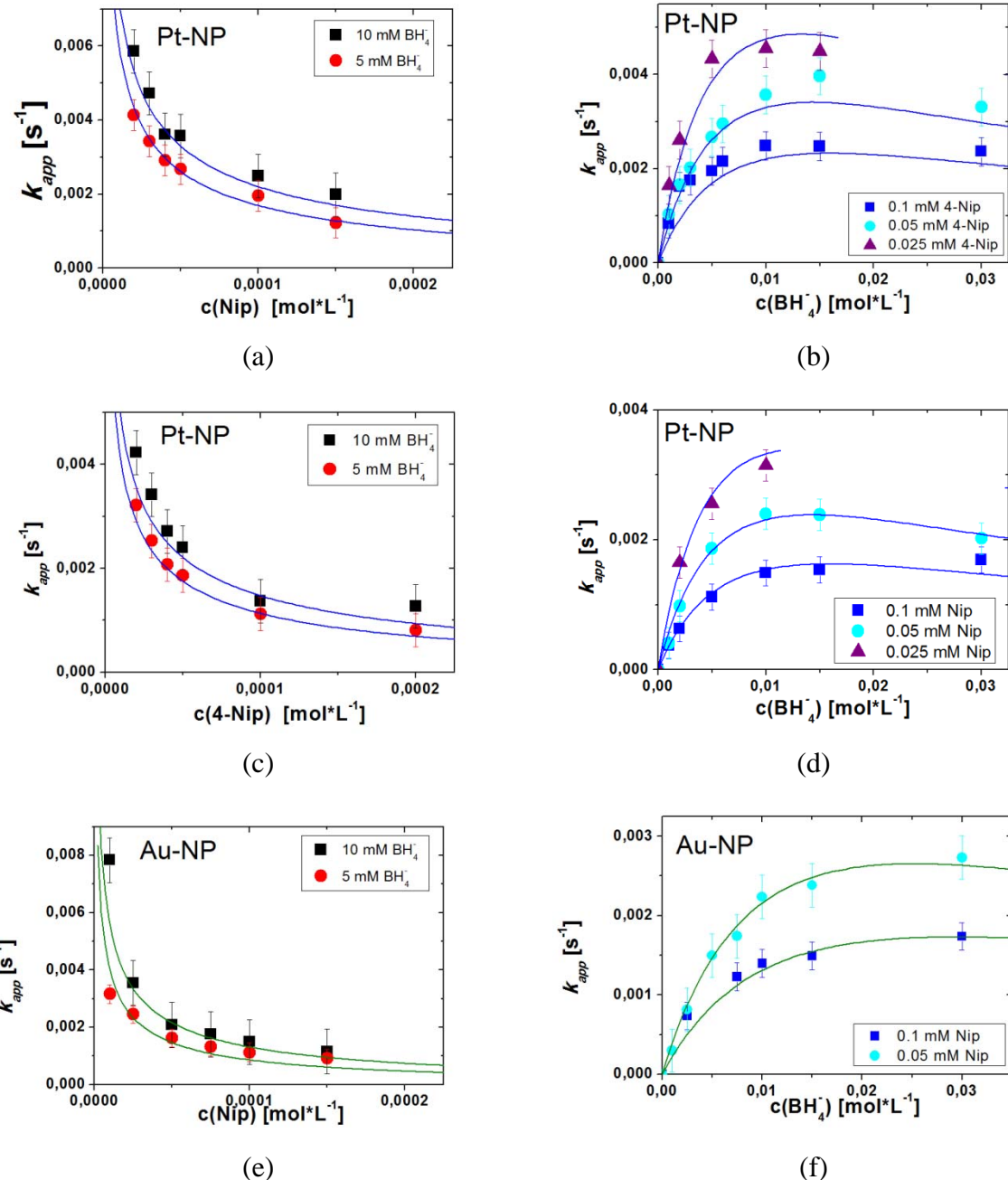


**Figure 6.4.3.** Dependence of the apparent rate constant  $k_{app}$  on the concentration of Nip (a,b,e) and  $\text{BH}_4^-$  (c,d,f). The blue solid lines are the fit of the Langmuir-Hinshelwood-model. The surface area of Pt nanoparticles is  $0.00687 \text{ m}^2 \text{ L}^{-1}$  for panels (a) and (c) and  $0.00481 \text{ m}^2 \text{ L}^{-1}$  for panels (b) and (d). Panels (e) and (f) describe the kinetic data taken for Au-nanoparticles. The green solid lines display the fits for LH-model. The surface area in the case of Au is  $0.01078 \text{ m}^2 \text{ L}^{-1}$ .

Two features command attention: First of all,  $k_{app}$  decreases markedly with increasing concentration of Nip. For constant concentration of Nip, on the other hand,  $k_{app}$  tends to a constant value or even goes through a shallow maximum with increasing  $c_{\text{BH}_4^-}$ . The latter

finding is in agreement with the recent report by Saha *et al.*<sup>32</sup> These two findings immediately show that the reaction cannot be controlled by diffusion of Nip or borohydride because this should lead to opposite trends. This is in clear contrast to recent data on the reduction of ferrocyanate(III) ions by borohydride in the presence of nanoparticles.<sup>48</sup> Carregal-Romero *et al.* demonstrated that the rate of reduction is limited by the diffusion of the ferrocyanate(III) ions to the surface of the metal particles.

### Kinetic analysis

The reaction of borohydride with metal surfaces and its decomposition in the presence of metallic nanoparticles have become the subjects of intense research during recent years. This is due to the potential of borohydrides for the hydrogen generation in fuel cells.<sup>49</sup> Moreover, it has been reported that metal nanoparticles can be charged by sodium borohydride and act as electron acceptors.<sup>50,48</sup> This can be deduced from shift of the surface plasmon band of the nanoparticles.<sup>51,52</sup> Previous mechanistic studies indicate that the adsorption of borohydride on metal catalyst is a fast and reversible process whereas the rate determining step in the hydrolysis is the cleavage of the OH-bond of the water molecule.<sup>53,54</sup> The interaction of the reagents with the surface of the metal nanoparticles can therefore be expressed in terms of a Langmuir adsorption isotherm.<sup>55</sup>

In the following, the data shown in Figure 6.4.3 will be discussed in terms of the Langmuir-Hinshelwood (LH) model<sup>44</sup> displayed schematically in Figure 6.4.4:

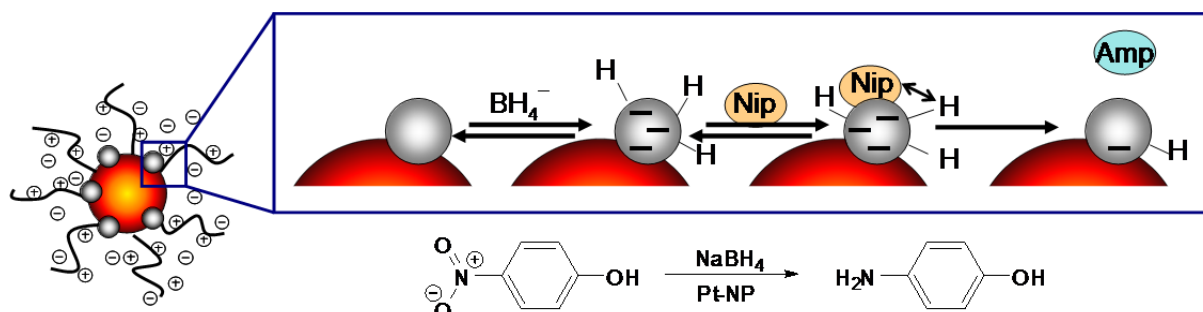


**Figure 6.4.4.** Mechanistic model (Langmuir-Hinshelwood mechanism) of the reduction of Nip by borohydride in the presence of metallic nanoparticles (gray spheres). The nanoparticles are bound to spherical polyelectrolyte brush (SPB) particles that consist of a polystyrene core and a shell of cationic polyelectrolyte chains. The catalytic reduction proceeds on the surface of the metal nanoparticles: The nanoparticles react with the borohydride ions to form the metal-hydride. Concomitantly, nitrophenol adsorbs onto the metal surface. The adsorption/desorption of both reagents on the surface is fast and can be modeled in terms of a Langmuir-isotherm. The rate-determining step is the reduction of the adsorbed Nip to Amp, which desorbs afterwards.

Borohydride ions react with the surface of the nanoparticles and transfer a surface-hydrogen species to the surface of the particles.<sup>30,49,54,56</sup> As discussed above, this step is reversible and can be modeled in terms of a Langmuir isotherm. Concomitantly, Nip molecules are adsorbed

on the surface of the nanoparticles. This step is also reversible and can be model by a Langmuir isotherm. Moreover, the diffusion of the reactants to the nanoparticles as well as all the adsorption/desorption equilibrium are assumed to be fast. The reduction of Nip, which is the rate-determining step, takes place by the reaction of adsorbed Nip with the surface-hydrogen species. Detachment of the product Amp creates a free surface and the catalytic cycle can start again.

For a quantitative comparison of the data with the model, the adsorption of the reactants is modelled in terms of the Langmuir-Freundlich-Isotherm:

$$\theta_i = \frac{(K_i \cdot c_i)^{n_i}}{1 + \sum_{j=1}^N (K_j \cdot c_j)^{n_j}} \quad (6.4.1)$$

Here,  $\theta_i$  is the surface coverage of compound  $i$ ,  $K_i$  is the adsorption constant of the respective component and  $c_i$  the concentration in solution. The exponent  $n$  is related to the heterogeneity of the sorbent.<sup>57</sup> The Langmuir-Freundlich equation takes into account that the adsorption energy is not the same for all sites and can be described by a Gaussian distribution. The broader the distribution, the higher is the heterogeneity of the surface, leading to a smaller the value of the exponent  $n$ .<sup>58</sup> The case of  $n = 1$  represents the classical Langmuir isotherm that all sites have the same adsorption energy. Hence, eq. (6.2.1) can be rewritten as:

$$-\frac{dc_{Nip}}{dt} = \frac{k \cdot S \cdot (K_{Nip} \cdot c_{Nip})^n \cdot (K_{BH_4} \cdot c_{BH_4})^m}{\left(1 + (K_{Nip} \cdot c_{Nip})^n + (K_{BH_4} \cdot c_{BH_4})^m\right)^2} = k_{app} \cdot c_{Nip} \quad (6.4.2)$$

Thus,  $k_{app}$  is given by

$$k_{app} = \frac{k \cdot S \cdot K_{Nip}^n \cdot c_{Nip}^{n-1} \cdot (K_{BH_4} \cdot c_{BH_4})^m}{\left(1 + (K_{Nip} \cdot c_{Nip})^n + (K_{BH_4} \cdot c_{BH_4})^m\right)^2} \quad (6.4.3)$$

Here  $k$  is the molar rate constant per square meter of the catalyst and  $K_{Nip}$  is the adsorption constant of Nip and  $K_{BH_4}$  is the adsorption constant of  $BH_4^-$ .

The solid lines in Figure 6.4.3 refer to the fit of the experimental data using eq. (6.4.3) while Table 6.1 gives the resulting parameters. We reiterate that the total surface  $S$  is known in both cases. Moreover, all rate constants  $k_{app}$  for a given metal have been fitted by the same set of parameters. Additional model calculations demonstrated that the entire system is quite stiff and small variations of the fit parameters lead to marked deviations from theory and experiment. All parameters related to these fits are listed in Table 6.1.

**Table 6.1. Summary of the Rate Constants, Adsorption Constants of Nip and  $\text{BH}_4^-$  According to Eq. (6.4.3).**

metal	$k$ [mol·m <sup>-2</sup> s <sup>-1</sup> ]	$K_{\text{Nip}}$ [L·mol <sup>-1</sup> ]	$K_{\text{BH}_4}$ [L·mol <sup>-1</sup> ]	$n$	$m$
Pt	$4.6 \pm 0.6 \cdot 10^{-4}$	$2300 \pm 500$	$89 \pm 10$	$0.6 \pm 0.1$	$1 \pm 0.1$
Au	$1.6 \pm 0.6 \cdot 10^{-4}$	$5500 \pm 1000$	$58 \pm 5$	$0.6 \pm 0.1$	$1 \pm 0.1$

$k$ : rate constant;  $K_{\text{Nip}}$ : adsorption constant of Nip;  $K_{\text{BH}_4}$ : adsorption constant of  $\text{BH}_4^-$ ;  $n, m$ : Freundlich-exponents (see eq. (6.4.2)).

This model gives a quantitative explanation of the kinetic data shown in Figure 6.4.3 for both the Pt as well as for the Au-NP. In particular, it explains the mutual dependence of  $k_{app}$  on the concentration of nitrophenol and borohydride: A high concentration of Nip molecules leads to nearly full coverage of the surface of the nanoparticles by Nip. This slows down the reaction with the borohydride ions and the injection of electrons to the metal surface. The non-linear relation of  $k_{app}$  with the borohydride concentration (panels 6.4.3c, d, f) and the saturation at high concentrations indicates directly that there must be a competition of both reactants for reactive sites on the metal surface. As a result there should be an optimal concentration where the reaction rate has a maximum.

The quality of the present comparison of the kinetic model with experimental data may be assessed in more detail by plotting  $k_{app} c_{\text{Nip}}$  versus the product of  $\theta_{\text{BH}_4} \theta_{\text{Nip}}$  according to eq. (6.4.2). Figure 6.4.5 displays the plot related to different concentrations of Nip (6.4.5a) and to different concentrations of borohydride (6.4.5b). The slope of the straight lines gives the product of the kinetic constant  $k$  and the surface  $S$  of the nanoparticles. Given the error propagation through both adsorption isotherms leading to  $\theta_{\text{BH}_4}$  and  $\theta_{\text{Nip}}$ , respectively, Figure 6.4.5 demonstrates that the present fit is a valid description of the kinetic data. Therefore the reduction of Nip can be described by the Langmuir-Hinshelwood ansatz with good accuracy.

As shown in Table 6.1 the adsorption constant for Nip on the Au-NP as well as on the Pt-NP is about 100 times higher than that of  $\text{BH}_4^-$ . The adsorption constant  $K_{\text{Nip}}$  is larger in case of the Au-nanoparticles. However, the kinetic constant  $k$ , which determines the reaction rate of the adsorbed molecules, is considerably smaller in case of Au. Thus, Au nanoparticles are less active catalyst than Pt particles for the reduction of Nip.

Evidently, the present analysis can only lead to the product of the kinetic constant  $k$  and the surface  $S$ , that is,  $k$  is calculated under the assumption that the entire surface of the metal nanoparticles is active. This need not be the case. The exponent  $n = 0.6$  related to the adsorption/desorption equilibrium of Nip points to a heterogeneity of the adsorption sites. It is interesting to note that surface heterogeneities can be directly shown by a study of the reaction kinetics on single nanoparticles by Zhou *et al.*<sup>59</sup> The authors explain the heterogeneities by both catalysis-induced and spontaneous surface restructuring. The present finding of an exponent  $n = 0.6$  may therefore point to the same direction and will be further discussed below.

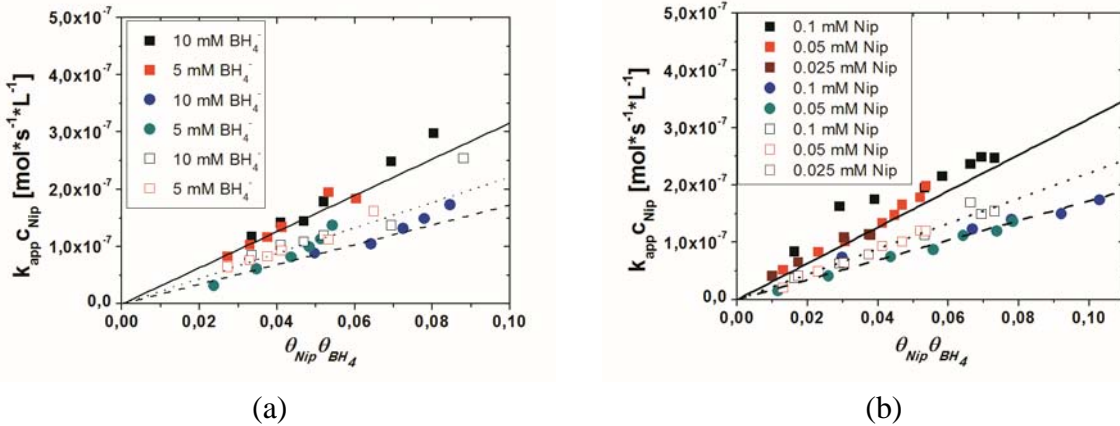


**Figure 6.4.5.** Langmuir-Hinshelwood kinetics of the reduction of nitrophenol. The product of the apparent rate  $k_{app}$  and the concentration of Nip is plotted against the product of  $\theta_{BH_4} \theta_{Nip}$  according to eq.(6.4.2). The lines are the product of the rate constant  $k$  and the surface  $S$  of the different metallic nanoparticles. The squares are related to the Pt-NP (filled squares for the surface area of  $0.00687 \text{ m}^2 \text{ L}^{-1}$  and open squares for a surface area of  $0.00481 \text{ m}^2 \text{ L}^{-1}$ ), whereas the filled circles represent the data deduced for the Au-NP (surface area of  $0.0107 \text{ m}^2 \text{ L}^{-1}$ ). The left hand side of the diagram displays the data referring to the variation of nitrophenol, while the right hand side displays the diagram referring to the variation of sodium borohydride.

As mentioned above, the activation energy of this reaction has been measured by several groups.<sup>12,17,22,24,28,31,32,35,36,39,43</sup> Figure 6.4.6 displays the Arrhenius plot of  $k_I$  and of the reciprocal induction time  $1/t_0$  of the Pt-NP used in the present work. The concentration of Nip and  $BH_4^-$  was 0.1 and 10 mM, respectively. These conditions were chosen to ensure a meaningful comparison with previous work.<sup>12,36,39</sup>

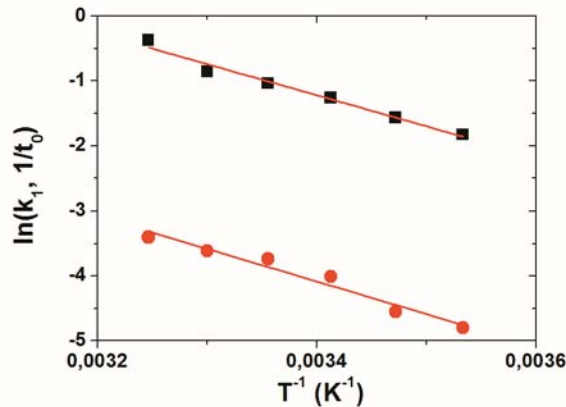


**Figure 6.4.6.** Arrhenius plot of the surface normalized rate constant  $k_I$  (eq. (6.2.1)) and the inverse induction time obtained for Pt nanoparticles. The concentration of Nip and  $BH_4^-$  was 0.1 and 10 mM, respectively. The black squares belong to the surface normalized rate constant  $k_I$  whereas the red circles refer to the invers induction period  $t_0$ .

The activation energy  $E_A$  for the normalized rate constant was  $40 \text{ kJ}\cdot\text{mol}^{-1}$ . This is in good agreement with our previous work for metal nanoparticles where  $E_A$  was found to be  $44 \text{ kJ}$ .<sup>12,36,39</sup> However, the data obtained for  $E_A$  for different systems differ appreciably. For example, Khalavka *et al.* found the activation energy for the CTAB-stabilized gold-rods to be  $38 \text{ kJ}\cdot\text{mol}^{-1}$ .<sup>35</sup> Chang *et al.* reported  $E_A$  of  $52 \text{ kJ}\cdot\text{mol}^{-1}$  for the magnetically recoverable Au-NP.<sup>22</sup> Mahmoud *et al.* compared Pt-nanocubes with nanocubes immobilized on PS-microspheres and obtained an  $E_A$  of  $14 \text{ kJ}\cdot\text{mol}^{-1}$  and  $12 \text{ kJ}\cdot\text{mol}^{-1}$ , respectively.<sup>24</sup> Moreover, Pal and coworkers pointed out that the activation energy is dependent on the surface of the catalyst. Thus, smaller particles exhibit a higher activity due to an increase in the roughness of the available surface.<sup>29</sup>

An activation energy of  $31 \text{ kJ}\cdot\text{mol}^{-1}$  was found for citrate-stabilized Au-NP and  $21 \text{ kJ}\cdot\text{mol}^{-1}$  for calcium alginate stabilized Au-NP.<sup>29,32</sup> Zeng *et al.* came to comparable conclusions in the course of measurements of the activation energy of differently shaped Au-NP. The activation energy varied from partially hollow Au-nanoboxes ( $55 \text{ kJ}\cdot\text{mol}^{-1}$ ), hollow Au-nanoboxes ( $44 \text{ kJ}\cdot\text{mol}^{-1}$ ) to Au-nanocages ( $28 \text{ kJ}\cdot\text{mol}^{-1}$ ).<sup>31</sup> The present analysis demonstrated clearly that  $E_A$  reflects the temperature dependence of the kinetic constants  $k$  and of the two thermodynamic adsorption constants  $K_{Nip}$  and  $K_{BH_4}$ . Evidently, the latter constants may depend quite strongly on the method of immobilizing or stabilizing the nanoparticles. The activation energy is therefore difficult to interpret and additional measurements of the reaction kinetics at different temperatures are necessary.

### **Induction time $t_0$**

It rests to explain the induction time  $t_0$  and its relation to the various parameters. Xia *et al.* have also observed this induction time and they assumed that the rate of adsorption of Nip is a dominant factor to  $t_0$ .<sup>31</sup> However, as already discussed diffusion control can be definitively ruled out for the present system. In the following,  $t_0$  is related to the rate constants  $k$  derived from the above analysis by. Thus,  $1/t_0$  is treated as a reaction rate. This assumption is valid because the dependence of  $1/t_0$  on temperature can be treated by an Arrhenius law. Moreover, the activation energy of  $1/t_0$  is practically the same as  $E_A$  of the apparent rate constant.<sup>12,36,39,43</sup> This was also observed here and the Arrhenius diagram for the Pt-NP used in present study is shown in Figure 6.4.6. It is interesting to note that Zhang *et al.* have observed a similar induction period in the catalytic hydrolysis of borohydride with Ru-NP.<sup>55</sup> They also found that the inverse induction period follows an Arrhenius behaviour which is in accord with the present results.

In Figure 6.4.7a we plot  $t_0$  for all experiments as the function of the concentration of borohydride. Within the present limits of error, the induction period is independent of the concentration of sodium borohydride. This finding clearly rules out that the initial step related to  $t_0$  is attributed to any reaction involving borohydride such as the transfer of a surface-hydrogen species to the metal nanoparticles. However, Figure 6.4.7b demonstrates that the rate  $1/t_0$  normalized to the rate constant  $k$  (see Table 6.1) is linearly dependent on the concentration of Nip, giving a master curve for both Au- and Pt-NP within the experimental

error. This finding suggests that  $t_0$  is related to a slow surface reconstruction that is related to the kinetic constant  $k$  found previously for the stationary surface reaction (see Table 6.1).

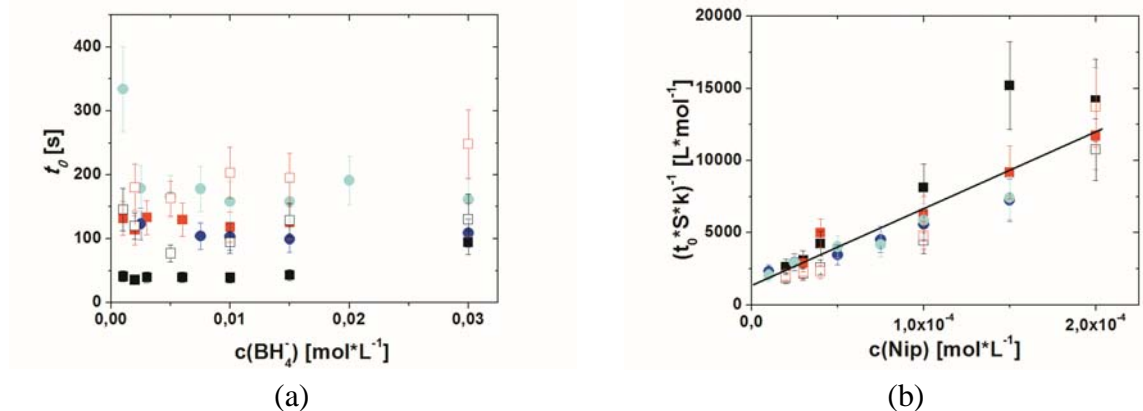


**Figure 6.4.7.** Induction time versus the concentration of  $\text{BH}_4^-$  (a) and of Nip (b). The squares show the data obtained for the Pt-NP. Filled squares refer to the surface area of  $0.00687 \text{ m}^2 \text{ L}^{-1}$  while open squares refer to a surface area of  $0.00481 \text{ m}^2 \text{ L}^{-1}$ . The filled circles represent data obtained for the Au-NP (surface area:  $0.0107 \text{ m}^2 \text{ L}^{-1}$ ). Figure 6.4.7a shows that the induction period is independent of the concentration of  $\text{BH}_4^-$  (a). The black and dark blue color represents a concentration of  $0.1 \text{ mM}$  Nip while the red and light blue color refer to the concentration of  $0.05 \text{ mM}$  Nip. Figure 6.4.7b demonstrates that the inverse induction time normalized by the kinetic constant  $k$  (see Table 6.1) scales linearly with the concentration of Nip. Here the black and dark blue color represents the  $\text{BH}_4^-$  concentration of  $10 \text{ mM}$  and the red and light blue color a concentration of  $5 \text{ mM}$ . The dashed line in Figure 6.4.7b presents a least-square fit of all data indicating a small but finite intercept.

This finding can be explained as follows: Recent work by Zhou *et al.* demonstrated that a time scale in the order of minutes may be caused by processes related to a dynamic restructuring of the surface of the nanoparticles.<sup>59</sup> These authors found a time scale for spontaneous surface restructuring of  $\sim 60 - 250 \text{ s}$  which is in the range of the time scale of  $t_0$  found for the present reaction in our study and by others. Moreover, Zhou *et al.* could clearly demonstrate that the surface restructuring is related to the rate of reaction, that is, the rate of restructuring is directly coupled to the catalysis.<sup>59</sup> In absence of catalytic activity, there is a finite rate of spontaneous surface restructuring which is more notable for small particles. These findings can be directly compared to Figure 6.4.7b where a finite intercept suggests a spontaneous effect on  $t_0$  in absence of Nip as well. Thus, a surface restructuring of the nanoparticles related to the presence of Nip and to the kinetic constant  $k$  seems to be a plausible explanation of the long induction periods for this reaction. However, the nature of the surface restructuring is not known. It may be related to a shift of single atoms or to a concerted rearrangement of surface atoms.<sup>59</sup> The present data only indicate that the restructuring is alleviated by the presence of Nip. Moreover, it is the necessary step that activates the nanoparticles.

## 6.5. Conclusion

In conclusion, we have demonstrated that the catalytic reduction of Nip by borohydride in the presence of metallic nanoparticles (Pt, Au) can be modeled in terms of the Langmuir-Hinshelwood model that assumes the adsorption of both reactants on the surface of the catalyst. The kinetics of the reaction can therefore be described in terms of three constants, a kinetic constant  $k$  describing the surface reactivity of the adsorbed species and the thermodynamic adsorption constants for both components, namely  $K_{Nip}$  for nitrophenol and  $K_{BH_4}$  for borohydride. The induction periods  $t_0$ , that may be of the order of minutes, could be directly related to the rate constant  $k$  found for the rate determining step of the stationary reaction. Most probably,  $t_0$  is related to a slow surface restructuring of the nanoparticles that is directly related to their catalytic activity.

## 6.6. Acknowledgment

Financial support by the Deutsche Forschungsgemeinschaft is gratefully acknowledged.

## 6.7. References

- <sup>1</sup> Astruc, D.; *Nanoparticles and Catalysis*, Wiley-VCH, 2008.
- <sup>2</sup> Narayanan, R.; El-Sayed, M.; *A. J. Phys. Chem. B* **2005**, *109*, 12663-12676.
- <sup>3</sup> Hashmi, A. S.; Hutchings, G. *J. Angew. Chem. Int. Ed.* **2006**, *45*, 7896-7936.
- <sup>4</sup> Astruc, D.; Lu, F.; Aranzaes, J. R. *Angew. Chem. Int. Ed.* **2005**, *44*, 7852-7872.
- <sup>5</sup> Pina, C. D.; Falletta, E.; Prati, L.; Rossi, M. *Chem Soc Rev.* **2008**, *37*, 2077-2095.
- <sup>6</sup> Gong, J.; Mullins, C. B. *Acc. Chem. Res.* **2009**, *42*, 1063-1073.
- <sup>7</sup> Shiju, N. R.; Gulianti, V. V. *Appl. Catal. A* **2009**, *356*, 1-17.
- <sup>8</sup> Haruta, M.; Dáte, M. *Appl. Catal. A* **2001**, *222*, 427-437.
- <sup>9</sup> Campelo, J. M.; Luna, D.; Luque, R.; Marinas, J. M.; Romero, A. A. *ChemSusChem* **2009**, *2*, 18-45.
- <sup>10</sup> Pradhan, N.; Pal, A.; Pal, T. *Colloids Surf. A* **2002**, *196*, 247-257.
- <sup>11</sup> Gosh, S. K.; Mandal, M.; Kundu, S.; Nath, S.; Pal, T. *Appl. Catal. A* **2004**, *268*, 61- 66.
- <sup>12</sup> Mei, Y.; Lu, Y.; Polzer, F.; Ballauff, M. *Chem. Mater.* **2007**, *19*, 1062-1069.
- <sup>13</sup> Kumar, S. S.; Kumar, C. S.; Mathiyarasu, J.; Phani, K. L. *Langmuir* **2007**, *23*, 3401-3408.
- <sup>14</sup> Liu, J.; Qin, G.; Raveendran, P.; Ikushima, Y. *Chem. Europ. J.* **2006**, *12*, 2131-2138.
- <sup>15</sup> Zhang, M.; Liu, L.; Wu, C.; Fu, G.; Zhao, H.; He, B. *Polymer* **2007**, *48*, 1989-1997.
- <sup>16</sup> Gao, Y.; Ding, X.; Zheng, Z.; Cheng, X.; Peng, Y. *Chem. Commun.* **2007**, 3720-3722.

- <sup>17</sup> Chen, X.; Zhao, D.; An, Y.; Zhang, Y.; Cheng, J.; Wang, B.; Shi, L. *J. Colloid Interface Sci.* **2008**, *322*, 414-420.
- <sup>18</sup> Rashid, M. H.; Mandal, T. K. *Adv. Funct. Mater.* **2008**, *18*, 2261-2271.
- <sup>19</sup> Lee, J.; Park, J. C.; Song, H. *Adv. Mater.* **2008**, *20*, 1523-1528.
- <sup>20</sup> Dandapat, A.; Jana, D.; De, G. *Appl. Mater. Interfaces* **2009**, *1*, 833-840.
- <sup>21</sup> Harish, S.; Mathiyarasu, J.; Phani, K. L. N.; Yegnaraman, V. *Catal. Lett.* **2009**, *128*, 197-202.
- <sup>22</sup> Chang, Y.-C.; Chen, D.-H. *J. Hazard. Mater.* **2009**, *165*, 664-669.
- <sup>23</sup> Behrens, S.; Heyman, A.; Maul, R.; Essig, S.; Steigerwald, S.; Quintilla, A.; Wenzel, W.; Bürck, J.; Dgany, O.; Shoseyov, O. *Adv. Mater.* **2009**, *21*, 3515-3519.
- <sup>24</sup> Mahmoud, M. A.; Snyder, B.; El-Sayed, M. A. *J. Phys. Chem. Lett.* **2010**, *1*, 28-31.
- <sup>25</sup> Esumi, K.; Isono, R.; Yoshimura, T. *Langmuir* **2004**, *20*, 237-243.
- <sup>26</sup> Wu, H.; Liu, Z.; Wang, X.; Zhao, B.; Zhang, J.; Li, C. *J. Colloid Interface Sci.* **2006**, *302*, 142-148.
- <sup>27</sup> Wang, Y.; Wei, G.; Zhang, W.; Jiang, X.; Zheng, P.; Shi, L.; Dong, A. *J. Mol. Catal. A* **2007**, *266*, 233-238.
- <sup>28</sup> Kuroda, K.; Ishida, T.; Haruta, M. *J. Mol. Catal. A* **2009**, *298*, 7-11.
- <sup>29</sup> Panigrahi, S.; Basu, S.; Praharaj, S.; Pande, S.; Jana, S.; Pal, A.; Gosh, S. K.; Pal, T. *J. Phys. Chem. C* **2007**, *111*, 4596-4605.
- <sup>30</sup> Zhang, H.; Li, X.; Chen, G. *J. Mater. Chem.* **2009**, *19*, 8223-8231.
- <sup>31</sup> Zeng, J.; Zhang, Q.; Chen, J.; Xia, Y. *Nano. Lett.* **2010**, *10*, 30-35.
- <sup>32</sup> Saha, S.; Pal, A.; Kundu, S.; Basu, S.; Pal, T. *Langmuir* **2010**, *26*, 2885-2893.
- <sup>33</sup> Chin, K. S.; Choi, J.-Y.; Park, C. S.; Jang, H. J.; Kim, K. *Catal. Lett.* **2009**, *133*, 1-7.
- <sup>34</sup> Yang, H.; Nagai, K.; Abe, T.; Homma, H.; Norimatsu, T.; Ramaraj, R. *ACS Appl. Mater. Interfaces* **2009**, *1*, 1860-1864.
- <sup>35</sup> Khalavka, Y.; Becker, J.; Sönnichsen, C. *J. Am. Chem. Soc.* **2009**, *131*, 1871-1875.
- <sup>36</sup> Mei, Y.; Sharma, G.; Lu, Y.; Ballauff, M. *Langmuir* **2005**, *21*, 12229-12234.
- <sup>37</sup> Lu, Y.; Wittemann, A.; Ballauff, M. *Macromol. Rapid Commun.* **2009**, *30*, 806-815.
- <sup>38</sup> Schrinner, M.; Ballauff, M.; Talmon, Y.; Kauffmann, J. T.; Möller, M.; Breu, J. *Science* **2009**, *323*, 617-620.
- <sup>39</sup> Schrinner, S.; Polzer, F.; Mei, Y.; Lu, Y.; Haupt, B.; Ballauff, M.; Göldel, A.; Drechsler, M.; Preussner, J.; Glatzel, U. *Macromol. Chem. Phys.* **2007**, *208*, 1542-1547.
- <sup>40</sup> Sharma, G.; Mei, Y.; Lu, Y.; Ballauff, M.; Irrgang, T.; Proch, S.; Kempe, R. *J. Catal.* **2007**, *246*, 10-14.
- <sup>41</sup> Proch, S.; Mei, Y.; Villanueva, J. M. R.; Lu, Y.; Karpov, A.; Ballauff, M.; Kempe, R. *Adv. Synth. Catal.* **2008**, *350*, 493-500.

- <sup>42</sup> Lu, Y.; Mei, Y.; Schrinner, M.; Ballauff, M.; Möller, M. W.; Breu, J. *J. Phys. Chem. C* **2007**, *111*, 7676-7681.
- <sup>43</sup> Lu, Y.; Mei, Y.; Walker, R.; Ballauff, M.; Drechsler, M. *Polymer* **2006**, *47*, 4985-4995.
- <sup>44</sup> Vannice, M. A. *Reactions*, Springer Science + Business Media 2005.
- <sup>45</sup> Xu, W.; Kong, J. S.; Yeh, Y.-T. E.; Chen, P. *Nature Mater.* **2008**, *7*, 992-996.
- <sup>46</sup> Xu, W.; Kong, J. S.; Chen, P. *J. Phys. Chem. C* **2009**, *113*, 2393-2404.
- <sup>47</sup> Cutnell, J. D.; Johnson, K. W. *Physics 4th Edition* New York: Wiley, 1998, 308.
- <sup>48</sup> Carregal-Romero, S.; Pérez-Juste, J.; Hevès, P.; Liz-Marzán, L.; Mulvaney, P. *Langmuir* **2010**, *26*, 1271-1277.
- <sup>49</sup> Liu, B. H.; Li, Z. B. *J. Power Sources* **2009**, *187*, 527-534.
- <sup>50</sup> Henglein, A.; Lilie, J. *J. Am. Chem. Soc.* **1981**, *103*, 1059-1066.
- <sup>51</sup> Ung, T.; Liz-Marzán, L.; Mulvaney, P. *J. Phys. Chem. B* **1999**, *103*, 6770-6773.
- <sup>52</sup> Sardar, R.; Funston, A. M.; Mulvaney, P.; Murray, R. W. *Langmuir* **2009**, *25*, 13840-13851.
- <sup>53</sup> Guella, G.; Zanchetta, C.; Patton, B.; Miotello, A. *J. Phys. Chem. B* **2006**, *110*, 17024-17033.
- <sup>54</sup> Guella, G.; Patton, B.; Miotello, A. *J. Phys. Chem. C* **2007**, *111*, 18744-18750.
- <sup>55</sup> Zhang, J. S.; Delgass, W. N.; Fisher, T. S.; Gore, J. P. *J. Power sources* **2007**, *164*, 772-781.
- <sup>56</sup> Kaufman, C. M.; Sen, B. *J. Chem. Soc. Dalton Trans.* **1985**, *2*, 307-313.
- <sup>57</sup> Lászlo, K.; Podkoscielny, P.; Daborwski, A. *Langmuir* **2003**, *19*, 5287-5294.
- <sup>58</sup> See the discussion in: Rill, C.; Kolar, Z. I.; Kickelbick, G.; Wolterbeek, H. T.; Peters, J. A. *Langmuir* **2009**, *25*, 2294-2301.
- <sup>59</sup> Zhou, X.; Xu, W.; Liu, G.; Panda, D.; Chen, P. *J. Am. Chem. Soc.* **2010**, *132*, 138-146.

*References*

---

## **7. Synthesis and Analysis of Zwitterionic Spherical Polyelectrolyte Brushes in Aqueous Solution**

*Frank Polzer, Johannes Heigl, Christian Schneider, Matthias Ballauff\**

\*Helmholtz-Zentrum Berlin für Materialien und Energie GmbH, Hahn-Meitner-Platz 1,  
14109 Berlin, Germany, and Department of Physics, Humboldt University Berlin, Newtonstr.  
15, 12489 Berlin, Germany

*Oleg V. Borisov*

Institut Pluridisciplinaire de Recherche sur l'Environnement et les Matériaux, UMR 5254  
CNRS/UPPA, Pau, France, and Institute of Macromolecular Compounds of the Russian  
Academy of Sciences, 199004 St. Petersburg, Russia

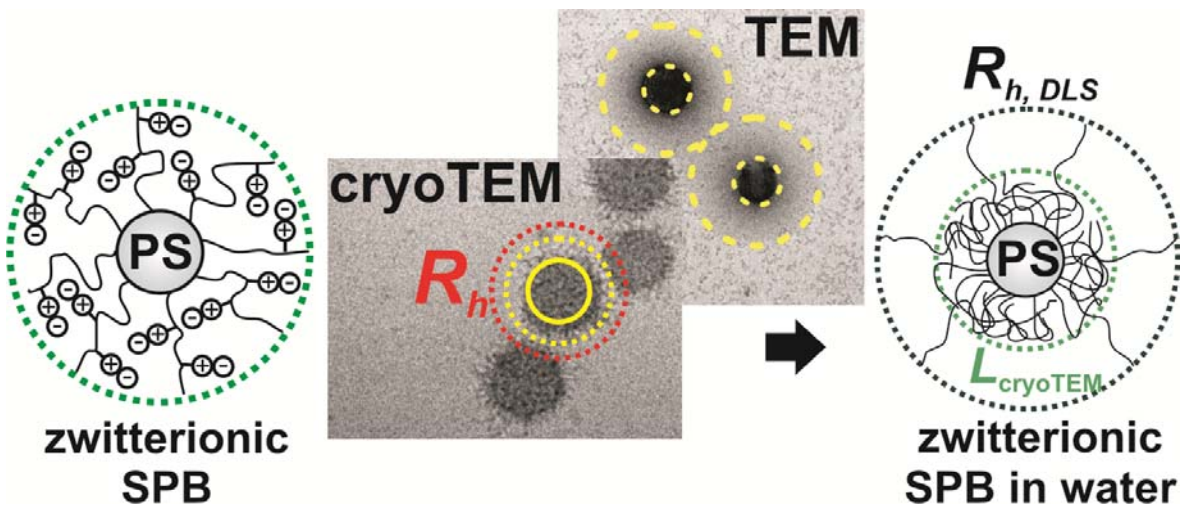
Email: [Matthias.Ballauff@helmholtz-berlin.de](mailto:Matthias.Ballauff@helmholtz-berlin.de)

**Published in Macromolecules**

Reproduced with permission from  
*Macromolecules*, **2011**, *44*, 1654.  
© 2011 American Chemical Society.

**DOI:** [10.1021/ma102927c](https://doi.org/10.1021/ma102927c)

### 7.1. Abstract



We present the synthesis and characterization of spherical polyelectrolyte brush (SPB) particles carrying zwitterionic polyelectrolyte chains. The colloidal particles consist of a divinyl benzene crosslinked poly(styrene) core (PS-co-DVB core) of about 100 nm in diameter onto which linear zwitterionic poly(2-(methacryloyloxy)ethyl dimethyl-(3-sulfopropyl)ammonium hydroxide) (pMEDSAH) chains are chemically grafted via ATRP. Zeta potential measurements demonstrated that the SPB has an electrophoretic mobility due to the net charge of the PS-co-DVB core particles. There is an increase of the brush thickness  $L$  of the zwitterionic brush at high concentrations of sodium chloride at room temperature. Temperature-dependent measurements by dynamic light scattering (DLS) showed that the zwitterionic SPBs swell reversibly with increasing temperature because of the upper critical solution temperature (UCST) of the pMEDSAH chains in water. This effect could be enhanced by the addition of salt. Cryogenic transmission electron microscopy (cryoTEM) showed that the shell of the particles is quite compact at room temperature. However, the hydrodynamic radius as measured by DLS was significantly larger than the particles radius inferred from microscopy. This result is explained in terms of a model in which the shell of the zwitterionic SPB undergoes a phase separation into a dense phase and a few chains sticking out into the aqueous phase.

## 7.2. Introduction

Polyampholytes in general and specifically zwitterionic polymers have become of great importance in the last decades due to their possible applications.<sup>1,2,3</sup> This includes ultra-low fouling coatings and high-tech applications as biocompatible components for drug delivery.<sup>4,5,6</sup> Colloidal polymer brushes in which the radius of gyration of the grafted polymer chains exceeds the average distance between the joints of the polymer chains can be prepared by surface polymerization of attached initiators (grafting-from).<sup>7,8</sup> Up to now, there is a large number of studies devoted to non-charged and charged polymer brushes.<sup>7-8</sup> However, there exists much less work on zwitterionic polyelectrolyte brushes so far. To the authors' best knowledge, there are only a few studies of planar zwitterionic brushes: Azzaroni and co-workers successfully synthesized zwitterionic polymer brushes consisting of poly(2-(Methacryloyloxy)ethyl dimethyl-(3-sulfopropyl)ammonium hydroxide) (pMEDSAH) by grafting-from bromide functionalized gold and silicon dioxide surfaces.<sup>9</sup> They observed hydrophilic and hydrophobic brush regimes depending on the height of the synthesized brush. In a further investigation they showed that one can tune the brush behavior by changing the temperature, which was explained by the upper critical solution temperature (UCST) of polysulfobetains.<sup>10</sup> Using atomic force microscopy and neutron reflectometry Terayama *et al.* showed that planar brushes made from poly(3-dimethyl(methacryloyloxyethyl)ammonium propane (pMPDSAH) swell by the addition of salt in aqueous solution.<sup>11</sup> The interaction of proteins with planar pMEDSAH and poly(1-carboxy-N,N-dimethyl-N-(2'-methacryloyloxyethyl) methanaminium inner salt) (pCBMA) brushes was thoroughly studied by Zhang and co-workers.<sup>12</sup> They observed that these systems possess a high resistance against nonspecific protein adsorption.<sup>13</sup> Moreover, planar brushes of poly(2-methacryloyloxyethyl phosphorylcholine) (pMPC) provide excellent lubrication in aqueous media which makes them promising candidates for applications as boundary lubricants in artificial joints or similar systems.<sup>14, 15</sup>

All systems mentioned so far are planar systems. Since one of the most interesting properties of zwitterionic polymer brushes is their resistance against nonspecific protein adsorption and their biocompatibility, a promising field of application is drug delivery.<sup>16,17,18</sup> Therefore these polyzwitterions were used as coatings for inorganic or organic nanoparticles and colloids such as gold, magnetite or silica nanoparticles, quantum dots, carbon nanotubes or even DNA.<sup>19,20,21,22,23,24</sup> However, the number of systematical studies investigating the solution behavior of zwitterionic SPB in aqueous medium is scarce. Matsuda *et al.* investigated the interactions of a zwitterionic SPB with a silica nanoparticle core and pMPC chains.<sup>25</sup> They observed no salt induced changes of the brush layer of the zwitterionic SPB investigated by DLS. Since pMEDSAH possesses a UCST, temperature dependent measurements were conducted in previous investigations on planar carboxybетaine and sulfobetaine brushes.<sup>26</sup>

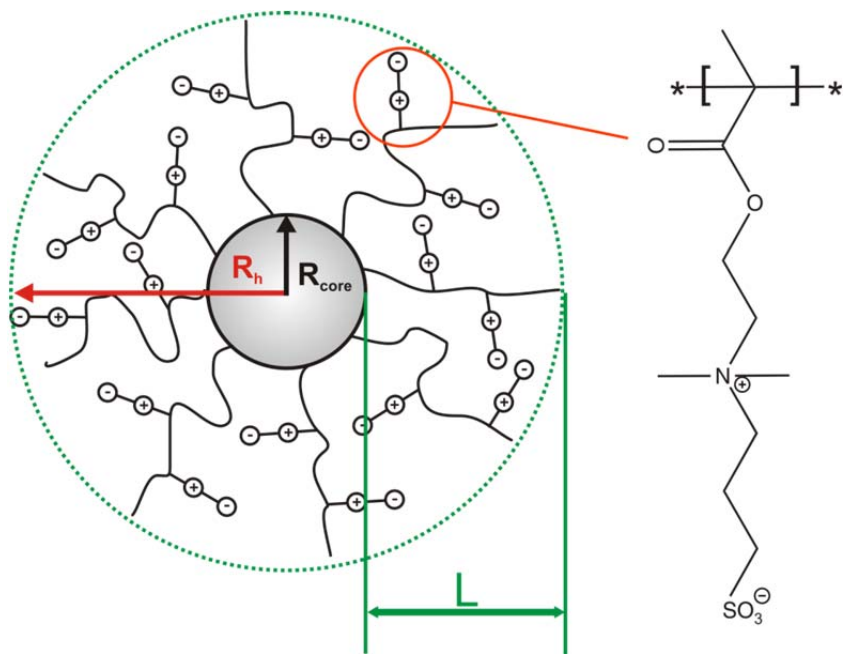


**Figure 7.2.1.** Schematic representation of the zwitterionic SPB with a PS-co-DVB/BIEM core and a shell of polysulfobetaine chains. The shell of the SPB consists of p[2-(Methacryloyloxy)ethyl dimethyl-(3-sulfopropyl)ammonium hydroxide] (pMEDSAH) which forms an inner salt. The brush thickness  $L$  is defined as the difference between the hydrodynamic radius of the core particles  $R_{core}$  and the  $R_h$  of the zwitterionic SPB particles.

Here we present a comprehensive study of a zwitterionic spherical polyelectrolyte brush in aqueous solution. Figure 7.2.1 gives the structure of these particles in a schematic fashion. A shell of densely grafted pMEDSAH has been affixed to nearly monodisperse core particles consisting of PS-co DVB and a thin surface layer of BIEM with a diameter of about 100 nm. Atom transfer radical polymerization (ATRP<sup>27</sup>) is used for grafting these polyzwitterionic chains to the surface. Since the core particles are practically monodisperse, the thickness of the brush layer can be easily monitored by dynamic light scattering (DLS). Moreover, the particles can be studied by cryoTEM in the aqueous phase, that is, *in-situ*. Special emphasis is laid on the dependence of the zwitterionic SPB on the salt concentration at different temperatures.

### 7.3. Experimental Section

**Materials.** All chemicals used in this study were of analytical grade. Styrene (Aldrich) was purified by column chromatography using inhibitor remover for 4-*tert*-butylcatechol (Aldrich) as column material. Copper(I)chloride (Aldrich), bipyridyl (bipy, Aldrich), potassium peroxodisulfate (KPS, Fluka), sodium dodecylsulfate (SDS, Merck), cesium iodide (CsI, Aldrich) and (2-(Methacryloyloxy)ethyl dimethyl-(3-sulfopropyl)ammonium hydroxide)

(MEDSAH, Aldrich) were used as received. In this work we always used 18 MΩ Millipore water.

**Synthesis of BIEM.** The synthesis of the vinyl functionalized ATRP initiator 2-(2-bromoisobutyryloxy) ethyl methacrylate (BIEM) was conducted as reported previously.<sup>28</sup> In a typical run 28.3 g of 2-hydroxyethyl methacrylate (217 mmol) and 20 mL of pyridine (248 mmol) were dissolved in 200 mL of dichlormethane (DCM). The mixture was degassed by bubbling nitrogen to the solution and cooled down in an ice bath. A solution of 50 g (217 mmol) of 2-bromoisobutyryl bromide in 50 mL DCM was slowly added under nitrogen flow using a KDS 100 syringe pump (KD Scientific). The reaction was then stirred for 4 h. The precipitated product was filtered and purified by washing three times with 50 mL of water and dried over MgSO<sub>4</sub>. Flash chromatography with mixtures of n-hexane/ethyl acetate with a ratio of 6:1 was conducted for purification. The successful synthesis of BIEM was proven by H<sup>1</sup>-NMR in CDCl<sub>3</sub>. The NMR spectrum can be found in the supporting information in Figure S7.1.

**Synthesis of PS-co-DVB/BIEM core-shell latex particles.** The core-shell latex particles were synthesized using a conventional emulsion polymerization under starved conditions as described recently.<sup>29</sup> For this purpose, 0.40 g (13.9 mmol) SDS was dissolved in 250 mL of water under stirring. Subsequently 20.16 g (0.19 mol) styrene mixed with 1.30 g (mmol) DVB was added. The polymerization was started by adding 0.30 g KPS dissolved in 15 mL of water to the solution. The reaction was run at 80 °C for one hour. 2.70 g of BIEM dissolved in 7.30 g acetone was added under starved conditions at 70 °C with a dosage rate of 30 mL·h<sup>-1</sup>. The addition of BIEM under starved conditions inhibits new particle formation and ensures the generation of a thin layer of BIEM on the surface of the PS-co-DVB core particles. After the addition was completed, the reaction was stirred at 70 °C for 7 h and then cooled down to room temperature. The dispersion was purified by ultrafiltration against a ten-fold excess of water.

**Synthesis of zwitterionic SPB.** The synthesis of the zwitterionic SPB was conducted using aqueous ATRP. 15 g of a 1 wt % aqueous dispersion of PS-co-DVB/BIEM1 core-shell latex particles, 4.86 g (17.4 mmol) of MEDSAH, 0.5 g (3.2 mmol) bipy and 15 mL of water were given in a flask equipped with a septum. The mixture was bubble with nitrogen for 30 minutes to remove oxygen. Meanwhile 0.16 g (1.6 mmol) of CuCl and 0.26 g (3.5 mmol) of KCl were also degassed by nitrogen treatment in a second vessel equipped with a septum. The polymerization was started by the transfer of the aqueous dispersion to the CuCl/KCl mixture in a second vessel under vigorous stirring and oxygen exclusion via a cannula. The reaction was run at room temperature over night and quenched by the exposition to air. The SPB dispersion was purified by dialysis against a 20 fold excess of water. For the analysis of the molecular weight of the grafted pMEDSAH chains, the SPB were put in 200 mL of 2 M NaOH. The reaction was heated to 100 °C for 10 days under reflux. After that, the mixture was cooled down to room temperature and neutralized with hydrochloric acid. The cleaved chains were separated from the core particles and cleaned by ultrafiltration. Aqueous GPC with poly(methacrylic acid) (pMAA) calibration was used to determine the number average molecular weight  $M_n$  and the molecular weight distribution  $MWD$ .

**Methods.** Dynamic light scattering (DLS) was performed with an ALV 4000 (ALV GmbH, Langen, Germany) light scattering goniometer. Transmission electron microscopy (TEM) and cryogenic transmission electron microscopy (cryoTEM) measurements were conducted with a Zeiss EM922 EFTEM (Zeiss NTS GmbH, Oberkochen, Germany) as described recently.<sup>30</sup> Some of the cryoTEM samples were mixed with CsI solution to increase the contrast of the shell. Therefore the SPB dispersion was diluted with CsI solution to reach a solid content of 0.1 wt % of SPB and the desired concentration of CsI. The molar amount of sulfur of the SPB, and thus the core to shell ratio  $m_c/m_s$ , was determined by inductive-coupled plasma optical emission spectroscopy (ICP-OES) using a Varian Vista-Pro Radial (Agilent Technologies, Santa Clara, USA). Ion chromatography (IC) was used to determine the amount of bromine on the PS-co-DVB/BIEM latex particles. Zeta potential measurements were performed with a Malvern Zetasizer Nano ZS equipped with a 50 mW He-Ne-Laser using folded capillary cells with gold electrodes (Malvern Instruments, UK). The zeta potentials were calculated out of the measured electrophoretic mobilities using the model of O'Brien and White.<sup>31</sup> For this, the software MPEK has been used.<sup>32</sup> Nuclear magnetic resonance spectroscopy (NMR) was conducted with a 250 MHz NMR (Bruker, Billerica, USA). The  $M_n$  and the polydispersity index ( $PDI$ ) of the cleaved polymer chains of the brush layer were determined by aqueous gel permeation chromatography (GPC) with a pMAA calibration.

## 7.4. Results and Discussion

**Synthesis of PS-co-DVB/BIEM core-shell latex particles.** We synthesized two batches of BIEM functionalized latex particles via conventional emulsion polymerization. The reactions differ only in the amount of BIEM used. 9.7 mmol of BIEM were used for the synthesis of the system PS-co-DVB/BIEM1 whereas for PS-co-DVB/BIEM2 the amount was doubled to 19.4 mmol. The mass fraction of bromide according to IC was  $2.3 \pm 0.1$  wt % for PS-co-DVB/BIEM1 and  $4.5 \pm 0.1$  wt % for PS-co-DVB/BIEM2. These results show that the incorporation of the ATRP initiator BIEM is controlled by the amount of BIEM added to the emulsion polymerization. DLS measurements gave a hydrodynamic radius  $R_h$  of  $48.1 \pm 0.2$  nm for the core particles PS-co-DVB/BIEM1 and  $59.9 \pm 0.2$  nm for PS-co-DVB/BIEM2. The increase in  $R_h$  can only be explained by the higher amount of BIEM used for the synthesis of PS-co-DVB/BIEM2 since all other parameters were kept constant.<sup>33</sup> TEM micrographs for both systems presented in Figure S7.2 reveal monodisperse core particles of spherical shape. This was also recently found for emulsion polymerization under starved conditions using a polymerizable photoinitiator for surface functionalization.<sup>34</sup> Small-angle X-ray studies for this type of core-shell latex particles revealed a shell thickness of about 2 nm of the photoinitiator on the surface of the core-shell latex particles.<sup>7</sup> The synthesis of the zwitterionic SPB presented in this study was conducted using the core particles PS-co-DVB/BIEM1.

### Synthesis of zwitterionic SPB.

A schematic representation of the complete synthesis of the zwitterionic SPB is given in Figure 7.4.1. The zwitterionic SPB with pMEDSAH chains were synthesized by aqueous ATRP using PS-co-DVB/BIEM1 core particles as the macroinitiator. The reactions were carried out under exclusion of oxygen to prevent oxidation of the catalyst Cu(I)Cl. This could be easily recognized by the color of the bipy-CuCl complex formed in water. The Cu(I) complex was of brownish color whereas the Cu(II) complex was of turquoise color and results after quenching of the reaction mixture with air. After intensive purification by dialysis, the zwitterionic SPB was characterized by DLS measurements at room temperature which gave a  $R_h$  of  $95.0 \pm 2.2$  nm. Thus  $R_h$  increased about 47 nm due to the generation of the pMEDSAH shell as compared to the bare core particles. This increase of  $R_h$  is in the same range as reported for the shell synthesis via a free radical polymerization described for anionic and cationic SPBs.<sup>34</sup> The ratio  $m_c/m_s$  was determined to  $2.06 \pm 0.25$  according to ICP-OES measurements of the sulfur content of the SPB. This value is higher than for SPBs prepared in earlier investigations by free radical photoemulsion polymerization. An explanation for this result is the higher molecular weight of the monomer used in this study. Furthermore, analysis of the cleaved polymer chains by GPC as displayed in Figure S7.3 revealed a  $M_n$  of about  $60.000 \text{ g} \cdot \text{mol}^{-1}$  with a polydispersity index of 1.16. The determination of absolute molecular weights by aqueous GPC using a pMAA calibration should be discussed with caution.

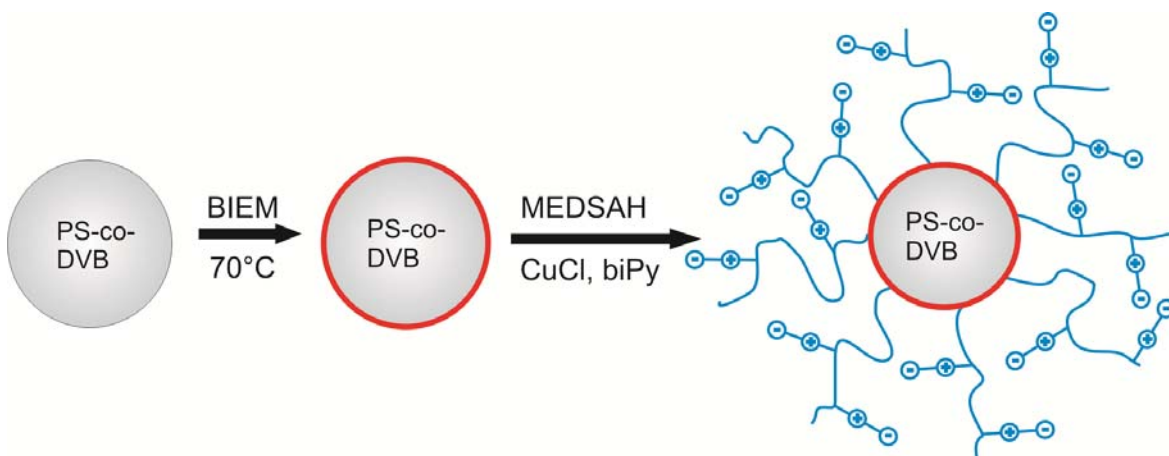


**Figure 7.4.1.** Scheme of the synthesis of zwitterionic SPB particles with pMEDSAH chains. In the first step, a PS-co-DVB latex particle is functionalized by the addition of ATRP initiator BIEM (red layer) in an emulsion polymerization under starved conditions. The pMEDSAH chains are covalently attached to the PS-co-DVB/BIEM particles via ATRP in aqueous solution.

Compared to SPBs generated by photoemulsion polymerization, the *PDI* is about two times lower.<sup>34</sup> This is due to the use of a controlled living radical polymerization instead of a free radical polymerization. A *PDI* of 1.16 is a satisfactory result for aqueous ATRP considering the fact that water-based ATRP is a fast polymerization process and therefore difficult to

control.<sup>35</sup> The grafting density was calculated to be  $0.08 \pm 0.01 \text{ nm}^{-2}$  based on  $R_{\text{core}}$ ,  $m_c/m_s$  and the degree of polymerization  $DP$  of the polymer chains in the shell. This grafting density is in the same order of magnitude as found for the grafting-from process using latex spheres as macroinitiators.<sup>36</sup> The value verifies that the generated zwitterionic core shell particles are within the limits of a spherical polymer brush.

Zeta potential measurements have been conducted to elucidate the net charge of the particles. In principle, the pMEDSAH brush particles should exhibit charge neutrality due to their zwitterionic nature. Therefore the zeta potential should be zero. However, electrophoretic mobility measurements of the zwitterionic SPB as a function of the KCl concentration reveal a negative zeta potential, as shown in Figure 7.4.2. Mary *et al.* also observed negative zeta potentials for linear pMEDSAH chains in their study.<sup>26</sup> The authors explained this effect by a partial hydrolysis of the ester bond of the side chain of MEDSAH during the synthesis of the polymer. This leads to a statistical random copolymer of pMEDSAH and pMAA which was proven by NMR spectroscopy. Since pMAA is partially deprotonated a negative excess charge is observed in aqueous solution. However, the particle synthesis presented here is performed in neutral medium so that hydrolysis of the chains is negligible small.

To investigate the negative zeta potential of the zwitterionic SPB particles in more detail, electrophoretic mobility experiments as a function of the KCl concentration were performed using the core particles before the grafting of the zwitterionic shell. The results are plotted in Figure 7.4.2. Here a negative zeta potential is observed as well which decreases towards zero with increasing salt content. The negative charge is due to KPS and anionic surfactant residues incorporated during the synthesis of the core particles which are present even after extensive cleaning.

The relation of the zeta potential  $\zeta$  to the surface charge as a function of the salt concentration for homogeneous spheres with an electrokinetic charge  $Q_{ek}$  is given by<sup>37</sup>

$$Q_{ek} = \frac{2R_h(1+R_h\kappa)}{l_B} \sin\left(\frac{ez\zeta}{2k_B T}\right) \quad (7.4.1)$$

where  $\kappa$  is the inverse Debye length,  $l_B$  is the Bjerrum length,  $e$  is the charge of an electron,  $z$  is the valence of the counter ions,  $k_B T$  is the thermal energy and  $a$  is the hydrodynamic radius of the colloids. Eq (7.4.1) can be used to fit the experimental data of the zeta potential where  $Q_{ek}$  is the only fitting parameter.<sup>38</sup> Furthermore,  $Q_{ek}$  is assumed to be constant and independent of the salt concentration. The respective fits are shown in Figure 7.4.2 (solid and broken lines). For both, the bare core and the SPB particles, good fits over three orders of magnitude in salt concentration could be achieved. The resulting electrokinetic charge densities are  $-2 \cdot 10^{-2} \text{ C} \cdot \text{m}^{-2}$  for the core particles and  $-1 \cdot 10^{-2} \text{ C} \cdot \text{m}^{-2}$  for the zwitterionic SPBs, respectively. Since the charge density of the SPB particles is smaller than the charge on the bare particles, there can be no additional contribution of any negative charges arising from the zwitterionic shell. Therefore, we conclude that the zeta potential of the zwitterionic SPBs is caused by the negative excess charges located on the surface of the core particles.

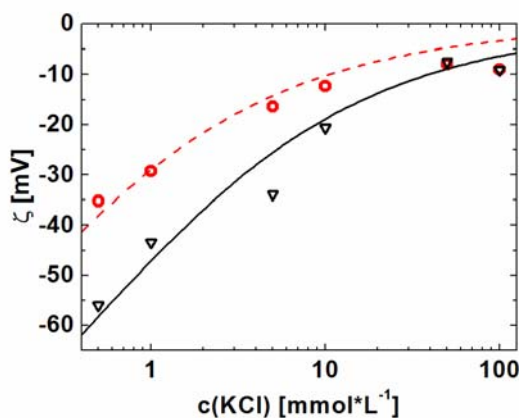


**Figure 7.4.2.** Measurements of the zeta potential  $\zeta$  of the zwitterionic SPB with pMEDSAH chains (○) and of the bare PS-co-DVB/BIEM latex particles ( $\nabla$ ) in dependence of the concentration of KCl. The lines show the best fit results of the zeta potential data for both systems using eq. (7.4.1) with a constant particle charge. The data points for the SPB and the bare core particles fall together at the two highest salt concentrations.

We now turn to the discussion of the TEM micrographs of the zwitterionic SPB. The contrast of the pMEDSAH shell of the particles was increased by adding CsI to the dispersion. This is due to the fact that both the  $\text{Cs}^+$ -ion and the  $\text{I}^-$ -ion act as counter ions in the shell which improves the electron contrast considerably (see Figure 7.4.3). The PS-co-DVB/BIEM core particles are visible as dark spherical objects with a characteristic size of about 100 nm in diameter. This size is in good agreement with DLS measurements of the bare core particles. Figure 7.4.3a also shows spherical shaped shells around each core particle due to the grafted pMEDSAH chains, which are marked with yellow dotted circles. Measurements of the shell thickness in the dried state according to the TEM micrographs reveal values of about 110 nm resulting in an overall radius of the SPB of about 160 nm. The chains of the shell are fully stretched when the particles are immobilized on a TEM grid. This indicates an attractive interaction of the zwitterionic chains with the carbon support (see Figure 7.4.3c). The effect is due to the pretreatment of the grids by a glim charge which generates negative surface charges on the support film and thus makes the support more hydrophilic. The surface charge of the carbon film then interacts with the charges of the pMEDSAH chains.<sup>39</sup>

Compared to the hydrodynamic shell thickness  $L$  of the dispersed zwitterionic SPB there is a discrepancy to the TEM shell thickness in the dried state of about 60 nm. This finding can be explained by the fact that the shell is not in a fully stretched state when the SPB particles are dispersed in water. The difference of the TEM images in which a fully stretched state is visible and the results from DLS measurements points out that the shell is in a collapsed state in aqueous solution.

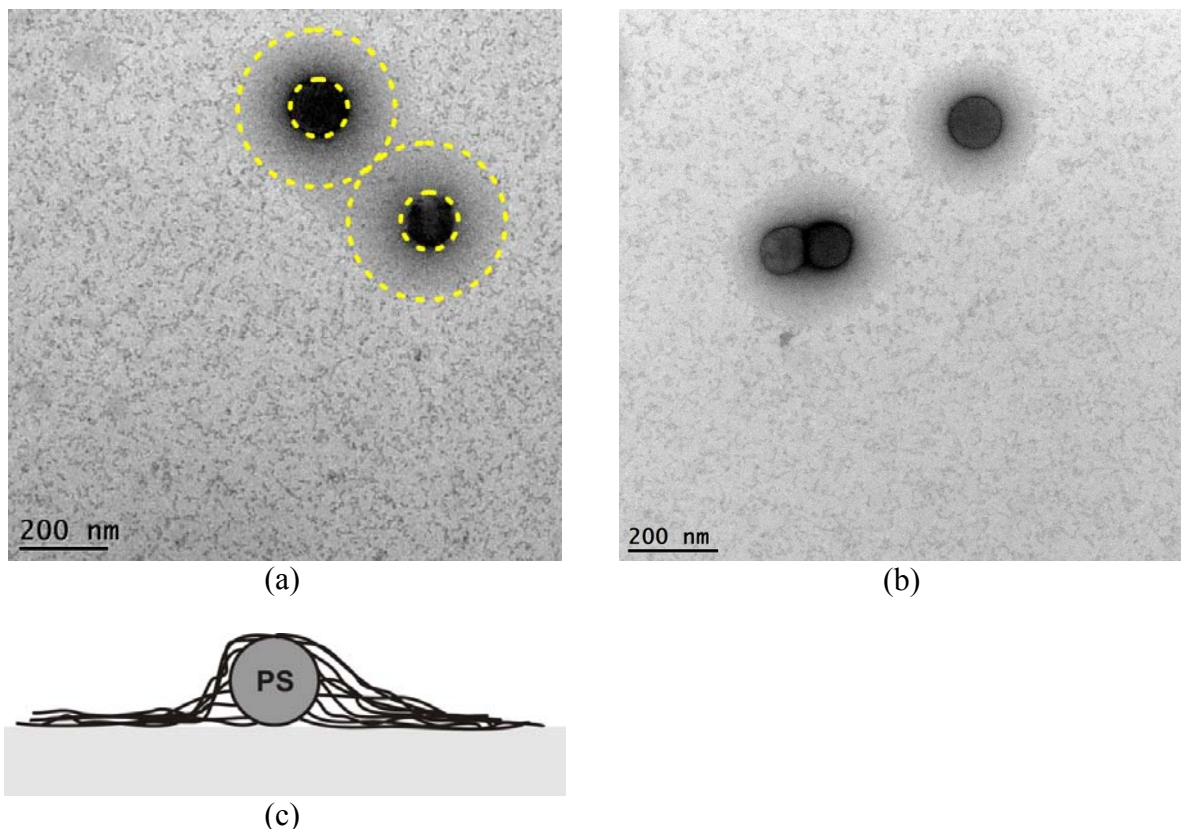


**Figure 7.4.3.** TEM micrographs of the zwitterionic SPB prepared on a carbon support. A 0.1 M CsI solution has been used to enhance the contrast of the shell. The lower part displays the structure of the particles on the surface in a schematic fashion.

To obtain detailed microscopic information of the zwitterionic SPB in aqueous solution, cryoTEM measurements have been conducted.<sup>40,41</sup> Figure 7.4.4 shows cryoTEM micrographs of the zwitterionic system dispersed in salt-free solution and in 0.1 M CsI solutions.

Figure 7.4.4a shows the dispersed zwitterionic SPB in non-saline environment. The radius of the particles increased compared to the radius of the bare core particles. Additionally, the surface of the SPB is corrugated because of the pMEDSAH shell on the core particles. Vitrifying the particles in 0.1 M CsI solution leads to a significant increase in the electron density of the shell as it can be seen in the cryoTEM micrographs in Figure 7.4.4b. In this way the shell can be visualized in a much better way. However, subsequent DLS data (see the discussion of Figure 7.4.4 below) demonstrates that the addition of salt in this concentration regime does not alter the conformation of the shell.

In Figure 7.4.4b the pMEDSAH chains of the shell are clearly visible due to the presence of CsI. The radius of the particles is about 80 nm. Figure 7.4.4b demonstrates that a closed shell of pMEDSAH is grafted onto the PS-co-DVB/BIEM core-shell latex particles. That directly proves that a closed shell of BIEM has been generated by the emulsion polymerization under starved conditions which is in agreement with past studies.<sup>7</sup> The deviation between the results for  $L$  and the shell thickness observed by cryoTEM gives important information about the conformation of the pMEDSAH shell of the zwitterionic SPB. The cryoTEM images show a shell thickness of pMEDSAH chains of about 32 nm, whereas  $L$  obtained by DLS is about 48

nm. The fact that the shell thickness according to cryoTEM and DLS differs can be explained by the fact that in light scattering the particle size is determined by the longest chains of the SPB.<sup>42</sup> The longest or most stretched pMEDSAH chains are not visible in the cryoTEM images because of the poor contrast of single polymer chains even after introducing CsI to the solution.

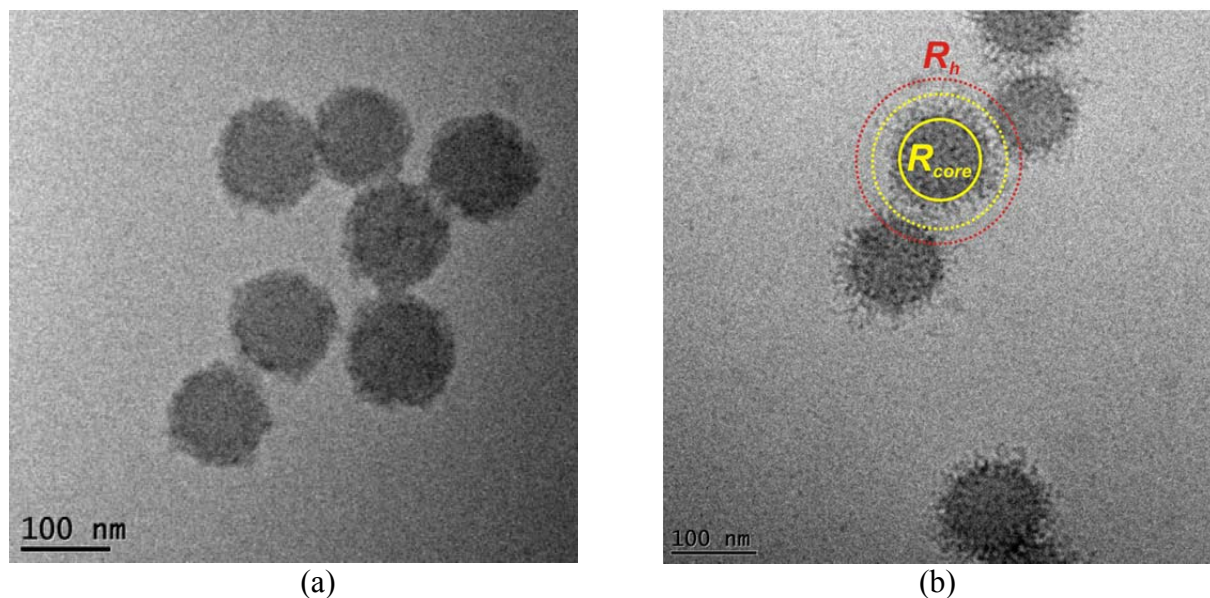


**Figure 7.4.4.** CryoTEM micrographs of the zwitterionic SPB in aqueous solution without any salt (a), and in 0.1 M CsI solution (b). Figure 7.4.4b includes hydrodynamic radii of the bare core particles  $R_{core}$  and of the core-shell particles  $R_h$  as determined by DLS.

This leads us to the conclusion that the zwitterionic shell of the SPB is not fully stretched in the dispersed state. Most of the chains are collapsed so that a layer of about 40 nm thickness results. Only a few chains stretch further away from the core and thus cause the measured  $L$  in the DLS experiment. This behavior is schematically depicted in Figure 7.4.5 and is in qualitative agreement with the model derived from Wagner *et al.*<sup>43</sup> These authors considered a collapse transition in a polymer brush caused by formation of clusters comprising  $n \geq 3$  monomer groups.<sup>43</sup> In our case, we can expect association of  $n \geq 3$  dipole groups inside the brush into stable clusters. Furthermore, the formation of stable clusters can also be induced by hydrophobic interactions of the polymer backbone of the pMEDSAH chains. Both effects lead to a collapse transition accompanied by the microphase segregation inside the brush: A dense phase is formed close to the grafting surface whereas the sparse periphery of the brush is formed by more extended chains. Thus, this phase separation causes a bimodal distribution of the polymer chains with respect to their extension. A similar trend has also been predicted for the complexation of polymer brushes with surfactants.<sup>44</sup> In the present case, water represents the poor solvent for the pMEDSAH chains, which leads to a collapse of the shell polymer.<sup>45</sup> A part of the pMEDSAH chains is not included in the surface-near layer leading to an internal phase separation which causes a lateral inhomogeneity. The chains in the dilute swollen layer

of the shell extend further out into the solution and cause a significant contribution to  $L$  in the DLS experiments.

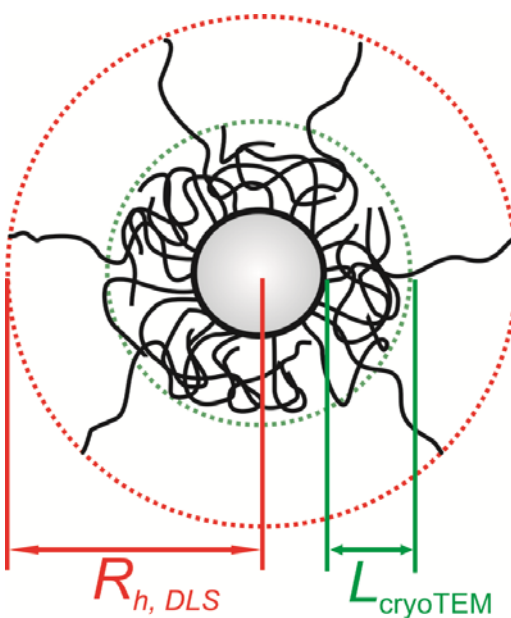


**Figure 7.4.5.** Model for the zwitterionic SPB in aqueous solution. In a poor solvent, e.g. in water, most of the chains are in a collapsed state. Only a small portion of the chains is stretched further away into solution. This fact is revealed by comparing the shell thickness observed in cryoTEM micrographs with the results for  $L$  determined by DLS. Thus, the shell of the zwitterionic SPB undergoes a phase separation into a condensed phase near the surface of the core particles and a dilute swollen layer of the shell which extends far into the solution.

Since in the model shown in Figure 7.4.5 the majority of the pMEDSAH chains are in a collapsed state, investigations have been conducted to elucidate if this structure can be influenced by external stimuli. Therefore DLS measurements of the core-shell particles at different concentrations of NaCl have been done. Figure 7.4.6 shows the results of the salt-dependent measurements. There is no notable increase in  $L$  of the zwitterionic SPB within the limits of error upon salt addition up to concentrations of  $0.5 \text{ mol}\cdot\text{L}^{-1}$ . These results are in good agreement with those of Matsuda and co-workers who also did not observe a swelling of the zwitterionic pMPC shell upon the addition of up to  $0.5 \text{ mol}\cdot\text{L}^{-1}$  salt.<sup>25</sup> They conclude that the chains are already fully extended even in non-saline solution due to the excluded volume effect of densely packed polymer chains in polymer brushes. However, Figure 7.4.6 indicates an increase of  $L$  starting at salt concentrations higher than  $0.5 \text{ mol}\cdot\text{L}^{-1}$ , which results in a 40 % higher  $L$  at  $2 \text{ mol}\cdot\text{L}^{-1}$  as compared to the non-saline state. The increase in  $L$  shows that the SPB shell is not fully extended in the non-saline state, which is in full accordance with the model proposed in Figure 7.4.5.

Figure 7.4.6 demonstrates that the solution behavior of the pMEDSAH chains is changed, if the salt concentration is sufficiently high. The observation that the onset of the swelling of the shell takes place at concentrations higher than  $0.5 \text{ mol}\cdot\text{L}^{-1}$  indicates that the swelling cannot be

related to the conventional anti-polyelectrolyte effect. The anti-polyelectrolyte effect is generally understood as a Coulomb screening effect which is typically observed for salt concentration up to  $0.01 \text{ mol}\cdot\text{L}^{-1}$ .<sup>46</sup> The response of the pMEDSAH shell at salt concentrations higher than  $0.5 \text{ mol}\cdot\text{L}^{-1}$  suggests that ion-specific and hydrophobic interactions may play a role in these systems.<sup>47</sup> An alternative explanation may be sought in the breaking of salt bridges in the zwitterionic layer that occurs only at high salt concentrations.<sup>48</sup>

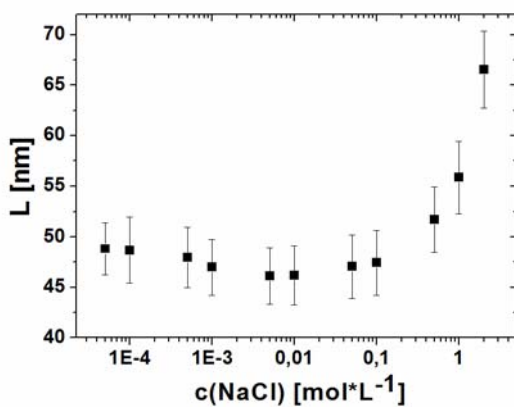


**Figure 7.4.6.** Salt dependent measurements of  $L$  of the zwitterionic SPB via DLS at a temperature of  $25 \text{ }^\circ\text{C}$ . The pMEDSAH shell shows a swelling of  $L$  at concentrations of NaCl higher than  $0.5 \text{ mol}\cdot\text{L}^{-1}$ .

We now turn to the investigations of the temperature-dependent behavior of the zwitterionic SPB. Figure 7.4.7 demonstrates that there is an increase in  $L$  of about 7 nm upon heating. The results for the cooling and reheating fully agree and show a good reproducibility. The stretching of the shell at high temperatures is due to the UCST behavior of the pMEDSAH chains. At higher temperatures, the solvent quality will increase for pMEDSAH chains due to their UCST temperature. This has been found by different groups in earlier works on planar brushes.<sup>9,10</sup>

In the system under consideration here, the expansion of the shell is not very pronounced as compared to the salt-dependent measurements presented in Figure 7.4.6. Since the results of the previous paragraph showed that the addition of high amounts of salt significantly increased  $L$  at room temperature, temperature-dependent DLS measurements at different salt concentrations have been conducted.

The results of these measurements are also presented in Figure 7.4.7 and show two important effects: On the one hand,  $L$  significantly increases at room temperature at salt concentrations higher than  $1 \text{ mol}\cdot\text{L}^{-1}$ . This finding has been shown earlier in Figure 7.4.6. Additionally, temperature cycles at different salt concentrations reveal a drastic swelling of the zwitterionic shell upon heating. This is due to the increase of the solvent quality for the zwitterionic polymer chains. The UCST behavior gets more pronounced after the addition of salt which was expected since both, the salt concentrations and the temperature, are increasing the solubility of the pMEDSAH chains. The influence of the amount of added salt onto the UCST of pMEDSAH homopolymer was also observed by Mary *et al.*<sup>26</sup>

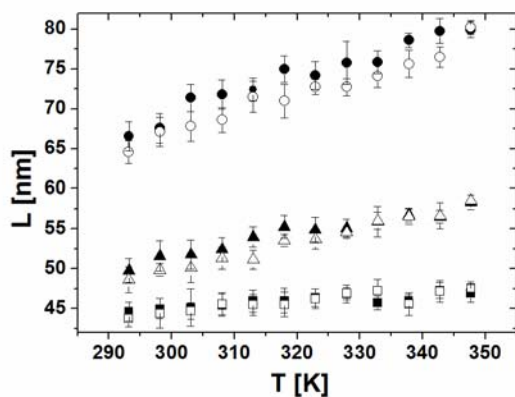


**Figure 7.4.7.** Temperature dependent measurements of  $L$  of the zwitterionic SPB with pMEDSAH chains by DLS. Increasing the temperature from 20 °C to 75 °C leads to a swelling of the brush layer of the zwitterionic SPB. The behavior is completely reversible, which was shown by subsequent cooling of the system. Therefore it can be assigned to the UCST of the pMEDSAH chains. The effect of swelling can be significantly enhanced by the addition of high amounts of salt. The lowest dataset represents a heating cycle of the zwitterionic SPB in salt-free solution (■ heating and □ cooling), the second curve shows the swelling of the zwitterionic SPB in 1 mol·L<sup>-1</sup> NaCl solution (▲ heating and △ cooling) and 2 mol·L<sup>-1</sup> NaCl solution for the uppermost curve (● heating and ○ cooling).

## 7.5. Conclusion

We presented a method for the synthesis of colloidal stable spherical polymer brushes with a zwitterionic brush layer of pMEDSAH chains. The extension of the shell can be influenced upon the addition of salt which may be due to ion-specific interactions. Furthermore, the zwitterionic shell showed a fully reversible swelling upon heating due to the UCST behavior of the pMEDSAH chains. This effect could be enhanced upon the addition of salt. By a combination of DLS, TEM and cryoTEM measurements we propose a model for the zwitterionic SPB including an internal phase separation of the pMEDSAH shell according to Wagner *et al.*<sup>43</sup> In this model the shell is mostly collapsed in a condensed state near the surface of the core particles whereas only a small portion of the shell is in a dilute swollen state with the pMEDSAH chains extending far out into solution.

## 7.6. Acknowledgements

We thank the Deutsche Forschungsgemeinschaft, Sonderforschungsbereich 840 Bayreuth. C.S. thanks the Elite Study Program Macromolecular Science in the Elite Network Bavaria and the Bavarian Graduate Support Program for financial support. We thank R. Hill for the extensive support provided for using the MPEK software and J. Dzubiella for helpful discussions.

## 7.7. Supporting Information

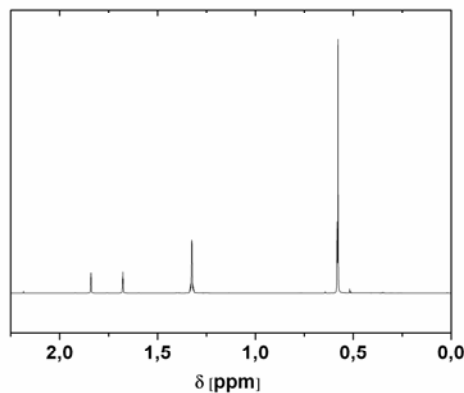


**Figure S7.1.**  $^1\text{H}$ -NMR of BIEM (250 MHz,  $\text{CDCl}_3$ ).  $\delta$  (ppm) = 6.07 (1H, s), 5.53 (1H, s), 4.35 (4H, t), 1.87 (3H, dd), 1.86 (6H, s).  $^{13}\text{C}$ -NMR (62.5 MHz,  $\text{CDCl}_3$ ) d (ppm) = 170.2, 135.7, 126.2, 63.4, 61.7, 54.9, 30.4, 18.3.

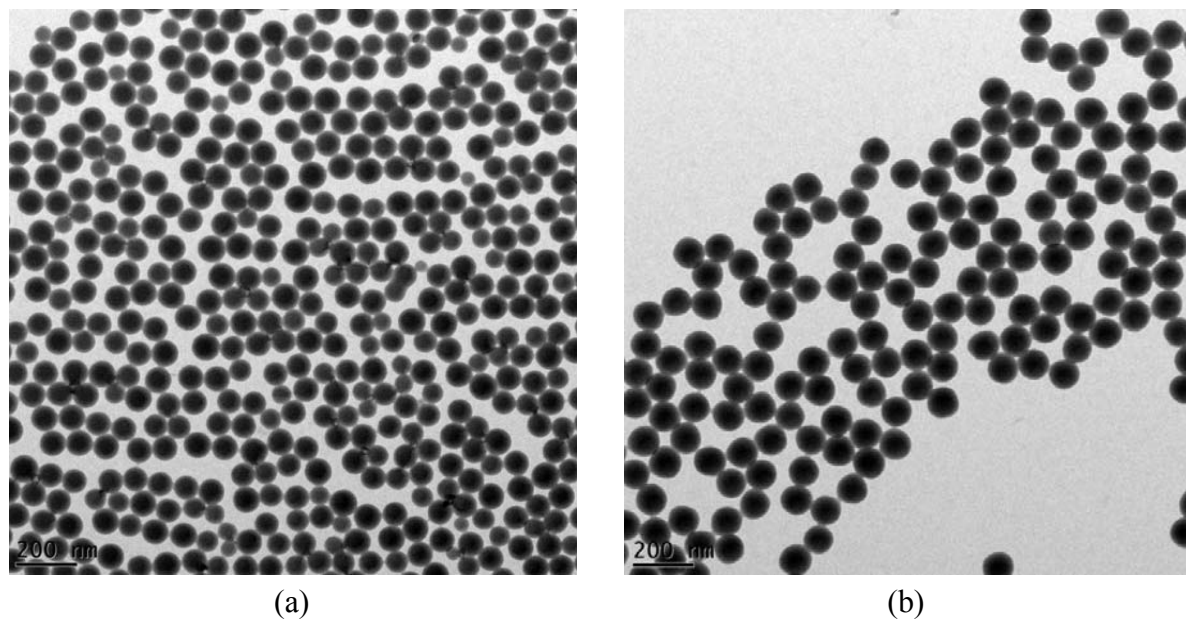


**Figure S7.2.** TEM micrographs of PS/BIEM1 (a) and PS-co-DVB/BIEM2 (b) core particles. The particles show a narrow size distribution with an average  $R_{core}$  of  $48.1 \pm 0.2$  nm for the core particles PS-co-DVB/BIEM1 and  $59.9 \pm 0.2$  nm for PS-co-DVB/BIEM2 according to DLS.

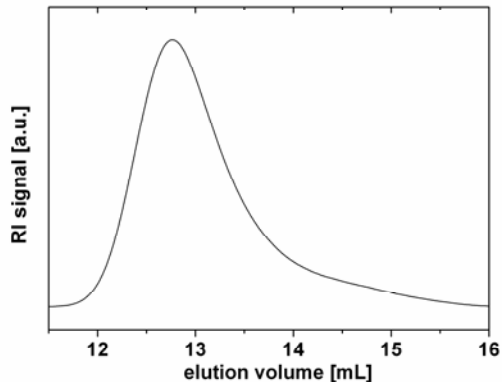


**Figure S7.3.** GPC curve of the cleaved chains of the brush polymer with a  $PDI$  of 1.16. The GPC was calibrated with pMAA standard.

## 7.8. References

- <sup>1</sup> Kudaibergenov, S. E.; Cifferi, A. *Macromol. Rapid Comm.* **2007**, 28, 1969-1986.
- <sup>2</sup> Kudaibergenov, S. E.; Jaeger, W.; Laschewsky, A. *Adv. Polym. Sci.* **2006**, 201, 157-224.
- <sup>3</sup> Das, M.; Sanson, N.; Kumacheva, E. *Chem. Rev.* **2008**, 20, 7157-7163.
- <sup>4</sup> Zhang, Z.; Finlay, J. A.; Wang, L.; Gao, Y.; Callow, J. A.; Callow, M. E.; Jinag, S. *Langmuir* **2009**, 25, 13516-13521.
- <sup>5</sup> Matsuno, R.; Ishihara, K. *Macromol. Symp.* **2009**, 279, 125-131.
- <sup>6</sup> Cho, A. K.; Kong, B.; Choi, I. S. *Langmuir* **2007**, 23, 5678-5682.
- <sup>7</sup> Ballauff, M. *Prog. Polym. Sci.* **2007**, 32, 1135-1151.
- <sup>8</sup> Advincula, R. C.; Brittain, W. J.; Caster, K. C.; Rühe, J. editors *Polymer Brushes*; Wiley-VCH: Weinheim, 2005.
- <sup>9</sup> Azaroni, O.; Brown, A. A.; Huck, W. T. S. *Angew. Chem.* **2006**, 118, 1802-1806.
- <sup>10</sup> Cheng, N.; Brown, A. A.; Azaroni, O.; Huck, W. T. S. *Macromolecules* **2008**, 41, 6317-6321.
- <sup>11</sup> Terayama, Y.; Kikuchi, M.; Kobayashi, M.; Hino, M.; Takahara, A. *J. Phys.: Conf. Ser.* **2009**, 184, 012011.
- <sup>12</sup> Zhang, Z.; Chao, T.; Chen, S.; Jiang, S. *Langmuir* **2006**, 22, 10072-10077.
- <sup>13</sup> Ladd, J.; Zhang, Z.; Chen, S.; Hower, J. C.; Jiang, S. *Biomacromolecules* **2008**, 9, 1357-1361.
- <sup>14</sup> Chen, M.; Briscoe, W. H.; Armes, S. P.; Klein, J. *Science* **2009**, 323, 1698-1701.
- <sup>15</sup> Kobayashi, M.; Terayama, Y.; Hosaka, N.; Kaido, M.; Suzuki, A.; Yamada, N.; Torikai, N.; Ishihara, K.; Takahara, A. *Soft Matter* **2007**, 3, 740-746.
- <sup>16</sup> Li, G.; Xue, H.; Gao, C.; Zhang, F.; Jiang, S. *Macromolecules* **2010**, 43, 14-16.
- <sup>17</sup> Lobb, E.; Ma, I.; Billingham, N. C.; Lewis, A. L.; Armes, S. P. *J. Am. Chem. Soc.* **2001**, 123, 7913-7914.
- <sup>18</sup> Matsuura, K.; Ohno, K.; Kagaya, S.; Kitano, H. *Macromol. Chem. Phys.* **2007**, 208, 862-873.
- <sup>19</sup> Yuan, J. J.; Schmid, A.; Armes, S. P. *Langmuir* **2006**, 22, 10022-10027.
- <sup>20</sup> Yuan, J. J.; Armes, S. P.; Takabayashi Y.; Prassides, K.; Leite, C. A. P.; Galembeck, F.; Lewis, A. L. M.; Schmid, A. *Langmuir* **2006**, 22, 10989-10993.
- <sup>21</sup> Yokohama, R.; Suzuki, S.; Shirai, K.; Yamauchi, T.; Tsubokawa, N.; Tsuchimochi, M. *Eur. Polym. J.* **2006**, 42, 3221-3229.
- <sup>22</sup> Matsuno, R.; Goto, Y.; Konno, T.; Takai, M.; Ishihara, K. *J. Nanosci. Nanotech.* **2009**, 9, 358-365.
- <sup>23</sup> Narain, R.; Housni, A.; Lane, L. *J. Polym. Sci. A* **2006**, 44, 6558-6568.
- <sup>24</sup> Giacomelli, C.; LeMen, L.; Borsali, R.; Him, J. L.-K.; Brisson, A.; Armes, S. P. *Biomacromolecules* **2006**, 7, 817-828.

- <sup>25</sup> Matsuda, Y.; Kobayashi, M.; Annaka, M.; Ishihara, K.; Takahara, A. *Langmuir* **2008**, *24*, 8772-8778.
- <sup>26</sup> Mary, P.; Bendejacq, D. D.; Labeau, M.-P.; Dupuis, P. *J. Phys. Chem. B* **2007**, *111*, 7767-7777.
- <sup>27</sup> Qiu, J.; Charleux, B.; Matyjaszewski, K. *Prog. Polym. Sci.* **2001**, *26*, 2083-2134.
- <sup>28</sup> Podwika, M.; Gaynor, G. S.; Kulfan, A.; Matyjaszewski, K. *Macromolecules* **1997**, *30*, 5192-5194.
- <sup>29</sup> Zhang, M.; Liu, L.; Zhao, H.; Yang, Y.; Fu, G.; He, B. *J. Colloid Interface Sci.* **2006**, *301*, 85-91.
- <sup>30</sup> Crassous, J. J.; Rochette, C. N.; Wittemann, A.; Schrinner, M.; Drechsler, M.; Ballauff, M. *Langmuir* **2009**, *25*, 7862-7871.
- <sup>31</sup> O'Brien, R. W.; White, L. R. *J. Chem. Soc. Faraday Trans II* **1978**, *2*, 1607-1626.
- <sup>32</sup> The manual for the MPEK-software package can be download from Reghan J. Hill from: <http://people.mcgill.ca/files/reghan.hill/MPEK-0.02.pdf>
- <sup>33</sup> Song, J.-S.; Winnik, M. A. *Macromolecules* **1995**, *38*, 8300-8307.
- <sup>34</sup> Guo, X.; Ballauff, M. *Langmuir* **2000**, *16*, 8719-8726.
- <sup>35</sup> Qiu, J.; Charleux, B.; Matyjaszewski, K. *Prog. Polym. Sci.* **2001**, *26*, 2083-2134.
- <sup>36</sup> Schrinner, M.; Haupt, B.; Wittemann, A. *Chem. Eng. J.* **2008**, *144*, 138-145.
- <sup>37</sup> Hanus, L. H.; Hartzler, R. U.; Wagner, N. J. *Langmuir* **2001**, *17*, 3136-3147.
- <sup>38</sup> Hoffmann, M.; Jusufi, A.; Schneider, C.; Ballauff, M. *J. Colloid Interface Sci.* **2009**, *338*, 566-572.
- <sup>39</sup> Mei, Y.; Wittemann, A.; Sharma, G.; Koch, T.; Gliemann, H.; Horbach, J.; Schimmel, T.; Ballauff, M. *Macromolecules* **2003**, *36*, 3452-3456.
- <sup>40</sup> Crassous, J. J.; Wittemann, A.; Siebenbürger, M.; Schrinner, M.; Drechsler, M.; Ballauff, M. *J. Colloid Interface Sci.* **2008**, *286*, 805-812.
- <sup>41</sup> Lu, Y.; Mei, Y.; Drechsler, M.; Ballauff, M. *J. Phys. Chem. B* **2006**, *110*, 3930-3937.
- <sup>42</sup> Samokhina, L.; Schrinner, M.; Ballauff, M. *Langmuir* **2007**, *23*, 3615-3619.
- <sup>43</sup> Wagner, M.; Brochard-Wyart, F.; Hervet, H.; de Gennes, P.-G. *Colloid Polym. Sci.* **1993**, *271*, 621-628.
- <sup>44</sup> Currie, E. P. K.; Fleer, G. J.; Cohen Stuart, M. A.; Borisov, O. *Eur. Phys. J. E* **2000**, *1*, 27-40.
- <sup>45</sup> Bektrouv, E. A.; Kudaibergenov, S. E.; Rafikov, S. R. *Macromol. Chem. Phys.* **1990**, *C30*, 233-240.
- <sup>46</sup> Salamone, J. C.; Tsai, C. C.; Watterson, A. C.; Olsen, A. P. *Polymer* **1978**, *19*, 1157-1162.
- <sup>47</sup> Mary, P.; Bendejacq, D. D. *J. Phys. Chem. B* **2008**, *112*, 2299-2310.
- <sup>48</sup> Kabanov, V. A. in *Multilayer thin films. Sequential assembly of nanocomposite materials* Decher, G. and Schlenoff, J. eds., Wiley-VCH: Weinheim, 2002.



*References*

---

# 8. Summary/Zusammenfassung

## Summary

The main objective of this thesis was the synthesis of colloidal stable managanese oxide nanoparticles ( $\text{MnO}_x\text{NP}$ ) for applications as a catalyst in aqueous solution. Spherical polyelectrolyte brushes (SPBs) with poly(2-trimethyl ammonium ethyl methacrylate chloride) (pTMAEMC) chains were used as support particles to stabilize the  $\text{MnO}_x\text{NP}$  by immobilization. In a first step we established and investigated the method of the *in situ* generation of the  $\text{MnO}_x\text{NP}$  within SPBs. It was found that no reducing agent is needed for the reduction of the  $\text{MnO}_4^-$  precursors and that the precursor does not react with the cationic polymer chains of the SPBs. Hence, the mechanism of the generation of  $\text{MnO}_x\text{NP}$  was explained by a catalytic decomposition of  $\text{KMnO}_4$  in the basic environment of the brush layer. By a combination of powder X-ray diffraction (PXRD), transmission electron microscopy (TEM) and cryogenic TEM (cryoTEM) it was found that the platelet-like  $\text{MnO}_x\text{NP}$  are of layered topology built up from  $\text{MnO}_6$  octahedra denoted as birnessite. The PXRD patterns revealed a disorder along the stacking direction of the single layers of hexagonal sheets. Furthermore, the structure of the composite material observed by TEM strongly differs compared to that in cryoTEM micrographs.

Due to the complicated characterization of the  $\text{MnO}_x\text{NP}$  by conventional methods, the composite material was furthermore analyzed by high resolution TEM (HRTEM). In addition, X-ray absorption fine structure (XAFS) analysis was conducted to study the local structure of the nanoparticles on an atomic scale. The qualitative X-ray absorption near-edge structure (XANES) analysis using several reference compounds confirmed the crystallographic similarity of the  $\text{MnO}_x\text{NP}$  to a c-disordered birnessite. The local structure of the  $\text{MnO}_x\text{NP}$  was investigated by a quantitative extended X-ray absorption fine structure (EXAFS) analysis. One main issue was the finding that no significant difference is present between the  $\text{MnO}_x\text{NP}@\text{SPB}$  in aqueous solution and in the dried state. In general, the hexagonal sheets predominantly composed of edge-share  $\text{MnO}_6$  octahedra are compressed along the c-direction, that is, along the stacking direction. This effect is accompanied by a slight elongation within the ab-plane that means within the two dimensional expansion of the sheets. Additionally, a new kind of composite material composed of star-shaped pTMAEMC homopolymer and  $\text{MnO}_x\text{NP}$  was synthesized. An analysis by HRTEM, PXRD and XAFS showed a high congruity to the structure of the disk-like  $\text{MnO}_x\text{NP}$  to that of the nanoparticles immobilized on SPBs.

To test the  $\text{MnO}_x\text{NP}@\text{SPB}$  composite material for its catalytic activity, the oxidation of morin by hydrogen peroxide was established as a model reaction. It could be shown by UV/vis measurements that the rate of the decomposition is highly depending on the ratio between morin and the oxidant  $\text{H}_2\text{O}_2$ . This finding was modeled by a Langmuir-Hinshelwood reaction mechanism, assuming the adsorption of both reactants and an adjacent surface reaction of the adsorbed species. The study proved the potential application of the composite material as a catalyst especially for water-based catalysis.

## Zusammenfassung

---

Furthermore, a detailed kinetic analysis of the reduction of 4-nitrophenol by NaBH<sub>4</sub> using gold and platinum nanoparticles immobilized on SPBs has been conducted. In analogy to the work on the oxidative decomposition of morin, a Langmuir-Hinshelwood model was used for the description of the reaction mechanism. Using this model, the adsorption constants for both reactants as well as the rate constant of the surface reaction could be determined for both noble metal nanoparticles. This showed that the higher catalytic activity of Pt is mainly due to the higher rate constant of the surface reaction. Additionally, the induction period of the reduction of 4-nitrophenol could be assigned to a surface reconstructing of the nanoparticles due to the adsorption of 4-nitrophenol.

Finally, the synthesis of a novel zwitterionic SPB could be realized using aqueous atom transfer radical polymerization. These particles show a surprisingly high colloidal stability in aqueous medium though the poly(2-(methacryloyloxy)ethyl dimethyl-(3-sulfopropyl)ammonium hydroxide) (pMEDSAH) chains are not soluble in pure water. The solution behavior in water was furthermore studied by dynamic light scattering, TEM and cryoTEM proving the collapsed state of the brush layer. The zwitterionic shell undergoes an internal phase separation leading to a surface-near layer whereas only a minor part of the chains reaches further out into the solution. The collapse was explained by the formation of aggregates of monomer units by zwitterionic or hydrophobic interactions. It was shown that the zwitterionic shell swells upon the addition of high amounts of salts. An increase of the temperature led to an increase of the hydrodynamic brush thickness due to the upper critical solution temperature behavior of the pMEDSAH chains.

In conclusion, this thesis presented a new method for the generation and stabilization of MnO<sub>x</sub>NP of layered topology using cationic SPBs. The mechanism of the *in situ* generation could be elucidated as well as the microscopic structure of the composite material in the aqueous dispersed state. Using state of the art characterization methods like XAFS, the local environment of the MnO<sub>x</sub>NP around the Mn absorber could be determined. The catalytic activity of the MnO<sub>x</sub>NP was studied in detail applying a Langmuir-Hinshelwood model to the catalytic degradation of morin. A similar study gave new insights into the reduction of 4-nitrophenol using noble metal nanoparticles applying a similar model. The synthesis and analysis of zwitterionic SPBs gave important information about their solution behavior.

## Zusammenfassung

Die Hauptaufgabenstellung dieser Arbeit lag in der Synthese und Charakterisierung von MnO<sub>x</sub>NP und deren Verwendung als Katalysator in wässriger Lösung. Die daher notwendige Stabilisierung der MnO<sub>x</sub>NP wurden durch Aufbringung auf sphärischen Polyelektrolytbürsten (SPBs) als Trägerpartikel erzielt. Es wurde eine Synthese zur *in-situ*-Generierung von MnO<sub>x</sub>NP auf SPBs entwickelt und diese anschließend im Detail untersucht. Dabei wurde gezeigt, dass keinerlei Zugabe eines Reduktionsmittels zur Reduktion des KMnO<sub>4</sub> notwendig ist und keine Reaktion der MnO<sub>4</sub><sup>-</sup>-Ionen mit den Monomereinheiten der Polymerschale des

SPB stattfindet. Darauf basierend wurde das Modell der basisch katalysierten Zersetzung der  $\text{MnO}_4^-$ -Ionen innerhalb der Polymerbürste aufgestellt. Pulverdiffraktometrie, TEM- und cryoTEM-Studien konnten den Aufbau der  $\text{MnO}_x\text{NP}$  aus zweidimensionalen, hexagonalen Schichten, welche aus kantenverknüpften  $\text{MnO}_6$ -Oktaedern bestehen, verdeutlichen. Die fehlende Stapelordnung der einzelnen Schichten konnte ebenfalls durch Pulverdiffraktometrie gezeigt werden. Außerdem konnte ein Vergleich von TEM und cryoTEM Aufnahmen des Kompositmaterials starke Abweichungen bezüglich der Morphologie im getrockneten und dispergierten Zustand aufzeigen.

Auf Grund der teils schwierigen Charakterisierung der  $\text{MnO}_x\text{NP}$  wurde zusätzlich HRTEM Untersuchungen durchgeführt. Weiterhin wurde die lokale Struktur innerhalb der  $\text{MnO}_x\text{NP}$  mittels XAFS untersucht. Ein Vergleich des XANES Bereichs des Kompositmaterials mit denen verschiedener Referenzverbindungen zeigte dessen starke Ähnlichkeit zu Birnessitstrukturen. Eine qualitative Bestimmung der lokalen Struktur der  $\text{MnO}_x\text{NP}$  erfolgte durch die Auswertung der EXAFS. Dabei wurden keine Unterschiede in der Kristallstruktur der  $\text{MnO}_x\text{NP}$  in dispergiertem und in getrocknetem Zustand gefunden. Die einzelnen hexagonalen Plättchen sind innerhalb ihrer Stapelrichtung gestaucht wohingegen sie eine leichte Expansion bezüglich ihrer lateralen, zweidimensionalen Ausdehnung aufweisen. Zusätzlich konnte ein weiteres Kompositmaterial hergestellt werden. Dieses besteht aus sternförmigen pTMAEMC Homopolymer und  $\text{MnO}_x\text{NP}$ . Untersuchungen mittels HRTEM, PXRD und XAFS zeigten die großen Gemeinsamkeiten der Nanopartikel zu denen auf SPB immobilisierten  $\text{MnO}_x\text{NP}$ .

Die Oxidation von Morin durch  $\text{H}_2\text{O}_2$  wurde als Modellreaktion zur Bestimmung der katalytischen Aktivität des Kompositmaterials  $\text{MnO}_x\text{NP}@\text{SPB}$  herangezogen. Durch UV/vis Messungen konnte die Abhängigkeit der Reaktionsgeschwindigkeit sowohl von der Morinkonzentration als auch der Konzentration an  $\text{H}_2\text{O}_2$  gezeigt werden. Dieses Verhalten wurde durch einen Reaktionsmechanismus nach Langmuir-Hinshelwood erklärt. Die Untersuchungen lieferten erste Hinweise auf die Eignung des Kompositmaterials als Oxidationskatalysator, v.a. im wässrigen Medium.

Des Weiteren wurde das Langmuir-Hinshelwood Modell auf die katalytische Reduktion von 4-Nitrophenol durch Natriumborhydrid unter Verwendung von Gold- und Platinnanopartikeln angewendet. Dadurch konnten sowohl die Adsorptionskonstanten der Edukte als auch die Geschwindigkeitskonstante der Oberflächenreaktion bestimmt werden. Dies zeigte, dass die höhere Aktivität der Platinanopartikel gegenüber den Goldnanopartikeln hauptsächlich auf die höhere Geschwindigkeitskonstante der Oberflächenreaktion zurückzuführen ist. Außerdem konnte die auftretende Induktionsperiode einer Oberflächenrestrukturierung durch die Adsorption von 4-Nitrophenol zugeordnet werden.

Zuletzt wurde die Synthese einer neuen Art von zwitterionischer SPB mittels wässriger ATRP realisiert. Die Partikel zeigten trotz der schlechten Löslichkeit der pMEDSAH Ketten der Polymerschale in Wasser eine erstaunliche Stabilität im dispergierten Zustand. Daher wurde ihr Verhalten in Lösung mit dynamischer Lichtstreuung, TEM und cryoTEM untersucht. Diese Untersuchungen zeigten, dass die zwitterionische Polymerschale hauptsächlich in einem kollabierten Zustand in Wasser vorliegt, wobei nur ein geringer Anteil

## Zusammenfassung

---

an pMEDSAH Ketten aus dieser Schichte weiter in Lösung herausragt. Der Kollaps der Schale wurde auf die Ausbildung zwitterionischer Aggregate bzw. auf hydrophobe Wechselwirkungen zurückgeführt. Die Aggregate werden bei hohen Salzkonzentrationen aufgelöst und die Polymerschale der SPBs dehnt sich aus. Auf Grund der „upper critical solution temperature“ von pMEDSAH führt eine Erhöhung der Temperatur zu selbigem Effekt, welcher durch Salzzugabe noch deutlich verstärkt werden kann.

Zusammenfassend lässt sich sagen, dass diese Arbeit eine neue Methode zur Herstellung und Stabilisierung von schichtartig aufgebauten  $MnO_xNP$  unter Verwendung von kationischen SPBs präsentiert. Es wurde sowohl der Mechanismus der Entstehung der Nanopartikel untersucht als auch eine detaillierte strukturelle Charakterisierung der  $MnO_xNP$  durchgeführt. Weiterhin wurde die Morphologie der Kompositpartikel in dispergiertem Zustand durch cryoTEM Aufnahmen aufgeklärt. Die katalytische Aktivität wurde im Rahmen der Untersuchungen zur Oxidation von Morin mit  $H_2O_2$  durch die Anwendung eines Langmuir-Hinshelwood Modells untersucht. Eine ähnliche Analyse lieferte neue Informationen zur katalytischen Reduktion von 4-Nitrophenol mittels  $NaBH_4$  in Anwesenheit von Gold- und Platinnanopartikeln. Zuletzt wurden neuartige SPBs mit einer zwitterionischen Schale mittels ATRP hergestellt. Untersuchungen zum Lösungsverhalten der Systeme in Wasser erbrachten neue Ergebnisse, die zu einem besseren Verständnis zwitterionischer SPBs führten.

# A List of Publications

## A1. Publications of this Thesis

Polzer, F.; Kunz, D. A.; Breu, J.; Ballauff, M.: Formation of Ultrathin Birnessite-Type Nanoparticles Immobilized on Spherical Polyelectrolyte Brushes, *Chem. Mater.* **2010**, 22, 2916-2922.

Polzer, F.; Holub-Krappe, E.; Rossner, H.; Erko, A.; Kirmse, H.; Plamper, F.; Schmalz, A.; Müller, A. H. E.; Ballauff, M.: Structural Analysis on Colloidal MnO<sub>x</sub> Composites by X-ray Absorption Fine Structure, submitted.

Polzer, F.; Wunder, S.; Ballauff, M.: Catalytic Oxidation of an Organic Dye by MnO<sub>x</sub> Nanoparticles Immobilized on Spherical Polyelectrolyte Brushes, accepted by the *Journal of Catalysis* **2012**.

Wunder, S.; Polzer, F.; Lu, Y.; Mei, Y.; Ballauff, M.: Kinetic Analysis of Catalytic Reduction of 4-Nitrophenol by Metallic Nanoparticles Immobilized in Spherical Polyelectrolyte Brushes, *J. Phys. Chem. C* **2010**, 42, 7122-7128.

Polzer, F.; Heigl, J.; Schneider, C.; Borisov, O.; Ballauff, M.: Synthesis and Analysis of Zwitterionic Spherical Polyelectrolyte Brushes in Aqueous Solution, *Macromolecules* **2011**, 44, 1654-1660.

## A2. Publications as a co-Author

Mei, Y.; Lu, Y.; Polzer, F.; Drechsler, M.; Ballauff, M.: Catalytic Activity of Palladium Nanoparticles Encapsulated in Spherical Polyelectrolyte Brushes and Core-Shell Microgels, *Chem. Mater.* **2007**, 19, 1062-1069.

Yu, M.; Lu, Y.; Schrinner, M.; Polzer, F.; Ballauff, M.: Spherical Polyelectrolyte Brushes as Carriers for Catalytically Active Metal Nanoparticles. *Macromol. Symp.* **2007**

Schrinner, M.; Polzer, F.; Mei, Y.; Lu, Y.; Haupt, B.; Goeldel, A.; Drechsler, M.; Preussner, J.; Glatzel, U.; Ballauff, M.: Mechanism of the Formation of Amorphous Gold Nanoparticles within Spherical Polyelectrolyte Brushes. *Macromol. Chem. Phys.* **2007**, 208, 1542-1547.

Bolisetty, S.; Schneider, C.; Polzer, F.; Ballauff, M.; Li, W.; Zhang, A.; Schlüter, D.: Formation of Stable Mesoglobules by a Thermosensitive Dendronized Polymer. *Macromolecules* **2009**, 42, 7122-7128.

Lu, Y.; Yuan, J.; Polzer, F.; Drechsler, M.; Preussner, J.: In-situ Growth of Catalytic Active Au-Pt Bimetallic Nanorods in Thermo-Responsive Core-Shell Microgels. *ACS Nano* **2010**, *4*, 7078-7886.

Rochette, C.; Rosenfeldt, S.; Henzler, K.; Polzer, F.; Mecking, S.; Tong, Q.; Drechsler, M.; Theyencheri, N.; Harnau, L.; Ballauff, M.: Annealing of Single Lamella Nanoparticles of Polyethylene, *Macromolecules* **2011**, *44*, 4845-4851.

Kaiser, J., Welz, H., Polzer, F.; Wunder, S.; Ballauff, M.; Lu, Y.; Wanderka, N.; Albrecht, M.; Lunkenbein, T.; Breu, J.; Leppert, L.; Kümmel, S.: Influence of Defects on the Catalytic Activity of Au-Pd Nanoalloys, To be submitted.

Crassous, J.; Millard, P.; Mihut, A.; Polzer, F.; Ballauff, M.; Schurtenberger, P.: Asymmetric Self-Assembly of Oppositely Charged Composite Microgels and Gold Nanoparticles, *Soft Matter* **2012**, *8*, 1648-1656.

### **A3. Patents submitted during the Course of the Thesis**

Patent zur Immobilisierung homogener Bleichkatalysatoren auf sphärischen Polyelektrolytbürsten in Zusammenarbeit mit der Henkel AG & Co. KGaA, submitted in **2009**.

Patent zur Herstellung von nanopartikulärem Braunstein auf sphärischen Polyelektrolytbürsten für die Anwendung in der Bleichkatalyse in Zusammenarbeit mit der Henkel AG & Co. KGaA, submitted in **2009**.

## **B Presentations at International Conferences and Meetings**

- Bayreuther Polymer Symposium, Bayreuth, Germany, September 9-11, 2007; *poster presentation*: Synthesis and Characterization of Metal Nanoparticles on Spherical Polyelectrolyte Brushes and Their Applications in Catalysis.
- 3<sup>rd</sup> International Workshop on Layered Materials: Design and Function; Bochum, Germany; May 14-15, 2010; *poster presentation*: Formation of Ultrathin Birnessite-Type Nanoparticles Immobilized on Spherical Polyelectrolyte Brushes.
- Conference of the European Colloids and Interfaces Society; Prague, Czech Republic; September 5 – 10, 2010; *poster presentation*: Spherical Polyelectrolyte Brushes as Colloidal Templates and Carriers for Ultrathin Manganese Oxide Nanoparticles.
- 2<sup>nd</sup> International Conference on Multifunctional, Hybrid and Nanomaterials; Strassburg, France; March 6 – 10, 2011; *poster presentation*: XAS Study on MnO<sub>x</sub> Nanoparticles Immobilized on Spherical Polyelectrolyte Brushes.

---

# C Abbreviations

Amp	4-aminophenol
ATRP	Atom transfer radical polymerization
BIEM	2-(2-bromoisobutyryloxy)ethyl methacrylate
Bipy	2,2'-bipyridyl
CN	Coordination number
CryoTEM	Cryogenic transmission electron microscopy
DCM	Dichlormethane
DLS	Dynamic light scattering
DP	Degree of polymerization
DVB	Divinyl benzene
EDX	Energy dispersive X-Ray analysis
ER	Eley-Rideal
EXAFS	Extended X-ray absorption fine structure
FESEM	Field emission scanning electron microscopy
FT	Fourier transform
GPC	Gel permeation chromatography
HMEM	2-[p-(2-hydroxy-2-methylpropiope-none)]-ethyleneglycol methacrylate
HRTEM	High resolution transmission electron microscopy
IC	Ion chromatography
ICP-OES	Inductive coupled plasma optical emission spectroscopy
KPS	Potassium peroxodisulfate
LH	Langmuir-Hinshelwood
MEDSAH	[2-(methacryloyloxy)ethyl]dimethyl(3-sulfopropyl) ammonium hydroxide
MnO <sub>x</sub> NP	MnO <sub>x</sub> nanoparticles
MWD	Molecular weight distribution
Nip	4-nitrophenol
NMR	Nuclear magnetic resonance spectroscopy
NP	Nanoparticle
OL	Octahedral layered
OMS	Octahedral molecular sieve
PCBMA	Poly(1-carboxy-N,N-dimethyl-N-(2'-methacryloyloxyethyl)methanaminium inner salt)
PDI	Polydispersity index
PDMAEMA	Poly(2-diethylamino)ethyl methacrylate
PE	Polyelectrolyte
PMAA	Poly(methacrylic acid)

---

PMEDSAH	Poly[2-(methacryloyloxy)ethyl]dimethyl(3-sulfopropyl) ammonium hydroxide
PMPC	Poly(2-methacryloyloxyethyl phosphoryl choline)
PS	Polystyrene
PTMAEMC	Poly(2-trimethylammonium ethyl methacrylate chloride)
PXRD	Powder X-ray diffraction
SDS	Sodium dodecylsulfate
SPB	Spherical polyelectrolyte brush
TEM	Transmission electron microscopy
TGA	Thermogravimetric analysis
TMAEMC	2-trimethylammonium ethyl methacrylate chloride
UCST	Upper critical solution temperature
UF	Ultrafiltration
UV/vis	UV/visible spectroscopy
XAFS	X-ray absorption fine structure
XANES	X-ray absorption near-edge structure

## D Danksagung

Mein Dank gilt in erster Linie allen meinen Freunden die mich während meines Studiums und meiner Promotion in Bayreuth und Berlin begleitet haben und die für den nötigen Ausgleich während der Doktorarbeit gesorgt haben.

Ein ganz besonderer Dank gilt meinem hochgeschätzten Doktorvater Herrn Prof. Matthias Ballauff, der stets hinter meiner Arbeit stand und diese jederzeit und bereitwillig mit interessanten Diskussionen und Anregungen bereichert hat. Sein Interesse hielt die Motivation stets hoch und die eingeräumten Freiheiten bei der Bearbeitung der Doktorarbeit empfand ich durchweg als sehr angenehm.

Bedanken möchte ich mich des Weiteren bei Marc Schrinner für die schöne gemeinsame Zeit im Labor in Bayreuth und für die stets sehr gute Zusammenarbeit.

Matthias Hanisch möchte ich ebenfalls für das entspannte Arbeitsklima im Labor danken. Ich wünsche ihm alles erdenklich Gute und viel Erfolg bei seiner eigenen Doktorarbeit.

Dr. Björn Haupt bin ich für die angenehme und unkomplizierte Zusammenarbeit im gemeinsamen Büro am Helmholtz-Zentrum Berlin sehr verbunden. Für seinen neuen Lebensabschnitt wünsche ich ihm alles Gute.

Weiterer Dank gilt meinen Praktikanten und Bachelorabsolventen Johannes Heigl und Hannes Welz für ihre engagierte Mitarbeit und freundliche Art. Den beiden wünsche ich auf ihrem weiteren Weg durch das Chemiestudium viel Erfolg.

Bei Herrn Karl-Heinz Lauterbach möchte ich mich für seine enorme Hilfsbereitschaft und sein großes Engagement für den Erhalt des geregelten Laborbetriebs in Bayreuth herzlich bedanken. Seine Anekdoten werden mich wohl auch in Zukunft noch des Öfteren erheitern.

Bei Frau Elisabeth Düngfelder und Frau Christa Bächer möchte ich mich für die administrative Hilfe während meines Aufenthalts in Bayreuth bedanken. Selbiges gilt für Frau Nikoline Hansen und Frau Marlies Schneider, die mich durch die Wogen der Bürokratie am Helmholtzzentrum Berlin gelöst haben.

Herrn Dr. Markus Drechsler möchte ich für die Einführung in die Transmissions-elektronenmikroskopie, v.a. aber für die Einarbeitung in die Technik der cryogenen Transmissionselektronenmikroskopie danken.

Dr. Holm Kirmse danke ich für angenehme Zusammenarbeit bei der Einweisung am hochauflösenden Transmissionselektronenmikroskop. Seine Unterstützung bei der Vorbereitung der Installation des Transmissionselektronenmikroskops für cryogenen Transmissionselektronenmikroskopie im „Joint Lab for Structural Research“ der Humboldt Universität zu Berlin und des Helmholtz-Zentrums Berlin war für mich von unschätzbarem Wert.

Frau Elisabeta Holub-Krappe und Herrn Hermann Rossner möchte ich vielmals für die sehr hilfreichen Diskussionen und Hilfestellungen zum Thema Röntgenabsortionsfeinstruktur-spektroskopie danken.

Bei allen Kollegen am Lehrstuhl Physikalische Chemie I an der Universität Bayreuth und am Institut für weiche Materie und funktionale Materialien am Helmholtz-Zentrum Berlin für Materialien und Energie möchte ich mich für das gute Arbeitsklima bedanken.

---

Besonders hervorheben möchte ich an dieser Stelle meinen langjährigen Kommilitonen, Kollegen, Mitbewohner und v.a. Freund, Christian Schneider. Seine fachliche Kompetenz und unsere Freundschaft haben mir sehr oft weitergeholfen. Ich wünsche Christian viel Erfolg für seine private und berufliche Zukunft.

Der größte Dank gilt meinen Eltern und meiner gesamten Familie. Ohne euer Vertrauen und eure stetige Unterstützung wäre all das nicht möglich gewesen. Ich hoffe ich kann euch an dieser Stelle etwas eurer Liebe und eures Engagements zurückgeben.

## **E Schlusserklärung**

Hiermit erkläre ich, dass ich die vorliegende Arbeit selbstständig verfasst und keine anderen als die angegebenen Quellen und Hilfsmittel benutzt habe. Ferner erkläre ich, dass ich nicht anderweitig mit oder ohne Erfolg versucht habe eine Dissertation einzureichen oder mich einer Doktorprüfung zu unterziehen.

Bayreuth, den 16. Februar 2011,

---

Frank Polzer

---